University of Cyprus

DEPARTMENT OF MATHEMATICS AND STATISTICS

VISCOPLASTIC FLOWS WITH WALL SLIP AND PRESSURE-DEPENDENT RHEOLOGICAL PARAMETERS

DOCTOR OF PHILOSOPHY DISSERTATION

PANDELITSA PANASETI

2018

University of Cyprus

DEPARTMENT OF MATHEMATICS AND STATISTICS

VISCOPLASTIC FLOWS WITH WALL SLIP AND PRESSURE-DEPENDENT RHEOLOGICAL PARAMETERS

PANDELITSA PANASETI

A dissertation submitted to the University of Cyprus in partial fulfillment of the requirements for the degree of Doctor of Philosophy

DECEMBER 2018

VALIDATION PAGE

Doctoral Candidate: Pandelitsa Panaseti

Thesis Title: Viscoplastic flows with wall slip and pressure-dependent rheological parameters

The present Doctoral Dissertation was submitted in partial fulfillment of the requirements for the degree of Doctor of Philosophy at the ***Department of Mathematics and Statistics*** *and was approved on the 19th of December, 2018 by the members of the* ***Examination Committee****.*

Examination Committee:

Georgios Georgiou (Research Supervisor), Professor, Department of Mathematics and Statistics, University of Cyprus: _____

Lorenzo Fusi, Professor, Department of Mathematics and Informatics, University of Florence, Italy: _____

Kostas Housiadas, Professor, Department of Mathematics, University of the Aegean, Samos: _____

Emmanouil Milakis, Associate Professor, Department of Mathematics and Statistics, University of Cyprus:_____

Christos Xenophontos (Chairman), Professor, Department of Mathematics and Statistics, University of Cyprus: _____

DECLARATION OF DOCTORAL CANDIDATE

The present doctoral dissertation was submitted in partial fulfillment of the requirements for the degree of Doctor of Philosophy of the University of Cyprus. It is a product of original work of my own, unless otherwise mentioned through references, notes, or any other statements.

Pandelitsa Panaseti

……..

Περίληψη

Τα ιξωδοπλαστικά υλικά συμπεριφέρονται ως ρευστά ή ως στερεά αν η τάση είναι μικρότερη ή μεγαλύτερη από την τάση διαρροής (yield-stress), αντίστοιχα. Αυτή η διττή συμπεριφορά έχει ως αποτέλεσμα το ότι το πεδίο ροής χωρίζεται σε περιοχές διαρροής και μη διαρροής. Είναι, επίσης, γνωστό ότι τα ιξωδοπλαστικά υλικά τείνουν να ολισθαίνουν στα τοιχώματα. Η παρούσα διατριβή έχει δύο κύριους στόχους. Ο πρώτος στόχος είναι η επίλυση της ροής Poiseuille ενός ρευστού Herschel-Bulkley με διαφορετική ολίσθηση στα δύο τοιχώματα και η επέκταση της έρευνας των Philippou et al. (2016), προκειμένου να διερευνηθεί η ανάπτυξη της ιξωδοπλαστικής ροής στην περίπτωση ενός αγωγού με ολίσθηση μόνο στο ένα τοίχωμα. Ο δεύτερος κύριος στόχος, αφορά στην επέκταση της 'λιπαντικής μεθόδου' (lubrication method) των Fusi et al. (2015) και την επίλυση της ροής ενός ρευστού Herschel-Bulkley με ρεολογικές παραμέτρους εξαρτώμενες από την πίεση, στην περίπτωση συμμετρικών ή μη συμμετρικών αγωγών.

Στο πρώτο μέρος της διατριβής, μελετούμε τη μόνιμη ροή ενός ρευστού Herschel-Bulkley υπό πίεση, υποθέτοντας ότι ισχύουν διαφορετικές εξισώσεις ολίσθησης στα δύο τοιχώματα. Καθώς ο συντελεστής πίεσης αυξάνεται, παρατηρούνται τρεις διαφορετικές περιοχές ροής. Η επέκταση των διαφορετικών περιοχών ροής εξαρτάται από το πλάτος του αγωγού. Τα θεωρητικά αποτελέσματα συμφωνούν με πειραματικά δεδομένα για μαλακά υαλώδη εναιωρήματα, τα οποία διεξήγαγαν οι Vayssade et al. (2014). Επιπλέον, μελετούμε τη ροή ενός ρευστού Herschel-Bulkley σε οριζόντιο αγωγό, υποθέτοντας ότι η ολίσθηση εμφανίζεται μόνο στο άνω τοίχωμα και χρησιμοποιώντας μια εξίσωση ολίσθησης εκθετικής μορφής. Παρουσιάζουμε τις μονοδιάστατες πλήρως ανεπτυγμένες λύσεις και προσδιορίζουμε τις διαφορετικές περιοχές ροής. Χρησιμοποιούμε τη Μέθοδο των Πεπερασμένων Στοιχείων και το μοντέλο Παπαναστασίου για εξομάλυνση της καταστατικής εξίσωσης και επιλύουμε αριθμητικά τη δυσδιάστατη αναπτυξιακή ροή. Δεδομένου ότι ο κλασικός ορισμός του μήκους ανάπτυξης δεν είναι εφαρμόσιμος, λαμβάνεται υπόψην το ολικό μήκος ανάπτυξης (global development length) καθώς και το μήκος ανάπτυξης ως προς το άνω τοίχωμα (upper-wall development length). Οι συνδυασμένες επιδράσεις της ολίσθησης και του αριθμού Bingham διερευνώνται, επίσης.

Στο δεύτερο μέρος της διατριβής, επεκτείνουμε την προσέγγιση που προτείνεται από τους Fusi et al. (2015) για πλαστικά Bingham, προκειμένου να μοντελοποιήσουμε τη ροή λίπανσης ενός ρευστού Herschel-Bulkley σε ένα συμμετρικό αγωγό διαφορετικού πλάτους, όπου τόσο ο δείκτης συνάφειας (consistency index) όσο και η τάση διαρροής (yield stress) εξαρτώνται από την πίεση. Επιλύοντας μια ολοκληρωτικό-διαφορική εξίσωση, υπολογίζουμε αριθμητικά την πίεση και χρησιμοποιώντας τις αναλυτικές λύσεις, υπολογίζουμε τη θέση της επιφάνειας διαρροής και τις δύο συνιστώσες της ταχύτητας. Δίνουμε, επίσης, καποιες αναλυτικές λύσεις για αγωγούς σταθερού και γραμμικά-μεταβαλλόμενου πλάτους και υπολογίζουμε αριθμητικά τις λύσεις λίπανσης για άλλες γεωμετρίες. Τέλος, επιλύουμε τη ροή λίπανσης ενός ρευστού Herschel-Bulkley με ρεολογικές παραμέτρους εξαρτώμενες από την πίεση σε έναν ασύμμετρο αγωγό, επεκτείνοντας την πιο πάνω προτεινόμενη μέθοδο.

Abstract

Yield-stress or viscoplastic materials flow like a fluid only when the stress exceeds the yield stress. Otherwise, they beahave as a solid. As a result, the flow field is divided into unyielded and yielded regions. Viscoplastic materials are dispersed systems known to also exhibit wall slip. Two are the main objectives of this thesis. First, to solve the plane Poiseuille flow of a Herschel-Bulkley fluid with asymmetric wall slip and extend the work of Philippou et al. (2016) in order to investigate the development of viscoplastic flow in the particular case of a channel with slip only along one wall. The second objective is the extension of the lubrication method of Fusi et al. (2015) in order to solve the flow of Herschel-Bulkley fluid with pressure-dependent yield stress and consistency index, in the case of long symmetric or asymmetric channels with a general wall functions.

In the first part of the thesis, we consider the steady, pressure-driven flow of a Herschel-Bulkley fluid in microchannel, assuming that different power-law slip equations apply at the two walls, resulting to the asymmetry of the velocity profile. We observe that, as the pressure gradient is increased; three different flow regimes are derived. The extension of the different flow regimes depends on the channel gap. The theoretical results are in agreement with experimental data on soft glassy suspensions, which are obtained by Vayssade et al. (2014). Further, we study the flow development of a Herschel-Bulkley fluid in a horizontal channel, assuming that slip occurs only along the upper wall. A power-law equation is employed. We derive the one-dimensional fully-developed solutions and identify the different flow regimes. We use finite elements along with the Papanastasiou regularization for the Herschel-Bulkley constitutive equation and we solve the two-dimensional development flow, numerically. Since the classical definition of the development length is not applicable, we consider the global and upper-wall development lengths. The combined effects of slip and the Bingham number are also investigated.

In the second part of the thesis, we extend the approach proposed by Fusi et al. (2015) for a Bingham plastic, in order to model the lubrication flow of a Herschel-Bulkley fluid in a symmetric long channel of varying width, where both the consistency index and the yield stress are pressure-dependent. Solving an integro-differential equation, we calculate the pressure, numerically; and using analytical solutions, we compute the position of the yield surface and the two velocity components. We also derive some analytical solutions for channels of constant and linearly-varying widths and calculate the lubrication solutions for other geometries, numerically. Finally, we solve the lubrication flow of a Herschel-Bulkley fluid with pressure-dependent rheological parameters in a long asymmetric channel, extending the above proposed method.

Acknowledgements

I would like to express my deepest appreciation to my supervisor, Professor Georgios Georgiou, for his excellent guidance, caring, patience and encouragement. His enthusiasm about my research inspired me and gave me confidence. His careful editing contributed enormously to the production of this thesis.

I would also like to thank the other members of my committee, Professor Christos Xenophontos, Associate Professor Emmanouil Milakis, Professor Kostas Housiadas and Professor Lorenzo Fusi for their valuable comments.

I am grateful to my beloved family for their unceasing encouragement and support throughout all my studies. Special acknowledgment goes to Iasonas Ioannou who was always willing to help and support my work, checking my calculations and running simulation codes.

Above all I would like to thank my husband Alejandro for his love, personal support and great patience at all times. He has selflessly given more to me than I ever could have asked for.

Pandelitsa Panaseti

Nicosia, December 2018

For Efthymios... who is the reason I smile every day...

For one so small you seem so strong to me...

Table of Contents

List of Figures

$n = 1$ (Bingham plastic) and $\alpha = 0$ (constant plastic viscosity): (a) $\beta = 0$ (constant yield stress); (b) $\beta = 0.2$; (c) $\beta = 0.4$. The unyielded region is shaded……

List of Tables

Chapter 1

Introduction

1.1 Yield-stress fluids

Newtonian fluids obey Newton's linear constitutive equation

$$\boldsymbol{\tau} = \eta\,\dot{\boldsymbol{\gamma}} \tag{1.1}$$

where $\boldsymbol{\tau}$ is the stress tensor, η is the constant shear viscosity,

$$\dot{\boldsymbol{\gamma}} \equiv \nabla\mathbf{u} + (\nabla\mathbf{u})^{T} \tag{1.2}$$

is the rate-of-strain tensor, $\mathbf{u}$ is the velocity vector, $\nabla\mathbf{u}$ is the velocity-gradient tensor and the superscript T denotes the transpose. However, most common materials and materials of industrial importance are not Newtonian. In this particular thesis, we are interested in generalized-Newtonian fluids, i.e. in fluids described by a constitutive relation of the form

$$\boldsymbol{\tau} = \eta\left(\dot{\gamma}\right)\dot{\boldsymbol{\gamma}} \tag{1.3}$$

where the viscosity is not constant but varies with the magnitude of the rate-of-strain tensor

$$\dot{\gamma} \equiv \sqrt{\frac{1}{2}II_{\dot{\gamma}}} = \sqrt{\frac{1}{2}\dot{\boldsymbol{\gamma}} : \dot{\boldsymbol{\gamma}}} \tag{1.4}$$

where the symbol II stands for the second invariant of a tensor (Mitsoulis, 2007). Representative generalized-Newtonian constitutive equations are shown in Fig. 1.1. These are briefly discussed below.

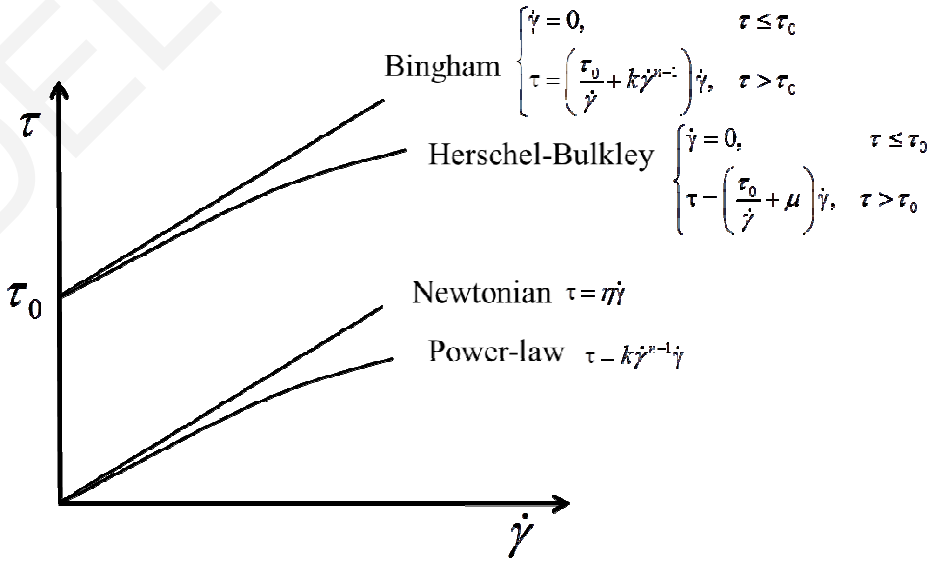

Figure 1.1: The most common generalized Newtonian models.

The power-law model

$$\boldsymbol{\tau} = k\dot{\gamma}^{n-1}\dot{\boldsymbol{\gamma}} \tag{1.5}$$

is the immediate generalization of the Newtonian model, where k is the consistency index and n is the power-law exponent. The power-law model is able to account for shear-thinning (n<1, in which case the viscosity decreases with $\dot{\gamma}$) and shear-thickening (n>1, in which case the viscosity increases with $\dot{\gamma}$) effects. The Newtonian fluid is recovered when n=1 (constant viscosity).

In this thesis, we are interested in yield-stress or viscoplastic materials, which exhibit a yield stress, τ_0 , i.e. a critical stress value below which no deformation (i.e. flow) is allowed and so, the fluid behaves as a rigid body (Mitsoulis, 2007). The material flows like a fluid as soon as the yield stress is exceeded. As a result, the flow field is divided into unyielded (i.e. plug) and yielded regions. The simplest and most widely used viscoplastic model is the Bingham plastic model (Bingham, 1922)

$$\begin{cases} \dot{\boldsymbol{\gamma}} = \mathbf{0}, & \tau \le \tau_0 \\ \boldsymbol{\tau} = \left(\dfrac{\tau_0}{\dot{\gamma}} + \mu \right) \dot{\boldsymbol{\gamma}}, & \tau > \tau_0 \end{cases} \tag{1.6}$$

where μ is the plastic viscosity, and τ is the magnitude of **τ,**

$$\tau \equiv \sqrt{\frac{1}{2} II_{\boldsymbol{\tau}}} = \sqrt{\frac{1}{2} \boldsymbol{\tau} : \boldsymbol{\tau}} \, . \tag{1.7}$$

The Newtonian fluid is recovered by setting τ_0=0. The Herschel-Bulkley model is the immediate generalization of the Bingham model

$$\begin{cases} \dot{\boldsymbol{\gamma}} = \mathbf{0}, & \tau \le \tau_0 \\ \boldsymbol{\tau} = \left(\dfrac{\tau_0}{\dot{\gamma}} + k\dot{\gamma}^{n-1} \right) \dot{\boldsymbol{\gamma}}, & \tau > \tau_0 \end{cases} \tag{1.8}$$

The power-law fluid and the Bingham plastic are special cases of the Herschel-Bulkley fluid, recovered by setting $\tau_0 = 0$ and n=1, respectively. Another well known viscoplastic model is the Casson fluid (Mitsoulis, 2007)

$$\begin{cases} \dot{\boldsymbol{\gamma}} = \mathbf{0}, & \tau \le \tau_0 \\ \boldsymbol{\tau} = \left(\sqrt{\mu} + \sqrt{\dfrac{\tau}{\dot{\gamma}}} \right)^2 \dot{\boldsymbol{\gamma}}, & \tau > \tau_0 \end{cases} \tag{1.9}$$

which is often used to describe the rheological behavior of blood.

Many materials exhibit viscoplastic behavior, such as certain polymer solutions, suspensions and slurries, emulsions, colloids, muds and clays, crystallizing lavas, heavy oils, cosmetic creams and hair gels, food stuff, such as liquid chocolate, pastes; paints, foam, biofluids, such as blood (Wang, 1998; Barnes, 1999). As a consequence, the theory of viscoplastic fluids has

applications in wide array of different fields, ranging from the oil, gas and chemical industries, to food processing, medical and geophysical fluid dynamics.

The existence of yield stress has been the subject of a long debate. Barnes and Walters (1985) claimed that the yield stress is an idealization and all fluids will show Newtonian behavior at small stresses below the apparent yield stress. This assertion caused a flurry of discussion and publication regarding the meaning of the word 'yield stress'. Hartnett and Hu (1989) concluded that 'yield stress is an engineering reality', where a year after, Astarita (1990) claimed that whether yield stress is or is not an engineering reality depends on the problem under consideration. Barnes (1999) stated that the concept of yield stress can be proved and, used correctly, once it is properly defined, delimited and circumscribed. According to Bonn et al. (2017), the existence of yield stress on an experimental base has been established, while Dinkgreve et al. (2017) claimed that the appearance of a Newtonian fluid regime at stresses below the yield value is an artifact.

As already mentioned, a viscoplastic material flows like a fluid as soon as the yield stress is exceeded; otherwise it remains unyielded and behaves as a solid. As a result, the flow field is divided into unyielded $\left(\tau \le \tau_0\right)$ and yielded $\left(\tau > \tau_0\right)$ regions. For example, in plane Poiseuille (i.e. pressure-driven) fully-developed flow of a Bingham plastic fluid the velocity is given by

$$u_x = \begin{cases} \dfrac{1}{2\mu}\dfrac{\tau_0}{y_0}\left(H - y_0\right)^2, & 0 \le y \le y_0 \\ \dfrac{1}{2\mu}\left(-\dfrac{\partial p}{\partial x}\right)\left(H^2 - y^2\right) - \dfrac{\tau_0}{\mu}\left(H - y\right), & y_0 \le y \le H \end{cases} \tag{1.10}$$

where

$$y_0 = \frac{\tau_0}{\left(-\partial p / \partial x\right)} \tag{1.11}$$

is the yield point at which the shear rate vanishes,

$$\dot{\gamma} = \left|\frac{du_x}{dy}\right| = 0 \tag{1.12}$$

H is the width of the channel and $\left(-\partial p / \partial x > 0\right)$ is the imposed pressure gradient. The geometry and some definitions for the particular flow are given in Fig. 1.2. It should be noted that flow occurs only when the pressure gradient exceeds the critical value

$$G_c = \frac{\tau_0}{H} \tag{1.13}$$

In the unyielded part of the flow domain ($0 \le y \le y_0$), the material moves as a solid at a constant speed.

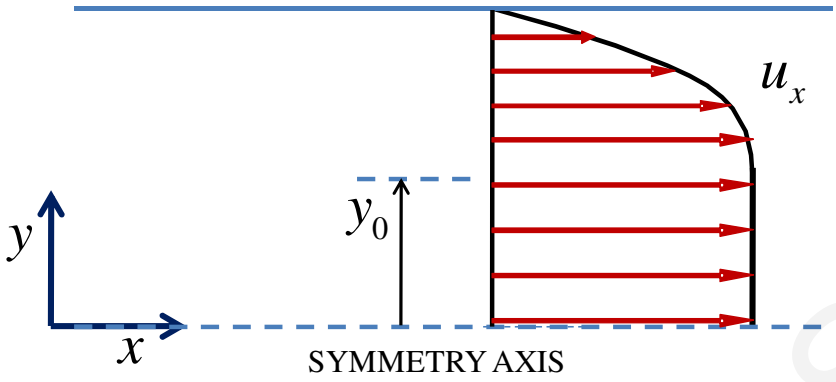

Figure 1.2: Plane Poiseuille flow of a Bingham plastic fluid.

Similarly, in axisymmetric fully-developed Poiseuille flow of a Bingham plastic fluid, the velocity is given by

$$u_z = \begin{cases} \dfrac{1}{2\mu}\dfrac{\tau_0}{r_0}\left(R-r_0\right)^2, & 0 \le r \le r_0 \\ \dfrac{1}{4\mu}\left(-\dfrac{\partial p}{\partial z}\right)\left(R^2-r^2\right)-\dfrac{\tau_0}{\mu}\left(R-r\right), & r_0 \le r \le R \end{cases} \tag{1.14}$$

where

$$r_0 = \frac{2\tau_0}{\left(-\partial p / \partial z\right)} \tag{1.15}$$

is the yield point and R is the radius of the tube (Fig. 1.3).

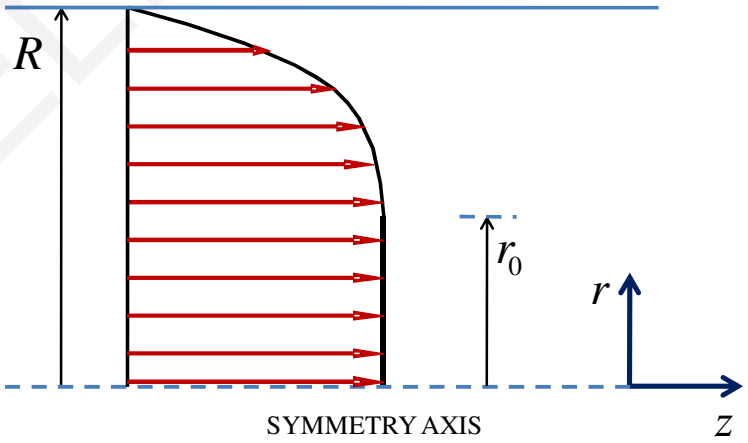

Figure 1.3: Axisymmetric Poiseuille flow of a Bingham plastic fluid.

The critical pressure gradient for the initiation of flow is

$$G_c = \frac{2\tau_0}{R} \tag{1.16}$$

1.2 Wall slip

The no-slip condition for viscous fluids dictates that at a solid boundary, the velocity of the fluid relative to that of the boundary is zero. In other words, the velocity of the fluid, u_F, immediately adjacent to a solid boundary, is identical to the velocity, u_S, of the boundary, i.e. $u_F = u_S$. However, as pointed out by Neto et al. (2005), the no-slip boundary condition remains an assumption not based on physical principles. Its physical origins are believed to be mainly the trapping of liquid in pockets and crevices present on the solid surface and the attractive forces between the molecules of the solid and those of the liquid (Neto et al., 2005). In the past few decades, the validity of the no-slip boundary condition has been questioned. In fact, a plethora of experimental observations provide strong evidence that not only complex but even Newtonian fluids exhibit slip (Neto et al., 2005).

Wall slip is important in many industrial applications, such as the extrusion of complex fluids, ink jet processes, oil migration in porous media, and in microfluidics. In the presence of wall slip, $u_F \neq u_S$ and the difference $u_w = |u_S - u_F|$ is known as the slip velocity.

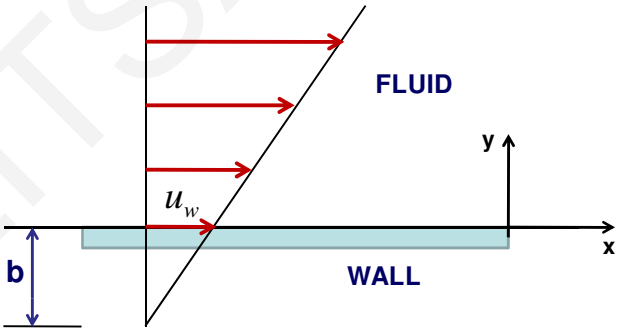

Figure 1.4: Slip velocity and slip length.

Navier (1827) was the first to propose a slip model relating linearly the slip velocity, to the wall shear stress, τ_w. The particular model reads

$$\tau_w = \beta u_w \tag{1.17}$$

where β is the slip coefficient. The latter coefficient incorporates the effects of temperature, the normal stress, the molecular parameters, and the properties of the fluid/wall interface (Denn, 2001; Hatzikiriakos, 2012). The no-slip and full-slip limiting cases are recovered when $\beta \to \infty$ and $\beta = 0$, respectively. In Newtonian flow, the slip coefficient is related to the slip or extrapolation

length b, by means of $\beta \equiv \eta / b$, where η denotes the viscosity. The extrapolation length b is defined as the distance from the wall at which the velocity of the fluid vanishes if this is linearly extrapolated, as illustrated in Fig. 1.4. (In the simple flow illustrated in the latter figure, $\tau_w = \left|\tau_{yx}\right|_w$). As an example, in the case of plane fully-developed Poiseuille flow, the wall shear stress is given by

$$\tau_w = -\tau_{yx}\Big|_{y=H} = H\left(-\frac{dp}{dx}\right) \tag{1.18}$$

Applying the Navier slip equation (1.17), one gets for the slip velocity

$$u_w = \frac{H}{\beta}\left(-\frac{dp}{dx}\right) \tag{1.19}$$

The above expression is valid even when the wall shear stress is below the yield stress or equivalently when the pressure gradient is below the critical value $G_c = \tau_0 / H$ above which the material yields; below this critical value, the material moves as a solid (unyielded) with a uniform velocity , u_w i.e.

$$u_x = u_w = \frac{H}{\beta}\left(-\frac{\partial p}{\partial x}\right) = constant \tag{1.20}$$

Otherwise, the velocity profile is given by

$$u_x(\mathrm{y}) = u_w + \frac{1}{2\mu}\left(-\frac{dp}{dx}\right)\begin{cases}(H-y_0)^2, & 0 \le y \le y_0\\ \left[(H-y_0)^2 - (y-y_0)^2\right], & y_0 \le y \le H\end{cases} \tag{1.21}$$

where the yield point is still given by Eq. (1.11). For the case of axisymmetric Poiseuille flow, the wall shear stress is given by

$$\tau_w = -\tau_{rz}\Big|_{r=R} = \frac{R}{2}\left(-\frac{dp}{dz}\right) \tag{1.22}$$

Applying the Navier slip equation (1.17), gives

$$u_w = \frac{R}{2\beta}\left(-\frac{dp}{dz}\right) \tag{1.23}$$

The velocity is given by

$$u_z = u_w = \frac{R}{2\beta}\left(-\frac{dp}{dz}\right) = constant \tag{1.24}$$

when the pressure gradient is below $G_c = 2\tau_0 / R$; otherwise, the velocity profile given by

$$u_z(r) = u_w + \frac{1}{4\mu}\left(-\frac{dp}{dz}\right)\begin{cases}(R-r_0)^2, & 0 \le r \le r_0\\ \left[(R-r_0)^2 - (r-r_0)^2\right], & r_0 \le r \le R\end{cases} \tag{1.25}$$

where the yield point is still given by Eq. (1.15).

Based on the analysis of apparent slip flows of Herschel-Bulkley fluids in various geometries, Kalyon (2005) proposed a power-law slip equation

$$\tau_w = \beta u_w^s \tag{1.26}$$

where s is the power exponent. Setting s=1 in Eq. (1.26) leads to the classical Navier-slip condition (1.17). It should be noted that both equations are static. Dynamic slip models are discussed in Hatzikiriakos (2012).

In the past thirty years, the power-law slip equation (1.26) has been widely used by several investigators working on various fluid systems. Particularly, Jiang et al. (1986) used Eq. (1.24) to describe the slip exhibited by gels used in hydraulic fracturing. A year earlier, Cohen and Metzner (1985) studied experimentally the occurrence of slip in aqueous and organic polymer solutions. A power-law relationship between the slip velocity and the wall shear stress was also predicted at constant temperature by theoretical model of Lau and Schowalter (1986), which was based on the concept of junctions at the wall/polymer interface and in the bulk of the polymer fluid. Equation (1.26) has also been employed for polyethylene melts (Hatzikiriakos and Dealy, 1992; Hay et al., 2000) and highly-filled suspensions (Yilmazer and Kalyon, 1989). Yilmazer and Kalyon (1989) discussed the validity of Eq. (1.26) and reported values of β and s for certain systems.

Experimental data on several fluid systems, such as colloidal suspensions (Ballesta et al., 2012), pastes (Adams et al., 1997) and highly entangled polymers (Piau and El Kissi, 1994), indicate that slip occurs only when the stress exceeds a critical value τ_c that can be viewed as a 'wall shear', 'interfacial', or, simply, 'slip' yield stress. Hatzikiriakos and Dealy (1991) pointed out that slip model (1.26) fails to describe the slip velocity in the neighborhood of τ_c, which is critical in understanding polymer slip phenomena. Thus, they used the following two-branch equation

$$\tau_w = \begin{cases} 0, & \tau_w \le \tau_c \\ \beta u_w^s, & \tau_w > \tau_c \end{cases} \tag{1.27}$$

Spikes and Granick (2003) reported that for water and tetradecane (which are Newtonian) the slip yield stress may become high for lyophilic wall surfaces and used the following slip equation:

$$\begin{cases} u_w = 0, & \tau_w \le \tau_c \\ \tau_w = \tau_c + \beta u_w & \tau_w > \tau_c \end{cases} \tag{1.28}$$

Also, the following general phenomenological slip equation

$$\begin{cases} u_w = 0, & \tau_w \le \tau_c \\ \tau_w = \tau_c + \beta u_w^s & \tau_w > \tau_c \end{cases} \tag{1.29}$$

has been used by other researchers in the analysis of squeeze flow of generalized Newtonian fluids with apparent wall slip (Yilmazer and Kalyon, 1989; Estellé and Lanos, 2007).

Viscoplastic materials, such as polymeric solutions, suspensions and gels, are dispersed systems known to exhibit wall slip, which arises due to the depletion of particles adjacent to the shearing surface (Yilmazer and Kalyon, 1989; Barnes, 1995; Meeker et al., 2004b; Ballesta et al., 2012; Aktas et al., 2014; Cloitre and Bonnecaze, 2017). Denn (2001) also noted that wall slip in pasty materials appears within a range of small strains in contrast to the case of polymer melts

where slip is observed at large rates of strains. Bonn et al. (2017) stated that wall slip emerges from the combined effects of microstructure (rigid and soft particles), of the chemical nature of the wall and the geometry. Shewan et al. (2017) claimed that the occurrence of slip must be considered as an important and intrinsic feature of the flow and deformation behavior of complex materials. Cloitre and Bonnecaze (2017) pointed out that slip is generally essential within many natural systems and biological processes and emphasized the importance of wall slip in the transport of many complex suspensions, such as mineral and oil suspensions, paints, foods, pharmaceuticals, sewage treatment and soils.

In conclusion, wall slip is an interesting, important and complicated phenomenon. Despite the large body of research regarding wall slip, there is no well-developed theory to predict or explain it, in general (Sochi, 2011). Particularly, it remains challenging to get microscopic insight into slip phenomena and understand their dependence on surface characteristic, flow rate and material properties (Cloitre and Bonnecaze, 2017). This is due to the diversity and complexity of the factors affecting it and also due to the fact that is difficult to observe and measure (Sochi, 2011).

1.3 Pressure-dependence of the viscosity

The idea of a fluid with pressure-dependent viscosity was introduced by Stokes (Stokes, 1845). Much later, Barus (1893) proposed an exponential isothermal equation of state for the Newtonian viscosity of the form

$$\eta(p) = \eta_0 \exp\left[\alpha(p - p_0)\right] \tag{1.30}$$

where p is the pressure, η_0 is the viscosity at the reference pressure p_0, and α is the viscosity-growth or piezo-viscous coefficient, which is positive, $\alpha \geq 0$. Equation (1.30) indicates that the viscosity increases with the pressure difference from the reference pressure. As noted by Rajagopal (2006) the dependence of the viscosity on pressure for fluids like polymer melts and lubricants may be several orders of magnitude stronger than that of density, which justifies the study of incompressible flows with pressure-dependent viscosity. The pressure-dependence of the viscosity becomes important in processes involving high pressures, such as polymer processing, fluid film lubrication, microfluidics, and geophysics (see Kalogirou et al. (2011) and references therein). Goubert et al. (2001) reviewed measurement techniques for evaluating the pressure dependence of viscosity. The viscosity growth coefficient is typically 1-5 10^{-8} Pa^{-1} for polymer melts (Denn, 2008), 1-2 10^{-8} Pa^{-1} for mineral oils (Venner and Lubrecht, 2000), and 2-5 10^{-8} Pa^{-1} for heavy petroleum fractions (Martín-Alfonso et al., 2007).

Other equations describing the pressure-dependence of the viscosity have also been proposed. For more information, the reader is referred to the review paper of Málek and Rajagopal (2007). The linear equation

$$\eta(p) = \eta_0 \left[1 + \alpha(p - p_0)\right] \tag{1.31}$$

which has also been used by various investigators (Renardy, 2003; Kalogirou et al., 2011), is essentially the approximation of the Barus equation (1.30) at low pressures and/or for low values of the viscosity growth coefficient. A source of major concern with Eq. (1.31) is the fact that it does not guarantee positive definiteness of the viscosity which requires the pressure to remain positive (Suslov and Tran, 2008). This limitation is not encountered when using the Barus equation (1.30) or in flows where the pressure difference remains positive, e.g. in Poiseuille flows (Kalogirou et al., 2011).

The effect of pressure has also been studied in the case of non-Newtonian materials. For example, Laun propose the following Barus-type equation for the consistency index of LDPE melts (Laun, 2003)

$$k(p,T) = k_0 \exp\left[\alpha(p - p_0) - \gamma(T - T_0)\right] \tag{1.32}$$

where T is the temperature, T_0 is the reference temperature, and $\gamma \geq 0$ is the temperature coefficient describing the reduction of the viscosity with temperature. Hermoso et al. (2014a) presented experimental viscosity data for shear thinning (non-viscoplastic) oil-based drilling fluids, which show that the viscosity follows a Sisko-Barus (i.e. with an exponential growth term) model in which the consistency and flow indices also vary linearly with pressure. The rheological behavior of drilling fluids is greatly affected by the temperature and pressure conditions and plays an important role in the bottom-hole pressure occurring in deep hot wells (Osisanya and Harris, 2005). Ibeh (2007) reported viscometric data on various drilling fluids suggesting linear and exponential variations of the viscosity with pressure and temperature, respectively. He also pointed out that the effects of temperature on the viscosity prevail at higher pressures, while pressure effects become more pronounced at lower temperatures.

The pressure-dependence of the yield stress is well established in the mechanics of solid and granular materials (see Ionescu et al. (2015) and references therein). The pressure- as well as the temperature-dependence of the rheological parameters has also been the subject of various experimental studies on other viscoplastic materials, especially in the oil and gas industry, e.g. in transport operations design (Darley and Gray, 1988) and in oil drilling, given the high pressures and temperatures encountered in the wells (Osisanya and Harris, 2005).

Politte (1985) proposed a seven-parameter empirical expression for the plastic viscosity of certain drilling fluids as a function of both temperature and pressure. He reported that the yield stress is not a 'strong' function of pressure and becomes even 'weaker' as temperature increases. Houwen and Geehan (1986) proposed a simple four-parameter model to determine both the yield stress and the high-shear-rate viscosity of invert muds as a function of pressure and temperature. Hermoso et al. (2014b) investigated the combined effects of pressure and temperature on the rheological behavior of two oil-based drilling fluids and found that this is described fairly well with the Bingham-plastic or the Herschel-Bulkley models. In the range of their experimental conditions, the power-law exponent was practically unaffected and the yield stress decreased linearly with

temperature and increased linearly with pressure. A similar trend has also been observed in the experiments of Ibeh (Ibeh, 2007) on oil-based drilling fluids at ultra-high pressures and temperatures. Hermoso et al. (2014b) suggested that the increase of yield stress with pressure is associated with the compression effect of different resulting organoclay microstructures. In order to model the isothermal yield-stress behaviour of the two drilling fluids, they employed the following linear equation

$$\tau_y(p) = \tau_0\left[1+\beta(p-p_0)\right] \tag{1.33}$$

where τ_0 denotes the yield stress at a reference pressure p_0 and β is the yield-stress growth coefficient.[1] Hermoso et al. (2014b) reported values of the dimensionless piezo-yield coefficient, $\beta_\tau = \tau_0\beta$, at different temperatures from 40 to 140 ^{o}C, in the range 1-132 10^{-4} Pa/bar. For the variation of the plastic viscosity, they employed a Barus-type (i.e. exponential) equation. The linear law (1.33) corresponds to the so-called Drucker-Prager plasticity (flow/no-flow) criterion in solid mechanics, which can be viewed as a simplification of the Mohr-Coulomb plasticity criterion, where τ_0 is the cohesion and $\tau_0\beta = \tan(\delta_s)$, δ_s being the internal frictional angle (Ionescu et al., 2015).

1.4 Lubrication approximation

The lubrication approximation is a simplification that applies to flows between 'nearly parallel' surfaces. This approximation was first used by Reynolds in 1886 in a study of problems of lubrication (Denn, 1980; Denn 2008). Denn (1980) pointed out that the lubrication approximation is fundamental to the study of polymer processing, coating, calendering, and molding operations. Hence, this method is considered to be one of the most important methods allowing the derivation of approximate solution of the Navier-Stokes equations.

As suggested by Langlois and Deville (2014), the lubrication theory is the hydrodynamical analog of the shell theory, capitalizing on the fact that the physical domain is thin in one direction compared with the others. In other words, lubrication theory describes the flow of the fluid in a geometry where one dimension (for example, the characteristic film thickness, H) is significantly smaller than the others (for example, the characteristic substrate length, L). Hence, assuming that the length L of the channel is much greater than its greatest semi-width, i.e. $L \gg H \equiv \max_{x\in[0,L]} h(x)$, the dimensionless parameter

$$\varepsilon \equiv \frac{H}{L} \ll 1 \tag{1.34}$$

is introduced, which is used for applying the classical lubrication approximation or thin-film approach (Frigaard and Ryan, 2004). The fact that the above ratio is small (that is, $\varepsilon \ll 1$) is the

[1]Note that the symbol β has also been used to denote the slip coefficient in the previous section. We kept the same symbol to be consistent with the symbols employed in the literature. In any case, in the flows with pressure-dependent yield stress considered in this thesis, the material is assumed to stick at the wall (no slip).

key requirement for lubrication theory (Papanastasiou et al., 2000). Hence, taking advantage of the disparity of the length scales, lubrication theory is based on the asymptotic procedure of reduction of the full set of governing equations and boundary conditions to a simplified, highly nonlinear, evolution equation or to a set of equations (Oron et al., 1997).

Lubrication flows are most applicable to processing of materials in liquid form, such as metals, polymers, composites and others (Papanastasiou et al., 2000). As already mentioned, the lubrication equations can be derived by dimensionless analysis, and by order of magnitude comparisons with the full Navier-Stokes equations. In the case of two-dimensional bidirectional, incompressible flow in the absence of gravity, where all changes occur in the $xy-$plane and there is no flow in the 'neutral' $z-$direction, the continuity equation and the two components of the momentum equation read as follows:

$$\frac{\partial v_x}{\partial x}+\frac{\partial v_y}{\partial y}=0 \tag{1.35}$$

$$\rho\left(\frac{\partial v_x}{\partial t}+v_x\frac{\partial v_x}{\partial x}+v_y\frac{\partial v_x}{\partial y}\right)=-\frac{\partial p}{\partial x}+\eta\left(\frac{\partial^2 v_x}{\partial x^2}+\frac{\partial^2 v_x}{\partial y^2}\right) \tag{1.36}$$

$$\rho\left(\frac{\partial v_y}{\partial t}+v_x\frac{\partial v_y}{\partial x}+v_y\frac{\partial v_y}{\partial y}\right)=-\frac{\partial p}{\partial y}+\eta\left(\frac{\partial^2 v_y}{\partial x^2}+\frac{\partial^2 v_y}{\partial y^2}\right) \tag{1.37}$$

where $v_x(x,y)$ and $v_y(x,y)$ are the velocity components in the $x-$ and $y-$directions respectively, and ρ is the mass density of the material. Equations (1.35) – (1.37) are made dimensionless using the following scalings

$$\begin{aligned} x^*&=\frac{x}{L},\quad \mathrm{y}^*=\frac{y}{\varepsilon L},\quad t^*=\frac{tV}{L},\quad h^*=\frac{H}{\varepsilon L},\\ v_x^*&=\frac{v_x}{V},\quad v_y^*=\frac{v_y}{\varepsilon V},\quad p^*=\frac{\varepsilon^2 pL}{\eta V}\end{aligned} \tag{1.38}$$

where ε is of the same order as the channel slope (Papanastasiou et al., 2000). Upon substitution and suppressing asterisks hereafter, the momentum equations read (Panastasiou, 1989):

$$\frac{\partial v_x}{\partial x}+\frac{\partial v_y}{\partial y}=0 \tag{1.39}$$

$$\varepsilon^2 Re\left(\frac{\partial v_x}{\partial t}+v_x\frac{\partial v_x}{\partial x}+v_y\frac{\partial v_x}{\partial y}\right)=-\frac{\partial p}{\partial x}+\varepsilon^2\frac{\partial^2 v_x}{\partial x^2}+\frac{\partial^2 v_x}{\partial y^2} \tag{1.40}$$

$$\varepsilon^4 Re\left(\frac{\partial v_y}{\partial t}+v_x\frac{\partial v_y}{\partial x}+v_y\frac{\partial v_y}{\partial y}\right)=-\frac{\partial p}{\partial y}+\varepsilon^4\frac{\partial^2 v_y}{\partial x^2}+\varepsilon^2\frac{\partial^2 v_y}{\partial y^2} \tag{1.41}$$

where

$$Re\equiv\frac{\rho VL}{\eta} \tag{1.42}$$

is the Reynolds number. The two velocity components and the pressure are expanded in terms of ε as follows:

$$\begin{aligned} v_x &= v_x^{(0)} + \varepsilon v_x^{(1)} + \varepsilon^2 v_x^{(2)} + \ldots \\ v_y &= v_y^{(0)} + \varepsilon v_y^{(1)} + \varepsilon^2 v_y^{(2)} + \ldots \\ p &= p^{(0)} + \varepsilon p^{(1)} + \varepsilon^2 p^{(2)} + \ldots \end{aligned} \tag{1.43}$$

Substituting the above expressions into Eqs. (1.39) - (1.41), and collecting the terms of the same order, leads to a system of ODEs at each order. For example, substituting into the continuity equation (1.39), one gets

$$\frac{\partial v_x^{(0)}}{\partial x} + \frac{\partial v_y^{(0)}}{\partial y} + \varepsilon\left(\frac{\partial v_x^{(1)}}{\partial x} + \frac{\partial v_y^{(1)}}{\partial y}\right) + \varepsilon^2\left(\frac{\partial v_x^{(2)}}{\partial x} + \frac{\partial v_y^{(2)}}{\partial y}\right) + \ldots = 0 \tag{1.44}$$

Similarly, we follow the same process for the two components of the momentum equation. Hence, since all dimensionless derivative terms in the resulting equations are of comparable order, the resulting dimensionless lubrication equations, in the limit of $\varepsilon \approx 0$ or $\varepsilon Re \approx 0,$ giving the zero-order problem,[2] are:

$$\frac{\partial v_x^{(0)}}{\partial x} + \frac{\partial v_y^{(0)}}{\partial y} = 0 \tag{1.45}$$

$$-\frac{\partial p^{(0)}}{\partial x} + \frac{\partial^2 v_x^{(0)}}{\partial y^2} = 0 \tag{1.46}$$

and

$$\frac{\partial p^{(0)}}{\partial y} = 0 \tag{1.47}$$

A consequence of the latter equation is that

$$p^{(0)} = p^{(0)}(x) \tag{1.48}$$

After solving the zero-order problem along with the zero-order boundary conditions, one may consider the first-order problem where the zero-order solution is taken as known.

In the last years, a number of studies concerned this large class of so-called lubrication problems, in which the thin-film asymptotic approximation can be used to analyze the flow in all, or at least part, of the flow domain (Leal, 1992). Fusi et al. (2015) presented a novel technique for modelling the lubrication flow of a Bingham plastic in a two-dimensional channel of non-uniform thickness. Under the lubrication approximation, the yield surface and the two velocity components are calculated from the pressure by means of closed form expressions, while the pressure satisfies an integro-differential equation. This was solved by Fusi et al. with an iterative procedure (Fusi et al., 2015).

The lubrication paradox in Bingham plastic flows arises from the fact that the predicted plug is not a true unyielded region since the leading order velocity varies in the $x-$ direction. Thus,

[2]It is also known as the thin-gap approximation (Denn, 2008).

the position of the yield surface needs to be corrected by calculating higher-order solutions (Frigaard and Ryan, 2004; Putz et al., 2009).

The advantage of the method of Fusi et al. (2015), is that the lubrication paradox is avoided and the correct shape of the yield surface which is opposite to that of the wall is approximated at zero order. With other approaches, the correct shape of the yield surface is obtained after calculating higher-order solutions (Frigaard and Ryan, 2004; Putz et al., 2009). Specifically, Frigaard and Ryan (2004) suggested the asymptotic technique that resolves the lubrication paradox and builds the consistent solution for thin layer problems. The same technique was also used by Balmforth and Craster (1999), a few years earlier. In their paper, Putz et al. (2009) completed the analysis of the flow of a Bingham fluid along a wavy-walled channel and they confirmed numerically the results of Frigaard and Ryan (2004). In asymptotic analyses where the pressure gradient is obtained from the constraint of a unit areal flux in the $x-$ direction at leading order, the yield surface variation (at zero order) is similar to that of the wall, due to the scaling with the mean velocity. In a later stage, Muravleva (2016) applied the asymptotic technique, suggested earlier by Balmforth and Craster (1999), and Frigaard and Ryan (2004), in order to obtain a consistent thin-layer solution for both planar and axisymmetric squeeze flows of a viscoplastic material. She obtained analytical expressions and numerical results that are in a very good agreement with the earlier works (Balmforth and Craster, 1999; Frigaard and Ryan, 2004).

1.5 Objectives

The objectives of this thesis are the following:

1. To solve the plane Poiseuille flow of a Herschel-Bulkley fluid with asymmetric wall slip, in order to determine the critical conditions for the transition to different flow regimes when the degree of confinement varies, in an attempt to interpret experimental data.
2. To extend the work of Philippou et al. (2016) in order to investigate the development of viscoplastic flow in the particular case of a channel with slip only along one wall (asymmetric flow).
3. To extend the lubrication method of Fusi et al. (2015) and derive an approximate semi-analytical solution of both planar and axisymmetric flow of a Herschel-Bulkley fluid with a general wall function and pressure-dependent yield stress and consistency index.
4. To derive analytical lubrication solutions of a Herschel-Bulkley fluid with a general wall function and pressure-dependent yield stress and consistency index, in the case of a long asymmetric channel.

1.6 Outline of the thesis

In Chapter 2, the steady, pressure-driven flow of a Herschel-Bulkley fluid in a microchannel is considered assuming that different power-law slip equations apply at the two walls due to slip

heterogeneities, allowing the velocity profile to be asymmetric. We demonstrate that three different flow regimes are observed as the pressure gradient is increased. Below a first critical pressure gradient G_1, the fluid moves unyielded with a uniform velocity and thus the two slip velocities are equal. In an intermediate regime between G_1 and a second critical pressure gradient G_2, the fluid yields in a zone near the weak-slip wall and flows with uniform velocity near the stronger-slip wall. Beyond this regime, the fluid yields near both walls and the velocity is uniform only in the central unyielded core. It is demonstrated that the central unyielded region tends towards the midplane only if the power-law exponent is less than unity; otherwise, this region rends towards the weak-slip wall, and asymmetry is enhanced. The extension of the different flow regimes depends on the channel gap; in particular the intermediate asymmetric flow regime dominates when the gap becomes smaller than a characteristic length which incorporates the wall slip coefficients and the fluid properties. The theoretical results compare well with experimental data on soft glassy suspensions, obtained by Vayssade et al. (2014). These results open new routes in manipulating the flow of viscoplastic materials in applications where the flow behavior depends not only on the bulk rheology of the material but also on the wall properties.

In Chapter 3, the flow development of a Herschel-Bulkley fluid in a horizontal channel is considered, assuming that slip occurs only along the upper wall due to slip heterogeneities. Hence, the velocity profile is allowed to be asymmetric as was the case with the experiments of Vayssade et al. (2014). A power-law slip equation is again employed. The one-dimensional fully-developed solutions are derived and the different flow regimes are identified. The two-dimensional development flow is solved numerically using finite elements along with the Papanastasiou regularization for the Herschel-Bulkley constitutive equation (Papanastasiou, 1987). Due to the asymmetry and the viscoplastic character of the flow, the classical definition of the development length is not applicable. The global and upper-wall development lengths are thus considered and the combined effects of slip and the Bingham number are investigated. It is demonstrated that the global development length increases with the Bingham number and that flow development is slower near the no-slip wall. The global development length increases with slip, exhibiting two plateaus and an intermediate rapid increase zone, and doubles in the limit of infinite slip.

In Chapter 4, the lubrication flow of a Herschel-Bulkley fluid in a long symmetric channel of varying width, $2h(x)$, is modeled extending the approach proposed by Fusi et al. (2015) for a Bingham plastic. Moreover, both the consistency index and the yield stress are assumed to be pressure-dependent. Under the lubrication approximation the pressure at zero order depends only on x and the semi-width of the unyielded core is found to be given by $\sigma(x) = -(1+1/n)h(x) + C$, where n is the power-law exponent and the constant C depends on the Bingham number and the consistency-index and yield-stress growth numbers. Hence, in a channel of constant width, the width of the unyielded core is also constant, despite the pressure dependence of the yield stress, and the pressure distribution is not affected by the yield-

stress function. With the present model, the pressure is calculated numerically solving an integro-differential equation and then the position of the yield surface and the two velocity components are computed using analytical expressions. Some analytical solutions are also derived for channels of constant and linearly-varying widths. The lubrication solutions for other geometries are calculated numerically. The implications of the pressure-dependence of the material parameters and the limitations of the method are discussed.

In Chapter 5, the lubrication flow of a Herschel-Bulkley fluid with pressure-dependent rheological parameters in a long asymmetric channel, the walls of which are described by two arbitrary functions, is solved extending the method of Chapter 4. The asymmetric unyielded core is defined by two yield surfaces. An interesting feature of the asymmetric flow is that the unyielded zone moves not only in the main flow direction but also in the transverse direction. The two velocity components in both the yielded and unyielded regions are calculated by means of closed-form expressions in terms of the calculated pressure and the two yield surfaces. The method is applicable in a range of Bingham numbers where the unyielded core extends from the inlet to the outlet plane of the channel. Semi-analytical solutions are derived in the case of an asymmetric channel with $h_1 = 0$ and linearly varying h_2.

Finally, in Chapter 6, we give the concluding remarks and recommendations for future work.

Chapter 2

Confined viscoplastic flows with heterogeneous wall slip

In this chapter we revisit the plane Poiseuille flow of a Herschel-Bulkley fluid with asymmetric wall slip, in order to determine the critical conditions for the transition to different flow regimes when the degree of confinement varies. We recover the experimental observations and provide quantitative criteria in order to get a particular flow regime and guidelines to predict confined flows of viscoplastic materials in the presence of strong surface heterogeneities.[3]

2.1 Introduction

Viscoplastic or yield-stress materials constitute a very interesting class which includes materials of industrial importance, such as polymeric solutions, suspensions and gels, but also biofluids like blood (Barnes, 1999). These materials behave as fluids if the stress exceeds the yield stress, τ_0, and as solids otherwise. Therefore, the constitutive equation of an ideal viscoplastic material consists of two branches. Let us denote the viscous stress tensor by $\boldsymbol{\tau}$ and the rate of strain tensor by $\dot{\boldsymbol{\gamma}}$, the latter being defined by

$$\dot{\boldsymbol{\gamma}} \equiv \nabla \mathbf{u} + (\nabla \mathbf{u})^T \tag{2.1}$$

where $\mathbf{u}$ is the velocity vector and the superscript T denotes the transpose. The magnitudes of $\dot{\boldsymbol{\gamma}}$ and $\boldsymbol{\tau}$, denoted respectively by $\dot{\gamma}$ and τ, are defined by $\dot{\gamma} \equiv \sqrt{II_{\dot{\gamma}}/2}$ and $\tau \equiv \sqrt{II_{\tau}/2}$. As mentioned above, in those areas of the flow field where $\tau \leq \tau_0$ the fluid is unyielded, i.e. there is no flow and $\dot{\boldsymbol{\gamma}} = \mathbf{0}$; otherwise the fluid is yielded and $\dot{\boldsymbol{\gamma}} \neq \mathbf{0}$. The Herschel-Bulkley constitutive equation is widely used to describe the shear rheology of many viscoplastic materials (Herschel and Bulkley, 1926)

[3]The material of this chapter appears in Panaseti et al. (2017).

$$\begin{cases} \dot{\boldsymbol{\gamma}} = \mathbf{0}, & \tau \le \tau_0 \\ \tau = \left(\dfrac{\tau_0}{\dot{\gamma}} + k\dot{\gamma}^{n-1} \right) \dot{\boldsymbol{\gamma}}, & \tau > \tau_0 \end{cases} \tag{2.2}$$

where k is the consistency index and n is the power-law exponent. For viscoplastic materials made of soft and deformable particles such as microgel particles or emulsion droplets, the power-law exponent n is close to 0.5 (Cloitre et al., 2003; Bécu et al., 2006; Ovarlez et al., 2008; Seth et al., 2011). The consistency index k has been found to be proportional to the storage modulus of the suspensions (Seth et al., 2011). By setting n=1 and k=μ, where μ is the plastic viscosity, the Bingham-plastic constitutive equation is recovered (Bingham, 1922). By taking τ_0=0, one gets the power-law model

$$\boldsymbol{\tau} = k\dot{\gamma}^{n-1}\dot{\boldsymbol{\gamma}} \tag{2.3}$$

Viscoplastic materials are prone to slip when they are sheared near smooth surfaces (Barnes, 1995; Cloitre and Bonnecaze, 2017). As a consequence of the solid-liquid duality of yield stress materials, slip essentially occurs at low shear rates below or near the yield point in contrast to slip of polymer melts which takes place at large shear rates (Denn, 2001). This generic feature is shared by many particulate materials such as highly-filled suspensions (Yilmazer and Kalyon, 1989; Kalyon, 2005), microgel suspensions (Meeker et al., 2004a; Meeker et al., 2004b; Aktas et al., 2014; Ortega-Avila et al., 2016), concentrated emulsions (Princen, 1985; Salmon et al., 2003; Seth et al., 2012), hard-sphere suspensions (Ballesta et al., 2008; 2012), and colloidal gels (Ballesta et al., 2013). At the microscopic scale, slip is due to the formation of a thin layer of liquid adjacent to the walls, which lubricates the contacts between the bulk suspension and the walls (Barnes, 1995; Cloitre and Bonnecaze, 2017). At the macroscopic scale, slip can be characterized using a power-law slip equation, relating the wall shear stress, τ_w, to the slip velocity, u_w, defined as the relative velocity of the fluid with respect to that of the wall (Kalyon, 2005)

$$\tau_w = \beta u_w^s \tag{2.4}$$

where s is the slip exponent and β is the slip coefficient. The latter coefficient incorporates the effects of several material properties affecting slip, such as the solvent viscosity and the particle properties. The no-slip and full-slip limiting cases are recovered in the limits $\beta \to \infty$ and $\beta = 0$, respectively. The classical Navier slip condition (Navier, 1827) is the special case of Eq. (2.4) for s=1

$$\tau_w = \beta u_w \tag{2.5}$$

in which case β is related to the slip or extrapolation length b, i.e. $\beta \equiv \eta / b$, where η is the fluid viscosity.

The slip exponent s depends on the properties of the lubricated films at the material/wall interface. Two main lubrication mechanisms have been identified (Seth et al., 2008; 2012). In simple hydrodynamic lubrication (HL), the wall is wetted by a thin film of solvent, which has a constant thickness independent of the flow velocity. For a Newtonian solvent, s is equal to 1; for a non-Newtonian solvent with a power-law viscosity $\eta = k\dot{\gamma}^{m-1}$, s is equal to $1/m$ (Kalyon, 2005). HL slip has been observed with highly-filled suspensions (Kalyon, 2005), soft particle suspensions with repulsive particle-wall interactions (Seth et al., 2008; 2012; Pérez-González et al., 2012), and hard-sphere glasses (Ballesta et al., 2008; 2012). In elastohydrodynamic lubrication (EHL), the lubricating film results from a coupling between flow in the lubricating film and particle deformation. EHL is relevant in jammed suspensions of soft particles in the presence of slightly attractive particle-wall interactions (Meeker et al., 2004a; 2004b; Seth et al., 2008; 2012). Below the yield stress, s is expected to be of the order of 2, which is observed in experiments (Meeker et al., 2004a; 2004b; Ortega-Avila et al., 2016; Ahonguio et al., 2016). Above the yield stress there exist no predictions and the situation is less clear. However experimental observations generally converge to the value s=1 (Aktas et al., 2014; Seth et al., 2012; Vayssade et al., 2014; Poumaere et al., 2014).

In real situations, complex fluids rarely flow in ideal geometries bounded by uniform surfaces but rather experience important slip heterogeneities induced by local variations of surface roughness and chemistry. In spite of its practical importance, this problem has retained little attention so far. Lauga and Stone (2003) analysed theoretically how surface heterogeneities, which were either transverse or parallel to the flow direction, affect the slip length of Newtonian fluids. In their study of the extrusion of viscoplastic suspensions in shallow channels, Lawal and Kalyon (1994) considered a Couette-Poiseuille model subject to different Navier-slip coefficients at the barrel and screw surfaces. The authors derived analytical solutions for the Couette-Poiseuille flow for the case where the imposed pressure gradient and the moving upper plate drive the flow in opposite directions. Different flow regimes were found depending on the velocity, both in magnitude and direction, of the upper wall. Recently Vayssade et al. (2014) imaged the motion of well-characterized soft glassy suspensions in microfluidic channels whose walls imposed different slip velocities. The rheology of the suspensions was well represented by a Herschel-Bulkley equation with n = ½ and the boundary slip conditions were of the Navier form, i.e. s = 1. It was found that, when the channel gap was large, the velocity profiles consisted of a central unyielded plug between two fluidized layers near the walls. When the gap was small, a remarkable behavior appeared: the fluidized layer adjacent to the wall with the highest slip velocity disappeared and the plug flow region extended down the wall.

These observations motivate the present work. We revisit the plane Poiseuille flow of a Herschel-Bulkley fluid with asymmetric wall slip, i.e. with different slip conditions at the two walls, in order to determine the critical conditions for the transition to different flow regimes when the degree of confinement varies. We successfully recover the experimental observations and

provide quantitative criteria to get a particular flow regime and guidelines to predict confined flows of viscoplastic materials in the presence of strong surface heterogeneities. The particular chapter is organized as follows. The governing equations and the general solution are presented in section 2.2. Three different flow regimes are identified, which are defined by the two critical values of the imposed pressure gradient at which the fluid yields at each wall. In section 2.3 we provide the analytical solutions for the flow of a power-law fluid subject to asymmetric Navier slip, which are very useful in interpreting the behavior of Herschel-Bulkley fluids at high pressure gradients (the power-law fluid can be viewed as the limit of a Herschel-Bulkley fluid as the pressure gradient goes to infinity). Section 2.4 is concerned with the variation of the critical pressure gradients with the gap size and the construction of flow diagrams. In section 2.5, we make comparisons with the experimental data of Vayssade et al. (2014).

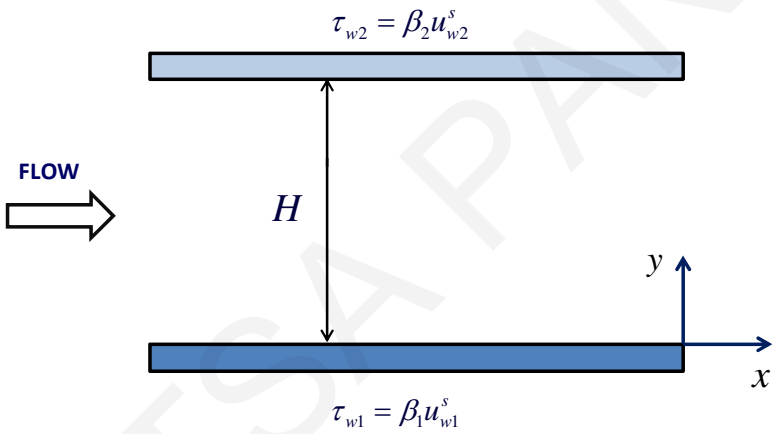

Figure 2.1: Geometry and boundary conditions of the flow development of a Herschel-Bulkley fluid in a channel with different slip laws at the walls.

2.2 General solutions for the asymmetric slip problem

We consider the laminar, steady, unidirectional pressure-driven flow of a Herschel-Bulkley fluid in a horizontal channel of width H, as illustrated in Fig. 2.1. Heterogeneous wall slip is assumed to occur at the walls according to

$$\tau_{wi} = \beta_i u_{wi}^s, \quad i = 1, 2 \tag{2.6}$$

where the lower and upper walls correspond to i =1 and 2, respectively. For the sake of simplicity, the slip exponents are considered to be the same at both walls. Since the flow is not symmetric, the origin is placed at the lower plate (Fig. 2.1).

Without loss of generality, it is assumed that slip at the upper wall is stronger than at the lower wall, i.e. $\beta_1 \geq \beta_2$ and thus $u_{w2} \geq u_{w1}$. With the above assumptions, the x-momentum equation for any generalized Newtonian fluid is simplified to

$$\frac{\partial \tau_{yx}}{\partial y} = -G \tag{2.7}$$

which yields

$$\tau_{yx} = -Gy + \tau_{w1} \tag{2.8}$$

where G is the imposed pressure gradient. The lower-wall shear stress, τ_{w1}, is a crucial parameter, in terms of which all other quantities of interest can be expressed. The upper-wall shear stress is given by

$$\tau_{w2} = \left|\tau_{yx}\right|_{y=H} = GH - \tau_{w1} \tag{2.9}$$

The two slip velocities u_{w1} and u_{w2} can be then calculated by means of Eq. (2.6).

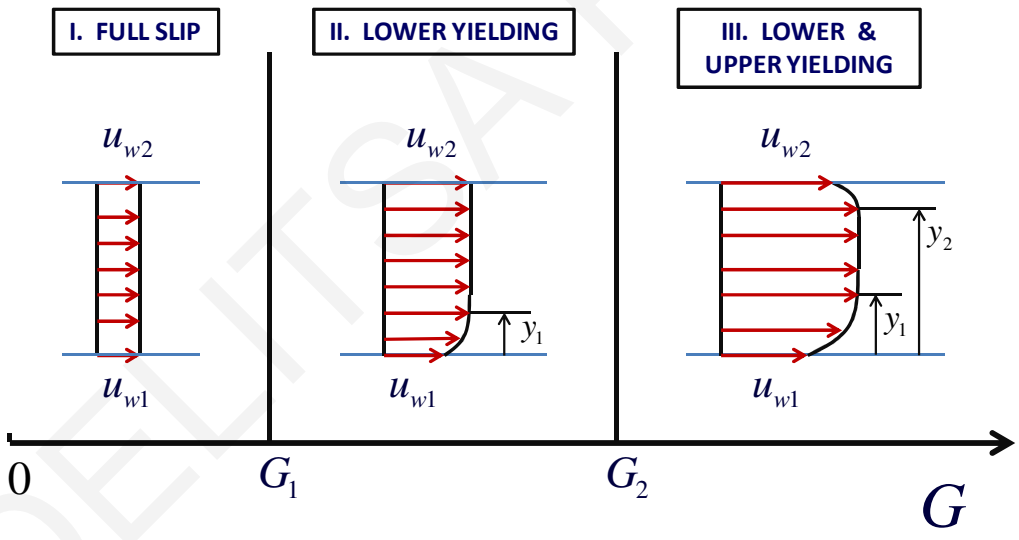

Figure 2.2: The three flow regimes encountered during viscoplastic Poiseuille flow with asymmetric slip. y_1 (and y_2) are the yield points which separate the yielded region(s) from the plug region and u_{w1} and u_{w2} are the slip velocities at the walls. It is assumed that slip is weaker at the lower plate (i.e. $u_{w1} < u_{w2}$).

For viscoplastic flow, we encounter the three regimes illustrated in Fig. 2.2 as the imposed pressure gradient is increased. In Regime I, the fluid simply slips and the velocity is constant (full-slip). This regime extends from zero up to the critical value G_1 of the pressure gradient at which the fluid adjacent to the lower wall (where slip is weaker) yields. Regime II extends from G_1 up to the critical value G_2 of the pressure gradient at which the fluid adjacent to the upper wall (where slip is

stronger) also yields. Hence in Regime II only the lower layer of the fluid up to $y = y_1$ is yielded. In Regime III, i.e. for pressure gradients above G_2, the fluid yields near both walls and the velocity profile is asymmetric with a plug core between the lower and the upper yield points, y_1 and y_2. It is clear that Regime I is not relevant in the special case where there is no slip along the lower wall ($u_{w1} = 0$) and Regime II is observed only if the flow is asymmetric ($\beta_1 > \beta_2$).

In the following analysis we introduce the dimensionless slip numbers

$$B_i \equiv \frac{k^{s/n}}{\beta_i H^s \tau_0^{s/n-1}}, \quad i = 1, 2 \tag{2.10}$$

With this definition we have $B_1 / B_2 = \beta_2 / \beta_1$ so that $B_1 \leq B_2$ under our assumptions. Note that there is no slip at the wall when $B_i = 0$.

2.2.1 Regime I ($0 \leq G \leq G_1$)

In Regime I, the pressure gradient is not sufficient to cause yielding of the material. However, since slip occurs along both walls and the material is unyielded, the two slip velocities are equal, $u_{w1} = u_{w2}$, and the material moves with uniform velocity

$$u_x(y) = \left(\frac{GH}{\beta_1 + \beta_2} \right)^{1/s} \tag{2.11}$$

The lower wall shear stress, given by

$$\tau_{w1} = \frac{\beta_1 GH}{\beta_1 + \beta_2} \tag{2.12}$$

is greater than or equal to τ_{w2} since $\beta_1 \geq \beta_2$. The critical pressure gradient G_1 which marks the transition between Regimes I and II is reached when the material adjacent to the lower wall yields ($\tau_{w1} = \tau_0$)

$$G_1 = \left(1 + \frac{B_1}{B_2}\right) \frac{\tau_0}{H} \tag{2.13}$$

G_1 depends only on the yield stress and not on the exponent and consistency index. The maximum slip velocity is attained when $G=G_1$

$$u_x = \left(\frac{\tau_{w1}}{\beta_1} \right)^{1/s} = \left(\frac{\tau_0}{\beta_1} \right)^{1/s} \tag{2.14}$$

2.2.2 Regime II ($G_1 \le G \le G_2$)

This flow regime exists only if the flow is asymmetric, i.e. if $\beta_1 > \beta_2$ (or $B_1 < B_2$). In this case, the material yields only close to the lower wall, i.e. for $0 \le y \le y_1$, where y_1 is the yield point (Fig. 2.2), and remains unyielded for $y_1 < y \le H$, moving with uniform velocity equal to the upper slip velocity u_{w2}. The yield point y_1 is found from Eq. (2.8) by demanding that $\tau_{yx} = \tau_0$. Hence,

$$y_1 = \frac{\tau_{w1} - \tau_0}{G} \tag{2.15}$$

In the yielded region ($0 \le y \le y_1$),

$$\tau_{yx} = \tau_0 + k\left(\frac{du_x}{dy}\right)^n = -Gy + \tau_{w1} \tag{2.16}$$

Integrating the above equation and demanding that $u_x(0) = u_{w1}$ and $u_x(y) = u_x(y_1) = u_{w2}$, one finds that

$$u_x(y) = \begin{cases} u_{w1} + \dfrac{nG^{1/n}}{(n+1)k^{1/n}}\left[y_1^{1/n+1} - (y_1 - y)^{1/n+1}\right], & 0 \le y \le y_1 \\ u_{w1} + \dfrac{nG^{1/n}}{(n+1)k^{1/n}} y_1^{1/n+1}, & y_1 \le y \le H \end{cases} \tag{2.17}$$

Requiring that $u_x(y_1) = u_{w2}$ leads to the following equation for the lower wall shear stress

$$\frac{n}{n+1}\left(\tau_{w1} - \tau_0\right)^{1/n+1} + \left[\left(B_1\tau_{w1}\right)^{1/s} - \left[B_2\left(GH - \tau_{w1}\right)\right]^{1/s}\right]\tau_0^{1/n-1/s}GH = 0 \tag{2.18}$$

The second critical pressure gradient G_2 signals the yielding of the fluid at the upper wall and therefore it can be found by demanding that $\tau_{w2} = \tau_0$, which leads to

$$\frac{n}{n+1}\left(GH - 2\tau_0\right)^{1/n+1} - \left[\left(B_2\tau_0\right)^{1/s} - \left[B_1\left(GH - \tau_0\right)\right]^{1/s}\right]\tau_0^{1/n-1/s}GH = 0 \tag{2.19}$$

2.2.3 Regime III ($G > G_2$)

In this regime, there are two yielded regions adjacent to the two walls separated by an intermediate unyielded region ($y_1 \le y \le y_2$). The solution derived above for $0 \le y \le y_1$ in Regime II still applies. The second yield point is given by

$$y_2 = \frac{\tau_{w_1} + \tau_0}{G} \tag{2.20}$$

and the three-branch velocity profile reads

$$u_x(y)=\begin{cases} u_{w1}+\dfrac{nG^{1/n}}{(n+1)k^{1/n}}\left[y_1^{1/n+1}-(y_1-y)^{1/n+1}\right], & 0\le y\le y_1 \\ u_{w1}+\dfrac{nG^{1/n}}{(n+1)k^{1/n}}\,y_1^{1/n+1}, & y_1\le y\le y_2 \\ u_{w2}+\dfrac{nG^{1/n}}{(n+1)k^{1/n}}\left[(H-y_2)^{1/n+1}-(y-y_2)^{1/n+1}\right], & y_2\le y\le H \end{cases} \tag{2.21}$$

By demanding that $u_x(y_1)=u_x(y_2)$, one finds the following equation for the lower wall shear stress

$$\frac{n}{n+1}\left[\left(\tau_{w1}-\tau_0\right)^{1/n+1}-\left(GH-\tau_{w1}-\tau_0\right)^{1/n+1}\right]+\left[\left(B_1\tau_{w1}\right)^{1/s}-\left[B_2\left(GH-\tau_{w1}\right)\right]^{1/s}\right]\tau_0^{1/n-1/s}GH=0 \tag{2.22}$$

2.3 Solutions for power-law fluids

2.3.1 Non-dimensional equations

In this section we solve the asymmetric slip equations for the special case of power-law fluids described by Eq. (2.3). Given that the power-law flow can be viewed as the limiting case of the Herschel-Bulkley flow at infinite pressure gradient, the results derived below will be useful in understanding the flow of Herschel-Bulkley fluids at high values of the pressure gradient. It is interesting to note that asymmetric flow profiles have also been observed with polymer solutions which are well represented by a power-law constitutive equation (Müller-Mohnssen et al., 2007). In the limit of a power-law fluid, the two yield points y_1 and y_2 collapse to the unique point y_M, where the velocity attains its maximum. The yield stress is zero and therefore there is no natural scale for stresses. The governing equations can be made dimensionless by scaling lengths by H, the pressure gradient by an arbitrary value, say G_s, so that $G^*\equiv G/G_s$, stresses by G_sH, and the velocity by $G_s^{1/n}H^{1+1/n}/k^{1/n}$. The slip numbers are redefined as

$$B_i\equiv\frac{k^{s/n}}{\beta_i H^{s/n+s-1}G_s^{s/n-1}},\quad i=1,2 \tag{2.23}$$

The non dimensional velocity profiles are then given by

$$u_x^*(y^*)=\begin{cases} u_{w1}^*+\dfrac{nG^{*1/n}}{n+1}\left[y_M^{*1/n+1}-(y_M^*-y^*)^{1/n+1}\right] & 0\le y^*\le y_M^* \\ u_{w2}^*+\dfrac{nG^{*1/n}}{n+1}\left[\left(1-y_M^{*1/n}\right)-(y^*-y_M^*)^{1/n+1}\right] & y_M^*\le y^*\le 1 \end{cases} \tag{2.24}$$

The position of the maximum velocity y_M^* is a root of

$$\frac{n}{n+1}G^{*1/n-1/s}\left[y_M^{*1/n+1}-\left(1-y_M^*\right)^{1/n+1}\right]+B_1^{1/s}y_M^{*1/s}-B_2^{1/s}\left(1-y_M^*\right)^{1/s}=0 \qquad (2.25)$$

If $B_1 = B_2$, the flow is symmetric and $y_M^* = 1/2$ for any value of the pressure gradient G^*. When $n = s$, y_M^* is independent of G^* and can be found by solving

$$\frac{n}{n+1}\left[y_M^{*1/n+1}-\left(1-y_M^*\right)^{1/n+1}\right]+B_1^{1/n}y_M^{*1/n}-B_2^{1/n}\left(1-y_M^*\right)^{1/n}=0 \qquad (2.26)$$

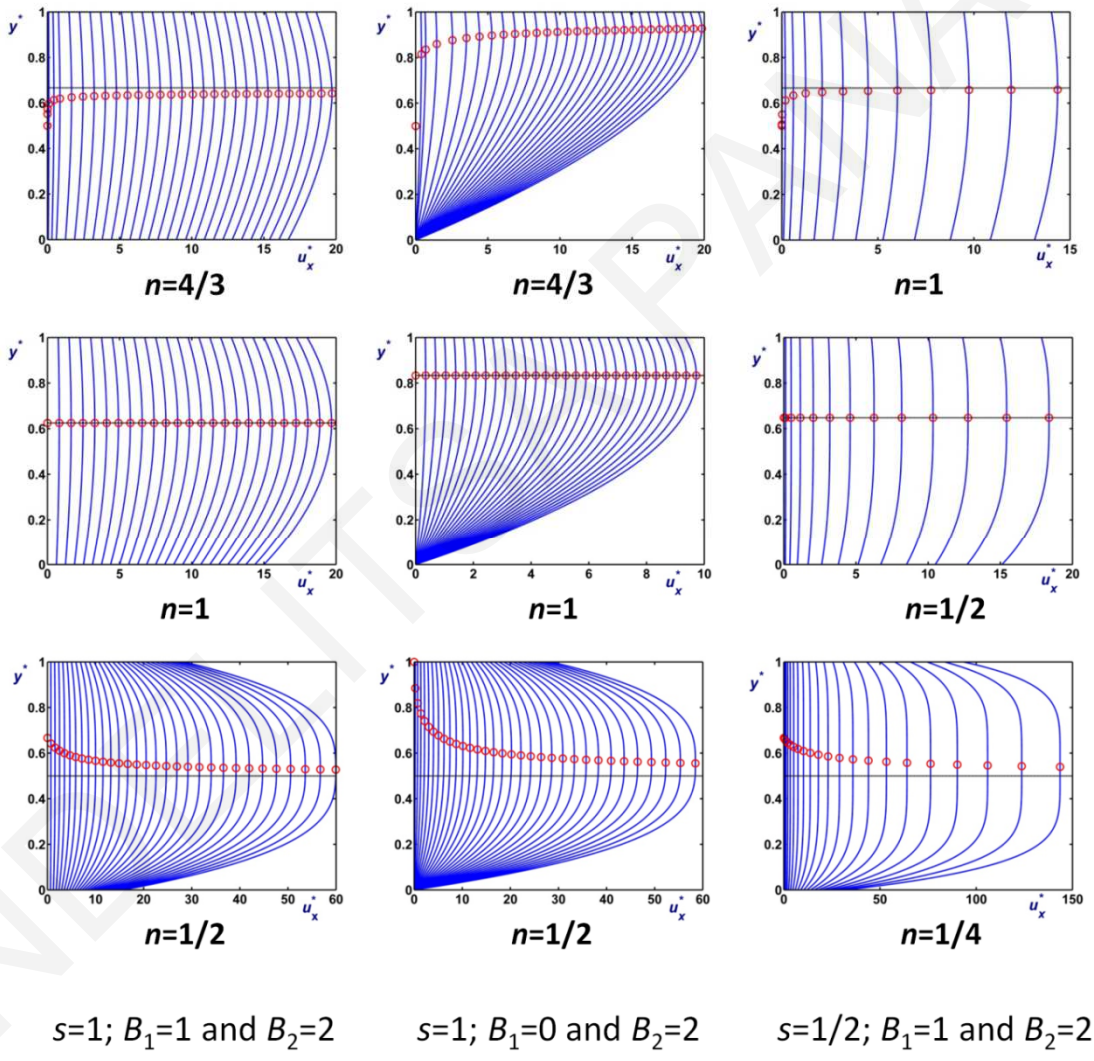

Figure 2.3: Velocity profiles of various power-law fluids for different values of the pressure gradient, different slip laws (s, B_1, B_2), and different power-law exponents (n). The circles show the maximum velocity and the horizontal lines show the asymptotic values y_∞^*.

For the particular case of Newtonian flow with Navier slip, i.e. for n=s=1, one finds

$$y_M^* = \frac{1+2B_2}{2(1+B_1+B_2)}, \quad n=s=1 \tag{2.27}$$

When $n \neq s$, the position of the maximum changes as the pressure gradient is increased. If n<s, it is easily shown that y_M^* decreases asymptotically to 1/2 starting from a finite value y_0^*

$$y_0^* \equiv \lim_{G^*\to 0} y_M^* = \frac{B_2}{B_1+B_2}, \quad y_\infty^* \equiv \lim_{G^*\to\infty} y_M^* = \frac{1}{2}, \quad n<s \tag{2.28}$$

If n>s, the two limits are reversed. Hence, for Navier slip (s=1),

$$y_0^* = \begin{cases} \dfrac{B_2}{B_1+B_2}, & n<1 \\ \dfrac{1+2B_2}{2(1+B_1+B_2)}, & n=1, \\ \dfrac{1}{2}, & n>1 \end{cases} \qquad y_\infty^* = \begin{cases} \dfrac{1}{2}, & n<1 \\ \dfrac{1+2B_2}{2(1+B_1+B_2)}, & n=1 \\ \dfrac{B_2}{B_1+B_2}, & n>1 \end{cases} \tag{2.29}$$

2.3.2 Discussion

The evolution of the velocity profiles as the pressure gradient is increased is shown in Fig. 2.3. In the first two columns of Fig. 2.3, we consider a shear thickening fluid (n=4/3), a Newtonian fluid (n=1), and a shear thinning fluid (n = ½), following Navier-slip laws (s=1) with B_2=2 and B_1=0 and 2, respectively. With shear-thinning fluids the velocity profiles tend to become more symmetric as the pressure gradient increases, whereas with shear-thickening fluids asymmetry is amplified. By comparing the first two columns of Fig. 2.3, we see that this effect becomes more pronounced when the fluid sticks at the lower wall (B_1=0). The position of the maximum of the velocity profiles decreases from y_0^* to $y_\infty^* = 1/2$ when the fluid is shear-thinning and increases from $y_0^* = 1/2$ to y_∞^* when the fluid is shear-thickening. Similar trends are shown in the third column of Fig. 2.3 where a power-law slip equation with s=1/2 is used. The second row of Fig. 2.3 shows that y_M^* is independent of the pressure gradient when n=s. Finally, in the third row of Fig. 2.3 we observe that when $n<s$ the velocity profiles tend to become symmetric with y_M^* decreasing asymptotically to ½ as the pressure gradient is increased.

2.4 Solutions for Herschel-Bulkley fluids

2.4.1 Non-dimensional equations

The asymptotic results discussed above are useful in understanding the flow of Herschel-Bulkley fluids at high values of the pressure gradient. The velocity profiles are computed from the general

equations established in section 2.2. It is convenient to scale lengths by H, stresses by τ_0, pressure gradient by $G_s=\tau_0/H$ and velocity by $u_s = H(\tau_0/k)^{1/n}$. The critical dimensionless pressure gradients G_1^* and G_2^* are then given by

$$G_1^* \equiv 1+\frac{B_1}{B_2} \quad \text{and} \quad \frac{n}{n+1}\left(G_2^*-2\right)^{1/n+1} - \left[B_2^{1/s} - B_1^{1/s}\left(G_2^*-1\right)^{1/s}\right]G_2^* = 0 \tag{2.30}$$

The velocity profiles, the yield points and the wall stresses in each regime are provided below.

Regime I

$$u_x^*(y^*) = \left(\frac{B_1 B_2 G^*}{B_1+B_2}\right)^{1/s} \tag{2.31}$$

$$\tau_{w1}^* = \frac{B_2 G^*}{B_1+B_2} \tag{2.32}$$

Regime II

$$u_x^*(y^*) = \begin{cases} u_{w1}^* + \dfrac{nG^{*1/n}}{n+1}\left[y_1^{*1/n+1} - (y_1^*-y^*)^{1/n+1}\right], & 0 \le y^* \le y_1^* \\ u_{w1}^* + \dfrac{nG^{*1/n}}{n+1} y_1^{*1/n+1}, & y_1^* \le y^* \le 1 \end{cases} \tag{2.33}$$

$$\frac{n}{n+1}\left(\tau_{w1}^*-1\right)^{1/n+1} + \left[\left(B_1\tau_{w1}^*\right)^{1/s} - B_2^{1/s}\left(G^*-\tau_{w1}^*\right)^{1/s}\right]G^* = 0 \tag{2.34}$$

$$y_1^* = \frac{\tau_{w1}^*-1}{G^*} \tag{2.35}$$

Regime III

$$u_x^*(y^*) = \begin{cases} u_{w1}^* + \dfrac{nG^{*1/n}}{n+1}\left[y_1^{*1/n+1} - (y_1^*-y^*)^{1/n+1}\right], & 0 \le y^* \le y_1^* \\ u_{w1}^* + \dfrac{nG^{*1/n}}{n+1} y_1^{*1/n+1}, & y_1^* \le y^* \le y_2^* \\ u_{w2}^* + \dfrac{nG^{*1/n}}{n+1}\left[(1-y_2^*)^{1/n+1} - (y^*-y_2^*)^{1/n+1}\right], & y_2^* \le y^* \le 1 \end{cases} \tag{2.36}$$

$$\frac{n}{n+1}\left[\left(\tau_{w1}^*-1\right)^{1/n+1} - \left(G^*-\tau_{w1}^*-1\right)^{1/n+1}\right] + \left[\left(B_1\tau_{w1}^*\right)^{1/s} - B_2^{1/s}\left(G^*-\tau_{w1}^*\right)^{1/s}\right]G^* = 0 \tag{2.37}$$

$$y_1^* = \frac{\tau_{w1}^*-1}{G^*} \text{ and } y_2^* = \frac{\tau_{w1}^*+1}{G^*} \tag{2.38}$$

In the general case, the second critical pressure gradient G_2^* and the lower wall shear stress τ_{w1}^*, in terms of which the solution is expressed, can only be calculated numerically. In the case of Navier slip (s=1), these quantities can be calculated analytically for certain values of n. The Bingham plastic flow (n=1) belongs to this category and the corresponding solutions are given in Appendix B.

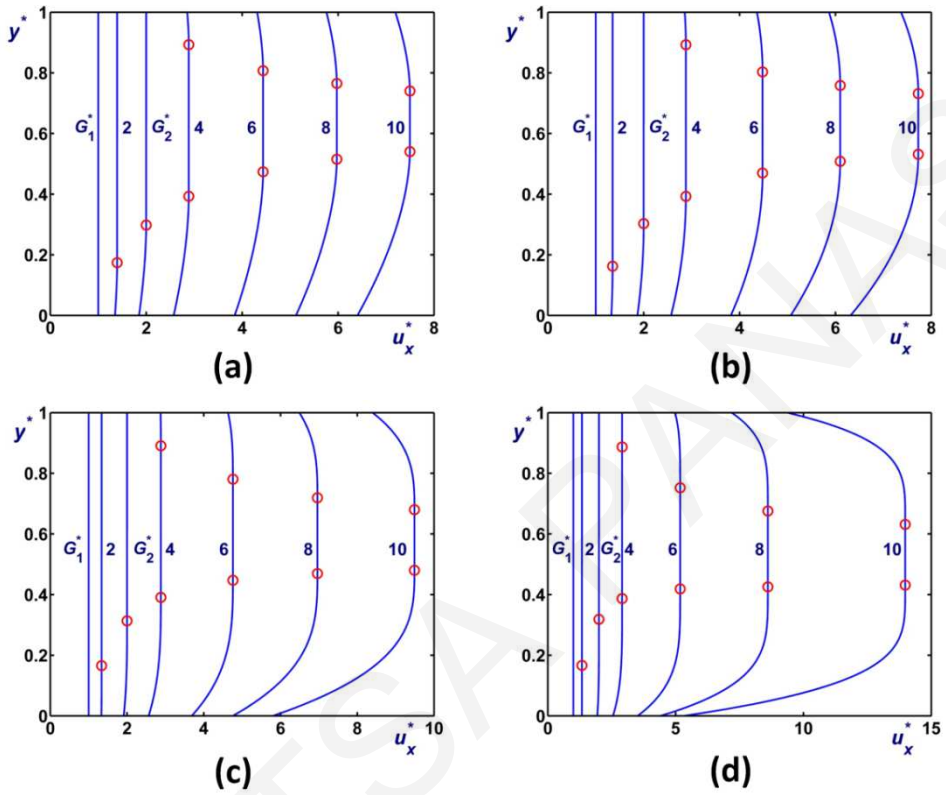

Figure 2.4: Velocity profiles of Herschel-Bulkley fluids for different values of the pressure gradient in the case of Navier slip (s=1) with B_1=1 and B_2=2: (a) n=4/3 with $G_2^* = 2.8943$ and $y_\infty^* = 2/3$; (b) n=1 with $G_2^* = 2.8685$ and $y_\infty^* = 5/8$; (c) n=1/2 with $G_2^* = 2.9129$ and $y_\infty^* = 1/2$; (d) n=1/3 with $G_2^* = 2.9349$ and $y_\infty^* = 1/2$. Note that $G_1^* = 1.5$ in all cases. Lengths (y), velocities (u_x) and pressure gradients (G) are scaled by H, $u_0 = H/(\tau_0/k)^{1/n}$ and $G_s = \tau_0/H$, respectively. The circles show the yield points.

2.4.2 Velocity profiles

Figure 2.4 shows velocity profiles for different values of the pressure gradient covering the three regimes, obtained for four different values of the exponent (n=4/3, 1, 1/2 and 1/3) assuming Navier slip (s=1) with B_1=1 and B_2=2. Recall that the velocity profiles in Regime I are independent of the exponent n and that $u_x^*(G_1^*) = B_1$ in all cases. Just as for the power-law fluids, shear thickening tends to enhance the flow asymmetry, in the sense that both yield points move away from the

midplane towards the upper wall, while shear thinning tends to favor symmetry and extends Regime II. As expected, both yield points tend to converge to the asymptotic point y_∞^* given by Eq. (2.29), which corresponds to the power-law solution. More specifically, the yield points for n=4/3 converge to $y_\infty^* = 2/3$ (Fig. 2.4a), those for n=1 to $y_\infty^* = 5/8$ (Fig. 2.4b), while those for n=1/2 and 1/3 converge to $y_\infty^* = 1/2$ (Figs. 2.4c and 4d). It is interesting to note that the variations of y_1^* and y_2^* with the pressure gradient are not always monotonic. For example, y_1^* is a monotonically increasing function of the pressure gradient only for large values of n (Figs. 2.4a-4c). When n=1/3 (Fig. 2.4d) y_1^* initially increases attaining a maximum and then decreases over a wide range of the pressure gradient before starting increasing again to asymptotically reach the value $y_\infty^* = 1/2$. Similarly, when n=4/3 (Fig. 2.4a), y_2^* decreases and reaches a minimum before increasing asymptotically to the limiting value $y_\infty^* = 2/3$ far from the midplane.

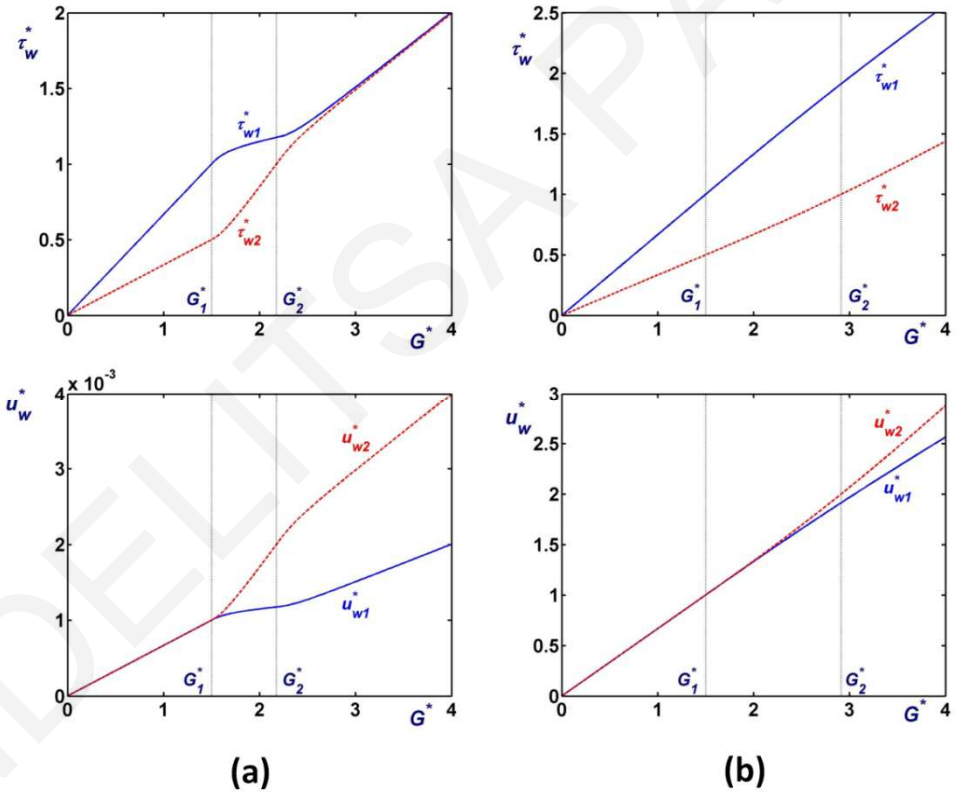

Figure 2.5: Wall shear stresses and slip velocities as functions of the pressure gradient when n=1/2 and s=1: (a) B_1=0.001 and B_2=0.002 (weak slip) in which case $G_1^* = 1.5$ and $G_2^* = 2.1752$; (b) B_1=1 and B_2=2 (strong slip) in which case $G_1^* = 1.5$ and $G_2^* = 2.9129$. The vertical lines indicate the two critical values of the pressure gradient.

2.4.3 Wall stress and slip velocity

The effect of the pressure gradient on the wall shear stresses and the slip velocities is illustrated in Fig. 2.5. Here, based on the behavior of soft glassy suspensions (Vayssade et al., 2014), we consider a Herschel-Bulkley material with exponent n=1/2 and assume that Navier slip (s=1) occurs along both walls. The lower plate slip number takes two extreme values, i.e. B_1=0.001 and 1, corresponding to weak and strong slip respectively; the ratio $B_1/B_2 = 0.5$ is fixed. From Eq. (2.30), we have $G_1^* = 1.5$ showing that Regime I is the same in all cases; G_2^* increases and Regime II expands as B_1 is increased. In Fig. 2.5, we observe that the variations of the slip velocities with the pressure gradient are correlated with the variations of the wall shear stresses. For weak slip (Fig. 2.5a), the difference between τ_{w1}^* and τ_{w2}^* increases in Regime I, decreases in Regime II, and finally vanishes in Regime III where eventually $\tau_{w1}^* = \tau_{w2}^*$. The corresponding velocities u_{w1}^* and u_{w2}^* increase as the pressure gradient is increased. These are equal in Regime I but in the other two regimes u_{w2}^* grows faster than u_{w1}^* and thus the difference $u_{w2}^* - u_{w1}^*$ increases. Strong slip (Fig. 2.5b) results in higher slip velocities as expected. Both τ_{w1}^* and τ_{w2}^* increase but the rate of increase is slowly changing over the entire range of pressure gradient explored. For a given value of the slip ratio, the difference of the two slip velocities in Regimes II and III is much smaller and its rate of increase is much lower for strong slip than for weak slip.

2.5 Confined flows with asymmetric slip

2.5.1 General solution

In this section we show that for a given viscoplastic material and fixed wall properties, the critical pressure gradients marking the onset of Regimes II and III, depend on the gap size H. In order to analyze this dependence, we need to introduce new length, pressure-gradient and velocity scales

$$\ell_s = \frac{k^{1/n}}{\tau_0^{1/n-1/s}\beta_2^{1/s}}, \quad G_s = \frac{\tau_0^{1+1/n-1/s}\beta_2^{1/s}}{k^{1/n}}, \quad \text{and} \quad u_s = \left(\frac{\tau_0}{\beta_2}\right)^{1/s} \tag{2.39}$$

The resulting dimensionless variables are denoted by a tilde (~). It is also important to note that the slip equation parameters β_2 and s (along the upper wall) are hidden in the non-dimensional scales (2.39). In particular, the non dimensional gap $\tilde{H} \equiv H / \ell_s$ incorporates the effects of the slip coefficient at the upper wall and the fluid properties. From Eq. (2.13) we get the following dimensionless expression for the first critical pressure gradient

$$\tilde{G}_1 = \frac{1+\kappa}{\tilde{H}} \tag{2.40}$$

where

$$\kappa \equiv \frac{\beta_2}{\beta_1} = \frac{B_1}{B_2} \tag{2.41}$$

is the slip parameter ratio which varies from 0 (no slip along the lower wall) to 1 (same slip along the walls). Hence the curve representing $\tilde{G}_1$ versus $\tilde{H}$ lies between $1/\tilde{H}$ and $2/\tilde{H}$. The second critical pressure gradient $\tilde{G}_2$ is the root of the dimensionless version of Eq. (2.19)

$$(\tilde{G}\tilde{H}-2)^{1/n+1} - \left(1+\frac{1}{n}\right)\left[1-\kappa^{1/s}(\tilde{G}\tilde{H}-1)^{1/s}\right]\tilde{G} = 0 \tag{2.42}$$

The above equation is amenable to analytical solution only in some special cases. Two of them of practical interest in experiments are discussed below.

2.5.2 Solution for no slip along the lower wall (κ=0)

In this case, $\tilde{G}_1 = 1/\tilde{H}$ and Eq. (2.42) is simplified to

$$(\tilde{G}_2\tilde{H}-2)^{1/n+1} = \left(1+\frac{1}{n}\right)\tilde{G}_2 \tag{2.43}$$

For a Bingham fluid (n=1) one finds

$$\tilde{G}_2 = \frac{2}{\tilde{H}} + \frac{1}{\tilde{H}^2}\left(1+\sqrt{1+4\tilde{H}}\right) \tag{2.44}$$

while for a Herschel-Bulkley fluid with n=1/2,

$$\tilde{G}_2 = \frac{2}{\tilde{H}}\left\{1+\frac{1}{\sqrt{\tilde{H}}}\cos\left[\frac{1}{3}\cos^{-1}\left(3\sqrt{\tilde{H}}\right)\right]\right\} \tag{2.45}$$

It is useful to note that if G_2 and H are known from experiments and if the upper wall experiences Navier slip (s=1) then the slip coefficient can be calculated from the dimensional version of Eq. (2.43)

$$\beta_2 = \frac{(1+1/n)k^{1/n}G}{\tau_0^{1/n}\left(GH/\tau_0-2\right)^{1/n+1}} \tag{2.46}$$

The first and second critical pressure gradients for n=1 and 1/2 are plotted as functions of $\tilde{H}$ in Fig. 2.6. These graphs can be viewed as flow diagrams giving the type of flow experienced by the fluid when the degree of confinement is varied. Regime I is situated below the curve $\tilde{G}_1 = f(\tilde{H})$, which is independent of exponent n. Regime II is the area between the curves of $\tilde{G}_1$ and $\tilde{G}_2$. Figure 2.6 highlights the importance of the characteristic length ℓ_s defined in (2.39).

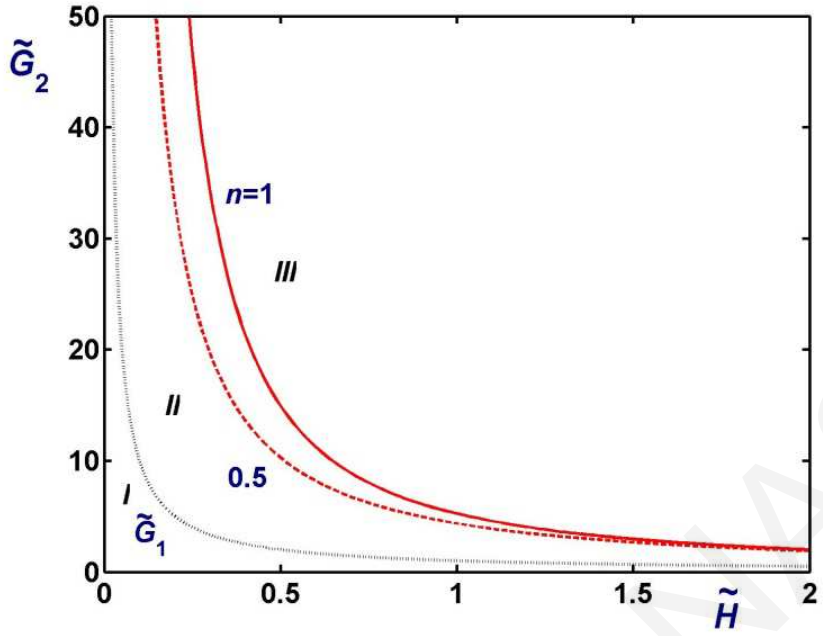

Figure 2.6: Effect of the power-law exponent *n* on the second critical pressure gradient $\tilde{G}_2$ for $\kappa = 0$ (no-slip at the lower wall) and *s*=1 (Navier-slip at the upper wall). The solid curve has been obtained with *n*=1 (Bingham fluid) and the dashed one with *n*=1/2 (Herschel-Bulkley). The lower dotted line is the plot of $\tilde{G}_1$, which is independent of the value of exponent *n*. The region between the curves of $\tilde{G}_1$ and $\tilde{G}_2$ corresponds to Regime II, while the area below the curve of $\tilde{G}_1$ corresponds to Regime I (full-slip flow).

When the gap *H* becomes lower than the characteristic length ℓ_s ($\tilde{H} < 1$), Regime II dominates and Regime III is hardly attained except at very large pressure gradients. When $\tilde{H}$ increases, the fluid is less confined and the extension of Regimes I and II is reduced. As expected, when the fluid is more shear-thinning, i.e. *n* is lower, the critical pressure gradient for yielding at the upper wall, $\tilde{G}_2$, is reduced and the extension of Regime II is reduced accordingly. At large values of $\tilde{H}$, $\tilde{G}_2$ becomes independent of *n*.

2.5.3 Solution for Navier slip along both walls (*s* = 1)

In this case, Eq. (2.42) is simplified to

$$(\tilde{G}\tilde{H} - 2)^{1/n+1} - \left(1 + \frac{1}{n}\right)\left[1 - \kappa(\tilde{G}\tilde{H} - 1)\right]\tilde{G} = 0 \qquad (2.47)$$

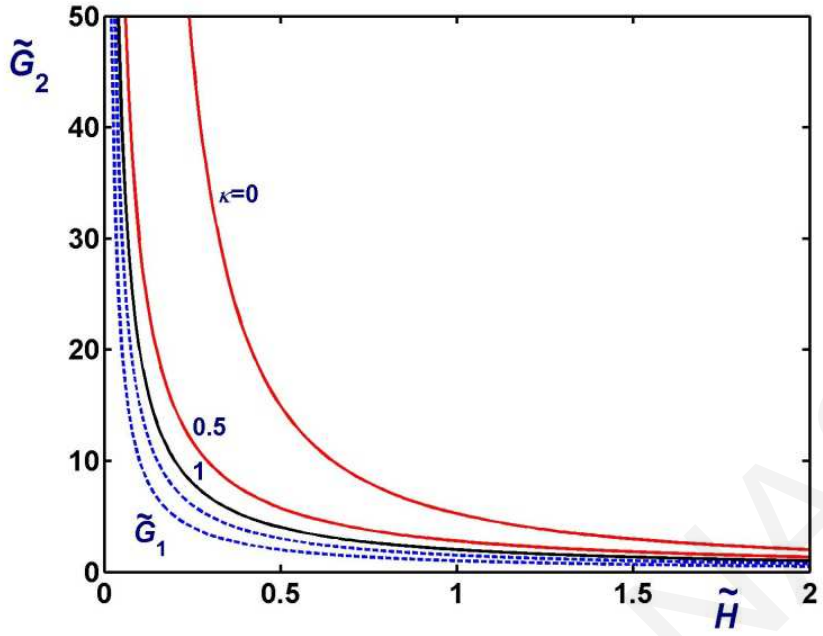

Figure 2.7: Effect of the slip number ratio $\kappa \equiv B_1 / B_2$ on the critical pressure gradients $\tilde{G}_1$ (dashed) and $\tilde{G}_2$ (solid) and the different flow regimes for n=1/2 (Herschel-Bulkley flow). The area between $\tilde{G}_1$ and $\tilde{G}_2$ corresponds to Regime II, while the area below the curve of $\tilde{G}_1$ corresponds to Regime I (full-slip flow). When κ=1 slip is symmetric and thus $\tilde{G}_1$ and $\tilde{G}_2$ coincide.

For Bingham fluids (n = 1) one gets

$$\tilde{G}_2 = \frac{1}{\tilde{H} + 2\kappa}\left\{2 + \frac{1}{\tilde{H}}\left[1 + \kappa + \sqrt{(1+\kappa)^2 + 4(1-\kappa)\tilde{H}}\right]\right\} \tag{2.48}$$

For Herschel-Bulkley fluids with n=1/2

$$\tilde{G}_2 = \frac{2}{\tilde{H}} + \frac{1}{\tilde{H}^2}\left[\frac{(1-3\kappa)\tilde{H} + \kappa^2}{C^{1/3}} + C^{1/3} - \kappa\right] \tag{2.49}$$

where

$$C = \frac{1}{2}\left[6(1-\kappa)\tilde{H}^2 + \left\{3\kappa(3\kappa-1) + \sqrt{36(1-\kappa)^2\tilde{H}^2 + 4(9\kappa^2-1)\tilde{H} - 3(1+\kappa)^2\kappa^2}\right\}\tilde{H} - 2\kappa^3\right] \tag{2.50}$$

Figure 2.7 shows flow diagrams for Herschel-Bulkley fluids with n=1/2 and different values of the slip parameter ratio κ. Again the results exemplify the importance of the characteristic length ℓ_S. Regime II has a significant extension when the gap H is comparable to or lower than ℓ_S.

It is shifted upwards when κ is reduced and reaches its maximum extension when κ=0. When κ=1, the critical pressure gradients $\tilde{G}_1$ and $\tilde{G}_2$ are equal to $2/\tilde{H}$ indicating that Regime II disappears and the flow shifts directly from pure slip to upper and lower yielded flows.

2.6 Discussion

In this section we relate our results with those of Vayssade et al. (2014) for the flow of Herschel-Bulkley glassy suspensions in microchannels.

2.6.1 Quantifying the asymmetry of the velocity profiles

Definition of the asymmetry parameter

Vayssade et al. (2014) solved the flow of Herschel-Bulkley fluid in microchannels by considering a frame of reference at the midplane of the channel, which translates at a mean velocity $(u_{w1} + u_{w2})/2$ so that the two walls move with opposite velocities $\pm U_s$, where

$$U_S = \frac{u_{w2} - u_{w1}}{2} \tag{2.51}$$

They also defined the dimensionless number

$$S = \frac{1}{2}\left(\frac{y_1}{H} + \frac{y_2}{H} - 1\right) \tag{2.52}$$

as a measure of the asymmetry in the positions of the yield points. Their analysis focused on the two slip velocities only and was independent of the slip laws at the two walls. However, it was restricted to the particular case n=1/2. In this section, we revisit the notion of the asymmetry parameter to compare our results to the experimental data, taking advantage of the general solutions derived in section 2.2. Generalizing the scaling forms proposed by Vayssade et al. (2014), we scale velocities by $nG^{1/n}H^{1+1/n}/(n+1)k^{1/n}$, distances by H, pressure gradients by τ_0 / H and stresses by GH. In order to avoid confusion with our previous adimensionalization systems, the dimensionless variables in this section are denoted by bars. According to Eq. (2.21), the difference between the two slip velocities in Regime III can be written in dimensionless form as

$$\bar{u}_{w2} - \bar{u}_{w1} = \bar{y}_1^{1/n+1} - (1 - \bar{y}_2)^{1/n+1}$$

or

$$\bar{U}_s = \frac{1}{2}\left[\bar{y}_1^{1/n+1} - (1 - \bar{y}_2)^{1/n+1}\right] \tag{2.53}$$

For $n \leq 1$,we conveniently set n=1/m, where m is an integer, to get

$$\bar{U}_s = \frac{1}{2}\left(\bar{y}_1 + \bar{y}_2 - 1\right)\sum_{k=1}^{m+1} \bar{y}_1^{m+1-k}(1 - \bar{y}_2)^{k-1} \tag{2.54}$$

Let us now assume that despite the fact that the slip velocities are not the same, the two yield points are almost symmetric about the midplane, i.e. $\bar{y}_1 \approx 1-\bar{y}_2$. As already discussed, this assumption is not reasonable when $n \geq s$ in which case the two yield points tend to merge at $\bar{y}_\infty > 1/2$, according to Eq. (2.29). It is valid when $n<s$ and the two slip velocities are close to each other. Setting $1-\bar{y}_2 = \bar{y}_1$ into Eq. (2.54) yields

$$\bar{U}_s = \frac{1}{2^{1/n+1}}\left(1+\frac{1}{n}\right)\bar{y}_1^{1/n}\left(\bar{y}_1+\bar{y}_2-1\right) \tag{2.55}$$

For $n<s$ and sufficiently high values of the pressure gradient, $\bar{y}_1$ can be approximated by $\bar{y}_\infty \approx 1/2$ and by combining Eqs. (2.52) and (2.55) the asymmetry parameter takes the form

$$S = \frac{2^{1/n}}{1+1/n}\bar{U}_s \tag{2.56}$$

Asymptotic values of the asymmetry parameter

The asymptotic value $S_\infty \equiv (2\bar{y}_\infty - 1)/2$ of S as the pressure gradient goes to infinity is of interest. For example, when $s = 1$ one gets from Eq. (2.29)

$$S_\infty = \bar{y}_\infty - \frac{1}{2} = \begin{cases} 0, & n<1 \\ \dfrac{B_2-B_1}{2(1+B_1+B_2)}, & n=1 \\ \dfrac{B_2-B_1}{2(B_1+B_2)}, & n>1 \end{cases} \tag{2.57}$$

For Bingham fluids ($n = 1$), the asymptotic value of $\bar{U}_s$ can be calculated from the slip velocities in the Newtonian case, which are known

$$\bar{U}_{s\infty} = \frac{B_2-B_1}{2(1+B_1+B_2)} = S_\infty \tag{2.58}$$

In the general case, when $s \neq 1$, S_∞ is calculated by means of

$$S_\infty = \frac{1}{2}(2\bar{y}_M - 1) \tag{2.59}$$

where $\bar{y}_M$ is the position of the maximum velocity in the flow of a power-law fluid, which can be found by solving Eq. (2.26). $\bar{U}_{s\infty}$ is then found by means of Eq. (2.56), which has been derived by assuming that $\bar{y}_\infty \approx 1/2$.

2.6.2 Relevance of the asymmetry parameter

The expression (2.57) for S_∞ is valid for high values of the pressure gradient and $n<s$. Let us test it against the exact solutions found in the previous sections. We consider the case n=1/2 with Navier slip (s=1), which is representative of the experiments of Vayssade et al. (2014). Figure 2.8a shows results of S versus $\bar{U}_s$ obtained for different values of the slip number B_2 and B_1=1 over a wide range of pressure gradients above G_2^*. It is important to note that for low values of the pressure gradient, S is actually double-valued when plotted against $\bar{U}_s$. As the pressure gradient is increased further both S and $\bar{U}_s$ are reduced and all the curves approach asymptotically the line $S = 4\bar{U}_s / 3$. The asymmetry parameter S increases as B_2 is increased (Fig. 2.8a) or as B_1 is reduced (data not shown), because the asymmetry of the velocity profile is enhanced.

The influence of the power-law exponent is illustrated in Fig. 2.8b, where results obtained for Navier slip, i.e. s = 1, with B_1=1 and B_2=2 and n=1, 1/2 and 1/4 are shown. A first observation is that in the Bingham-plastic case for which $n = s$, S is a decreasing function of $\bar{U}_s$ and there is no branch approaching asymptotically the line $S = \bar{U}_s$ predicted by Eq. (2.56).

Actually, as the pressure gradient is increased, the calculated values of S and $\bar{U}_s$ converge to the point ($\bar{U}_{s\infty}$, S_∞) instead of approaching asymptotically the line $S = \bar{U}_s$. This is due to the fact that the asymptotic forms derived for S are only valid for $n<s$. For low values of the pressure gradient the variation of S is essentially the same for all values of the power-law exponent. When $n<s$ the curves of S bend to approach asymptotically the lines predicted by Eq. (2.56).

2.6.3 Comparison with experiments

For the rest of this section we fix the values of all material parameters, again based on the experiments of Vayssade et al. (2014), n = ½, s =1, and $\kappa \equiv B_1 / B_2 = 0.53$, and vary the gap size, H, from 7 up to 100 μm.

The first dimensionless slip number B_1 is in the range from 0.15 (H = 100 μm) to 3 (H=7 μm). The critical pressure gradients $\bar{G}_1$ and $\bar{G}_2$ are equal to G_1^* and G_2^* given by Eq. (2.30). Hence, the first critical pressure gradient is $G_1^* = 1.53$, independently of the gap size. The second critical pressure gradient G_2^* ranges from 2.6534 (H = 100 μm) to 2.8530 (H = 7 μm). Figure 2.9 shows the velocity profiles corresponding to G^* =3, 4, 5, 6, and 8 for H=7, 20, 50, and 100 μm. To facilitate the comparison with the results of Vayssade et al. (2014), we plot the reduced velocity $u_x - u_{w1}$, where u_{w1} is the smallest slip velocity, versus $y^* = \bar{y} = y / H$. The two yield points in the velocity profiles are marked with red circles. Given that $n<s$, the yield points tend asymptotically to the center of the channel ($\bar{y}_\infty = 1/2$) as the pressure gradient is increased.

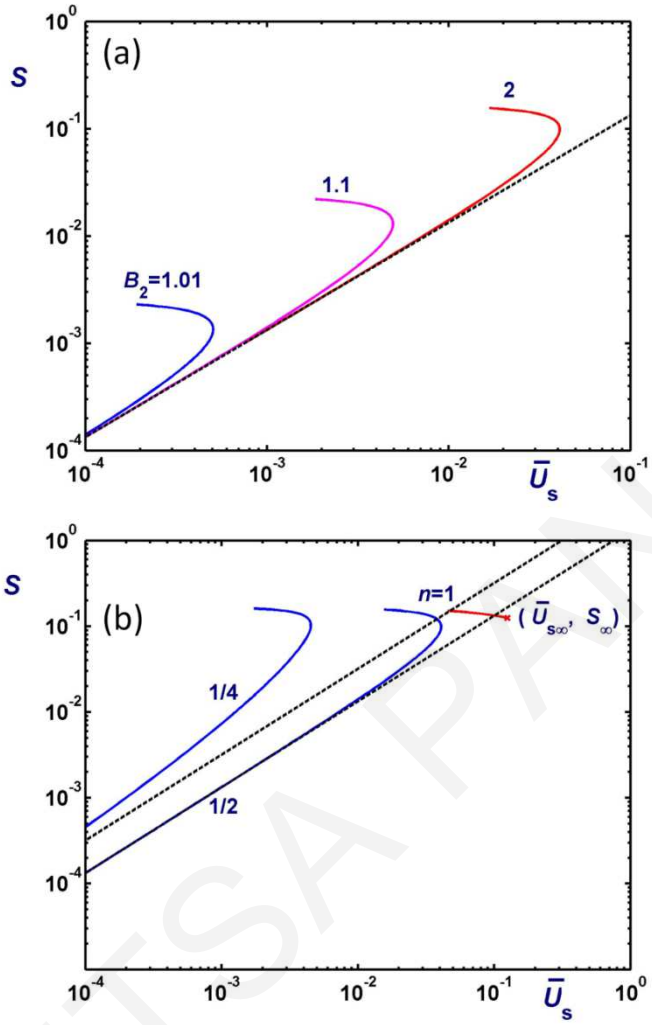

Figure 2.8: (a) Effect of the slip parameters on the variation of the asymmetry parameter S with $\bar{U}_s$ when n=1/2; B_1=1 is kept constant and the ratio B_1/B_2 is varied by varying B_2. All curves approach asymptotically the dashed line $S = 4\bar{U}_s / 3$ as the pressure gradient is increased. (b) Effect of the power-law exponent for s=1 (Navier slip) with B_1=1 and B_2=2. As the pressure gradient is increased, the results for $n<s$ (i.e. for n=1/2 and 1/4) approach asymptotically the corresponding dashed lines $S = 2^{1/n}\bar{U}_s / (1+1/n)$, while the results for $n=s=1$ converge to the point $(\bar{U}_{s\infty}, S_{s\infty}) = (1/8, 1/8)$.

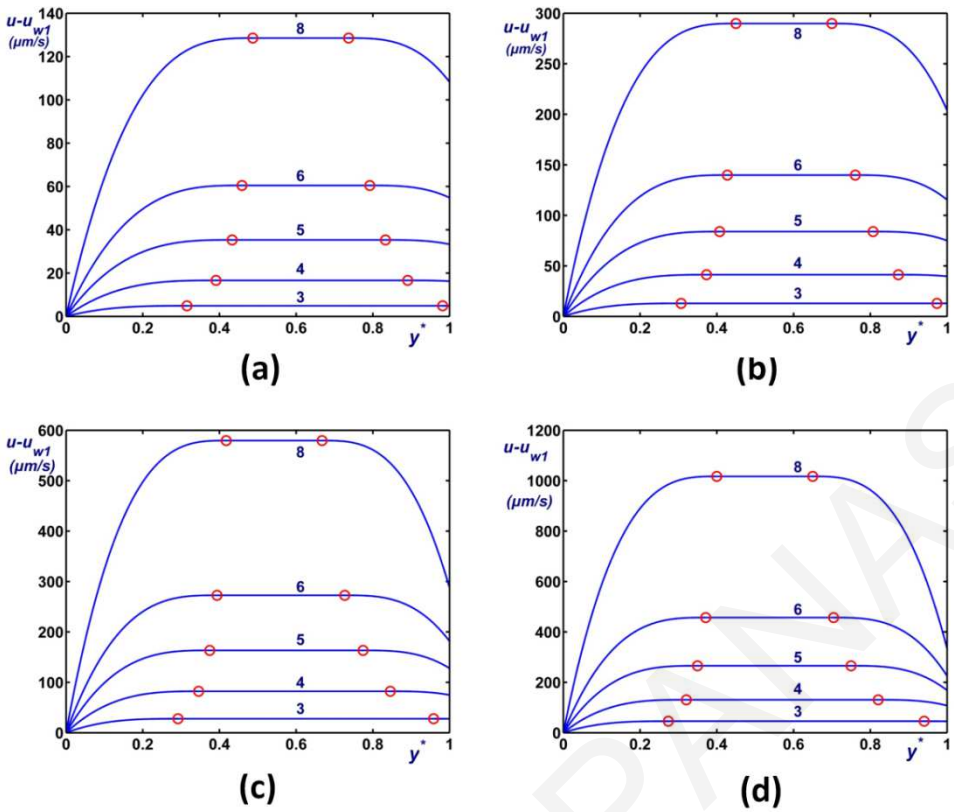

Figure 2.9: Velocity profiles for different channel gaps and various dimensionless pressure for n=1/2, κ=4.1 Pa $s^{1/2}$, τ_0=11.2 Pa, β_1= 10^5 Pa $m^{-1}s$, β_2=0.53 10^5 Pa $m^{-1}s$, and s=1 (taken from the data of Vayssade et al., (2014)) (a) H=7 μm with B_1=2.1441, B_2=4.0455, and $G_2^* = 2.8530$; (b) H=20 μm with B_1=0.7504, B_2=1.4159, and $G_2^* = 2.8044$; (c) H=50 μm with B_1=0.3002, B_2=0.5664, and $G_2^* = 2.7291$; (d) H=100 μm with B_1=0.1501, B_2=0.2832, and $G_2^* = 2.6534$. $G_1^* = 1.53$ in all cases.

Given the experimental uncertainties discussed below, the agreement between the computed velocity profiles and the experimental ones is quite satisfactory. Quantitatively the computed profile lay below the experimental profiles but we noted that a moderate uncertainty on the consistency parameter (≅ 10%) can explain the discrepancy. Although all values of the pressure gradient should fall into Regime III, the velocity profiles expected for low pressure gradient exhibit the asymmetrical semi-plateau shape observed in experiments. Again, this can be associated with experimental uncertainties on the slip parameter, since it is delicate to control the preparation of the surfaces with a high accuracy. Moreover, the asymmetry significantly decreases when the pressure gradient and/or the gap size are increased. This unambiguously confirms that the observed velocity profiles result from confinement effects.

Let us now turn our attention towards the asymmetry parameter. For n=1/2, one easily derives the asymptotic limit valid for large pressure gradients: $S = 4\bar{U}_s / 3$, which is the expression (apart from a minor typo) derived by Vayssade et al. (2014). In Fig. 2.10, the theoretical variations

of the asymmetry parameter S with $\overline{U}_s$ are shown for the same gap sizes as in Fig. 2.9, together with the experimental data (which also include points obtained for H=75 and 80 μm). All the curves collapse into the asymptotic limit expected for large pressure gradients, in excellent agreement with the corresponding experimental data. When the gap size increases, the asymmetry parameter increases as B_1 is reduced, and the asymmetry curves are shifted toward low values of U_s when the pressure gradient is small. The full symbols in Fig. 2.10 represent values of the asymmetry parameter either in Regime II or in the lower part of Regime III. This choice is justified by the fact that experimentally it is difficult to attribute unambiguously a velocity profile to a particular flow regime. Indeed Regime II is quite narrow so that some velocity profiles that look like having a semi plateau shape may well belong to Regime III theoretically. In any case, the values of S in all these points are in the range from 0.1 to 0.5. This can be explained by noting that the experimental asymmetry parameter in Regime II has been calculated by setting $\overline{y}_2 = 1$, i.e. assuming that $S_{II} = \overline{y}_1 / 2$. Given that $\overline{y}_1$ also tends to unity as the pressure gradient is reduced from $\overline{G}_2$ to $\overline{G}_1$ (at which the velocity is plug) the theoretical limiting value of S_{II} is 0.5 while the corresponding value of $\overline{U}_s$ vanishes, independently of the gap size. It should be pointed out, however, that the measured slip velocities (full symbols) in Fig. 2.10 are lower than their counterparts in the upper part of Regime III (open symbols), as it is easily deduced from Fig. 2.9, which implies that the relative error in $\overline{U}_s$ may be higher.

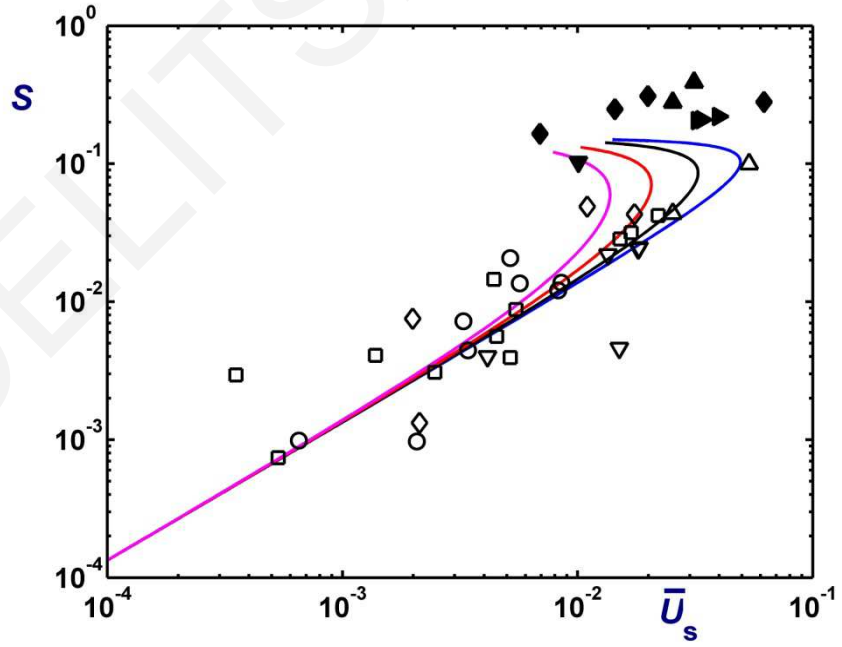

Figure 2.10: Asymmetry parameter S versus slip parameter $\overline{U}_s$ for n=1/2, s=1 and H=7 μm (rightmost curve), 20 μm, 50 μm, and 100 μm (leftmost curve) compared with experimental data for H=7 μm (▲,Δ), 20 μm (♦,◊), 50 μm (□), 75 μm (▼,∇), 80 μm (►) and 100 μm (o). Solid symbols correspond to Regime II (semi-plateau velocity profiles) and open symbols to Regime III (asymmetric velocity profiles).

2.7 Conclusions

We have analyzed the plane Poiseuille flow of a Herschel-Bulkley fluid with asymmetric wall slip. Three different flow regimes have been identified by means of two critical pressure gradients G_1 and G_2: (a) in Regime I ($0 \le G \le G_1$), the two slip velocities are the same and the velocity is uniform; (b) in Regime II ($G_1 < G \le G_2$), the fluid yields in a zone near the weak-slip wall and flows with uniform velocity near the stronger-slip wall; and (c) in Regime III ($G > G_2$), the fluid yields near both walls and the velocity is uniform only in the central unyielded core. The asymptotic limit flow of the Herschel-Bulkley flow as the pressure gradient tends to infinity is simply the flow of a power-law fluid which was also analysed and shed light to the flow of interest. The theoretical results compare well with the experimental data of Vayssade et al. (2014) on soft glassy suspensions. One important finding concerns the asymmetry parameter *S*, defined in Eq. (2.52), which is multi-valued for low and moderate pressures (in Regime III) and thus should be used with caution in interpreting the experimental data.

To close this discussion we would like to stress out that the phenomena analyzed in this chapter constitute a new and interesting situation of non local rheology where the flow behavior is controlled by the surface and not only by the bulk rheology of the material. By changing the topography and the particle-wall interactions it is thus possible to manipulate the flow and get different velocity profiles. This is particularly important in real situations, for instance during oil migration in porous media, where surface roughness and chemistry locally vary so that slip heterogeneities naturally exist. Many other relevant applications concern confined flows in microfluidic devices where surface effects dominate: dispensing nozzles of colloidal inks in 3D printing systems, inkjet printing, and extrusion of complex fluids.

Appendix A - General solution in Regime I

In the general case with different slip exponents at the two walls

$$\tau_{wi} = \beta_i \, u_{wi}^{s_i}, \quad i = 1, 2 \tag{2.60}$$

and the two slip velocities satisfy

$$\beta_1 \, u_{w1}^{s_1} + \beta_2 \, u_{w2}^{s_2} = GH \tag{2.61}$$

In Regime I, $u_{w1} = u_{w2} = u_w$ and thus

$$\beta_1 \, u_w^{s_1} + \beta_2 \, u_w^{s_2} = GH \tag{2.62}$$

After solving the above equation for u_w we can calculate the two wall shear stresses by means of Eq. (2.60). The first critical pressure gradient can be then found by setting the hydrophilic wall shear stress equal to the yield stress, $\tau_{w1} = \tau_0$.

Independent experiments of Vayssade et al. (2014) on soft glassy suspensions showed that s_1=1 and s_2=1/2. From Eq. (2.62) we get

$$u_w = \frac{\beta_2^2}{4\beta_1^2}\left(\sqrt{1+\frac{4\beta_1 GH}{\beta_2^2}}-1\right)^2 \tag{2.63}$$

The first critical pressure gradient is given by

$$G_1 = \left(1+\frac{\sqrt{\beta_1\tau_0}}{\beta_2}\right)\frac{\beta_2\sqrt{\tau_0/\beta_1}}{H} \tag{2.64}$$

Appendix B – Bingham-plastic flow with Navier slip

It is clear from Eq. (2.13) that the first critical pressure G_1 required for the material to yield at the lower wall is independent of the consistency index and the power-law exponent. In the case of Bingham plastic flow with Navier slip (n=s=1), Eq. (2.19) for the second critical pressure gradient (the pressure gradient at which the material adjacent to the upper wall yields) is simplified as follows

$$\frac{1}{2}\left(GH-2\tau_0\right)^2-\left[\left(B_1+B_2\right)\tau_0-B_1GH\right]GH=0 \tag{2.65}$$

and thus G_2 is given by

$$G_2 = \frac{2\tau_0/H}{1+\frac{B_1+B_2}{2}\left[1\pm\sqrt{1+4(B_2-B_1)/(B_1+B_2)^2}\right]} \tag{2.66}$$

The lower root is chosen if it is greater than G_1 and the higher one otherwise.

The lower-wall shear stress in the three regimes is given by

$$\frac{\tau_{w1}}{GH} = \begin{cases} \dfrac{B_2}{B_1+B_2}, & 0\le G\le G_1 \\ \dfrac{\tau_0}{GH}+\sqrt{(B_1+B_2)^2+2B_2-2(B_1+B_2)\dfrac{\tau_0}{GH}}-B_1-B_2, & G_1\le G\le G_2 \\ \dfrac{1+2B_2-2\tau_0/GH}{2(1+B_1+B_2-2\tau_0/GH)}, & G_2\le G \end{cases} \tag{2.67}$$

The two slip velocities can be calculated by means of

$$u_{w1} = \frac{\tau_{w1}}{\beta_1} \text{ and } u_{w2} = \frac{GH - \tau_{w1}}{\beta_2} \tag{2.68}$$

and the positions of the yield points by

$$\frac{y_1}{H} = \frac{\tau_{w1} - \tau_0}{GH} = \begin{cases} \sqrt{(B_1 + B_2)^2 + 2B_2 - 2(B_1 + B_2)\dfrac{\tau_0}{GH}} - B_1 - B_2, & G_1 \le G \le G_2 \\ \dfrac{1 + 2B_2 - 2\tau_0 / GH}{2(1 + B_1 + B_2 - 2\tau_0 / GH)} - \dfrac{\tau_0}{GH}, & G_2 \le G \end{cases} \tag{2.69}$$

and

$$\frac{y_2}{H} = \frac{\tau_{w1} + \tau_0}{GH} = \frac{1 + 2B_2 - 2\tau_0 / GH}{2(1 + B_1 + B_2 - 2\tau_0 / GH)} + \frac{\tau_0}{GH}, \quad G_2 \le G \tag{2.70}$$

Finally, the velocity in Regimes I-III is given respectively by

$$u_x^I(y) = \frac{GH}{\beta_1 + \beta_2}, \tag{2.71}$$

$$u_x^{II}(y) = \begin{cases} u_{w1} + \dfrac{G}{2\mu}\left[y_1^2 - (y_1 - y)^2 \right], & 0 \le y \le y_1 \\ u_{w1} + \dfrac{G}{2\mu} y_1^2, & y_1 \le y \le H \end{cases} \tag{2.72}$$

and

$$u_x^{III}(y) = \begin{cases} u_{w1} + \dfrac{G}{2\mu}\left[y_1^2 - (y_1 - y)^2 \right], & 0 \le y \le y_1 \\ u_{w1} + \dfrac{G}{2\mu} y_1^2, & y_1 \le y \le y_2 \\ u_{w2} + \dfrac{G}{2\mu}\left[(H - y_2)^2 - (y - y_2)^2 \right], & y_2 \le y \le H \end{cases} \tag{2.73}$$

The solution for the symmetric problem is obtained by setting $\beta_1 = \beta_2$. The two critical pressure gradients are then equal, $G_1 = G_2 = 2\tau_0 / H$, so that the intermediate Regime II disappears. Moreover, $\tau_{w1} = \tau_{w2} = GH / 2$ and the positions of the yield points in Regime III are given by

$$y_1 = \frac{H}{2} - \frac{\tau_0}{G}, \quad y_2 = \frac{H}{2} + \frac{\tau_0}{G} \tag{2.74}$$

Hence, $u_x^I = GH / (2\beta)$ while u_x^{III} is given by Eq. (2.73).

Chapter 3

Viscoplastic flow development in a channel with slip along one wall

In this chapter we investigate the case of viscoplastic flow in a channel with slip only along one wall. We also derive the analytical solutions corresponding to fully-developed flow for the case of a power-law slip equation and identify the various flow regimes. We further present the numerical method and discuss the numerical results[4].

3.1 Introduction

Many materials of industrial interest, such as polymeric solutions, suspensions, and gels, are viscoplastic, i.e. they exhibit yield stress. These materials behave as fluids when the exerted stress exceeds the yield stress and as solids otherwise. A popular viscoplastic constitutive equation which also describes shear-thinning or shear thickening is the Herschel-Bulkley model, which involves three material parameters, i.e. the yield stress τ_0, the consistency index k, and the power-law exponent, n (Mitsoulis, 2007). The tensorial form of this model is as follows

$$\begin{cases} \dot{\boldsymbol{\gamma}} = \mathbf{0}, & \tau \le \tau_0 \\ \boldsymbol{\tau} = \left(\dfrac{\tau_0}{\dot{\gamma}} + k\dot{\gamma}^{n-1} \right) \dot{\boldsymbol{\gamma}}, & \tau > \tau_0 \end{cases} \tag{3.1}$$

where $\boldsymbol{\tau}$ is the viscous stress tensor, $\dot{\boldsymbol{\gamma}} \equiv \nabla\mathbf{u} + (\nabla\mathbf{u})^T$ is the rate of strain tensor, $\mathbf{u}$ is the velocity vector, $\nabla\mathbf{u}$ is the velocity gradient tensor, and the superscript T denotes its transpose. The magnitudes of $\dot{\boldsymbol{\gamma}}$ and $\boldsymbol{\tau}$, denoted respectively by $\dot{\gamma}$ and τ, are defined by $\dot{\gamma} \equiv \sqrt{\dot{\boldsymbol{\gamma}} : \dot{\boldsymbol{\gamma}} / 2}$ and $\tau \equiv \sqrt{\boldsymbol{\tau} : \boldsymbol{\tau} / 2}$. The Herschel-Bulkley model is reduced to the power-law model when the yield stress is zero and to the Bingham-plastic model when n=1.

In flows of ideal yield-stress fluids, the flow domain consists of the so-called unyielded ($\tau \le \tau_0$) and yielded regions ($\tau > \tau_0$) where the two branches of the constitutive equation apply. The former regions include zones where the material moves undeformed as a rigid body

[4]The material of this chapter appears in Panaseti and Georgiou (2017).

and dead zones where it is stagnant. Determining the interfaces between yielded and unyielded regions is a key computational challenge with viscoplastic fluid flows, especially in two- and three-dimensional flows (Balmforth et al., 2014). Two are the main approaches to tackle this problem: (a) Augmented Lagrangian Methods (ALMs); and (b) Regularization methods. ALMs are based on the variational formulation of the Navier-Stokes equations and employ optimization algorithms to determine the flow solution (Balmforth et al., 2014). They are exact in the sense that they respect the non-differentiable form of the constitutive equation. However, ALMs are generally slower and more difficult to implement than regularization methods (Balmforth et al., 2014).

In regularization methods, the constitutive equation is modified by introducing an additional parameter in order to combine the two branches of Eq. (3.1) into one smooth function, so that the resulting regularized equation applies everywhere in the flow field in both yielded and (practically) unyielded regions. The most popular regularization in the literature is that proposed by Papanastasiou (1987) for a Bingham plastic and subsequently by Ellwood et al. (1990) for a Herschel-Bulkley fluid

$$\boldsymbol{\tau} = \left\{ \frac{\tau_0 \left[1 - \exp\left(-m\dot{\gamma} \right) \right]}{\dot{\gamma}} + k\dot{\gamma}^{n-1} \right\} \dot{\boldsymbol{\gamma}} \tag{3.2}$$

where m is the stress growth exponent, which has dimensions of time. For sufficiently large values of m, the Papanastasiou model provides a satisfactory approximation of the Bingham-plastic model. The regularized approach is easier to implement than ALMs but eliminates the yield surfaces replacing unyielded regions with regions of very high viscosity. The interface of yielded /"unyielded" regions can approximately be tracked down a posteriori by using the von Mises criterion $\tau = \tau_0$ (Mitsoulis, 2007; Mitsoulis and Tsamopoulos, 2017). The advantages and disadvantages of ALMs and regularization methods are discussed in the recent articles of Balmforth et al. (2014), and Saramito and Wachs (2017).

Wall slip is important in many industrial applications, such as the extrusion of complex fluids, ink jet processes, oil migration in porous media, and in microfluidics. Viscoplastic materials are known to exhibit wall slip (Yilmazer and Kalyon, 1989; Ballesta et al., 2012; Cloitre and Bonnecaze, 2017). While wall slip with polymer melts is observed at large rates of strains, with pasty materials it appears within a range of rather small strains (Denn, 2001). Based on the analysis of apparent slip flows of Herschel-Bulkley fluids in various geometries, Kalyon (2005) proposed a power-law slip equation, relating the wall shear stress, τ_w, to the slip (or sliding) velocity, u_w, defined as the relative velocity of the fluid with respect to that of the wall,

$$\tau_w = \beta \mathrm{u}_w^s \tag{3.3}$$

where s is the exponent, and β is the slip coefficient. The latter coefficient incorporates the effects of temperature, the normal stress, the molecular parameters, and the properties of the fluid/wall interface (Denn, 2001). The no-slip and full-slip limiting cases are recovered when $\beta \to \infty$ and $\beta = 0$, respectively. Experimental values of the exponent s have been reviewed by Panaseti et al. (2017). The value s=1 has been reported in different experimental studies for stresses above the yield stress (see Panaseti et al., (2017) and references therein). Setting s=1 in Eq. (3.3) leads to the classical Navier-slip condition (Navier, 1827)

$$\tau_w = \beta u_w \tag{3.4}$$

in which case the slip coefficient is related to the slip length b, by means of $\beta \equiv \mu / b$, where μ denotes the viscosity.

The present work is motivated by the recent findings of Vayssade et al. (2014), who imaged the motion of well characterized softy glassy suspensions in microchannels whose walls impose different slip velocities. Their experiments showed that as the channel height decreases the flow ceases to be symmetric and slip heterogeneities effects become important. Interestingly, some of the experimental velocity profiles reported by Vayssade et al. are characterized by overshoots similar to those encountered in entry flows (Vayssade et al., 2014). We thus revisit here the classical flow development problem of a Bingham plastic in a horizontal channel assuming, however, that power-law slip occurs along the upper wall only. The one-dimensional fully-developed flow with asymmetric slip along the two walls has been analyzed by Panaseti et al. (2017). The theoretical results compare well with the (fully-developed) experimental data of Vayssade et al. (2014).

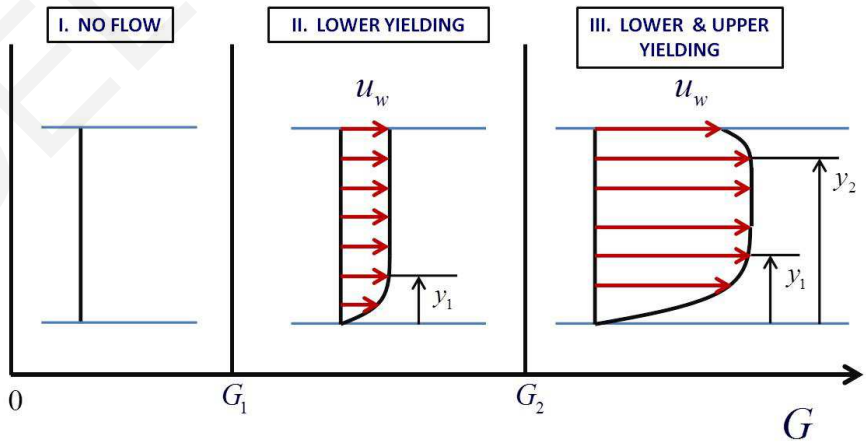

Figure 3.1: Different flow regimes in the case of one-dimensional plane viscoplastic Poiseuille flow when slip occurs only along the upper wall.

For the sake of simplicity, the special case where there is no slip along the lower wall is studied here. As illustrated in Fig. 3.1, three regimes are observed for the one-dimensional steady-state Poiseuille flow, as the pressure gradient G is increased. Below a certain critical value G_1 (Regime I) the lower wall shear stress is below the yield stress and thus there is no flow. In Regime II above G_1 and below a second critical pressure gradient G_2, the fluid yields only near the lower plate and the fluid adjacent to the upper wall slides as an unyielded plug. Finally, above G_2 at which the upper-wall shear stress also exceeds τ_0 (Regime III), the fluid yields near both the walls and the velocity profile is asymmetric with a plug core. In the special case when there is no slip along the upper wall, the classical symmetric Poiseuille solution is recovered and Regime II is not relevant.

The flow development problem is obviously two-dimensional: the fluid enters a tube or a channel at a uniform velocity and decelerates near the wall(s) and accelerates in the central region. In other words, the axial velocity tends from a flat profile at the inlet to the fully-developed profile downstream. The development length is usually defined as the length required for the maximum velocity to attain 99% of its fully-developed value scaled either by the pipe diameter or the channel width (Shah and London, 1978). This definition implies that the maximum velocity in the central acceleration region develops more slowly than its counterparts at any other vertical distance from the axis or plane of symmetry. This may not be the case in all geometries and for all fluids, especially viscoplastic ones which are characterized by a maximum flat velocity. It is also clear that such a definition is not applicable in the case of asymmetric Poiseuille flow which is of interest here. In a recent study of the effect of wall slip on the development of planar and axisymmetric Newtonian Poiseuille flows, Kountouriotis et al. (2016) pointed out that in addition to the standard definition of the development length, L, as the length required for the maximum velocity to attain 99% of its fully-developed value, the wall development length L_w is also relevant in the presence of slip. This is defined as the length required for the slip velocity to decrease to 1.01% of its fully-developed value. The numerical simulations of Kountouriotis et al. (2016) showed that both L and L_w increase with slip passing through a maximum and vanish at a critical value of the slip parameter corresponding to the full slip case. They also revealed that, in contrast to the axisymmetric flow, the planar flow develops more slowly at the wall than at the midplane, i.e. $L_w>L$.

In a subsequent work, Philippou et al. (2016) studied numerically the development of Bingham plastic flow in tubes and channels using the Papanastasiou regularization and finite element simulations. They considered alternative definitions of the development length noting that this is a function of the transversal coordinate. Their results demonstrated that the classical development length, L_c, and the development length, L_{95}, proposed by Ookawara et al. (2000) for Bingham flow are not good choices for measuring viscoplastic flow development (with or without slip). L_{95} is defined as the axial distance required for the velocity to reach 99% of the calculated maximum value at a radial location corresponding to 95% of the plug radius (Ookawara et al.,

2000). To avoid the inconsistencies resulting from the use of L_c and L_{95}, Philippou et al. (2016) employed the global development length which in the case of a channel of width H is defined as follows

$$L_g \equiv \max_{0 \le y \le H} L(y) \tag{3.5}$$

$L(y)$ is the (smallest) length required for the two-dimensional axial velocity $u(x, y)$ to become equal to $0.99\overline{u}(y)$ or $1.01\overline{u}(y)$ when $\overline{u}(y) > \overline{u}_m$ or $\overline{u}(y) < \overline{u}_m$, respectively, where $\overline{u}(y)$ is the fully-developed velocity profile and $\overline{u}_m$ is the mean velocity.

The present work can be viewed as an extension of Philippou et al. (2016), to the case of viscoplastic flow in a channel with slip only along one wall (asymmetric flow). The governing equations are presented in section 3.2, where the analytical solutions corresponding to fully-developed flow for the case of a power-law slip equation are also derived and the various flow regimes are identified. In section 3.3, the numerical method is briefly presented and the numerical results are discussed. Finally, the conclusions are summarized in section 3.4.

3.2 Governing equations

The governing equations are de-dimensionalized scaling lengths by the gap height H of the channel, the velocity vector by the uniform inlet velocity U, and the pressure and the stress tensor components by kU^n/H^n. By denoting the de-dimensionalized variables with stars, the continuity and momentum equations for steady, incompressible flow with zero gravity can be written as follows

$$\nabla^* \cdot \mathbf{u}^* = 0 \tag{3.6}$$

and

$$Re\,\mathbf{u}^* \cdot \nabla^* \mathbf{u}^* = -\nabla^* p^* + \nabla^* \cdot \boldsymbol{\tau}^* \tag{3.7}$$

where

$$Re \equiv \frac{\rho U^{2-n} H^n}{k} \tag{3.8}$$

is the Reynolds number, ρ being the constant mass density of the material.

The Pananastasiou regularization (Papanastasiou, 1987) is employed here for the Herschel-Bulkley model. The dimensionless form of the regularized constitutive equation may be written as follows

$$\boldsymbol{\tau}^* = \left[Bn \frac{1-\exp(-M\dot{\gamma}^*)}{\dot{\gamma}^*} + \dot{\gamma}^{*n-1} \right] \dot{\boldsymbol{\gamma}}^* \tag{3.9}$$

where

$$Bn \equiv \frac{\tau_0 H^n}{kU^n} \tag{3.10}$$

is the Bingham number and

$$M \equiv \frac{mU}{H} \tag{3.11}$$

is the dimensionless growth exponent, which has to be sufficiently high so that the flow of the ideal discontinuous Herschel-Bulkley fluid is approximated satisfactorily (Papanastasiou, 1987; Ellwood et al., 1990; Mitsoulis and Tsamopoulos, 2017).

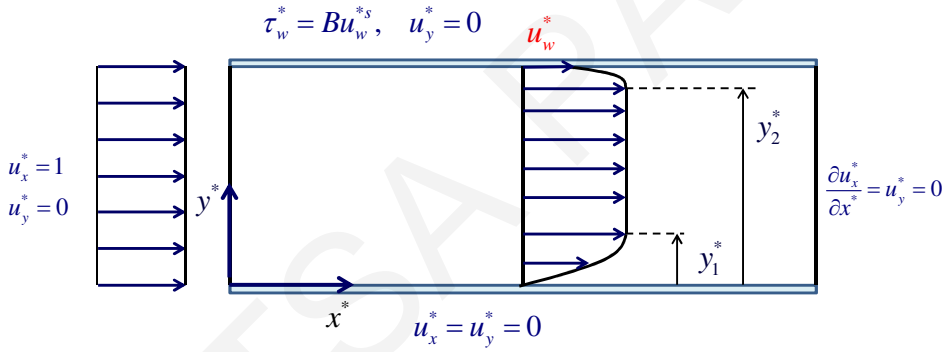

Figure 3.2: Geometry and boundary conditions of the flow development of a Bingham plastic in a horizontal channel with slip along the upper wall.

The geometry and the boundary conditions of the flow are illustrated in Fig. 3.2. At the inlet plane, the velocity component in the direction of the flow is uniform ($u_x^* = 1$) and the transversal one vanishes. At the lower wall, there is no slip and no penetration and thus both velocity components are zero. At the upper wall the vertical velocity is again zero and slip is assumed to occur following a power-law slip equation,

$$\tau_w^* = Bu_w^{*s} \tag{3.12}$$

where

$$B \equiv \frac{\beta H^n}{kU^{n-s}} \tag{3.13}$$

is the (dimensionless) slip number. Note that B is the inverse of the slip number defined by Panaseti et al. (2017). Finally, the exit plane is taken sufficiently far downstream so that the flow can be assumed fully-developed.

3.2.1. Fully-developed solutions

The de-dimensionalization introduced above is based on the mean velocity, which implies that there is flow, i.e. Regime I of Fig. 3.1 is not relevant. The no-slip case, which corresponds to a symmetric velocity profile with respect to the mid-plane of the channel, is recovered for $B \to \infty$. The two yield points, y_1^* and y_2^*, are thus symmetric, i.e. $y_2^* = 1 - y_1^*$, and the flow is in Regime III (there is no Regime II). Keeping the Bingham number constant and decreasing the slip number, enhances slip at the upper wall and the velocity becomes asymmetric: the two yield points move towards the upper wall so that the width of the plug core ($y_2^* - y_1^*$) increases while its velocity is reduced. This trend continues up to a critical slip number, B_c, at which the upper yield point reaches the wall (the dimensionless upper wall shear stress is equal to Bn) signaling the transition from Regime III to Regime II. Deriving the analytical solution is straightforward (Panaseti et al., 2017). However, this is presented here for convenience and in order to account for the present scalings used and to identify the different flow regimes. The general dimensionless solution for $B_c \le B < \infty$ is given by

$$u_x^*(y^*) = \begin{cases} \dfrac{1}{A_{III}}\left[y_1^{*1/n+1} - (y_1^* - y^*)^{1/n+1} \right], & 0 \le y^* \le y_1^* \\ \dfrac{y_1^{*1/n+1}}{A_{III}}, & y_1^* \le y^* \le y_2^* \\ u_w^* + \dfrac{1}{A_{III}}\left[(1-y_2^*)^{1/n+1} - (y^* - y_2^*)^{1/n+1} \right], & y_2^* \le y^* \le 1 \end{cases} \tag{3.14}$$

where

$$u_w^* = \frac{1}{A_{III}}\left[y_1^{*1/n+1} - (1-y_2^*)^{1/n+1} \right] \tag{3.15}$$

and

$$A_{III} = y_1^{*1/n+1}\left(1 - \frac{n}{1+2n} y_1^* \right) - \frac{n}{1+2n}(1-y_2^*)^{1/n+2} \tag{3.16}$$

The positions of the two yield points can be found by solving the following system of equations

$$(2 - y_1^* - y_2^*)Bn - (y_2^* - y_1^*)Bu_w^{*s} = 0 \tag{3.17}$$

and

$$(1+1/n)^n (y_2^* - y_1^*) - 2Bn\, A_{III}^n = 0 \tag{3.18}$$

No-slip case

In the no-slip case ($u_w^* = 0$), Eq. (3.15) yields $y_2^* = 1 - y_1^*$, which indicates that the flow is symmetric with respect to the mid-plane of the channel. Substituting into Eq. (3.16) gives

$$A_{III} = y_1^{*1/n+1}\left(1 - \frac{2n}{1+2n}\, y_1^*\right) \tag{3.19}$$

and Eq. (3.18) becomes

$$(1+1/n)^n (1 - 2y_1^*) - 2Bn\, y_1^{*n+1}\left(1 - \frac{2n}{1+2n}\, y_1^*\right)^n = 0 \tag{3.20}$$

Critical value of the slip number

The critical value B_c of the slip number can be found by setting $y_2^* = 1$. Denoting the corresponding critical values of y_1^* and u_w^* by y_{1c}^* and u_{wc}^*, respectively, we get from Eq. (3.17)

$$B_c u_{wc}^{*s} = Bn \tag{3.21}$$

which simply says that the (dimensionless) upper-wall shear stress is equal to *Bn*. The critical slip velocity is given by

$$u_{wc}^* = \frac{1}{1 - \dfrac{n}{1+2n}\, y_{1c}^*} \tag{3.22}$$

and, therefore,

$$B_c = \left(1 - \frac{n}{1+2n}\, y_{1c}^*\right)^s Bn \tag{3.23}$$

Finally, from Eq. (3.18) one gets

$$(1+1/n)^n (1 - y_{1c}^*) - 2Bn\, A_{IIIc}^n = 0 \tag{3.24}$$

or

$$(1+1/n)^n (1 - y_{1c}^*) - 2Bn\, y_{1c}^{*n+1} / u_{wc}^{*n} = 0 \tag{3.25}$$

which is used to calculate y_{1c}^*. It should be noted that the value of y_{1c}^* is independent of the slip equation parameters. For example, in the Bingham plastic case (n=1), y_{1c}^* is a root of

$$Bn\, y_{1c}^{*3} - 3Bn\, y_{1c}^{*2} - 3y_{1c}^* + 3 = 0 \tag{3.26}$$

while the value of B_c can then be calculated from Eq. (3.23) for any value of s.

Solution in Regime II

If the slip number is reduced below B_c, the yield point keeps moving towards the upper wall and the width of the plug core is thus reduced while its velocity increases. Finally, in the limit $B = 0$ (full slip), the velocity profile corresponds to the no-slip solution in a channel of double width ($2H$), i.e. to the no-slip solution corresponding to the modified Bingham number

$$Bn' = \frac{\tau_0 (2H)^n}{kU^n} = 2^n Bn \tag{3.27}$$

Hence, when $0 < B \le B_c$, the flow corresponds to Regime II and the dimensionless velocity is given by

$$u_x^*(y^*) = \begin{cases} \left[y_1^{*1/n+1} - (y_1^* - y^*)^{1/n+1} \right] / \left[y_1^{*1/n+1} \left(1 - \dfrac{n}{1+2n} y_1^* \right) \right], & 0 \le y^* \le y_1^* \\ u_w^*, & y_1^* < y^* \le 1 \end{cases} \tag{3.28}$$

where

$$u_w^* = \frac{1}{1 - \dfrac{n}{1+2n} y_1^*} \tag{3.29}$$

and y_1^* is the root of

$$(1+1/n)^n (1 - y_1^*) - \left(Bn + Bu_w^{*s} \right) y_1^{*n+1} / u_w^{*n} = 0 \tag{3.30}$$

Substituting Eq. (3.21) into the above equation yields Eq. (3.25) for y_{1c}^*. For n=1 (Bingham plastic) and s=1 (Navier slip) Eq. (3.30) is simplified to

$$Bn\, y_1^{*3} - 3(Bn + B)\, y_1^{*2} - 6y_1^* + 6 = 0 \tag{3.31}$$

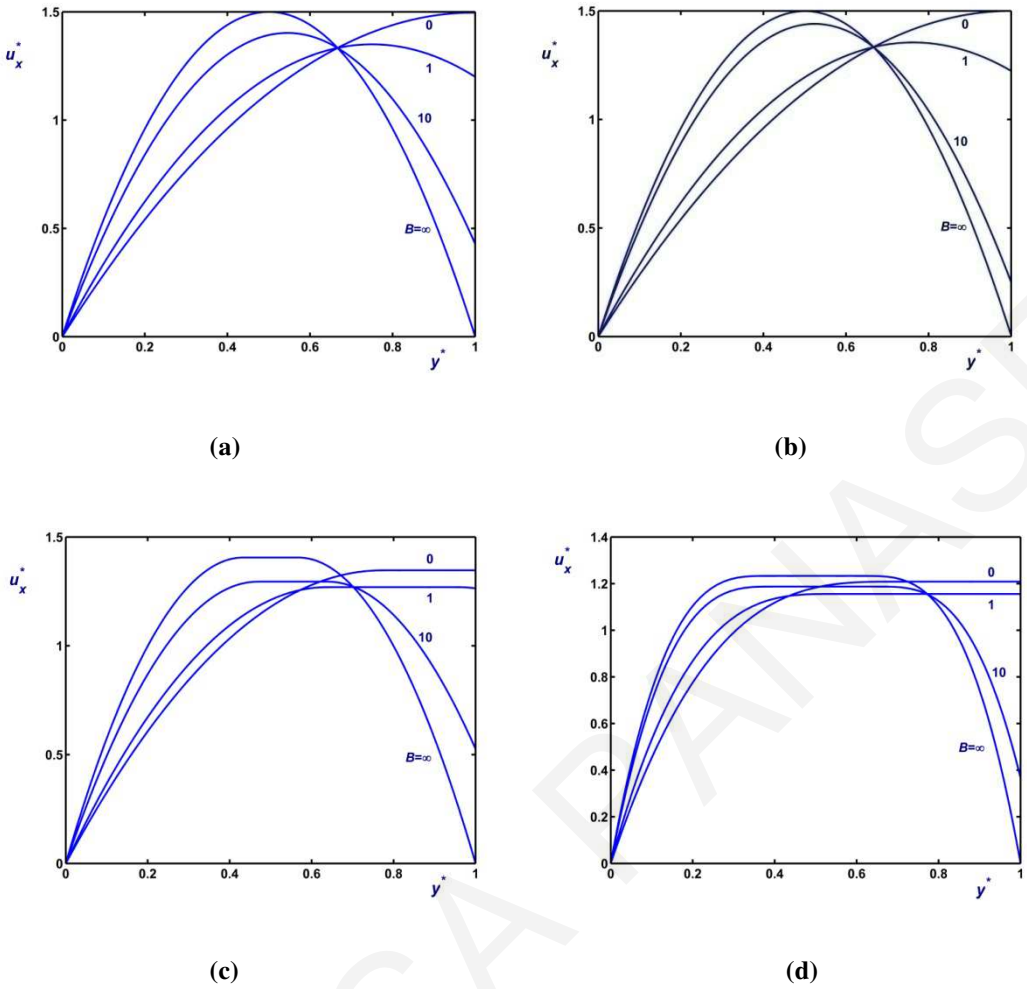

Figure 3.3: Fully-developed velocity profiles for different values of the slip number in plane Poiseuille flow with no-slip along the lower wall and slip along the upper one: (a) *Bn*=0 (Newtonian flow) and *s*=1 (Navier slip); (b) *Bn*=0 (Newtonian flow) and *s*=1/2; (c) *Bn*=1, *n*=1 (Bingham flow) and *s*=1 (Navier slip); (d) *Bn*=1, *n*=1/2 (Herschel-Bulkley flow) and *s*=1 (Navier slip).

Before discussing the Herschel-Bulkley solutions, it is instructive to consider the Newtonian case in which the velocity is a parabola. For any value of the slip exponent *s*, the velocity can be written in the form

$$u_x^* = y^* \left[6 - 2u_w^* + 3(u_w^* - 2)\, y^* \right] \tag{3.32}$$

where the slip velocity u_w^* is a root of

$$2u_w^* \left(3 - 2u_w^* \right) = B u_w^{*s} \tag{3.33}$$

For example, with *s*=1 (Navier slip)

$$u_w^* = \frac{6}{B+4} \tag{3.34}$$

and with s=1/2

$$u_w^* = \frac{3}{2} - \frac{B^2}{32}\left(\sqrt{1+\frac{96}{B^2}} - 1\right) \tag{3.35}$$

When $B = \infty$ (no slip with $u_w^* = 0$) and $B = 0$ (full slip with $u_w^* = 3/2$) the standard no-slip Poiseuille solutions in channels of dimensionless widths 1 and 2, respectively, are recovered, i.e.

$$u_x^* = 6y^*(1-y^*) \quad \text{and} \quad u_x^* = \frac{3}{2}y^*(2-y^*) \tag{3.36}$$

Figures 3.3a and 3.3b show the velocity profiles for s=1 and s=1/2, respectively, with $B = \infty$, 10, 1 and 0. It is easily verified that all curves intersect at the point (2/3,4/3), independently of the value of s. Figures 3.3c and 3.3d show similar velocity profiles for Herschel-Bulkley fluids with Bn=1 and n=1 (Bingham plastic) and n=1/2 in the Navier-slip case (s=1). As the slip number is reduced the solution passes from Regime III (two yield points) to Regime II below the critical slip number, which is B_c=0.7800 for n=1 and 0.8610 for n=1/2.

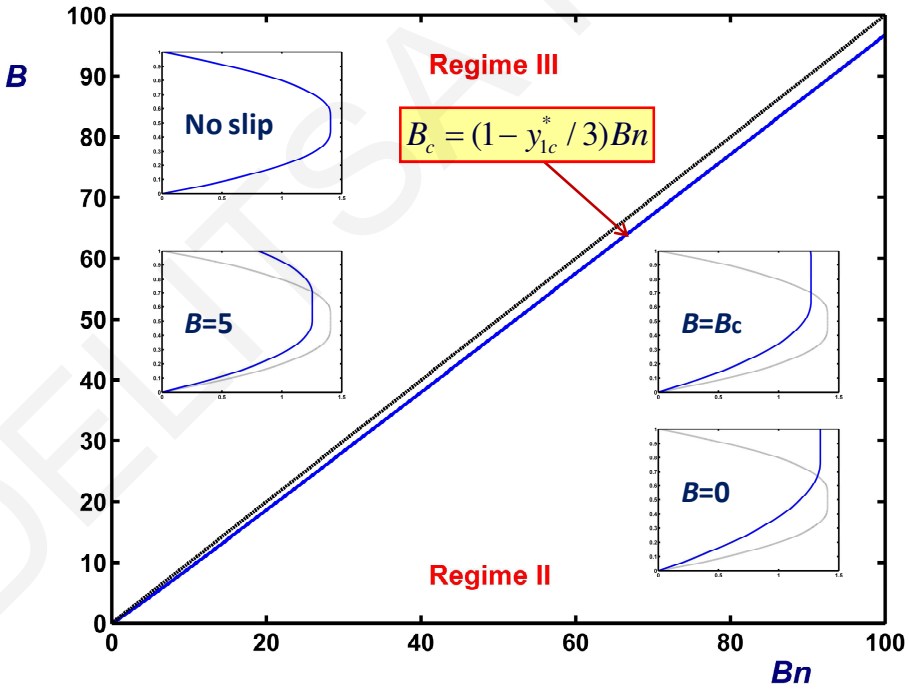

Figure 3.4: Flow regimes and representative velocity profiles in plane Bingham-plastic flow with no-slip along the lower wall and Navier slip (s=1) along the upper one. The velocity profiles have been obtained for Bn=1 and various slip numbers.

Figure 3.4 illustrates the two flow regimes on the (*Bn*,*B*) plane in the case of a Bingham plastic (*n*=1). These are separated by the curve $B_c = (1 - y_{1c}^* / 3)Bn$, which is slightly below the straight line $B = Bn$. Four representative velocity profiles, obtained taking *Bn*=1 and Navier slip (*s*=1), are also shown. Two of them are in Regime III. The first profile corresponds to no-slip at both walls ($B \to \infty$) and it is thus symmetric. As slip at the upper wall is enhanced (e.g. for *B*=5), symmetry is destroyed and the two yield points move upwards and the maximum velocity decreases. The upper yield point moves faster than the lower one reaching the wall when $B = B_c$ =0.7800. The velocity profile for this critical case is also shown in Fig. 3.4. Below this number, i.e. in Regime II, the yield point continues moving upwards as slip is increased, but the maximum velocity is now increasing. In the limit of *B*=0 (full slip), the maximum velocity is lower than that for $B \to \infty$, since it corresponds to the no-slip flow for a modified Bingham number equal to $Bn' = 2^n Bn = 2Bn$.

3.3 Numerical results and discussion

The system of the governing equations and the boundary conditions presented in section 3.2 was solved numerically using the finite element method (*u*-*v*-*p* formulation) with standard biquadratic basis functions for the two velocity components and bilinear ones for the pressure field. The Galerkin forms of the continuity and the momentum equations were used. The resulting nonlinear system of the discretized equations was solved with a Newton-Raphson iterative scheme with a convergence tolerance equal to 10^{-4}. The inhouse finite-element code developed and tested in the past thirty years (most recently in Philippou et al. (2016)) was used. Results have been obtained for Bingham numbers ranging from 0 (Newtonian flow) to 10, for power-law exponents from 1 (Bingham plastic) down to 1/2, for slip numbers from 0 (full-slip) to ∞ (no-slip), and for Reynolds numbers from 0 (creeping flow) to 10. Based on our previous studies (see Philippou et al. (2016)), the rather high value of *M*=100000 has been used in all viscoplastic simulations. For the low Reynolds number considered here, we took L_{mesh}=20 for $Re \le 1$ and L_{mesh}=50 for $1 < Re \le 10$. Some convergence difficulties have been observed in the weak-slip regime (i.e. for finite high values of the slip number *B*) when the value of *n* was less than unity. These are due to the fact that the slip velocity is of the order of the convergence tolerance and to the increased nonlinearity of the problem. The convergence of the results has also been investigated using meshes of different refinement. The results presented here have been obtained with a non-uniform mesh consisting of 368×80=29440 elements with 118657 velocity nodes (L_{mesh}=20). The total number of nodal unknowns with this mesh is 267203. This was graded with the element size increasing far from the walls and the inlet plane. The size of the smallest element at the corner of the inlet plane with the lower wall was 0.005.

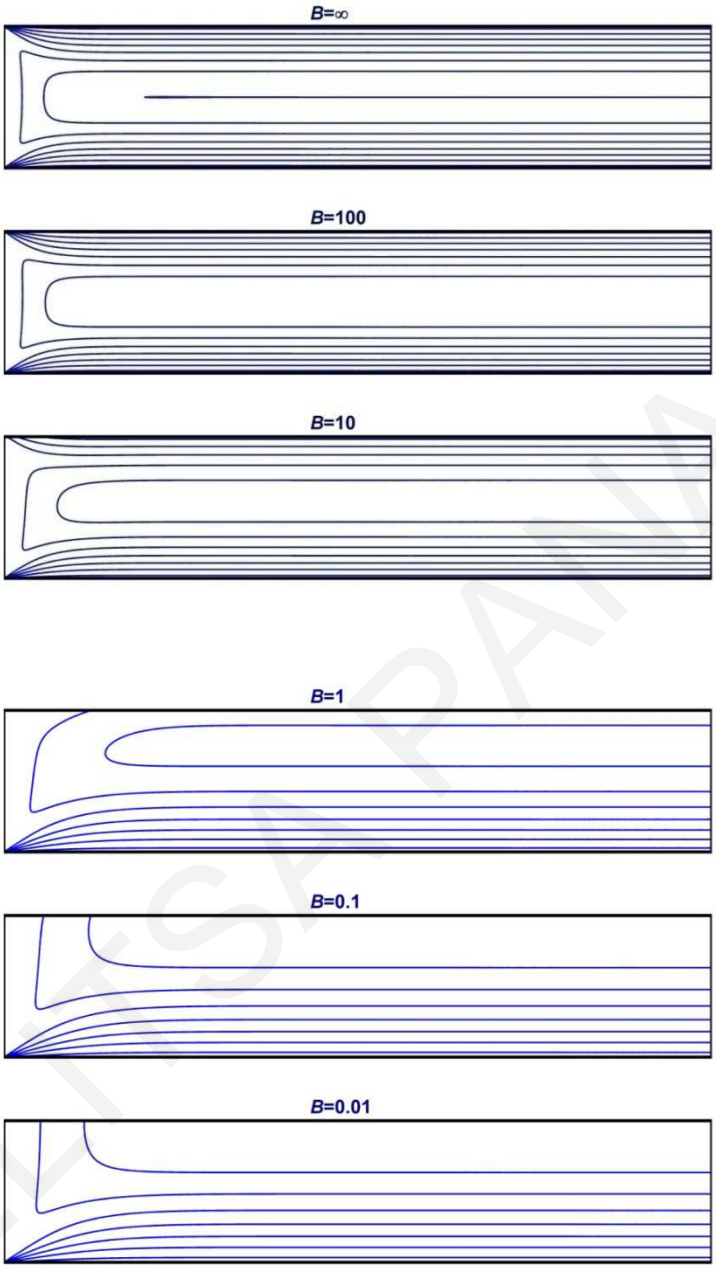

Figure 3.5: Velocity contours in flow development of creeping (*Re*=0) planar Newtonian Poiseuille flow with no-slip along the lower wall and Navier slip (*s*=1) along the upper one for various slip numbers.

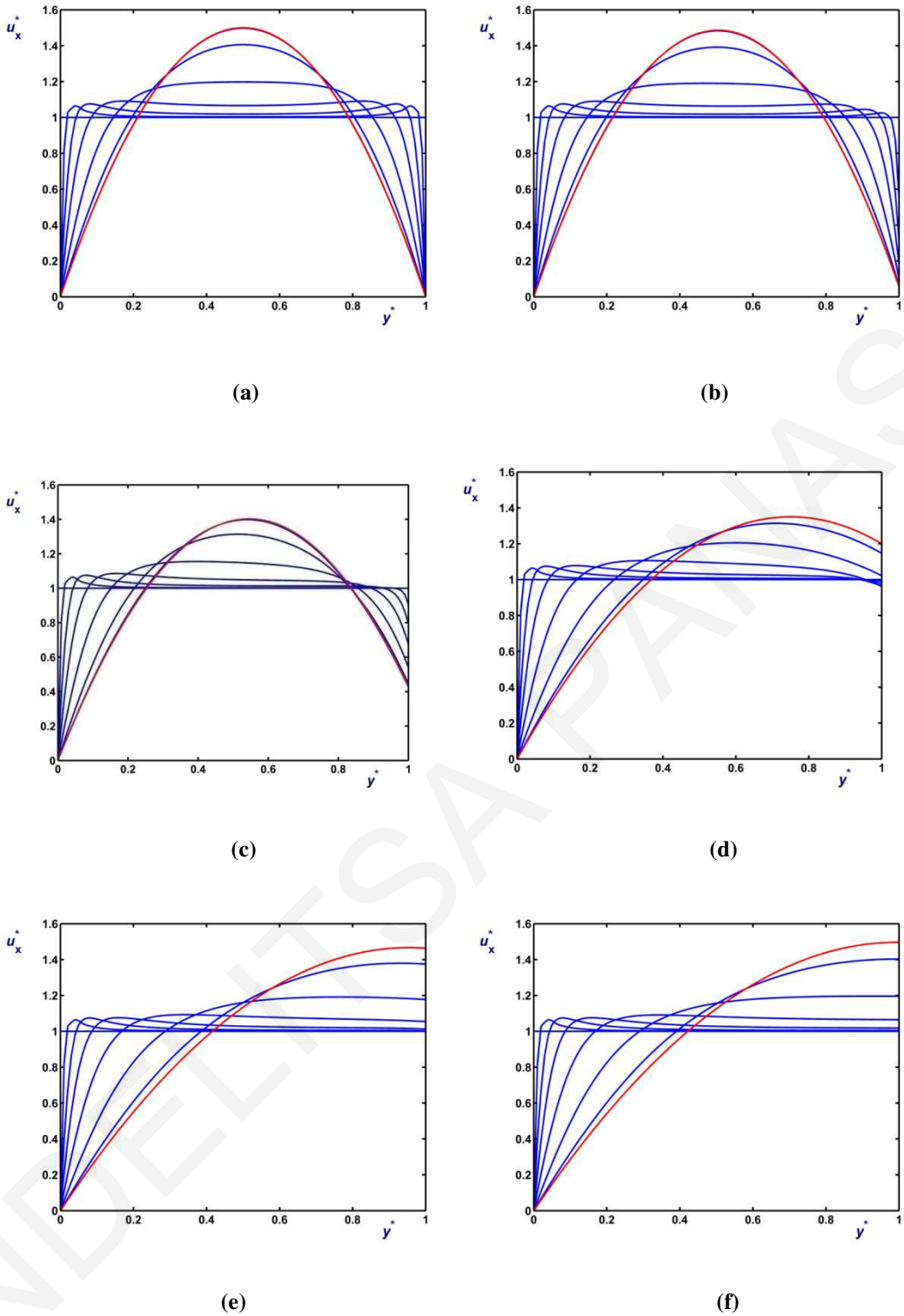

Figure 3.6: Development of the velocity in creeping (*Re*=0) planar Newtonian Poiseuille flow with no-slip along the lower wall and Navier slip (*s*=1) along the upper one: (a) *B*=∞ (no-slip); (b) *B*=100; (c) *B*=10; (d) *B*=1; (e) *B*=0.1; (f) *B*=0.01. Profiles at x^*=0, 0.02, 0.05, 0.1, 0.2, 0.4, 0.8 and ∞ (fully-developed flow).

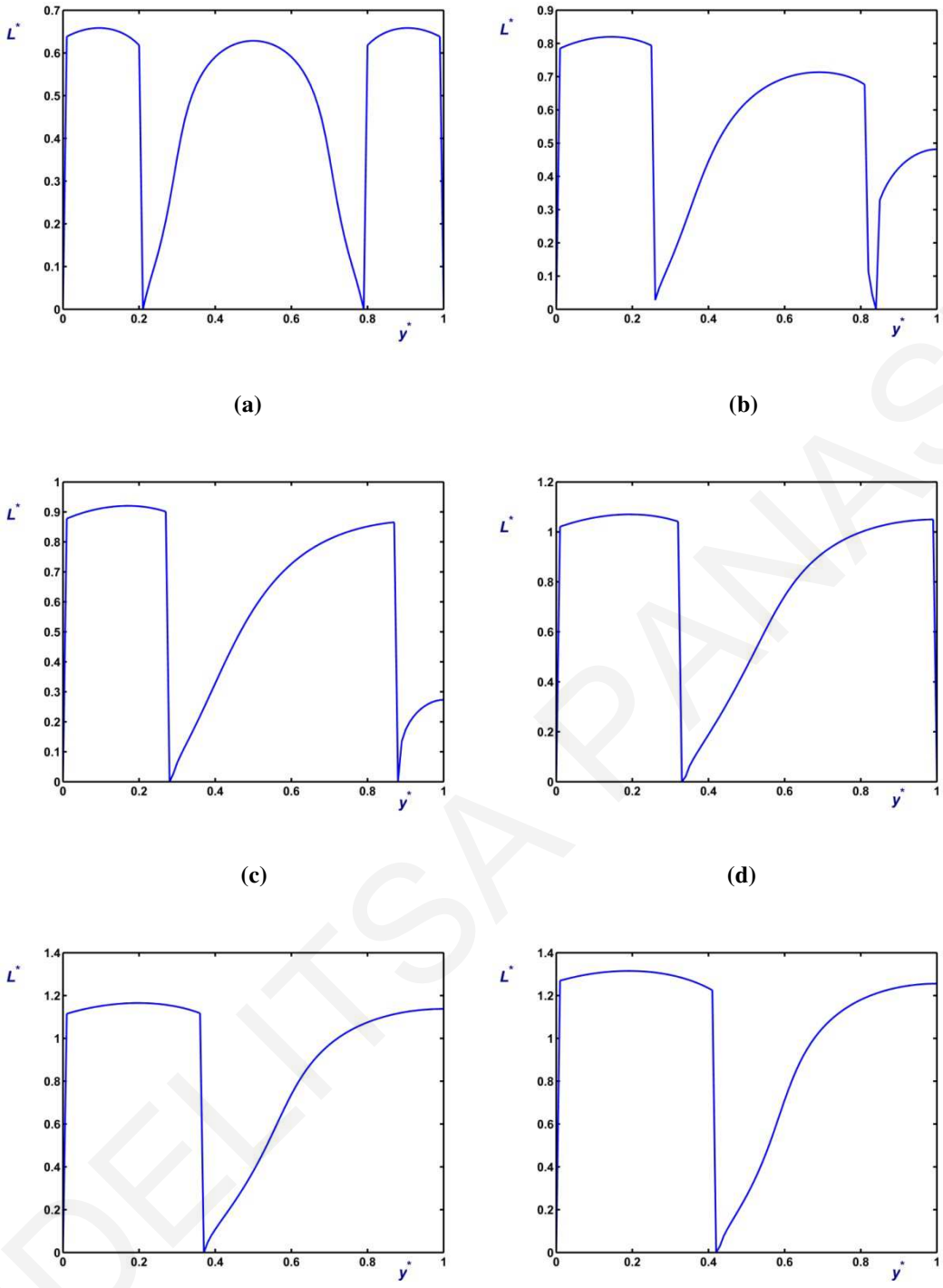

Figure 3.7: Development length functions in creeping (*Re*=0) planar Newtonian Poiseuille flow with no-slip along the lower wall and Navier slip (*s*=1) along the upper one for the slip numbers of Fig.3.6: (a) $B=\infty$ (no slip); (b) *B*=10; (c) *B*=5; (d) *B*=2; (e) *B*=1; (f) *B*=0.01.

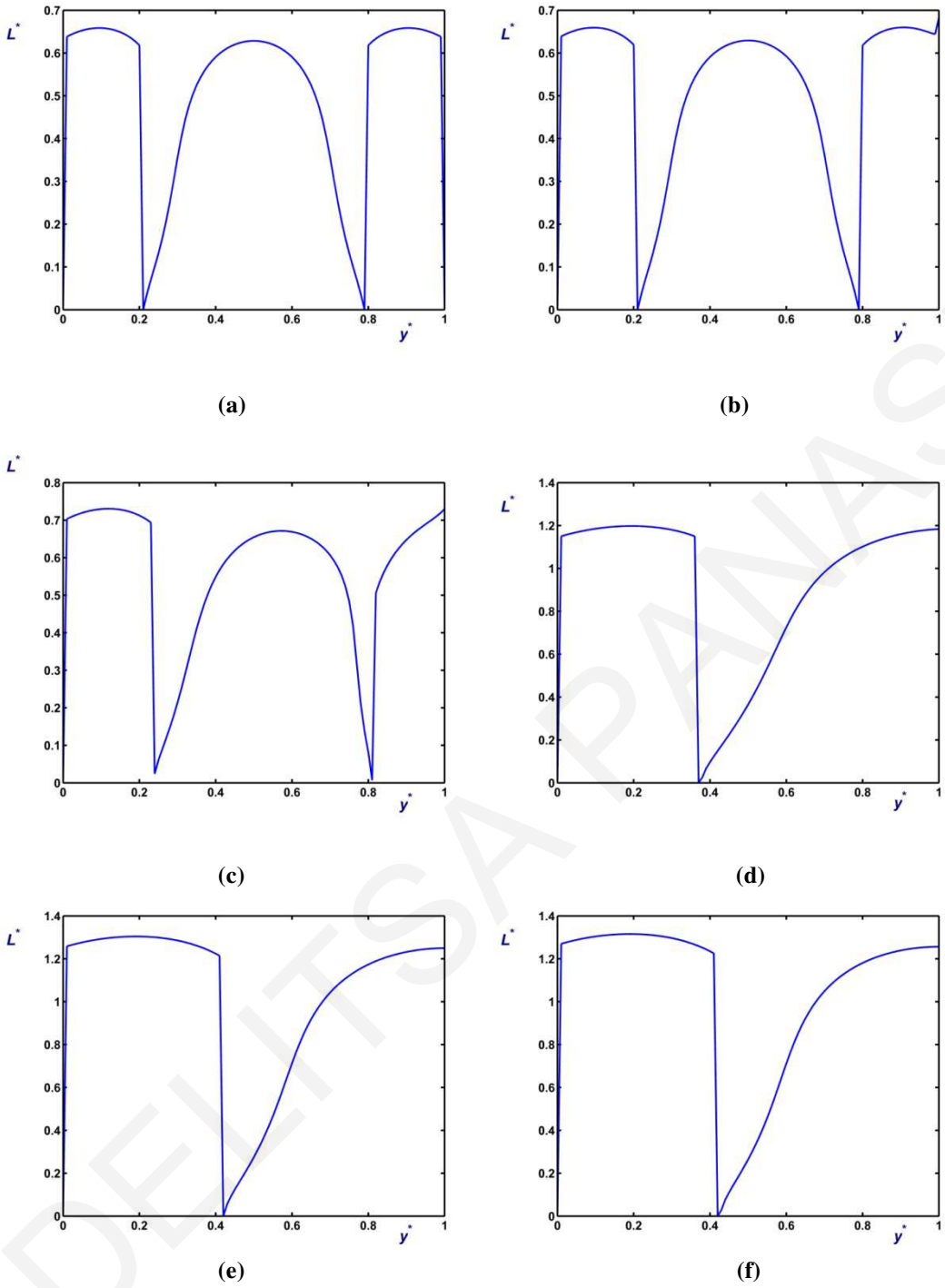

Figure 3.8: Development length functions in creeping (*Re*=0) planar Newtonian Poiseuille flow with no-slip along the lower wall and power-law slip (*s*=1/2) along the upper one for the slip numbers of Fig.3.6: (a) $B=\infty$ (no slip); (b) *B*=100; (c) *B*=10; (d) *B*=1; (e) *B*=0.1; (f) *B*=0.01.

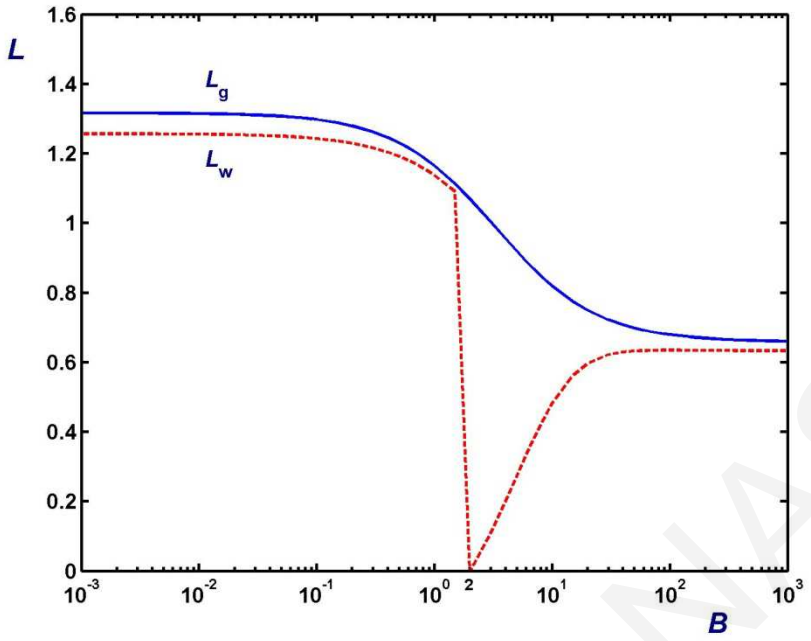

(a)

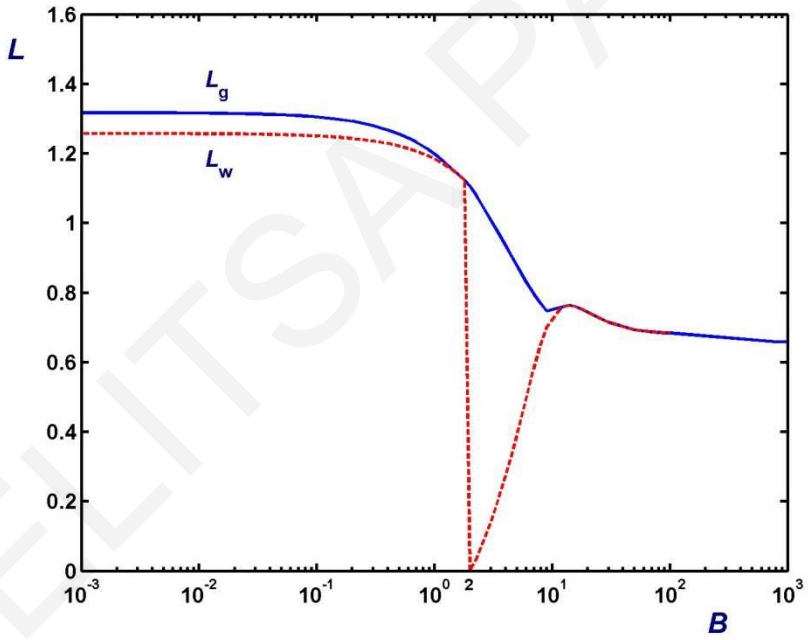

(b)

Figure 3.9: Global (solid) and wall (dashed) development lengths in creeping (*Re*=0) planar Newtonian Poiseuille flow with no-slip along the lower wall and slip along the upper one versus the slip number *B*. (a) *s*=1 (Navier slip); (b) *s*=1/2.

3.3.1 Newtonian flow

The Newtonian flow was investigated first. The effect of Navier slip (s=1) on the axial velocity contours in the case of creeping flow (Re=0) is illustrated in Fig. 3.5 for various values of the slip number ranging from B=∞ (no-slip) to B=0.01 (very strong slip). When B=∞ the velocity contours are symmetric about the midplane of the channel. As slip is introduced at the upper wall the flow becomes more and more asymmetric; in the limit of full slip (B=0) the flow corresponds to flow in a channel of double width with no slip at either wall and the upper wall serves simply as the symmetry plane of the latter flow. The flow development for the same slip numbers is also illustrated in Fig. 3.6, where the velocity profiles at different distances from the inlet are plotted. Note that while the velocity overshoot near the lower wall is unaffected, the one that is near the upper wall appears only when slip is rather weak (i.e. for B=∞ and 100).

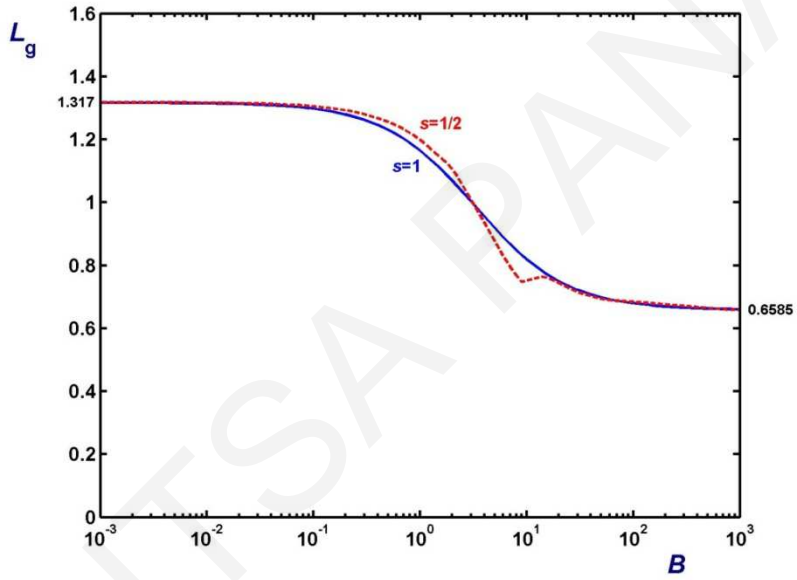

Figure 3.10: Global development lengths in creeping (Re=0) planar Newtonian Poiseuille flow with no-slip along the lower wall and slip along the upper one with s=1 (Navier slip) and s=1/2.

In Fig. 3.7, the plots of the development length function $L(y)$ for most of the slip numbers considered in Figs. 3.5 and 3.6 are shown. For high values of B there are two decelerating zones adjacent to the walls and one intermediate accelerating zone defined by the two points at which the fully-developed velocity is equal to the mean velocity and thus $L(y)$ vanishes. Below a critical slip number (~2) slip is so strong that the fluid at the wall actually accelerates and thus the upper deceleration zone disappears. For B=∞ (no-slip at the upper wall), $L(y)$ is of course symmetric. As already pointed out in Philippou et al. (2016), the global development length L_g does not occur in the accelerating zone at the plane of symmetry but in the two symmetric decelerating zones near the walls (L_g=0.6585, whereas the classical center-plane development length is L_c=0.6285). In the no-slip case the upper-wall development length, defined by $L_w \equiv L(1)$, is not relevant. As slip

along the upper wall is enhanced so does the asymmetry and the flow develops faster near the upper wall where slip occurs and near the lower wall more slowly so that the global development length increases (note that the y-axis is not the same). Hence, L_g occurs in the lower decelerating zone and L_w is much less than L_g. As B is reduced, L_g keeps increasing, while L_w is further reduced till the upper decelerating zone disappears, in which case the fluid at the upper wall actually accelerates and consequently there is only one decelerating region near the lower wall. Thus, below a certain slip number both L_g and L_w increase as B is reduced. The global development length increases asymptotically to twice its counterpart for the no-slip flow, i.e. L_g=1.3168.

In order to investigate the effect of the slip exponent s, calculations similar to those of Figs. 3.5-3.7 have been carried out taking s=1/2. It turns out that the velocity contours are not affected significantly, but, given that the fully-developed slip velocities for s=1/2 are lower, there are some noticeable differences between the velocity profiles, especially when slip is weak, i.e. for high or moderate values of the slip number. Interestingly, the slip exponent has a striking effect on the development length. (It should be noted that the dimensionless slip number depends on s.) As shown in Fig. 3.8, with s=1/2 the flow development for high values of B (weak slip) is slower in the zone near the upper wall rather than in the zone near the lower (no-slip) wall.

The dependence of the two development lengths on the slip number B for s=1 and 1/2 is illustrated in Fig. 3.9. L_g increases with slip exhibiting two plateaus in the weak- and strong-slip limits and a sharp change in the range (0.5, 5) of the slip number. The wall development length L_w exhibits a sharp non-monotonic behavior in the latter range due to the suppression and the disappearance of the decelerating region near the upper wall and vanishes at the critical slip number B=2 at which $u_w^* = 1$, independently of the slip exponent s (see Eq.(3.33)). With s=1, L_w is always less than L_g, while with s=1/2 the two lengths coincide when slip is weak. As pointed out in Kountouriotis et al. (2016), the wall development length can be defined only if the magnitude of the slip velocity exceeds a critical value. By demanding that 1% of the critical slip velocity must be equal to the tolerance used in the numerical simulations, then this critical slip velocity is equal to 0.01. From Eq. (3.33), the corresponding critical value of the slip number is then $B_{\text{crit}} = 5.96\times10^{2s}$. We thus find that $B_{\text{crit}} = 596$ for s=1 and $B_{\text{crit}} = 59.6$ for s=1/2. Therefore, the plots of L_w beyond these critical values in Fig. 3.9 (i.e. in the weak-slip regime) should be viewed with caution. Note also that the wiggle in the curve of L_g is simply due to the fact as slip is increased the flow development is initially slower in the upper deceleration zone which eventually disappears and thus the value of L_g is suddenly calculated in the lower deceleration zone. The global development lengths for s=1 and s=1/2 are compared in Fig. 3.10. As expected, the two lengths differ only for moderate values of the slip number and practically coincide in both the weak- and strong-slip regimes, where the effect of the slip exponent is insignificant. It should be noted that the development length corresponding to full slip (B=0) is twice the development length

for the no-slip case (infinite B), since it corresponds to the no-slip flow in a channel of a gap width equal to 2.

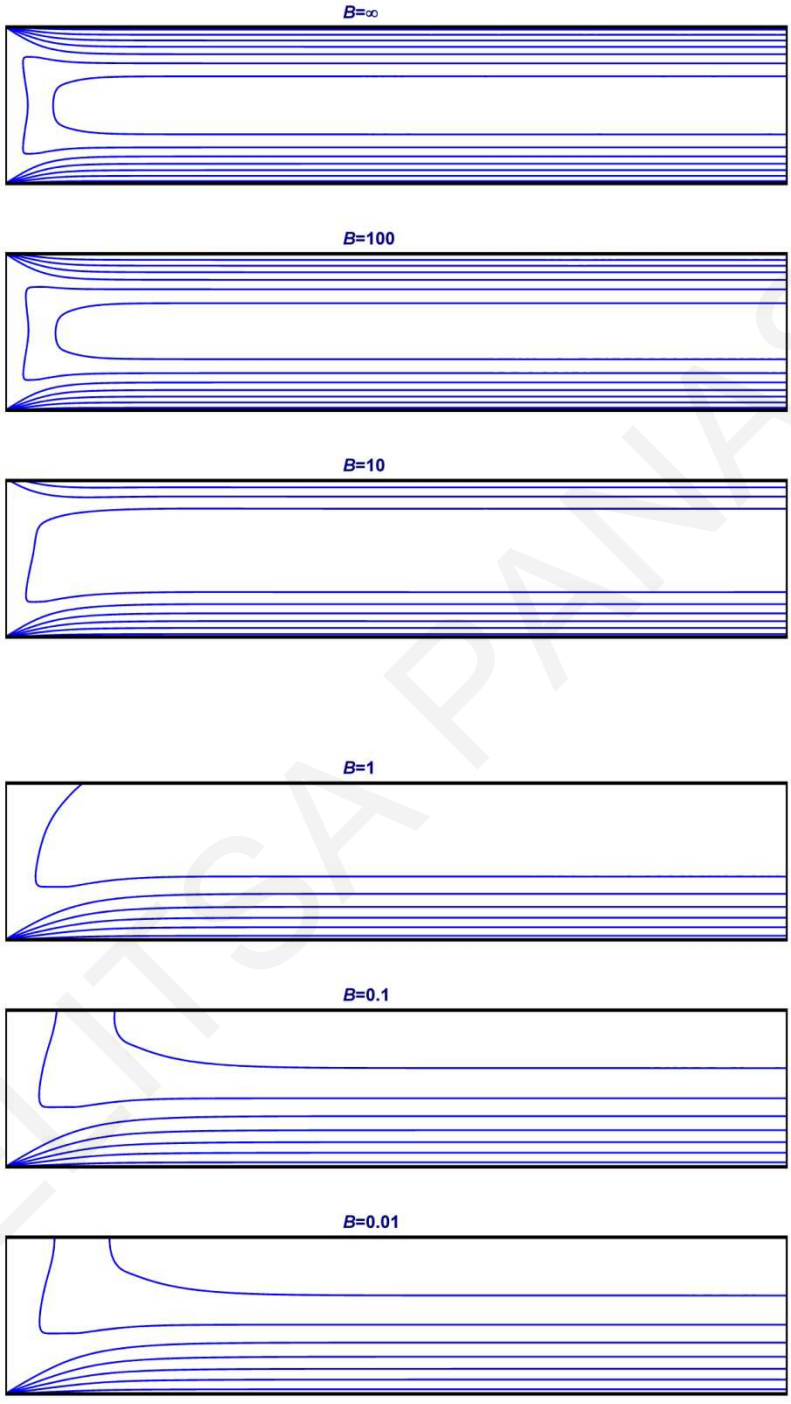

Figure 3.11: Velocity contours in flow development of creeping (Re=0) planar Bingham-plastic (n=1) Poiseuille flow with no-slip along the lower wall and Navier slip (s=1) along the upper one for Bn=1 and various slip numbers.

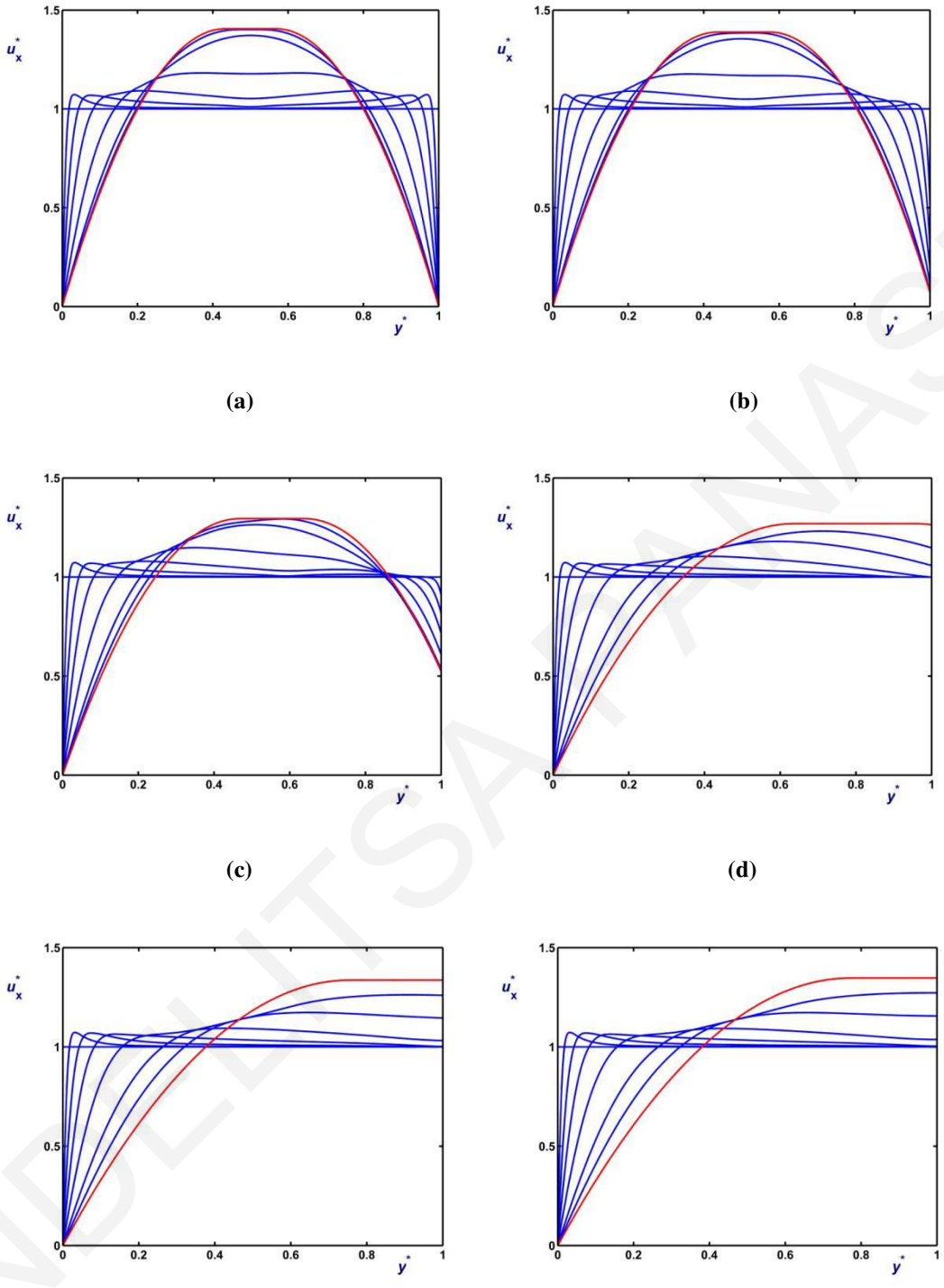

Figure 3.12: Development of the velocity in creeping (*Re*=0) planar Bingham-plastic (*n*=1) Poiseuille flow with no-slip along the lower wall and Navier slip (*s*=1) along the upper one with *Bn*=1: (a) *B*=∞ (no-slip); (b) *B*=100; (c) *B*=10; (d) *B*=1; (e) *B*=0.1; (f) *B*=0.01. Profiles at x^*=0, 0.02, 0.05, 0.1, 0.2, 0.4, 0.6 and ∞ (fully-developed flow).

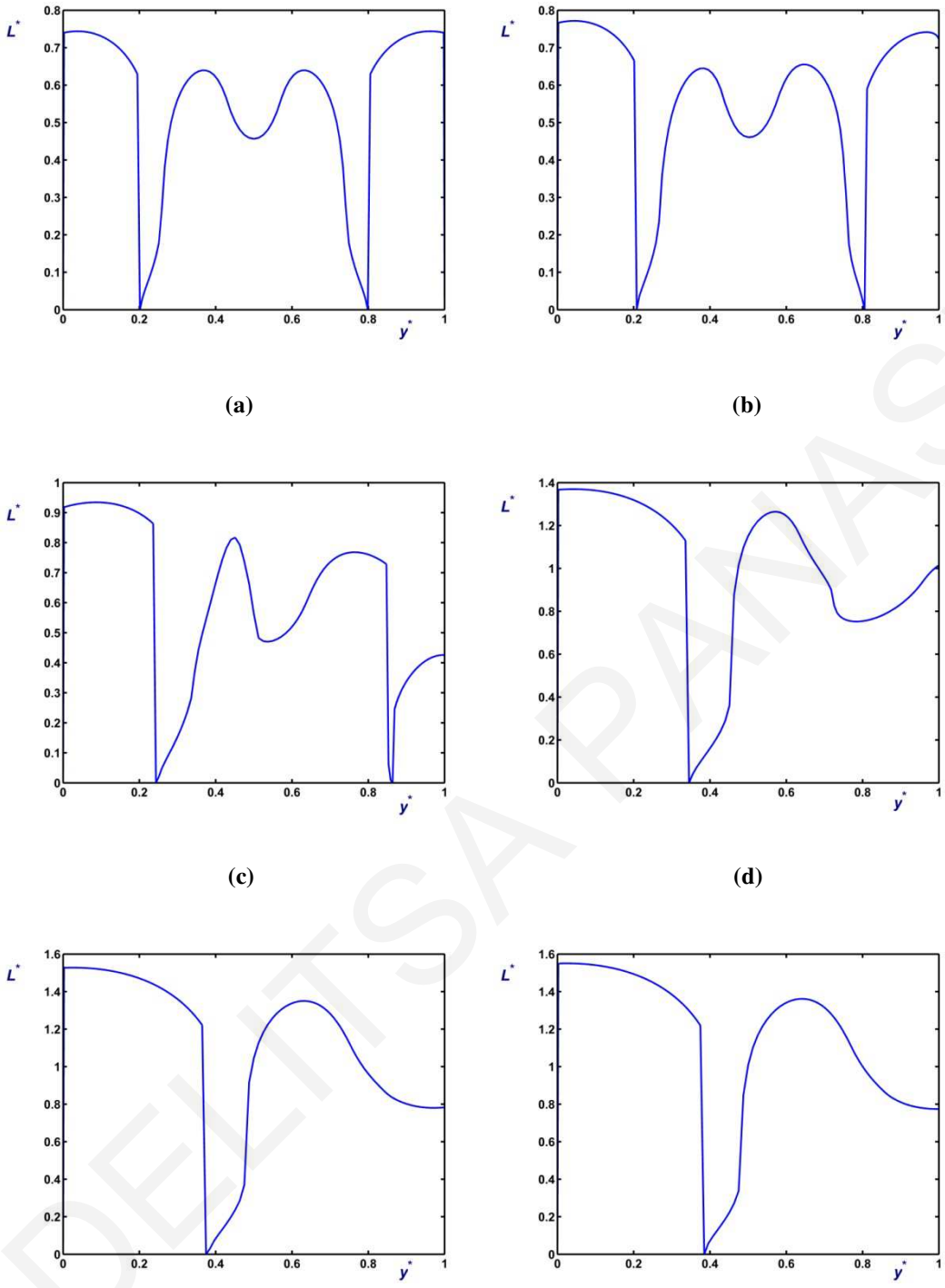

Figure 3.13: Development length functions in creeping (Re=0) planar Bingham-plastic (n=1) Poiseuille flow with no-slip along the lower wall and Navier slip (s=1) along the upper one for Bn=1 and the slip numbers of Fig 3.10: (a) B=∞ (no slip); (b) B=100; (c) B=10; (d) B=1; (e) B=0.1; (f) B=0.01.

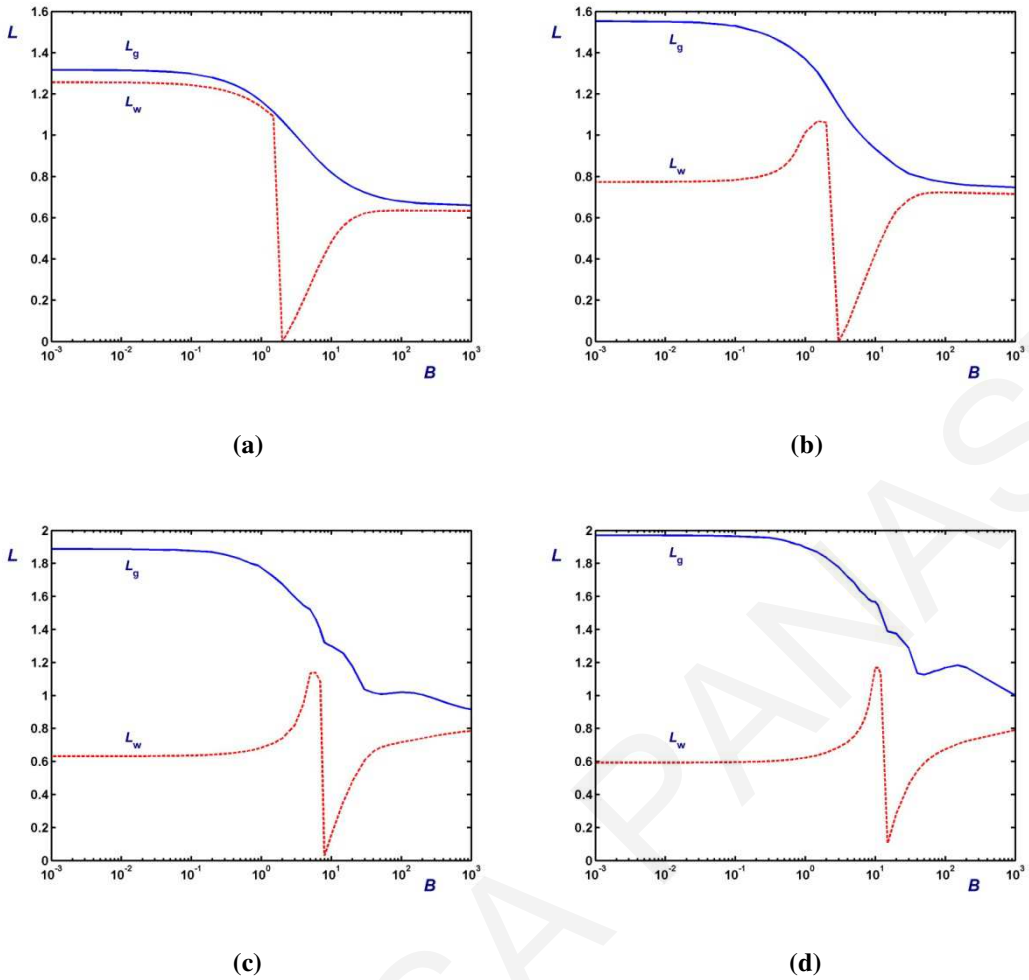

Figure 3.14: Global (solid) and wall (dashed) development lengths in creeping (*Re*=0) planar Bingham-plastic Poiseuille flow with no-slip along the lower wall and Navier slip (*s*=1) along the upper one versus the slip number *B*: (a) *Bn*=0 (Newtonian); (b) *Bn*=1; (c) *Bn*=5; (d) *Bn*=10.

3.3.2 Viscoplastic flow

In this subsection, numerical results for Bingham plastics (*n*=1) and Herschel-Bulkley fluids (*n*=1/2) are discussed. We then considered the Bingham plastic case (*n*=1) with *Bn*=1 for *Re*=0 (creeping flow). Figure 3.11 shows the axial velocity contours for various values of the slip number *B*. Figure 3.12 shows how the velocity component in the flow direction develops downstream attaining the fully-developed profile. When $B=\infty$ (no slip), the velocity profiles are symmetric exhibiting a central unyielded region. As slip is increased, asymmetry is enhanced, the velocity overshoot near the upper wall is suppressed, and the unyielded region moves towards the upper wall and increases in size. If slip becomes even stronger then Regime II is eventually reached, i.e. the unyielded region reaches the upper wall. The velocity overshoot near the no-slip wall persists in all cases, while its counterpart near the slip wall appears only when slip is weak (i.e. for high values of *B*).

The development length functions for various values of the slip number are shown in Fig. 3.13. These plots may be more complicated than their Newtonian counterparts in Fig. 3.8 but the main features remain the same: (a) L_g occurs near the no-slip wall, i.e. the flow develops more slowly in the decelerating zone adjacent to the no-slip wall than in the accelerating zone; (b) The fluid adjacent to the upper wall decelerates only when slip is weak, i.e. above a critical slip number.

Similar results have been obtained for higher values of the Bingham number. In Fig. 3.14, the global and wall development lengths for creeping flow (Re=0) and Bn=0 (Newtonian), 1, 5 and 10 are plotted versus the slip number. We observe that L_g increases with slip and with the Bingham number, whereas L_w exhibits a non-monotonic behavior. When slip is strong, L_w decreases rapidly with Bn. For moderate slip numbers, however, the dependence of L_w on the Bingham number is variable. It is clear that using L_w may lead to erroneous results regarding flow development.

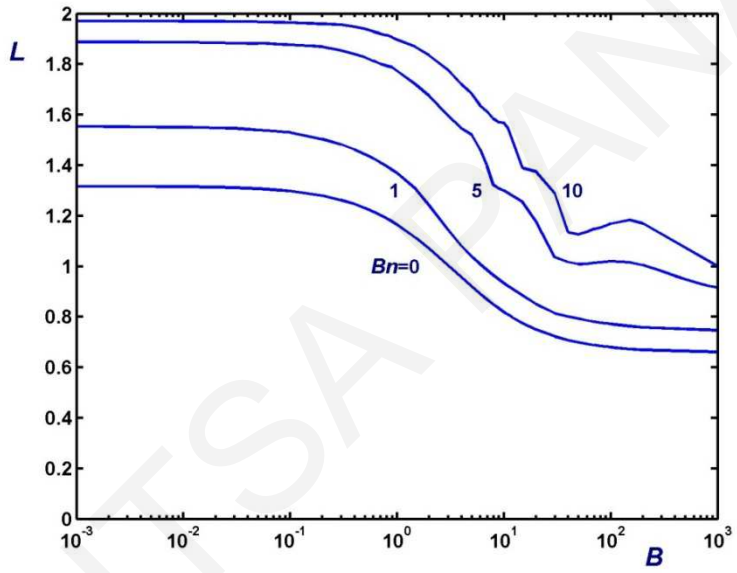

Figure 3.15: Global development lengths in creeping (Re=0) planar Bingham-plastic Poiseuille flow with no-slip along the lower wall and Navier slip (s=1) along the upper one versus the slip number B for different Bingham numbers.

The global development lengths for Bn=0, 1, 5, and 10 are compared in Fig. 3.15. Based on L_g, flow development is slower as viscoplasticity and slip are increased. Again, the wiggles in the curves for Bn=5 and 10 indicate transition of L_g to a different deceleration or acceleration zone. As mentioned above, in Newtonian flow (Bn=0) the development length for full slip (B=0) is two times the development length for the no-slip case (infinite B), since it corresponds to the flow development in a channel with no slip and with a gap width equal to 2. This is not the case for Bingham flow; the development length in the full-slip case is two times the no-slip development length corresponding to 2Bn and not to Bn.

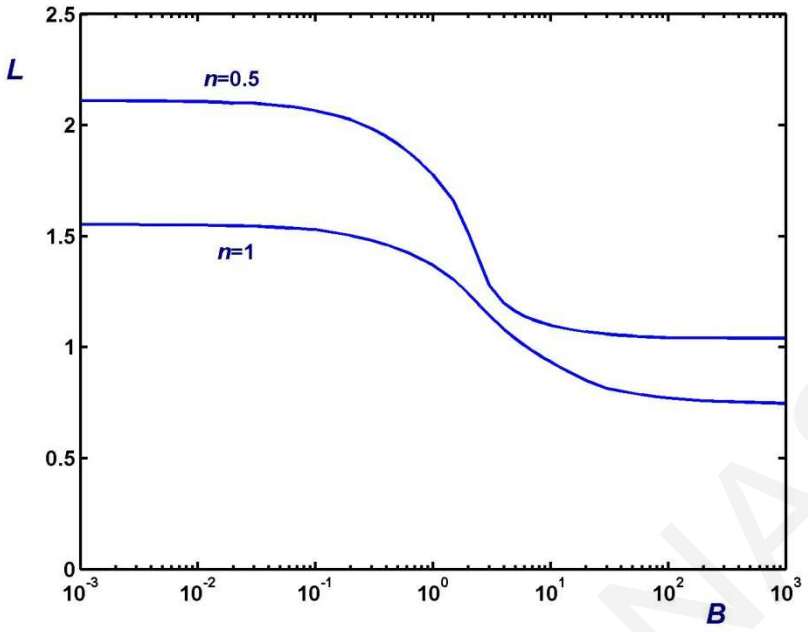

Figure 3.16: Global development lengths in creeping (*Re*=0) planar Herschel-Bulkley Poiseuille flow with no-slip along the lower wall and Navier slip (*s*=1) along the upper one versus the slip number *B* for *Bn*=1 and *n*=1 (Bingham plastic) and *n*=1/2.

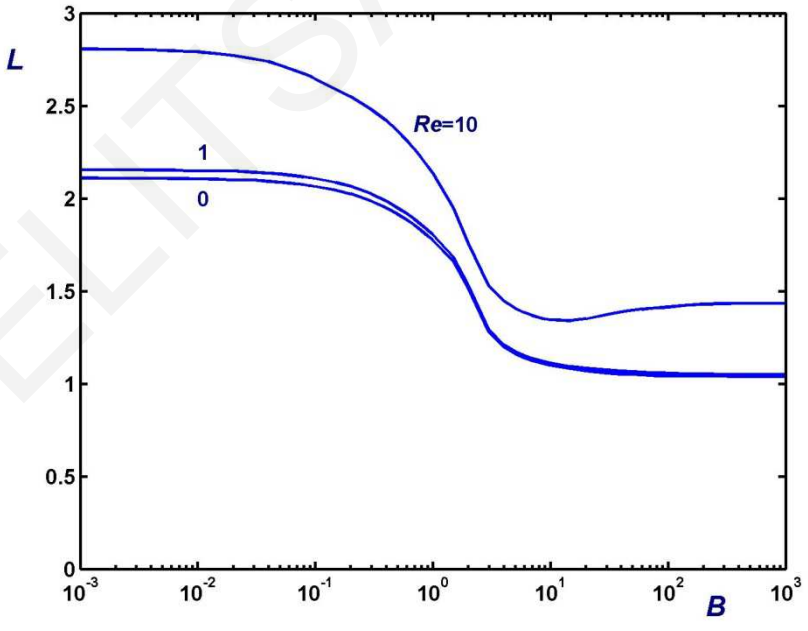

Figure 3.17: Global development lengths in planar Herschel-Bulkley Poiseuille flow with no-slip along the lower wall and Navier slip (*s*=1) along the upper one versus the slip number *B* for different Reynolds numbers, *Bn*=1 and *n*=1/2.

Simulations have also been carried out for Herschel-Bulkley flow with Bn=1, n=1/2 and s=1 (Navier slip). The global development lengths for n=1 and n=1/2 are compared in Fig. 3.16. As expected, shear thinning results in bigger development lengths. Finally, the effect of the Reynolds number is illustrated in Fig. 3.17, where the global development length for Bn=1 and Re=0, 1, and 10 is plotted versus the slip number. For the moderate numbers employed here, the global development length increases with inertia. The relative increase of L_g is much higher when slip is weak, moderate in the strong-slip regime, and becomes smaller in the intermediate slip regime when the upper deceleration zone disappears.

An interesting issue not addressed in the present work is the accurate determination of yielded and unyielded regions in viscoplastic flow development. Our calculations with "reasonable" meshes showed that this may not be possible for moderate or higher Bingham numbers.

More acceptable results, in the sense that the entry unyielded region which moves horizontally as a solid body at unit velocity is separated from the unyielded region of the fully-developed flow which moves at a higher velocity, may be obtained for rather low Bingham numbers. At higher Bingham numbers these two regions appear to merge, which is obviously inadmissible. Hence, the flow development problem is a challenging test for any numerical method proposed for solving viscoplastic flows. To our knowledge, only recently Dimakopoulos et al. (2018) made some preliminary calculations of yielded/unyielded regions in viscoplastic flow development and compared the predictions of the Augmented Lagrangian Method (ALM) and the regularization method.

3.4 Conclusions

The entry flow of a Herschel-Bulkley fluid in a horizontal channel with slip along the upper wall has been investigated numerically using finite elements and the Papanastasiou regularization for the constitutive equation. The different flow regimes for the one-dimensional fully-developed flow were identified and the corresponding solutions have been presented. The global development length is considered so that both the acceleration and deceleration zones are included.

Representative numerical solutions for the two-dimensional flow development have been presented and the effects of the Bingham and slip numbers on the development of the velocity and on the development length have been discussed for various values of the power-law exponent of the slip equation. The global development length increases with the Bingham number and inertia and decreases with the power-law exponent. In general, the global development length increases with slip exhibiting two plateaus for low and strong slip and a sharp increase in the moderate slip regime.

Chapter 4

Pressure-driven flow of a Herschel-Bulkley fluid with pressure-dependent rheological parameters

In this chapter we present the lubrication equations for the general case of a Herschel-Bulkley fluid with the consistency index and the yield stress being functions of pressure. We also derive analytical solutions for the case of a channel of constant width with special forms of the consistency-index and yield-stress pressure-dependence functions. We consider channels of linearly varying width and we derive semi-analytical solutions for the case of a Bingham plastic with both the yield stress and plastic viscosity varying linearly with pressure.[5]

4.1 Introduction

Yield-stress fluids, also known as viscoplastic fluids, are encountered in a variety of industrial applications, such as oil drilling and transport, fresh concrete manufacturing, waste management and food processing, and in many environmental, geological and biological processes (Barnes, 1999; Balmforth et al., 2014). Viscoplastic materials are commonly assumed to behave as fluids only if the stress exceeds the yield stress τ_y^*; otherwise, they behave as solids. (It should be noted that throughout this chapter, symbols with stars denote dimensional quantities.) For an update on the ongoing debate about the concept of a yield-stress fluid and the definition of yield stress, the reader is referred to the recent reviews by Malkin et al. (2017) and by Dinkgreve et al. (2017). As noted by Coussot et al. (2017), most researchers now consider that the yield stress marks a limit between the existence of steady-state flows -above the yield stress- and the observation of continuously slowed down flows.

The most popular constitutive equation describing viscoplastic behavior is the Bingham-plastic equation (Bingham, 1922). This involves two material parameters, i.e. the yield stress and the plastic viscosity μ^*, and has the following tensorial form

[5] The material of this chapter appears in Panaseti et al. (2018).

$$\begin{cases} \mathbf{D}^* = \mathbf{0}, & \tau^* \le \tau_y^* \\ \boldsymbol{\tau}^* = 2\left(\dfrac{\tau_y^*}{\dot{\gamma}^*} + \mu^*\right)\mathbf{D}^*, & \tau^* > \tau_y^* \end{cases} \tag{4.1}$$

where $\boldsymbol{\tau}^*$ is the viscous stress tensor,

$$\mathbf{D}^* \equiv \frac{1}{2}\left[\nabla^*\mathbf{v}^* + (\nabla^*\mathbf{v}^*)^T\right] \tag{4.2}$$

is the rate of deformation tensor, $\mathbf{v}^*$ is the velocity vector, and $\dot{\gamma}^* \equiv \sqrt{2\mathrm{tr}\mathbf{D}^{*2}}$ and $\tau^* \equiv \sqrt{\mathrm{tr}\boldsymbol{\tau}^{*2}/2}$ are the magnitudes of $2\mathbf{D}^*$ and $\boldsymbol{\tau}^*$, respectively. Setting $\tau_y^* = 0$, the Bingham-plastic is reduced to the Newtonian constitutive equation and μ^* is simply the familiar Newtonian viscosity. A generalization of the Bingham-plastic equation is the Herschel-Bulkley model (Herschel and Bulkley, 1926), which involves three material parameters

$$\begin{cases} \mathbf{D}^* = \mathbf{0}, & \tau^* \le \tau_y^* \\ \boldsymbol{\tau}^* = 2\left(\dfrac{\tau_y^*}{\dot{\gamma}^*} + k^*\dot{\gamma}^{*n-1}\right)\mathbf{D}^*, & \tau^* > \tau_y^* \end{cases} \tag{4.3}$$

where k^* is the consistency index and n is the flow index (power-law exponent). Setting the latter to unity yields the Bingham-plastic model. Setting $\tau_y^* = 0$ results in the power-law model, which is able to account for shear-thinning (n<1) and shear-thickening (n>1) effects. Due to the two-branch nature of viscoplastic constitutive equations, the flow domain consists of yielded regions (viscous domain) where $\tau^* > \tau_y^*$ and unyielded regions (rigid domain) where $\tau^* \le \tau_y^*$. The latter regions include stagnant zones where the velocity is zero and zones where the material moves as a solid body. The location of the interface between yielded and unyielded regions is not known a priori and causes severe difficulties in solving viscoplastic flows, especially in two and three dimensions (Mitsoulis and Tsamopoulos, 2017).

In the last few years, a number of studies concerned numerical simulations of flows of viscoplastic materials with pressure-dependent material parameters. Staron et al. (2012) investigated numerically the discharge of a granular silo, which, for small and moderate outlets, is characterized by a constant discharge rate in contrast with the clepsydra for which the flow velocity depends on the height of the fluid left in the container. Implementing plastic rheology (i.e., $\mu(I)$ rheology), they were able to explain the so-called Beverloo scaling only by means of the pressure dependence of the yield stress. Ionescu et al. (2015) carried out finite-element simulations of the granular column collapse problem over inclined planes using the Bingham-plastic constitutive equation and assuming that the yield stress varies linearly with pressure. The plastic viscosity was taken either constant or variable depending on both the pressure and the rate of strain. Daviet and Bertails-Descourbes (2016) proposed a non-smooth complex optimization numerical framework

for the simulation of dense granular flows assuming that the material behaves as a Bingham plastic whose yield stress varies linearly with pressure while the plastic viscosity is constant. They pointed out that this assumption implies that grain-grain interactions mostly involve rigid-body contacts with Coulomb friction. Khouja et al. (2015) analyzed a regularized Bingham model with pressure-dependent yield stress in the framework of stationary flows and investigated existence, uniqueness and regularity. They showed that the model can be solved and approximated as far as the frictional parameter is small enough.

Recently, Fusi (2017) considered non-isothermal flows of a Bingham plastic with the plastic viscosity and the yield stress depending on both the temperature and pressure. More specifically, he used a perturbation approach to derive the Oberbeck-Boussinesq approximation for a Bingham fluid under the assumption that the Reynolds number is of order one and considered the cases where the Froude number is either small or of order one. Fusi used an exponential expression describing the dependence of the plastic viscosity on the pressure and the temperature and a linear one for the yield stress (such that both rheological parameters increase with pressure and decrease with temperature) (Fusi, 2017).

The present work is motivated by the recent work of Fusi et al. (2015) who presented a novel technique for modelling the lubrication flow of a Bingham plastic in a two-dimensional channel of non-uniform thickness. Under the lubrication approximation, the yield surface and the two velocity components are calculated from the pressure by means of closed form expressions, while the pressure satisfies an integro-differential equation. This was solved by Fusi et al. with an iterative procedure (Fusi et al., 2015). Fusi et al. (2015) also considered briefly the case of pressure-dependent plastic viscosity and provided some approximations for the case of a slowly varying linear wall.

The advantage of the method of Fusi et al. (2015), is that the lubrication paradox is avoided and the correct shape of the yield surface which is opposite to that of the wall is approximated at zero order. With other approaches, the correct shape of the yield surface is obtained after calculating higher-order solutions (Frigaard and Ryan, 2004; Putz et al., 2009). In asymptotic analyses where the pressure gradient is obtained from the constraint of a unit areal flux in the x-direction at leading order, the yield surface variation (at zero order) is similar to that of the wall, due to the scaling with the mean velocity. The lubrication paradox arises from the fact that the predicted plug is not a true unyielded region since the leading order velocity varies in the x-direction. Thus, the position of the yield surface needs to be corrected by calculating higher-order solutions (Frigaard and Ryan, 2004; Putz et al., 2009).

Nevertheless, since the pressure is scaled with the pressure difference between and inlet and outlet planes of the channel and the stress components with the pressure difference times the (small) aspect ratio of the channel, a prerequisite of the model of Fusi et al. is that the unyielded region (plug) extends from the inlet to the outlet plane as well (Fusi et al., 2015). Therefore, the model cannot be applied when the plug is broken. Consequently, the results of Fusi et al. (2015) in

this latter case are not reliable. For example, the calculated transverse velocity contours cross the symmetry plane where this velocity component should vanish.

The objectives of the present work are: (a) the extension of the method of Fusi et al. (2015) for solving the lubrication flow of a Herschel-Bulkley fluid with pressure-dependent consistency index and yield stress in a symmetric channel of non-constant width; (b) the derivation of analytical solutions for certain limiting cases, such as the flows in a channel of constant or linearly-varying width; and (c) the investigation of the advantages and the limitations of the method.

Fusi et al. (2014) derived solutions of plane Poiseuille and Couette flows of a Bingham plastic and determined conditions for existence or non-existence of a rigid plug under the assumption that the velocity is one-dimensional while the pressure in the yielded region is two-dimensional. They derived explicit solutions for the case where the yield stress follows the linear equation

$$\tau_y(p) = \tau_0\left[1+\beta(p-p_0)\right] \tag{4.4}$$

where τ_0 denotes the yield stress at a reference pressure p_0 and β is the yield-stress growth coefficient; and the plastic viscosity also varies linearly and vanishes at zero relative pressure, i.e.

$$\mu^*(p^*) = \bar{\alpha}^*(p^* - p_0^*) \tag{4.5}$$

where the constant $\bar{\alpha}^*$ has time units. With the latter assumption, the derivation of an analytical solution becomes easier but the flows of a Bingham plastic with constant rheological parameters or with constant plastic viscosity are not special cases of the flow considered. This shortcoming was avoided by Damianou and Georgiou (2017) who analyzed the same flow using

$$\mu^*(p^*) = \mu_0^*\left[1+\alpha^*(p^* - p_0^*)\right] \tag{4.6}$$

instead. In the present work, with the use of the lubrication method of Fusi et al. (2015), the study of viscoplastic Poiseuille flows with a general wall function and pressure-dependent rheological parameters is possible.

In section 4.2 the lubrication equations are presented for the general case of a Herschel-Bulkley fluid with the consistency index and the yield stress being (general) functions of pressure. The zero-order solution is derived semi-analytically, in the sense that closed-form expressions are derived for the two velocity components in terms of the pressure, which is found by solving an integro-differential equation numerically. As mentioned above, the solutions hold as long as the unyielded core extends continuously from the inlet to the outlet plane. Compared to Fusi et al. (2015), the presentation of the method is considerably simpler despite considering a more general flow problem. In section 4.3, we derive analytical solutions for the case of a channel of constant width with special forms, i.e. linear and exponential, of the consistency-index and yield-stress pressure-dependence functions. The yield-stress growth parameter is allowed to be negative and the

applicability windows of the method in terms of the various parameters are determined. In section 4.4, channels of linearly varying width (converging and diverging channels) are considered and semi-analytical solutions are derived for the case of a Bingham plastic with both the yield stress and the plastic viscosity varying linearly with pressure. The applicability and the limitations of the method are again discussed. In section 4.5, we present numerical results for more complex geometries. In contrast to the work of Fusi et al. (2015), the integro-differential equation for the pressure is solved directly (not iteratively) by means of a standard pseudo-spectral numerical method. Finally, in section 4.6, the conclusions are summarized.

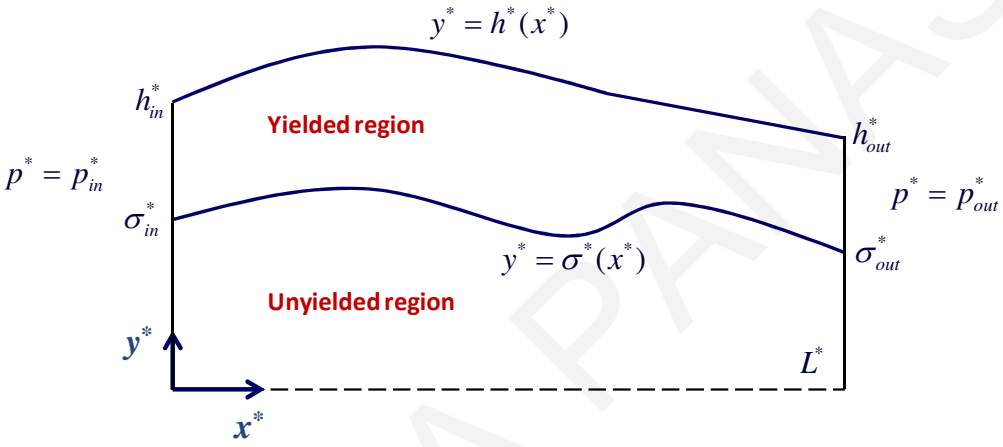

Figure 4.1: Geometry, some definitions and boundary conditions for the dimensional flow in a symmetric channel of length L^* and variable width $2h^*(x^*)$ with an unyielded core of width $\sigma^*(x^*)$. Due to symmetry, only half of the flow domain is shown.

4.2 Derivation of the model

We consider a Herschel-Bulkley fluid, i.e. a fluid obeying constitutive equation (4.3), where however the consistency index k^* and the yield stress τ_y^* are pressure dependent. For the sake of generality, we assume that

$$k^*(p^*) = k_0^* f(\alpha^*(p^* - p_0^*)) \tag{4.7}$$

and

$$\tau_y^*(p^*) = \tau_0^* g(\beta^*(p^* - p_0^*)) \tag{4.8}$$

where k_0^* is the consistency index at the reference pressure (assumed to be the same for the two material parameters) and f and g are appropriate increasing functions, such that $f(0) = g(0) = 1$.

Assume now the pressure-driven flow of an incompressible Herschel-Bulkley fluid in a symmetric long channel of length L^* and variable width $2h^*(x^*)$, as illustrated in Fig. 4.1, where only the upper part of the domain is shown, due to symmetry. A pressure p_{in}^* is applied at the inlet of the channel ($x^* = 0$) while the pressure at the exit ($x^* = L^*$) is $p_{out}^* < p_{in}^*$, i.e., the imposed pressure difference is $\Delta p^* = p_{in}^* - p_{out}^*$. The main flow is in the x^* direction and the z^*-velocity component is zero. Hence, the velocity vector is of the form $\mathbf{v}^* = v_x^*(x^*, y^*)\mathbf{i} + v_y^*(x^*, y^*)\mathbf{j}$. In the flow of interest (Fig. 4.1), the yielded and the unyielded regions are separated by the interface $y^* = \sigma^*(x^*)$ for $0 \le x^* \le L^*$, where $0 < \sigma^*(x^*) < h^*(x^*)$. Hence, the unyielded region extends from the inlet to the outlet plane, i.e. the plug is not broken. Moreover, if $\sigma^*(x^*) = h^*(x^*)$ at any point x^*, the unyielded region touches the wall and due to the no-slip boundary condition, there is no flow. Let also $\sigma_{in}^* \equiv \sigma^*(0)$ and $\sigma_{out}^* \equiv \sigma^*(L^*)$.

In the yielded region, the continuity equation and the *x*- and *y*-components of the momentum equation are simplified as follows:

$$\frac{\partial v_x^*}{\partial x^*} + \frac{\partial v_y^*}{\partial y^*} = 0 \tag{4.9}$$

$$\rho^*\left(v_x^*\frac{\partial v_x^*}{\partial x^*} + v_y^*\frac{\partial v_x^*}{\partial y^*}\right) = -\frac{\partial p^*}{\partial x^*} + \frac{\partial \tau_{xx}^*}{\partial x^*} + \frac{\partial \tau_{yx}^*}{\partial y^*} \tag{4.10}$$

$$\rho^*\left(v_x^*\frac{\partial v_y^*}{\partial x^*} + v_y^*\frac{\partial v_y^*}{\partial y^*}\right) = -\frac{\partial p^*}{\partial y^*} + \frac{\partial \tau_{xy}^*}{\partial x^*} + \frac{\partial \tau_{yy}^*}{\partial y^*} \tag{4.11}$$

where ρ^* is the mass density. The non-zero components of the stress tensor in the yielded regime read:

$$\left.\begin{aligned}
\tau_{xx}^* &= 2\left\{\frac{\tau_0^* g(\beta^*(p^* - p_0^*))}{\dot\gamma^*} + k_0^* f(a^*(p^* - p_0^*))\dot\gamma^{*n-1}\right\}\frac{\partial v_x^*}{\partial x^*} \\
\tau_{yx}^* &= \left\{\frac{\tau_0^* g(\beta^*(p^* - p_0^*))}{\dot\gamma^*} + k_0^* f(a^*(p^* - p_0^*))\dot\gamma^{*n-1}\right\}\left(\frac{\partial v_x^*}{\partial y^*} + \frac{\partial v_y^*}{\partial x^*}\right), \quad \sigma^*(x^*) \le y^* \le h^*(x^*) \\
\tau_{yy}^* &= 2\left\{\frac{\tau_0^* g(\beta^*(p^* - p_0^*))}{\dot\gamma^*} + k_0^* f(a^*(p^* - p_0^*))\dot\gamma^{*n-1}\right\}\frac{\partial v_y^*}{\partial y^*}
\end{aligned}\right\} \tag{4.12}$$

where

$$\dot\gamma^* = \sqrt{4\left(\frac{\partial v_x^*}{\partial x^*}\right)^2 + \left(\frac{\partial v_x^*}{\partial y^*} + \frac{\partial v_y^*}{\partial x^*}\right)^2} \tag{4.13}$$

(note that the continuity equation has been used). Similarly, the magnitude of the stress tensor is given by

$$\tau^* = \sqrt{\frac{1}{2}\mathrm{tr}\boldsymbol{\tau}^{*2}} = \sqrt{\frac{1}{2}\tau_{xx}^{*2} + \frac{1}{2}\tau_{yy}^{*2} + \tau_{yx}^{*2}} \tag{4.14}$$

Without loss of generality, we assume here that the reference pressure that appears in Eqs. (4.7) and (4.8) is $p_0^* = p_{out}^*$.

The unyielded core, defined by $\Omega^* = \left\{(x^*, y^*) : x^* \in [0, L^*],\ y^* \in [0, \sigma^*]\right\}$, moves in the x-direction as a solid, i.e. at constant velocity v_c^*. Thus,

$$v_x^* = v_c^* \quad \text{and} \quad v_y^* = 0 \quad \text{for} \quad 0 \le y^* \le \sigma^*(x^*) \tag{4.15}$$

For steady-state flow in the absence of body forces, the integral balance of linear momentum of the whole plug core yields the following equation (Fusi et al., 2015)

$$\int_0^{L^*} \left[-\sigma_x^*(-p^* + \tau_{xx}^*) + \tau_{yx}^*\right]_{y^*=\sigma^*} dx^* + p_{in}^*\sigma_{in}^* - p_{out}^*\sigma_{out}^* = 0 \tag{4.16}$$

where $\sigma_x^* \equiv d\sigma^*/dx^*$. Equation (4.16) simply implies that τ_{yx}^* acts on dx^* and $-p^* + \tau_{xx}^*$ acts on $dy^* = \sigma_x^* dx^*$, where dx^* and dy^* define an infinitesimal element of the longitudinal side of the core.

4.2.1 Non-dimensional formulation

We assume that the length L^* of the channel is much greater than its greatest semi-width, i.e. $L^* \gg H^* \equiv \max_{x \in [0, L^*]} h^*(x^*)$, and introduce the dimensionless parameter

$$\varepsilon \equiv \frac{H^*}{L^*} \ll 1 \tag{4.17}$$

which is used for applying the classical lubrication approximation or thin-film approach (Frigaard and Ryan, 2004). The problem is non-dimensionalised by scaling x^* by L^*, y^*, h^*, and σ^* by H^*, $(p^* - p_{out}^*)$ by Δp^*, v_x^* by $H^*(\varepsilon \Delta p^*/k_0^*)^{1/n}$, v_y^* by $\varepsilon H^*(\varepsilon \Delta p^*/k_0^*)^{1/n}$, and the stress components by $\varepsilon \Delta p^*$. The dimensionless forms of the continuity equation and the two components of the momentum equation are as follows

$$\frac{\partial v_x}{\partial x} + \frac{\partial v_y}{\partial y} = 0 \tag{4.18}$$

$$\varepsilon^{2/n-1} Re\left(v_x \frac{\partial v_x}{\partial x} + v_y \frac{\partial v_x}{\partial y}\right) = -\frac{\partial p}{\partial x} + \varepsilon \frac{\partial \tau_{xx}}{\partial x} + \frac{\partial \tau_{yx}}{\partial y} \tag{4.19}$$

$$\varepsilon^{2/n+1} Re\left(v_x \frac{\partial v_y}{\partial x} + v_y \frac{\partial v_y}{\partial y} \right) = -\frac{\partial p}{\partial y} + \varepsilon^2 \frac{\partial \tau_{yx}}{\partial x} + \varepsilon \frac{\partial \tau_{yy}}{\partial y} \tag{4.20}$$

where *Re* is the Reynolds number defined by

$$Re \equiv \frac{\rho^* H^{*3} \Delta p^{*2/n-1}}{k_0^{*2/n} L^*} \tag{4.21}$$

Note that for *n*=1, the equations for the Bingham case are recovered, in agreement with the analysis of Fusi et al. (2015). For the stress components one gets

$$\left.\begin{aligned} \tau_{xx} &= 2\varepsilon \left[\frac{Bn\, g(\beta p)}{\dot{\gamma}} + f(\alpha p) \dot{\gamma}^{n-1} \right] \frac{\partial v_x}{\partial x} \\ \tau_{yx} &= \left[\frac{Bn\, g(\beta p)}{\dot{\gamma}} + f(\alpha p) \dot{\gamma}^{n-1} \right] \left(\frac{\partial v_x}{\partial y} + \varepsilon^2 \frac{\partial v_y}{\partial x} \right) \\ \tau_{yy} &= 2\varepsilon \left[\frac{Bn\, g(\beta p)}{\dot{\gamma}} + f(\alpha p) \dot{\gamma}^{n-1} \right] \frac{\partial v_y}{\partial y} \end{aligned}\right\}, \quad \sigma(x) \le y \le h(x) \tag{4.22}$$

where

$$\dot{\gamma} = \sqrt{4\varepsilon^2 \left(\frac{\partial v_x}{\partial x} \right)^2 + \left(\frac{\partial v_x}{\partial y} + \varepsilon^2 \frac{\partial v_y}{\partial x} \right)^2} \tag{4.23}$$

In Eq. (4.22), there appear three dimensionless numbers, the Bingham number *Bn* and the consistency-index and yield-stress growth numbers *a* and β, which are defined by

$$Bn \equiv \frac{\tau_0^*}{\varepsilon \Delta p^*}, \quad \alpha \equiv a^* \Delta p^*, \quad \beta \equiv \beta^* \Delta p^* \tag{4.24}$$

It is clear that when $\beta \ge 0$ the dimensionless yield stress is reduced from $g(\beta)Bn$ at the inlet plane to Bn at the exit plane. When $\beta < 0$ then the dimensionless yield stress increases from $g(\beta)Bn$ to Bn. We thus have the constraint $g(\beta) > 0$ so that the unyielded core extends from the inlet to the outlet plane (otherwise the present model is not valid).

Finally, the dimensionless form of Eq. (4.16) is

$$\int_0^1 \left[-\sigma_x (-p + \varepsilon \tau_{xx}) + \tau_{yx} \right]_{y=\sigma} dx + \sigma_{in} = 0 \tag{4.25}$$

where the dimensionless pressure satisfies the following boundary conditions

$$p(0, \sigma_{in}) = 1, \quad p(1, \sigma_{out}) = 0 \tag{4.26}$$

4.2.2 The zero-order problem

Following Fusi et al. (2015) we solve the zero-order problem. For the sake of simplicity, we will avoid introducing new symbols for the zero-order variables; hence, hereafter all variables are the zero-order ones. The continuity and momentum equations at zero order read as follows

$$\frac{\partial v_x}{\partial x}+\frac{\partial v_y}{\partial y}=0 \tag{4.27}$$

$$-\frac{\partial p}{\partial x}+\frac{\partial \tau_{yx}}{\partial y}=0 \tag{4.28}$$

$$-\frac{\partial p}{\partial y}=0 \tag{4.29}$$

From the last equation, it is deduced that $p=p(x)$. At zero order $\tau_{xx}=\tau_{yy}=0$ while

$$\tau_{yx}=\left[\frac{Bn\,g(\beta p)}{\dot{\gamma}}+f(\alpha p)\dot{\gamma}^{n-1}\right]\frac{\partial v_x}{\partial y},\quad \sigma(x)\le y\le h(x) \tag{4.30}$$

Working in the upper part of the channel we note that in the yielded region $\dot{\gamma}=\left|\partial v_x/\partial y\right|=-\partial v_x/\partial y$ and thus

$$\tau_{yx}=-Bn\,g(\beta p)-f(\alpha p)\left(-\frac{\partial v_x}{\partial y}\right)^n,\quad \sigma(x)\le y\le h(x) \tag{4.31}$$

Substituting the above expression into the *x*-momentum equation (4.28), integrating twice, and applying the boundary conditions $\partial v_x/\partial y(x,\sigma)=v_x(x,h)=0$, the following expression is obtained for v_x

$$v_x(x,y)=\left[1-\frac{(y-\sigma)^{1+1/n}}{(h-\sigma)^{1+1/n}}\right]v_c,\quad \sigma(x)\le y\le h(x) \tag{4.32}$$

where

$$v_c=\frac{(-p_x)^{1/n}(h-\sigma)^{1+1/n}}{(1+1/n)\,f^{1/n}(\alpha p)} \tag{4.33}$$

is the velocity of the unyielded core and $p_x\equiv dp/dx$. The fact that the RHS of the above equation is constant will be utilised below in order to derive the integro-differential equation governing the pressure.

The transverse velocity component is found from the continuity equation (4.27). Given that $v_y(x,h)=0$, we can write

$$v_y = \int_y^h \frac{\partial v_x}{\partial x} dy \tag{4.34}$$

Substituting v_x from Eq. (4.32) and carrying out the required differentiation and integration one gets

$$v_y = \frac{v_c}{2+1/n}\left[\sigma_x + (1+1/n)h_x - (2+1/n)\left(\frac{y-\sigma}{h-\sigma}\right)^{1+1/n}\sigma_x - (1+1/n)(h_x-\sigma_x)\left(\frac{y-\sigma}{h-\sigma}\right)^{2+1/n}\right] \tag{4.35}$$

where $h_x \equiv dh/dx$. The satisfaction of condition $v_y(x,\sigma) = 0$ requires that

$$\sigma_x + (1+1/n)h_x = 0 \tag{4.36}$$

Equation (4.35) can then be simplified to

$$v_y = (1+1/n)v_c \frac{(y-\sigma)^{1+1/n}}{(h-\sigma)^{2+1/n}}(h-y)h_x \tag{4.37}$$

From Eq. (4.36) it is deduced that the semi-width of the unyielded core is given by

$$\sigma(x) = -(1+1/n)h(x) + C \tag{4.38}$$

where C is an unknown constant to be determined. The above result generalizes the result of Fusi et al. (2015) for a Bingham plastic (n=1). Equation (4.38) implies that the width of the unyielded core increases when the wall function $h(x)$ is decreasing and vice versa. The rate of change of σ is (1+1/n) times the rate of change of h and is independent of the other material and flow parameters, which affect only the constant C. Hence, decreasing the power-law exponent n in a converging channel causes the plug to expand faster, which is expected given that the velocity profile becomes flatter as shear thinning is enhanced. To determine the constant C, we return to the plug momentum balance equation (4.25), which at zero order becomes

$$\int_0^1 \left[\sigma_x p + \tau_{yx}\right]_{y=\sigma} dx + \sigma_{in} = 0 \tag{4.39}$$

Since at the rigid core surface ($y = \sigma$) the rate of strain vanishes, $\partial v_x / \partial y = 0$, Eq. (4.31) gives

$$\tau_{yx}\Big|_{y=\sigma} = -Bn\, g(\beta p) \tag{4.40}$$

Therefore

$$\int_0^1 \left[\sigma_x p - Bn\, g(\beta p)\right] dx + \sigma_{in} = 0 \tag{4.41}$$

Using integration by parts and Eq. (4.38) we find that

$$C = Bn\int_0^1 g(\beta p)\,dx - (1+1/n)\int_0^1 p_x h\,dx = Bn\int_0^1 g(\beta p)\,dx + (1+1/n)\left[h_{in} + \int_0^1 p h_x\,dx\right] \quad (4.42)$$

From Eq. (4.33) we observe that

$$\frac{d}{dx}\left[\frac{p_x}{f(\alpha p)}(h-\sigma)^{n+1}\right] = 0 \quad (4.43)$$

which gives

$$p_{xx} - \frac{\alpha f'(\alpha p)\,p_x^2}{f(\alpha p)} + \frac{p_x}{h-\sigma}(n+1)(h_x - \sigma_x) = 0 \quad (4.44)$$

By means of Eqs. (4.36) and (4.42) we get the following integro-differential equation for the pressure

$$p_{xx} + \left[\frac{(n+1)(2+1/n)h_x}{(2+1/n)h - Bn\int_0^1 g(\beta p)\,dx + (1+1/n)\int_0^1 p_x h\,dx} - \frac{\alpha f'(\alpha p)\,p_x}{f(\alpha p)}\right] p_x = 0 \quad (4.45)$$

subject to the boundary conditions $p(0)=1$ and $p(1)=0$. An alternative form of Eq. (4.45) is

$$p_{xx} + \left[\frac{(n+1)(2+1/n)h_x}{(2+1/n)h - (1+1/n)h_{in} - Bn\int_0^1 g(\beta p)\,dx - (1+1/n)\int_0^1 p h_x\,dx} - \frac{\alpha f'(\alpha p)\,p_x}{f(\alpha p)}\right] p_x = 0 \quad (4.46)$$

Once the pressure $p(x)$ is known, the yield surface, the unyielded core velocity, and the two velocity components are readily calculated by means of Eqs. (4.38), (4.33), (4.32) and (4.37), respectively. For the volumetric flow rate (which is, of course, constant along the channel) we have

$$Q = 2\left(\int_0^\sigma v_c dy + \int_\sigma^h v_x dy\right) = \frac{2v_c}{2+1/n}\left[\sigma + (1+1/n)h\right] = \frac{2v_c C}{2+1/n} \quad (4.47)$$

Equation (4.46) can be solved numerically, using, for example, finite element or pseudo-spectral methods. Analytical solutions are possible only for channels of constant or linearly-varying width when functions f and g are of simple form. These are presented and discussed in the next two sections.

4.3 Flow in a channel of constant width

In the case of a channel of constant width, h=1 and h_x=0; thus, Eq. (4.46) is simplified to

$$p_{xx} - \frac{\alpha f'(\alpha p)}{f(\alpha p)}\,p_x^2 = 0 \quad (4.48)$$

which implies that the pressure distribution is independent of the yield-stress function and the power-law exponent. The former affects only the location of the yield point, which is constant along the channel, since Eqs. (4.38) and (4.42) give

$$\sigma = Bn\int_0^1 g(\beta p)dx \tag{4.49}$$

Moreover, the transverse velocity component vanishes, $v_y = 0$, while $v_x = v_x(y)$.

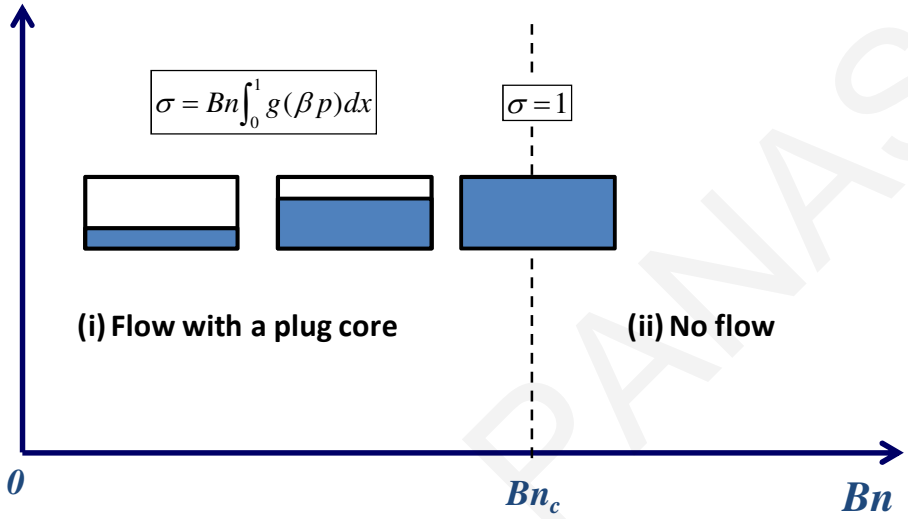

Figure 4.2: Flow regimes as the Bingham number is increased in lubrication flow of a viscoplastic fluid in a channel of constant width. When $Bn < Bn_c$ an unyielded region of constant height is predicted even when the yield stress and the consistency index are pressure-dependent. Note that $Bn \equiv \tau_0^* / (\varepsilon \Delta p^*)$.

It is clear that when σ=1, there is no flow, since the unyielded core touches the wall at which no-slip applies. There are thus two flow regimes depending on the value of the Bingham number, as illustrated in Fig. 4.2. The critical Bingham number at which there is no flow,

$$Bn_c = \frac{1}{\int_0^1 g(\beta p)dx} \tag{4.50}$$

is obviously inversely proportional to the lowest dimensional pressure difference above which yielding occurs ($\Delta p_c^* = \tau_0^* / (\varepsilon Bn_c)$).

From Eq. (4.48) we observe that

$$\frac{p_x}{f(\alpha p)} = -K \tag{4.51}$$

where K is a constant that can be determined along with the pressure p upon integration and application of the two boundary conditions for p. It is easily found that

$$v_c = \frac{K^{1/n}(1-\sigma)^{1+1/n}}{(1+1/n)} \tag{4.52}$$

and

$$v_x(y) = \left[1 - \frac{(y-\sigma)^{1+1/n}}{(1-\sigma)^{1+1/n}}\right] v_c, \quad \sigma \le y \le 1 \tag{4.53}$$

Table 4.1: Expressions for the constant K, the pressure $p(x)$ and the yield point σ for different functions describing the pressure-dependence of the consistency index ($f(x)$) and the yield stress ($g(x)$) in the case of a channel of constant width. These are independent of the power-law exponent n.

$f(x)$	K	$p(x)$	$g(x)$	$\frac{\sigma}{Bn} = \int_0^1 g(\beta p)\,dx$
1	1	$1-x$	1	1
			$1+x$	$1+\frac{\beta}{2}$
			e^x	$\frac{e^\beta - 1}{\beta}$
$1+x$	$\frac{\ln(1+\alpha)}{\alpha}$	$\frac{1}{\alpha}\left[(1+\alpha)^{1-x} - 1\right]$	1	1
			$1+x$	$1+\left[\frac{1}{\ln(1+\alpha)} - \frac{1}{\alpha}\right]\beta$
			e^x	$e^{-\beta/a}\int_0^1 e^{\frac{\beta}{a}(1+\alpha)^{1-x}}\,dx$
e^x	$\frac{1-e^{-\alpha}}{\alpha}$	$\frac{1}{\alpha}\ln\frac{1}{\left(1-e^{-\alpha}\right)x + e^{-\alpha}}$	1	1
			$1+x$	$\frac{\beta\left[1-(1+\alpha)e^{-a}\right]}{\alpha(1-e^{-a})}$
			e^x	$\frac{\alpha}{1-e^{-a}}, \quad \beta = \alpha$ $\frac{\alpha(1-e^{\beta-a})}{(\alpha-\beta)(1-e^{-a})}, \quad \beta \neq \alpha$

Table 4.1 tabulates expressions of K, $p(x)$ and σ for the cases where f and g are linear and/or exponential. Note that these results are independent of the power-law exponent n, which affects only the velocity profile (4.53).

Below we discuss the case where both the consistency index and the yield stress vary linearly with pressure, i.e. $f(x) = g(x) = 1 + x$. From Table 4.1, we see that when $\alpha > 0$

$$p(x) = \frac{1}{a}\left[(1+\alpha)^{1-x} - 1\right] \tag{4.54}$$

and

$$\sigma = \left\{1 + \left[\frac{1}{\ln(\alpha+1)} - \frac{1}{\alpha}\right]\beta\right\} Bn \tag{4.55}$$

Flow occurs provided that the Bingham number is lower than the critical value

$$Bn_c \equiv \frac{1}{1 + \left[\frac{1}{\ln(\alpha+1)} - \frac{1}{\alpha}\right]\beta} \tag{4.56}$$

(Recall that the above number is inversely proportional to the lowest dimensional pressure difference above which yielding occurs.) Note that β may be negative in which case the yield stress is increasing downstream and thus Bn_c may be greater than unity. If $\beta = 0$, then $Bn_c = 1$ and $\sigma = Bn$, i.e. σ is independent of the consistency-index growth parameter α (this is due to the fact that the pressure is scaled by the inlet pressure Δp^*). As discussed below, this is also the case when solving the standard Poiseuille flow problem without the lubrication approximation. The present lubrication model is valid provided that $\sigma \geq 0$, i.e.

$$\beta \geq \frac{\alpha \ln(\alpha+1)}{\ln(\alpha+1) - \alpha} \tag{4.57}$$

so that the plug is not broken. As already mentioned, β may be negative and, more specifically, $\beta \geq -1$ (so that the yield stress in the channel remains positive), which ensures that condition (4.57) is satisfied (the left hand side is always less than -2).

For a Bingham plastic (n=1) the velocity is given by

$$v_x = \begin{cases} \dfrac{\ln(\alpha+1)}{2\alpha}(1-y)(1+y-2\sigma), & \sigma \leq y \leq 1 \\ \dfrac{\ln(\alpha+1)}{2\alpha}(1-\sigma)^2, & 0 \leq y \leq \sigma \end{cases} \tag{4.58}$$

where the effects of Bn and β are accounted for via the yield point σ.

When the plastic viscosity is pressure-independent ($\alpha = 0$), we find the standard linear pressure distribution for Poiseuille flow

$$p(x) = 1 - x \tag{4.59}$$

where, however, the yield point depends on the yield-stress growth number

$$\sigma = \left(1 + \beta/2\right) Bn \tag{4.60}$$

For the velocity, we now have

$$v_x = \begin{cases} \dfrac{1}{2}(1-y)(1+y-2\sigma), & \sigma \le y \le 1 \\ \dfrac{1}{2}(1-\sigma)^2, & 0 \le y \le \sigma \end{cases} \tag{4.61}$$

and the critical Bingham number above which there is no flow is

$$Bn_c \equiv \frac{1}{1+\beta/2} \tag{4.62}$$

(Recall that $\beta \ge -1$).

For the case of a Bingham plastic (n=1) with linearly-varying yield stress and plastic viscosity ($g(x)$=$f(x)$=1+x), the analytical Poiseuille flow solution can be obtained (Damianou and Georgiou, 2017)

$$p(x,y) = \begin{cases} \dfrac{1}{\alpha}\left[(1+\alpha)^{1-x} \dfrac{\cosh\left[\varepsilon \ln(1+\alpha)(y-\sigma) + \tanh^{-1}(\varepsilon Bn\beta)\right]}{\cosh\left[\tanh^{-1}(\varepsilon Bn\beta)\right]} - 1 \right], & \sigma \le y \le 1 \\ \dfrac{1}{\alpha}\left[(1+\alpha)^{1-x} - 1\right], & 0 \le y < \sigma \end{cases} \tag{4.63}$$

As for the velocity, one finds

$$v_x(y) = \begin{cases} \dfrac{1}{\alpha\varepsilon^2 \ln(1+\alpha)} \ln \dfrac{\cosh\left[\varepsilon \ln(1+\alpha)(1-\sigma) + \tanh^{-1}(\varepsilon Bn\beta)\right]}{\cosh\left[\varepsilon \ln(1+\alpha)(y-\sigma) + \tanh^{-1}(\varepsilon Bn\beta)\right]} - \dfrac{Bn\beta}{\alpha}(1-y), & \sigma \le y \le 1 \\ \dfrac{1}{\alpha\varepsilon^2 \ln(1+\alpha)} \ln \dfrac{\cosh\left[\varepsilon \ln(1+\alpha)(1-\sigma) + \tanh^{-1}(\varepsilon Bn\beta)\right]}{\cosh\left[\tanh^{-1}(\varepsilon Bn\beta)\right]} - \dfrac{Bn\beta}{\alpha}(1-\sigma), & 0 \le y < \sigma \end{cases} \tag{4.64}$$

where σ is given by Eq. (4.55), i.e. it is the same as that predicted by the lubrication approximation. The main difference between the above analytical solution from the lubrication one is that the pressure in the yielded domain is two dimensional. The pressure in the unyielded core is identical to the pressure predicted by the lubrication approximation for both yielded and unyielded regions. Setting $\sigma = Bn = 0$ yields the solution of a Newtonian fluid with a pressure-dependent viscosity (Kalogirou et al., 2011) and taking only the first term of the Taylor expansion of Eq. (4.64) in terms of ε yields the lubrication solution (4.58). The effects of the

various parameters on the yield point σ, as discussed in Damianou and Georgiou (2017), apply here (see also a recent solution of the axisymmetric flow in Fusi and Rosso, 2018). With the lubrication assumption, the velocity profile is slightly overestimated and the relative differences are enhanced as α assumes rather high values (Damianou and Georgiou, 2017).

4.4 Flow in a channel of linearly-varying width

In this section, we consider a channel of linearly-varying width, such that

$$h(x) = h_{in} + (h_{out} - h_{in})x = h_{in} + \Delta h\, x \quad \text{and} \quad h_x(x) = \Delta h \tag{4.65}$$

From Eq. (4.38) we know that the yield surface also varies linearly

$$\sigma(x) = -(1+1/n)\Delta h\, x - (1+1/n)h_{in} + C \tag{4.66}$$

where, by means of Eq. (4.42), the constant C is given by

$$C = Bn\int_0^1 g(\beta p)\, dx + (1+1/n)h_{in} + (1+1/n)\Delta h\int_0^1 p dx \tag{4.67}$$

In this case, Eq. (4.46) can be written as follows

$$p_{xx} + \left[\frac{n+1}{x+A} - \frac{\alpha f'(\alpha p) p_x}{f(\alpha p)}\right] p_x = 0 \tag{4.68}$$

where

$$A = \frac{h_{in} - Bn\int_0^1 g(\beta p)\, dx - (1+1/n)\Delta h\int_0^1 p\, dx}{(2+1/n)\Delta h} \tag{4.69}$$

Once A is calculated, the constant C is readily found by means of

$$C = (2+1/n)(h_{in} - \Delta h A) \tag{4.70}$$

Combining Eqs. (4.66) and (4.70) one gets

$$\sigma(x) = -(1+1/n)\Delta h\, x + h_{in} - (2+1/n)\Delta h A \tag{4.71}$$

In the general case, Eq. (4.68) is not amenable to analytical solution. We thus consider here the case of constant (pressure-independent) consistency index. Assuming that $\alpha = 0$, Eq. (4.68) becomes

$$p_{xx} + \frac{n+1}{x+A} p_x = 0 \tag{4.72}$$

The solution of the above equation with $p(0)=1$ and $p(1)=0$ is

$$p(x)=\frac{\left(\frac{A+1}{A+x}\right)^n-1}{(1+1/A)^n-1} \tag{4.73}$$

Substituting the pressure into Eq. (4.69) results in a non-linear algebraic equation which is solved in order to determine the unknown constant *A*.

For the sake of simplicity, we consider here the case where $g(x)=1+x$ (the yield stress varies linearly with the pressure). It is easily shown that Eq. (4.69) takes the form

$$\left[\beta Bn+(1+1/n)\Delta h\right]I+(2+1/n)\Delta hA=h_{in}-Bn \tag{4.74}$$

where

$$I\equiv\int_0^1 p\,dx=\begin{cases}A\left[(A+1)\ln(1+1/A)-1\right], & n=1\\ \dfrac{(A+1)(1+1/A)^{n-1}-A-n}{(n-1)\left[(1+1/A)^n-1\right]}, & n\neq 1\end{cases} \tag{4.75}$$

In a linearly-converging channel with a slope $\Delta h<0$, the core thickness increases with a slope equal to $(1+1/n)(-\Delta h)$. The value of *A* can be found analytically only in the two extreme cases between which the lubrication model applies: (a) at the lowest value of *Bn*, Bn_{c1}, at which the unyielded domain varies from 0 to 1 (it is not broken); (b) at the lowest value of *Bn*, Bn_{c2}, at which the flow comes to a stop. As illustrated in Fig. 4.3, for $Bn\geq Bn_{c2}$ there is no flow anyway, while for $Bn<Bn_{c1}$ the plug is broken and the unyielded region is restricted only near the channel exit; the fluid near the inlet is fully yielded and thus the present lubrication model does not apply.

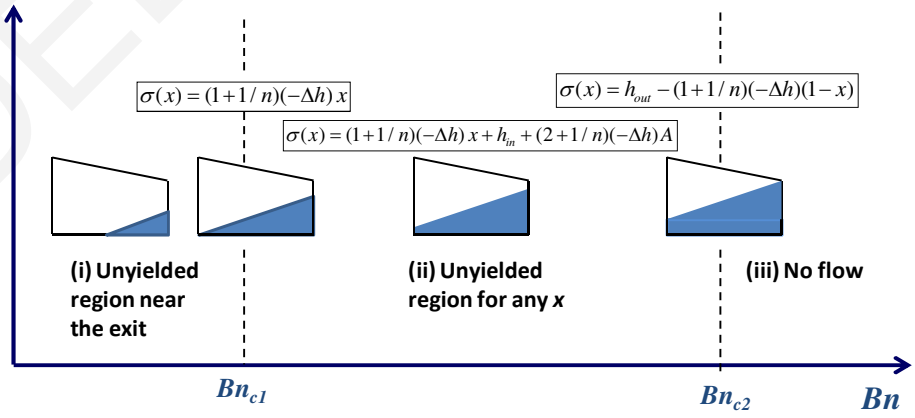

Figure 4.3: Flow regimes for Herschel-Bulkley flow in the case of a linearly converging channel. The present lubrication analysis holds only in Regime II.

The first critical value Bn_{c1} below which the plug is broken corresponds to $\sigma(0)=0$. Hence, Eq. (4.71) yields

$$A=-\frac{h_{in}}{(2+1/n)(-\Delta h)}$$

and from Eq. (4.74) we find that

$$Bn_{c1}=\frac{(1+1/n)(-\Delta h)I}{1+\beta I} \tag{4.76}$$

The pressure is given by Eq. (4.73) and

$$\sigma(x)=-(1+1/n)(-\Delta h)x \tag{4.77}$$

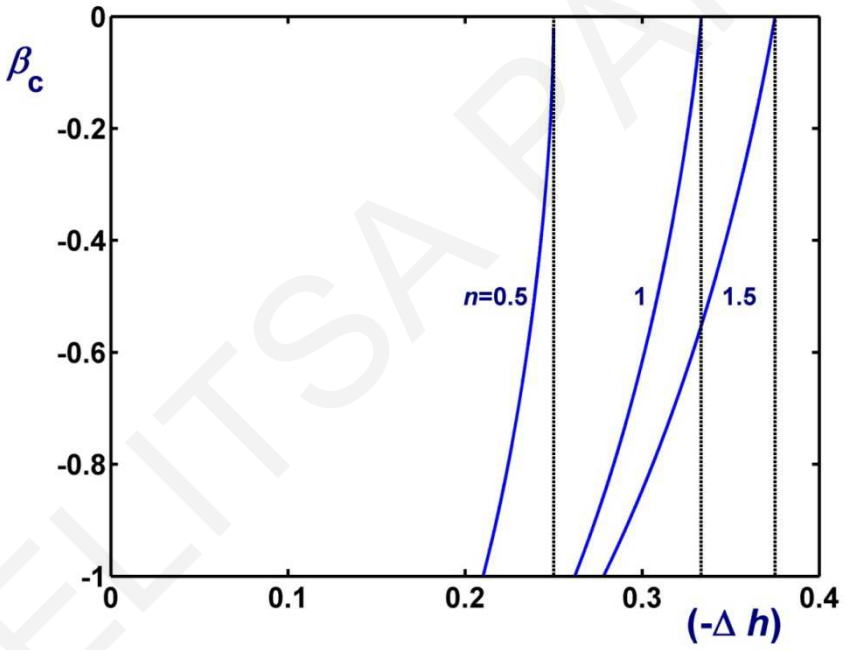

Figure 4.4: Lower bounds of the yield-stress growth parameter for flow of a Herschel-Bulkley fluid with constant consistency index (α=0) and yield stress varying linearly with pressure in a converging channel with $h(x)=1+\Delta h\,x$ for various values of the power-law exponent. As $(-\Delta h)$ is increased from 0 (flat channel) to the critical value of 1/(2+1/n) (corresponding to no flow and indicated by the vertical line in each case), the lower admissible value of β is initially -1 and then increases rapidly to 0.

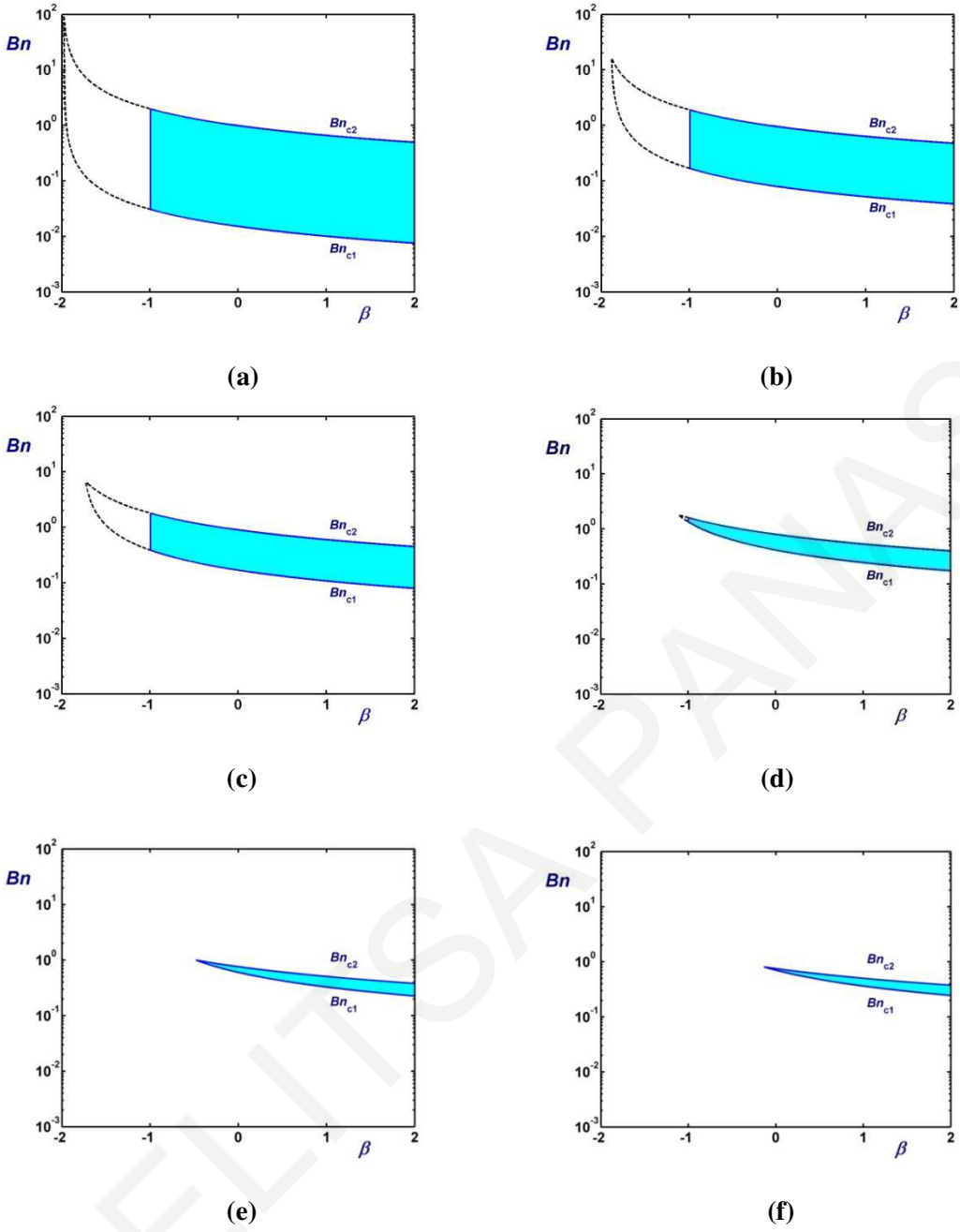

Figure 4.5: Critical Bingham numbers in the case of Hesrchel-Bulkley flow with n=0.5 in a linearly converging channel ($h_{in} = 1$) with constant consistency index (α=0) and linearly varying yield stress: (a) $\Delta h = -0.01$; (b) $\Delta h = -0.05$; (c) $\Delta h = -0.1$; (d) $\Delta h = -0.2$; (e) $\Delta h = -0.24$; (f) $\Delta h = -0.249$. The shaded region is the applicability domain of the present method. As $(-\Delta h)$ is increased from 0 (flat channel) to the critical value of 0.25 (no flow) the lower admissible value of β increases from -1 to 0.

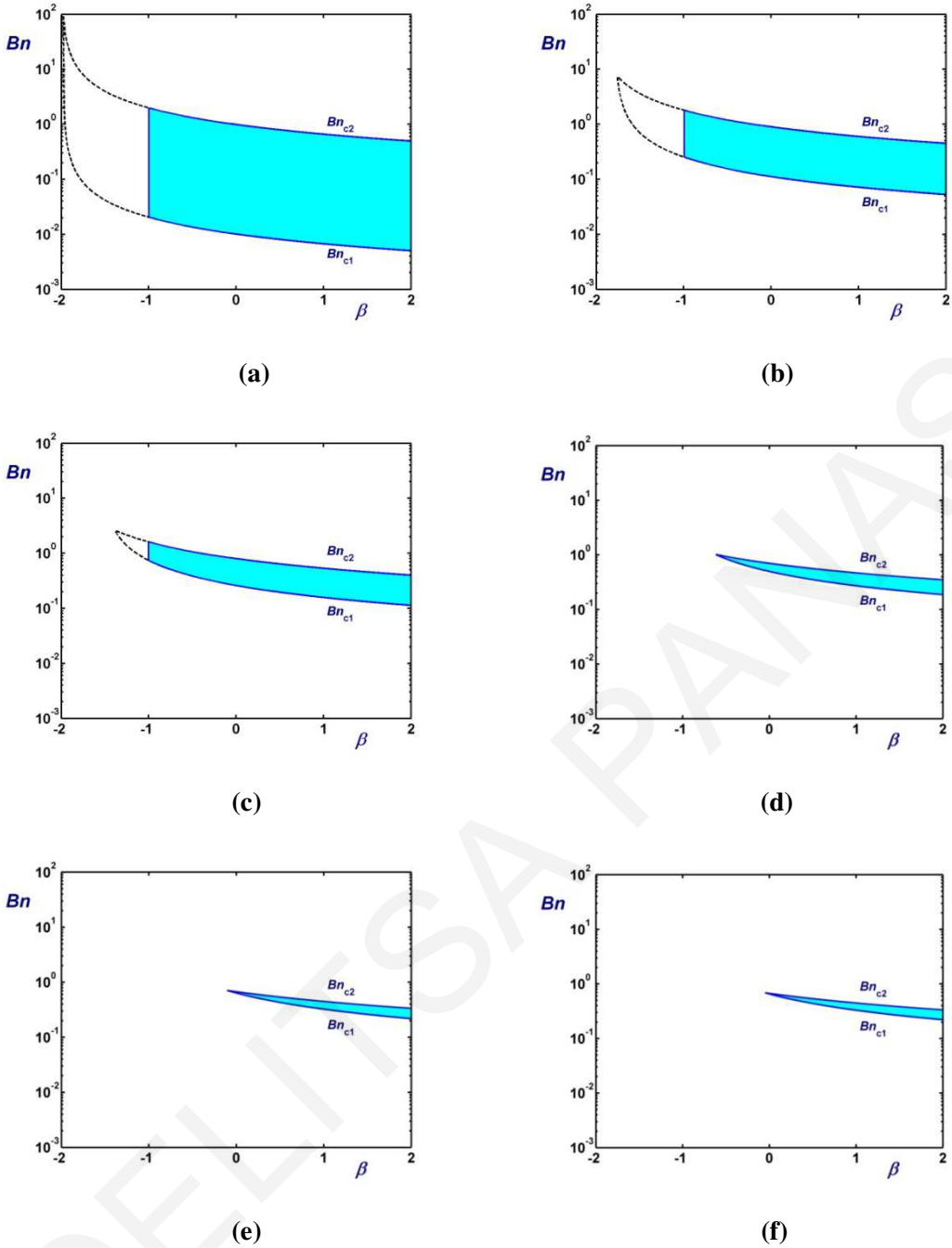

Figure 4.6: Critical Bingham numbers in the case of Bingham-plastic flow (n=1) in a linearly converging channel ($h_{in}=1$) with constant plastic viscosity (α=0) and linearly varying yield stress: (a) $\Delta h=-0.01$; (b) $\Delta h=-0.1$; (c) $\Delta h=-0.2$; (d) $\Delta h=-0.3$; (e) $\Delta h=-0.33$; (f) $\Delta h=-0.332$. The shaded region is the applicability domain of the present method. As $(-\Delta h)$ is increased from 0 (flat channel) to the critical value of 1/3 (no flow) the lower admissible value of β increases from -1 to 0.

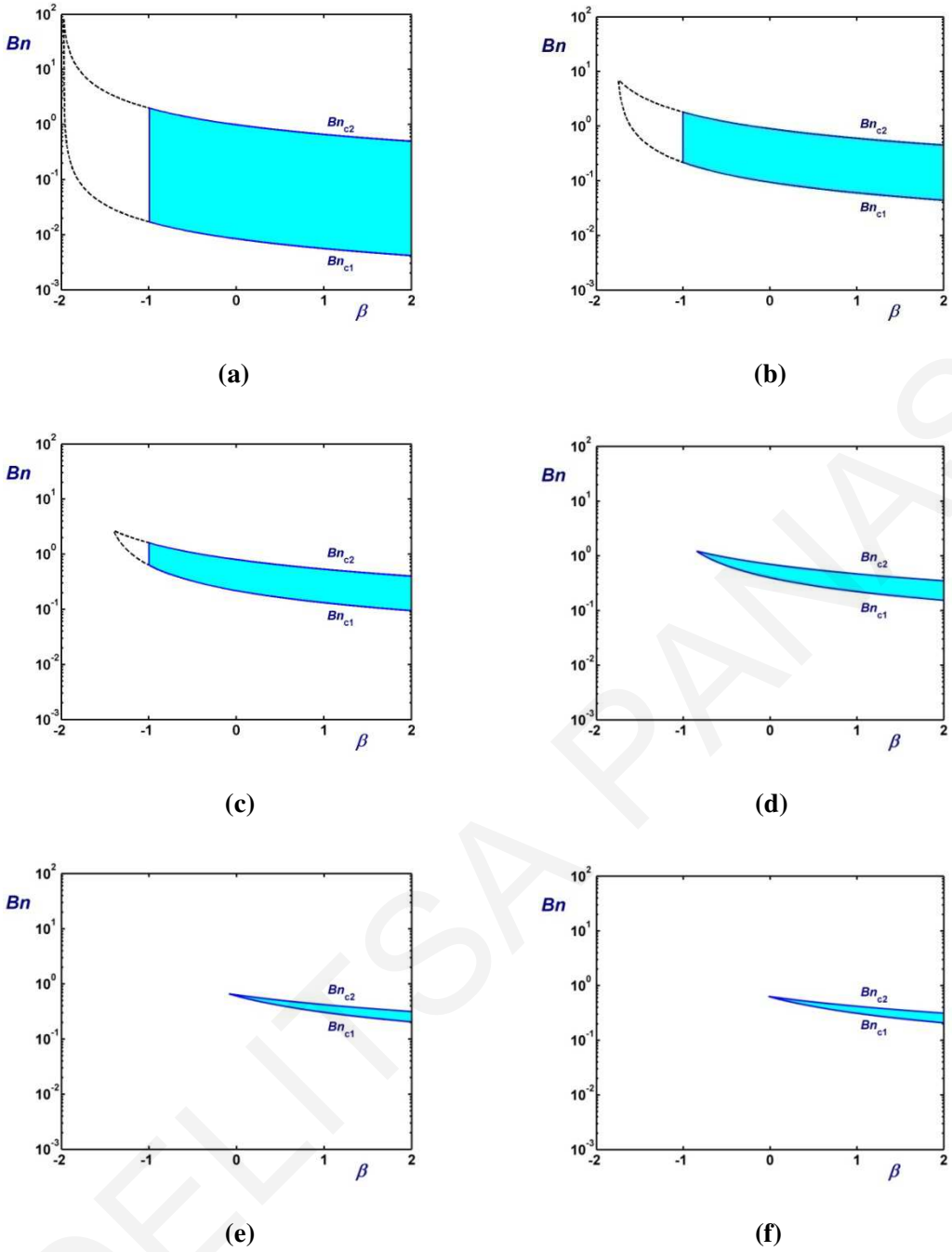

Figure 4.7: Critical Bingham numbers in the case of Hesrchel-Bulkley flow with n=1.5 in a linearly converging channel ($h_{in}=1$) with constant consistency index (α=0) and linearly varying yield stress: (a) $\Delta h=-0.01$; (b) $\Delta h=-0.1$; (c) $\Delta h=-0.2$; (d) $\Delta h=-0.3$; (e) $\Delta h=-0.37$; (f) $\Delta h=-0.374$. The shaded region is the applicability domain of the present method. As $(-\Delta h)$ is increased from 0 (flat channel) to the critical value of 3/8 (no flow) the lower admissible value of β increases from -1 to 0.

In general, the second critical value Bn_{c2} is simply the one predicted by Eq. (4.62) for a flat channel of height equal to the minimum value of $h(x)$:

$$Bn_{c2} = \frac{h_{\min}}{1+\beta/2} \tag{4.78}$$

where $h_{\min}$ is the minimum channel height. Hence, for a converging channel

$$Bn_{c2} = \frac{h_{out}}{1+\beta/2} = \frac{h_{in}+\Delta h}{1+\beta/2} \tag{4.79}$$

At the critical value Bn_{c2} the flow stops since $\sigma(1) = h_{in} + \Delta h = h_{out}$. In this case, Eq. (4.71) gives $A = -1$ and the yield surface is given by

$$\sigma(x) = h_{out} - (1+1/n)(-\Delta h)(1-x) \tag{4.80}$$

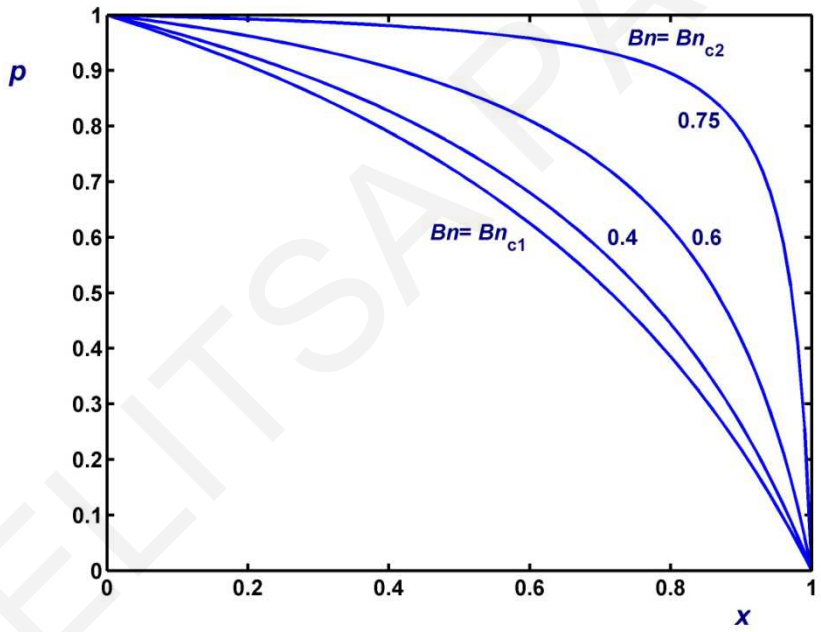

Figure 4.8: Pressure distributions in the case of flow of a Bingham plastic (n=1) with constant rheological parameters ($\alpha = \beta = 0$) in a linearly converging channel with $h(x) = 1 - 0.2x$ for various values of the Bingham number ranging from $Bn_{c1} = 0.2594$ to $Bn_{c2} = 0.8$.

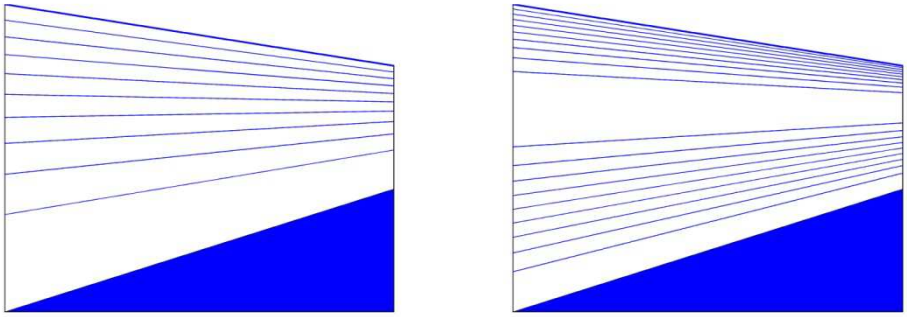

(a) **(b)**

Figure 4.9: Velocity contours in the case of flow of a Bingham plastic (n=1) with constant rheological parameters (α=β=0) in a linearly converging channel with $h(x) = 1 - 0.2x$ for $Bn = Bn_{c1} = 0.2594$: (a) v_x; (b) v_y. The unyielded core is shaded and the contour values are equally spaced.

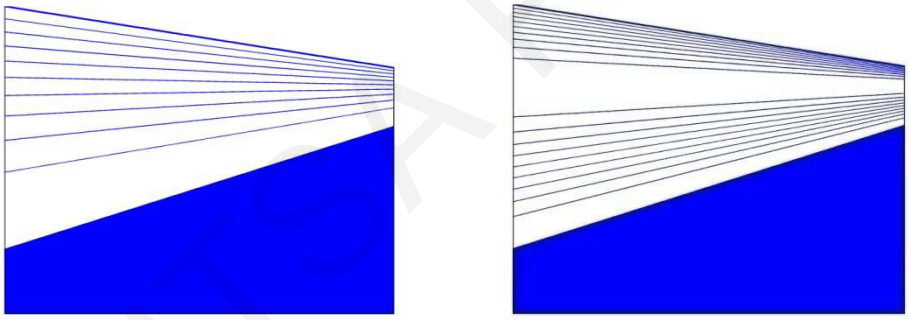

(a) **(b)**

Figure 4.10: Velocity contours in the case of flow of a Bingham plastic (n=1) with constant rheological parameters (α=β=0) in a linearly converging channel with $h(x) = 1 - 0.2x$ for $Bn_{c1} < Bn = 0.5 < Bn_{c2}$: (a) v_x; (b) v_y. The unyielded core is shaded and the contour values are equally spaced.

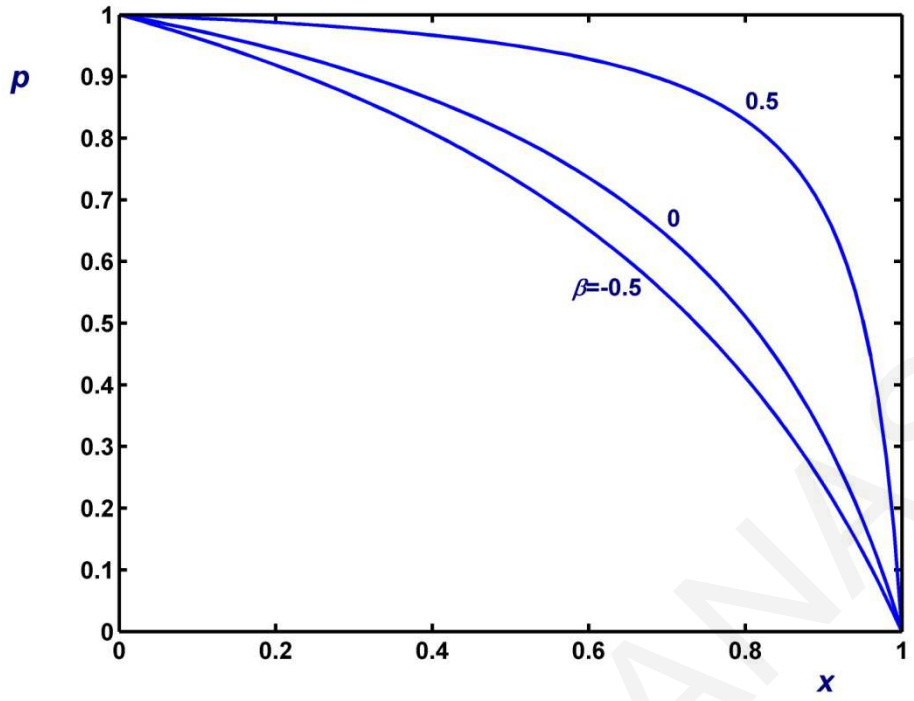

Figure 4.11: Effect of the yield-stress growth parameter on the pressure distribution in the case of flow of a Bingham plastic (n=1) with constant plastic viscosity (α=0) in a linearly converging channel with $h(x) = 1 - 0.2x$ for $Bn = 0.5$; the yield stress is assumed to vary linearly with pressure.

In summary, the method is applicable only when $Bn_{c1} \le Bn \le Bn_{c2}$. When $Bn_{c1} < Bn < Bn_{c2}$, the constant A can be found numerically as the root of Eq. (4.74) satisfying

$$-\frac{h_{in}}{(2+1/n)(-\Delta h)} < A < -1 \tag{4.81}$$

It is obvious that for a given power-law exponent n, Bn_{c2} can be defined only when $\sigma(0) = (2+1/n)h_{out} - (1+1/n)h_{in} > 0$ or

$$h_{out} > \frac{(1+1/n)}{(2+1/n)} h_{in} \tag{4.82}$$

Otherwise, the solution is actually in Regime I; thus, Regime II is not observed and the present analysis is not relevant. In other words, the three regimes of Fig. 4.3 are observed provided that condition (4.82) is satisfied. Likewise, for a given linearly converging channel, there is a critical value n_c of the power-law exponent below which Regime II is not observed

$$n_c = \frac{(-\Delta h)}{h_{out} + \Delta h} \tag{4.83}$$

In the case of a flat channel (Δh=0), Bn_{c1} is zero, Bn_{c2} coincides with Bn_c, given by Eq. (4.62), and the admissible values of β are in $[-1,\infty)$. In the case of a linearly-varying channel ($\Delta h \neq 0$), the lower bound of β, denoted by β_c, may increase and the applicability of the method is further reduced. This critical value is the maximum of -1 and the value of β at which $Bn_{c1} = Bn_{c2}$. From Eqs. (4.79) and (4.76) we then find that

$$\beta_c = \max\left\{-1,\ 2\frac{[h_{in}/(-\Delta h)-1]/I-1-1/n}{3+1/n-2h_{in}/(-\Delta h)}\right\} \tag{4.84}$$

Figure 4.4 shows the variation of β_c with $(-\Delta h)$ for n=0.5, 1, and 1.5; β_c is initially -1 and then at a critical value of (-Δh) starts increasing to become zero at the maximum admissible value of $(-\Delta h)$, which is determined from Eq. (4.82)

$$\left.\frac{(-\Delta h)}{h_{in}}\right|_{\max} = \frac{1}{2+1/n} \tag{4.85}$$

(1/4, 1/3 and 3/8 for n=0.5, 1, and 1.5, respectively).

Figures 4.5-4.7 illustrate the effect of the yield-stress-growth parameter β on the two critical Bingham numbers for different values of Δh with $h_{in}=1$, and n=0.5 (shear-thinning), 1 (Bingham plastic), and 1.5 (shear-thickening). The applicability domain of the method corresponds to the shaded regions between the curves of Bn_{c1} and Bn_{c2} (recall that below Bn_{c1} the plug is broken and above Bn_{c2} there is no flow). As $(-\Delta h)$ is increased, this regime is squeezed, with β_c eventually moving to the right, Bn_{c1} increases rapidly, and Bn_{c2} is reduced slightly both tending asymptotically to the curve

$$Bn_c = \frac{1+1/n}{(2+1/n)(1+\beta/2)} \tag{4.86}$$

reached when $(-\Delta h) = 1/(2+1/n)$, in which case there is no flow. Comparing Figs. 4.5-4.7 we observe that the applicability of the method is increased with n.

The analysis for a linearly-diverging channel ($\Delta h > 0$) is analogous. The unyielded core now contracts linearly following Eq. (4.71). Below a critical Bingham number Bn_{c1}, the unyielded core does not reach the exit plane and above a second critical number Bn_{c2} the unyielded core touches the wall at the inlet plane and thus there is no flow. The analysis for the diverging channel holds provided that

$$h_{out} < \frac{2+1/n}{1+1/n} h_{in} \tag{4.87}$$

Let us now consider the flow of a Bingham-plastic (n=1) with constant plastic viscosity (α=0) and constant yield stress (β=0) in a converging channel with $h(x) = 1 - 0.2x$ ($\Delta h = -0.2$), in which case $Bn_{c2} = h_{out} = 0.8$. From Eq. (4.76) we get $Bn_{c1} \simeq 0.2594$. Figure 4.8 shows the pressure distributions for different values of the Bingham number in the range from Bn_{c1} to Bn_{c2}. Note that when $Bn = Bn_{c2}$ the pressure is equal to unity for $0 \le x < 1$. The velocity contours for $Bn = Bn_{c1} = 0.2594$ and $Bn = 0.5$ are shown in Figs. 4.9 and 4.10, respectively.

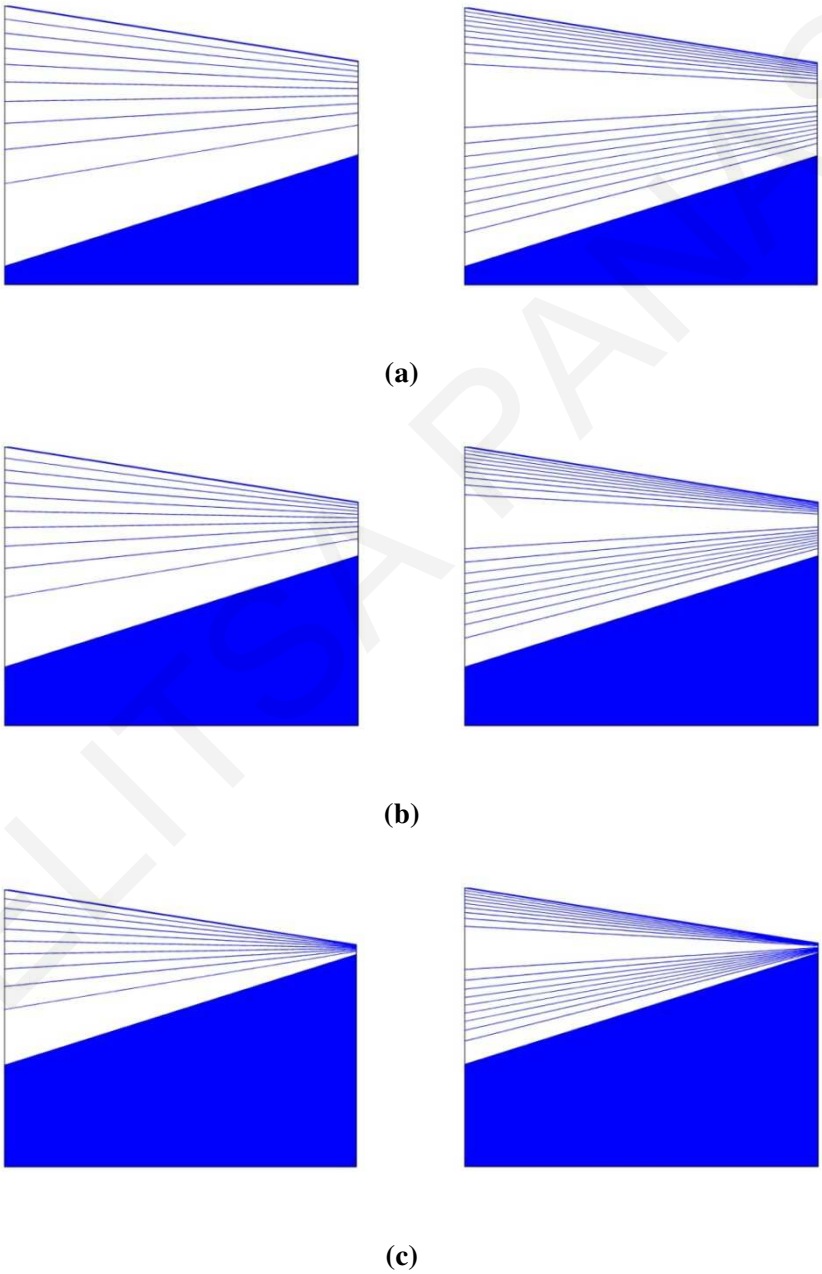

(a)

(b)

(c)

Figure 4.12: Effect of the yield-stress growth parameter on the contours of v_x (left) and v_y (right) in the case of flow of a Bingham plastic (n=1) with constant plastic viscosity (α=0) in a converging channel with $h(x) = 1 - 0.2x$ for $Bn = 0.5$: (a) β=-0.5; (b) β=0; (c) β=0.5; the unyielded core is shaded and the contour values are equally spaced. The yield stress is assumed to vary linearly with pressure.

The effect of the yield-stress growth coefficient β on the pressure distribution and the velocity contours is illustrated in Figs. 4.11 and 4.12, respectively, which show results for Bn=0.5 and β=-0.5, 0, and 0.5. The value of the Bingham number was chosen to lie between Bn_{c1} and Bn_{c2} for all the selected values of β (Fig. 4.11). As β is increased the dimensionless pressure increases while the pressure gradient becomes lower upstream and higher downstream. As shown in Fig. 4.12, the slope of the unyielded region remains the same but this grows bigger as β is increased, reaching the wall at the exit plane when $\beta=\beta_c$ (no flow).

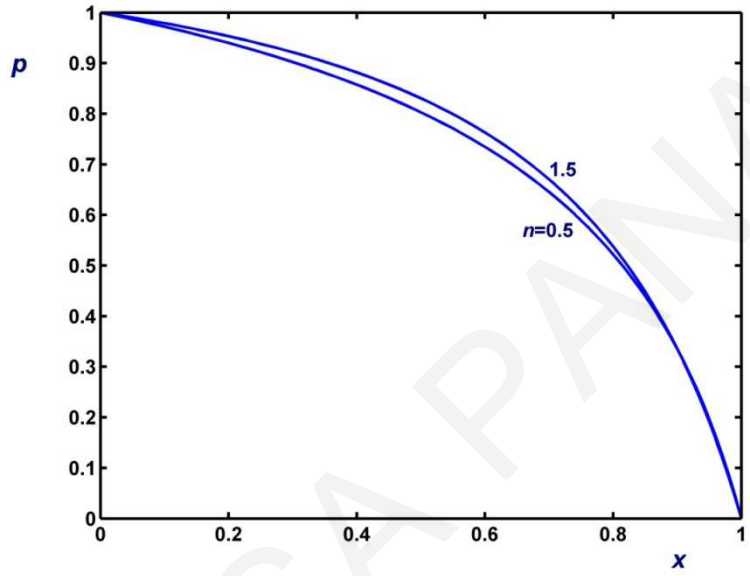

Figure 4.13: Effect of the power-law exponent on the pressure distribution in the case of flow of a Herschel-Bulkley fluid with constant rheological parameters ($\alpha = \beta = 0$) in a converging channel with $h(x) = 1 - 0.2x$ for $Bn = 0.5$.

The effect of the power-law exponent in the same geometry ($h(x) = 1 - 0.2x$) can be seen in Figs. 4.13 and 4.14, where we show results for n=1, 0.5, and 1.5 and constant rheological parameters (α=β=0). The pressure distribution may be only slightly affected, but the slope of the unyielded region increases as n is reduced. At the critical value n_c=1/3 (Eq. (4.83)), $\sigma(0)$=0 and $\sigma(1)=h_{out}$ (thus, the second flow regime where the plug is unbroken is not observed). The material is so shear thinning that the plug hits the wall and no flow occurs.

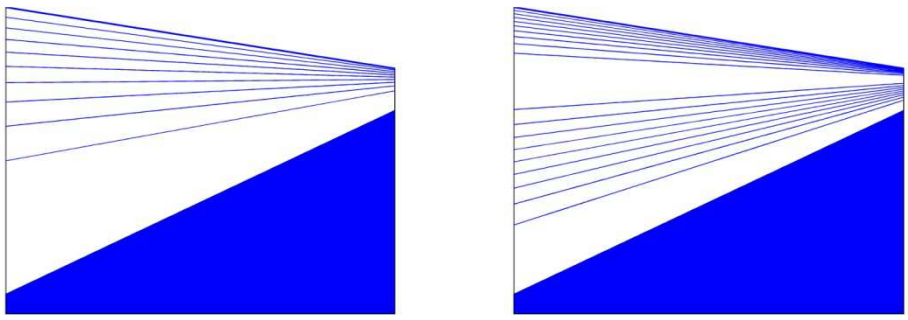

(a)

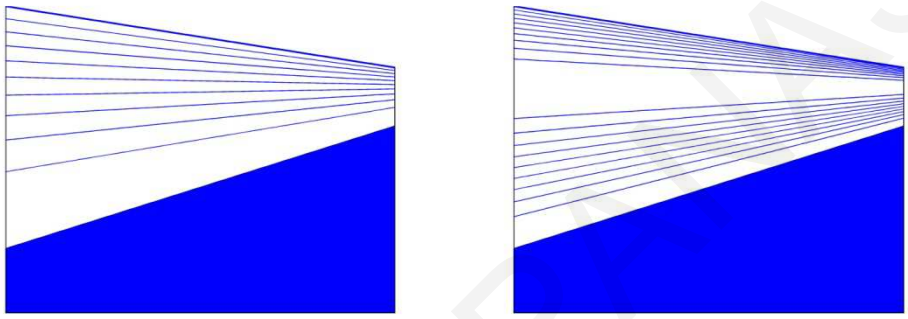

(b)

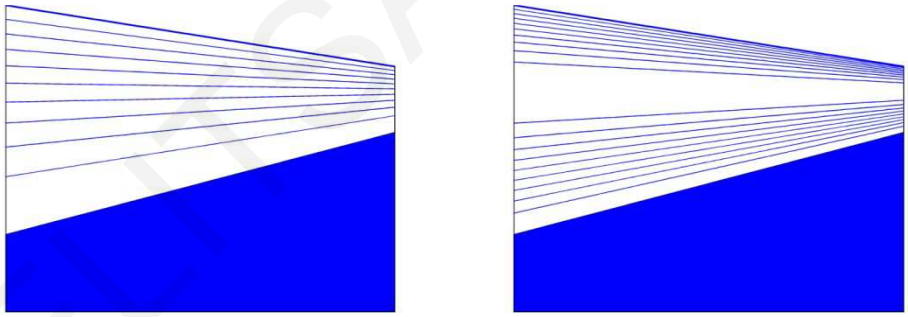

(c)

Figure 4.14: Effect of the power-law exponent on the contours of v_x (left) and v_y (right) in the case of flow of a Herschel-Bulkley fluid with constant rheological parameters ($\alpha = \beta = 0$) in a converging channel with $h(x) = 1 - 0.2x$ for $Bn = 0.5$: (a) n=0.5; (b) n=1; (c) n=1.5; The unyielded core is shaded and the contour values are equally spaced.

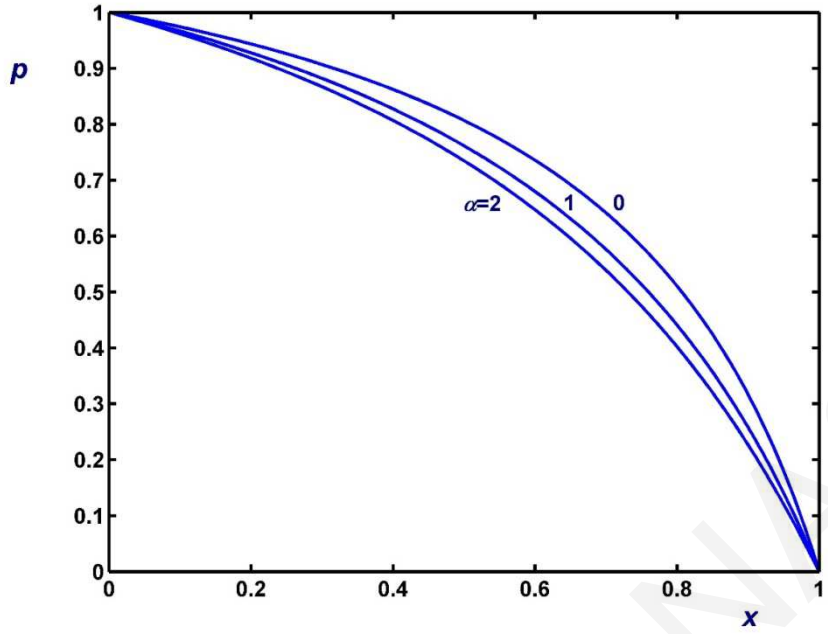

Figure 4.15: Effect of the plastic-viscosity growth parameter on the pressure distribution in the case of flow of a Bingham plastic (n=1) with constant yield stress (β=0) in a linearly converging channel with $h(x) = 1 - 0.2x$ for $Bn = 0.5$; the plastic viscosity is assumed to vary linearly with pressure.

We close this section with results for a Bingham-plastic (n=1) with constant yield stress (β=0) and with plastic viscosity varying linearly with pressure. Since it is not amenable to analytical solution, this flow is solved numerically using the method briefly described below. Figures 4.15 and 4.16 show results obtained again in a channel with $h(x) = 1 - 0.2x$ for Bn=0.5 and α=0, 1, and 2. As α is increased the dimensionless pressure decreases (see Fig. 4.15), but it should be kept in mind that the applied dimensional pressure driving the flow is increased. The velocity contours for the three values of α are given in Fig. 4.16. Note that the width of the unyielded region increases with α.

4.5 Flow in a channel with a nonlinear wall function

As already mentioned, the integro-differential Eq. (4.46) for the pressure distribution has been solved using a standard pseudo-spectral numerical method (Hesthaven et al., 2007). Chebyshev orthogonal polynomials are used to represent the unknown pressure.

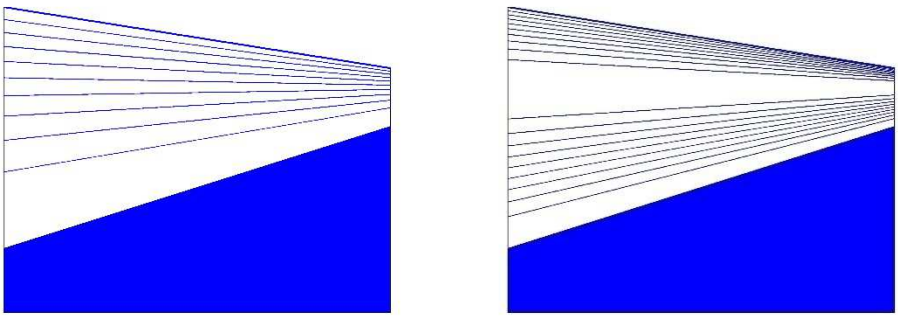

(a)

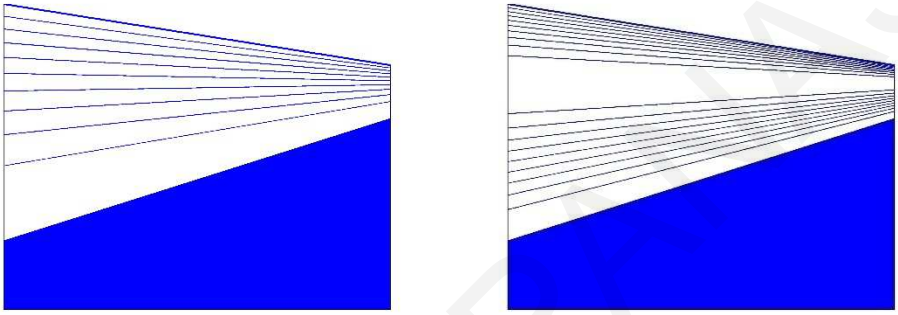

(b)

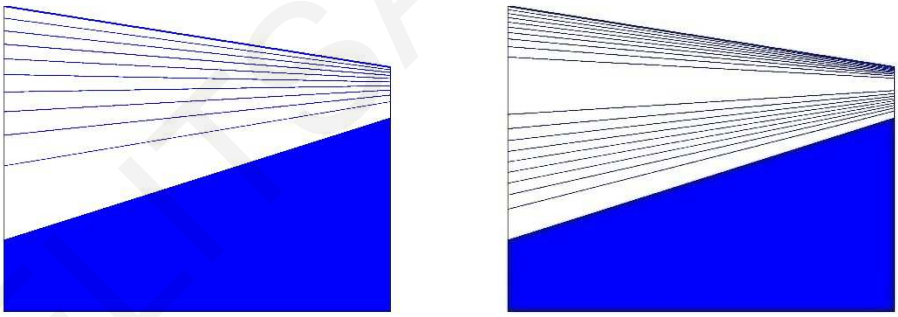

(c)

Figure 4.16: Effect of the plastic-viscosity growth parameter on the contours of v_x (left) and v_y (right) in the case of flow of a Bingham plastic (n=1) with constant yield stress (β=0) in a converging channel with $h(x) = 1 - 0.2x$ for $Bn = 0.5$: (a) α=0; (b) α=1; (c) α=2; the unyielded core is shaded and the contour values are equally spaced. The plastic viscosity is assumed to vary linearly with pressure.

For each parameter set, the number of spectral coefficients is adjusted so that a fully resolved pressure field is calculated; 12-18 spectral coefficients are usually required to achieve a decrease of the magnitude of the coefficients about seven to eight orders. To achieve maximum accuracy, all other quantities of interest are also calculated spectrally. Then, the yield surface, the unyielded core velocity, and then two velocity components are calculated using the analytical expressions derived in section 4.2.

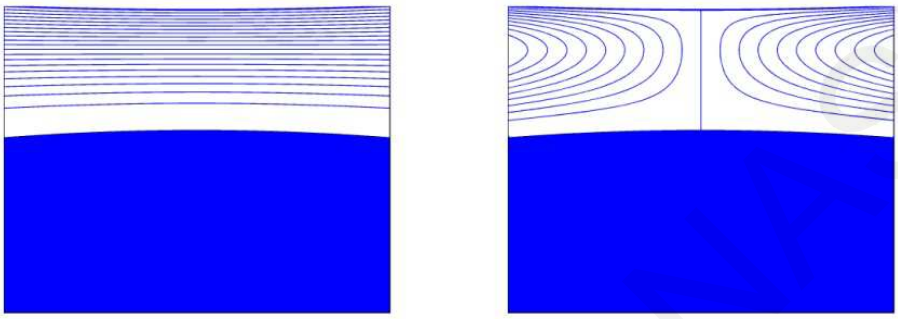

(a) **(b)**

Figure 4.17: Velocity contours in the case of flow of a Bingham plastic (n=1) with constant rheological parameters ($\alpha = \beta = 0$) in a wavy channel described by Eq. (4.88) for $Bn = 0.4762, \delta = 0.1$ and $\theta = 0.2$: (a) v_x; (b) v_y. The unyielded core is shaded and the contour values are equally spaced.

We considered the wavy channel used by Fusi et al. (2015) and Frigaard and Ryan (2004)

$$h(x) = 1 - \theta \cos\left[2\pi\delta\left(x - \frac{1}{2}\right)\right] \tag{4.88}$$

where δ>0 and $0 \le \theta \ll 1$. Figure 4.17 shows the velocity contours for a Bingham plastic (n=1) with constant rheological parameters (α=β=0) obtained with the values chosen in Fusi et al. (2015): Bn=0.4762, δ=0.1 and $\theta = 0.2$. In Fig. 4.18, we zoom in order to compare with the results of Fusi et al. (2015). Excellent agreement is observed regarding the shape of the plug region. In all our tests the contours of v_x were similar to those reported by Fusi et al. (2015). This was not the case, however, with the v_y contours. Since they intersect the yield surface, the v_y contours of Fusi et al. (2015) are in error.

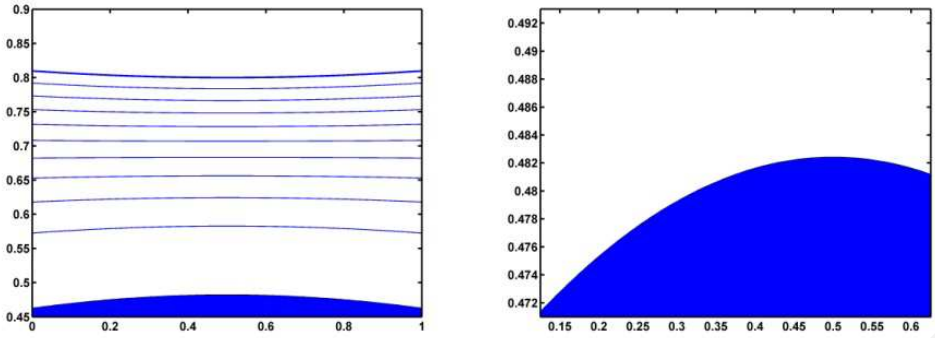

(a) **(b)**

Figure 4.18: Zooms of the yielded region in the case of flow of a Bingham plastic (n=1) with constant rheological parameters ($\alpha = \beta = 0$) in a wavy channel described by Eq. (4.88) for $Bn = 0.4762, \delta = 0.1$ and $\theta = 0.2$ corresponding to Figs. 3 and 4 in Fusi et al. (2015): (a) v_x; (b) v_y. The unyielded core is shaded and the contour values are equally spaced.

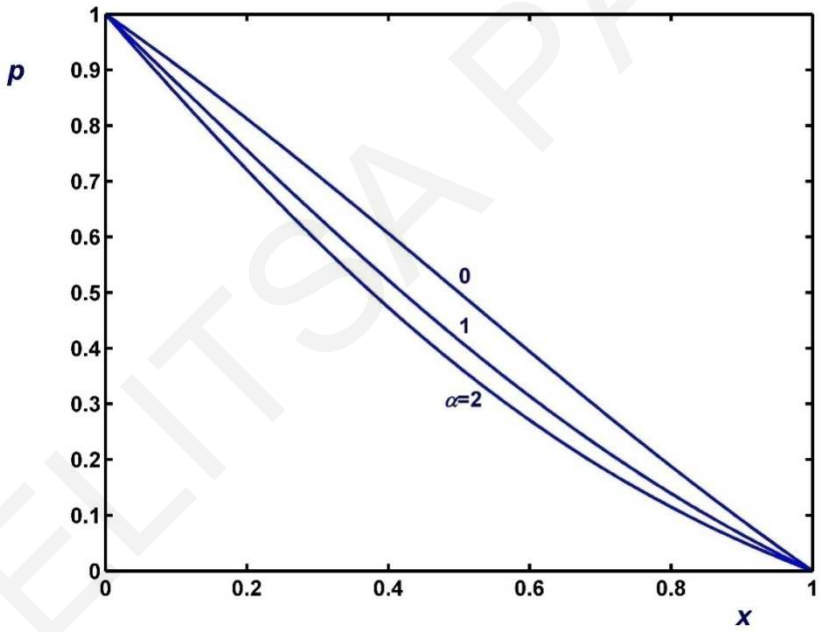

Figure 4.19: Effect of the plastic-viscosity growth coefficient on the pressure distribution in the case of flow of a Bingham plastic (n=1) with constant yield stress (β=0) in a wavy channel described by Eq. (4.88) with Bn=0.5, δ=0.1 and $\theta = 0.2$. The plastic viscosity varies linearly with pressure.

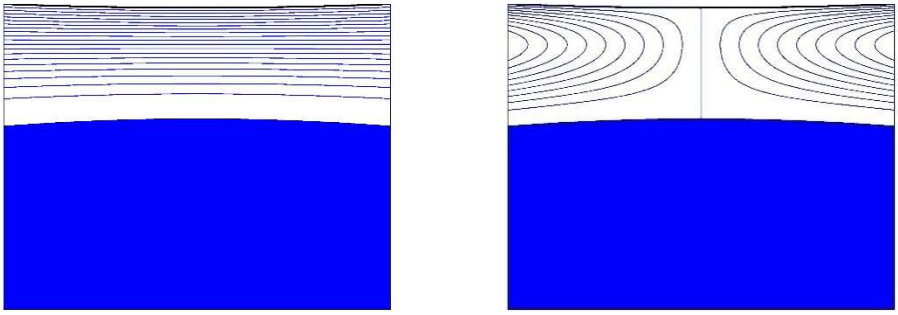

(a)

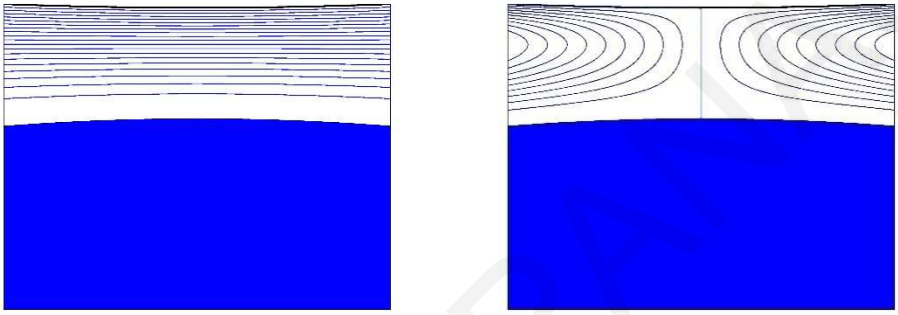

(b)

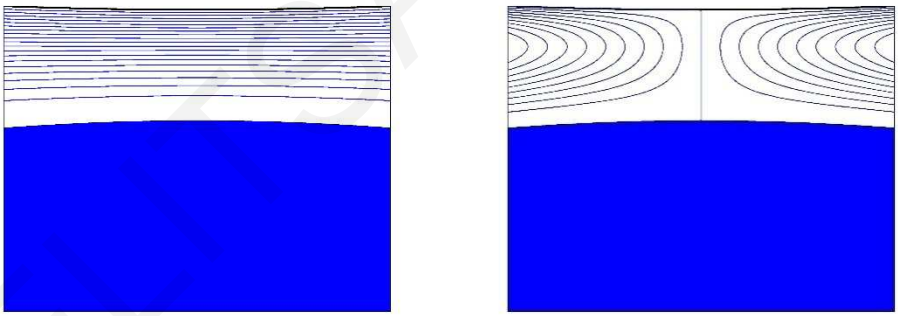

(c)

Figure 4.20: Effect of the plastic-viscosity growth coefficient on the contours of v_x (left) and v_y (right) in the case of flow of a Bingham plastic (n=1) with constant yield stress (β=0) in a wavy channel described by Eq. (4.88) with Bn=0.5, δ=0.1, and $\theta = 0.2$: (a) α=0; (b) α=1; (c) α=2; The unyielded core is shaded and the contour values are equally spaced. The plastic viscosity varies linearly with pressure.

Figures 4.19 and 4.20 show respectively the pressure distributions and the velocity contours for the flows of a Bingham plastic (n=1) with constant yield stress (β=0) and plastic viscosity varying linearly with pressure when Bn=0.5 and α=0 (constant plastic viscosity), 1, and 2. As before, the dimensionless pressure decreases with α and the pressure gradient increases in

magnitude near the inlet and decreases near the exit (Fig. 4.19). However, as shown in Fig. 4.20, the elevation of the yield surface is essentially the same (in reality, this increases slightly) and so are the velocity contours.

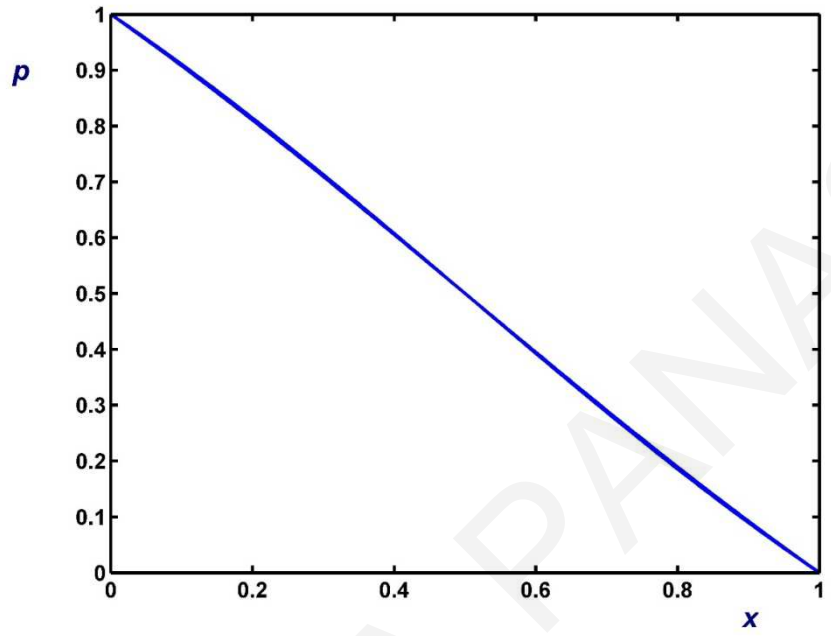

Figure 4.21: Effect of the yield-stress growth coefficient on the pressure distribution in the case of flow of a Bingham plastic (n=1) with constant plastic viscosity (α=0) in a wavy channel described by Eq. (4.88) with Bn=0.5, δ=0.1, $\theta = 0.2$, and β=-0.2, 0 and 2 (the three curves essentially coincide). The yield stress varies linearly with pressure.

The results when the yield stress varies linearly with pressure and the plastic viscosity is constant (α=0) seem to follow an opposite trend. Figure 4.21 shows that the dimensionless pressure distribution is insensitive to β, while the width of the unyielded region increases and the velocity contours in Fig. 4.22 are re-adjusted accordingly. A more careful look on the magnitude of the pressure gradient reveals that this is actually reduced near both the inlet and exit and increases in the middle of the channel as β is increased.

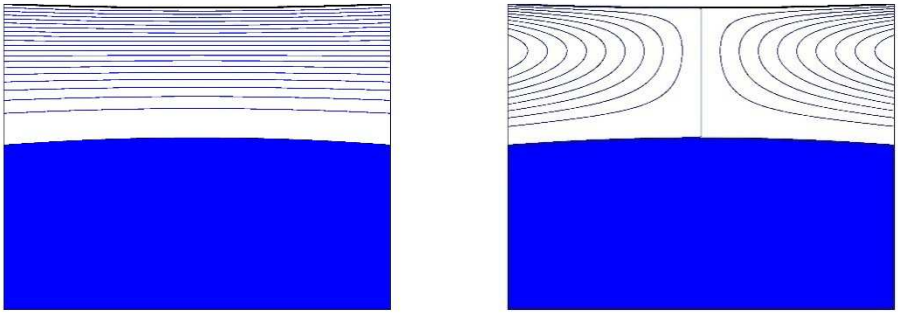

(a)

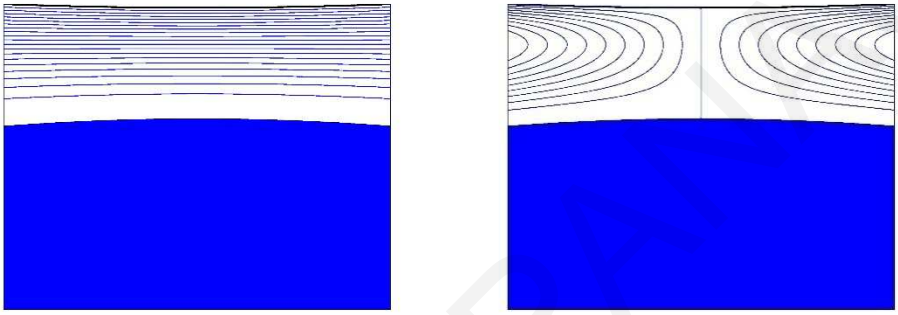

(b)

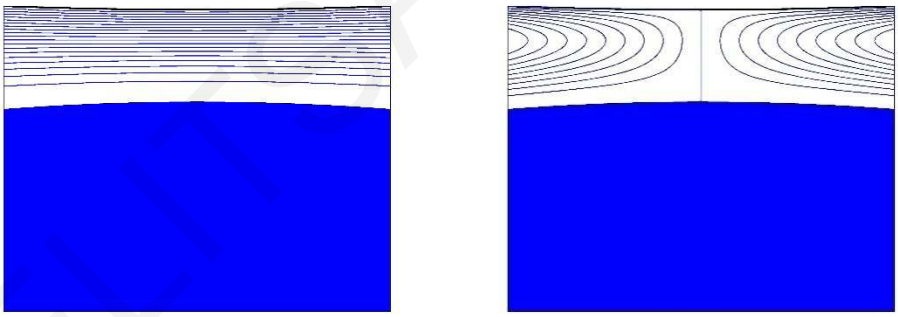

(c)

Figure 4.22: Effect of the yield-stress growth coefficient on the contours of v_x (left) and v_y (right) in the case of flow of a Bingham plastic (n=1) with constant plastic viscosity (α=0) in a wavy channel described by Eq. (4.88) with Bn=0.5, δ=0.1, and $\theta = 0.2$: (a) β=-0.2; (b) β=0; (c) β=0.2; The unyielded core is shaded and the contour values are equally spaced. The yield stress varies linearly with pressure.

4.6 Conclusions

The flow of a Herschel-Bulkley fluid with pressure-dependent rheological parameters in a channel of varying width has been analyzed extending the lubrication approximation model of Fusi et al. (2015) for a Bingham plastic (n=1). The zero-order problem in terms of the channel aspect ratio leads to a simple ordinary integro-differential equation for the pressure $p(x)$, which is solved using standard numerical methods (pseudo-spectral method in the present work). Once the pressure is obtained the yield surface and the two velocity components are easily calculated by means of closed-form expressions. Analytical solutions for the special cases of channels of constant and linearly varying regimes have also been obtained.

The present results generalize those of Fusi et al. (2015) for a Bingham plastic with constant rheological parameters. The lubrication paradox is avoided and the correct shape of the yield surface is approximated satisfactorily at zero order. The model predicts that at zero order the yield surface variation is opposite to that of the wall multiplied by a factor depending only on the power-law exponent. The pressure dependence of the consistency index and the yield stress affects only the elevation and not the shape of the yield surface. With previous approaches, such a result is obtained only if higher-order solutions are calculated (Frigaard and Ryan, 2004).

A limitation of the method is that it is valid, provided that the unyielded region extends continuously from the inlet to the outlet plane of the channel, i.e. when the plug is not broken. For example, Balmforth and Craster (1999) studied the broken-plug regime for the thin-film flow down an inclined plane by means of a consistent thin-layer theory for Bingham plastics. Frigaard and Ryan (2004) completed their analysis of viscoplastic flow in a channel of slowly-varying width by considering the structure of the flow after the plug was broken.

Chapter 5

Lubrication solution of the flow of a Herschel-Bulkley fluid with pressure-dependent rheological parameters in an asymmetric channel

In this chapter we consider a Herschel-Bulkley fluid with the consistency index and the yield stress being functions of pressure. We also derive analytical lubrication solutions of the flow in the case of an asymmetric long channel. Further, we consider the cases where firstly, the lower plate is horizontal, then, where the variable width is symmetrical and finally, the case where the upper wall function, varies linearly.

5.1 Introduction

In a recent work (Panaseti et al., 2018), we have extended a lubrication approximation method proposed by Fusi et al. (2015) for solving pressure-driven flow of a Bingham-plastic in a symmetric channel, in order to solve the flow of a Herschel-Bulkley fluid with pressure-dependent consistency index k^* and yield stress τ_y^*. Thus, we have employed the following constitutive equation

$$\begin{cases} \mathbf{D}^* = \mathbf{0}, & \tau^* \le \tau_y^* \\ \boldsymbol{\tau}^* = 2\left(\dfrac{\tau_y^*}{\dot{\gamma}^*} + k^* \dot{\gamma}^{*n-1}\right)\mathbf{D}^*, & \tau^* > \tau_y^* \end{cases} \tag{5.1}$$

where $\boldsymbol{\tau}^*$ is the viscous stress tensor,

$$\mathbf{D}^* \equiv \frac{1}{2}\left[\nabla^* \mathbf{v}^* + (\nabla^* \mathbf{v}^*)^T\right] \tag{5.2}$$

is the rate of deformation tensor, $\mathbf{v}^*$ is the velocity vector, $\dot{\gamma}^* \equiv \sqrt{2\mathrm{tr}\mathbf{D}^{*2}}$ and $\tau^* \equiv \sqrt{\mathrm{tr}\boldsymbol{\tau}^{*2}/2}$ are the magnitudes of $2\mathbf{D}^*$ and $\boldsymbol{\tau}^*$, respectively, and n is the power-law exponent. It should be noted that throughout this paper, symbols with stars denote dimensional quantities. As

mentioned above, the consistency index and the yield stress are pressure dependent, such that

$$k^*(p^*) = k_0^* f(\alpha^*(p^* - p_0^*)) \tag{5.3}$$

and

$$\tau_y^*(p^*) = \tau_0^* g(\beta^*(p^* - p_0^*)) \tag{5.4}$$

where k_0^* is the consistency index and τ_0^* is the yield stress at the reference pressure p_0^* (assumed to be the same for both material parameters), and f and g are appropriate functions, such that $f(0) = g(0) = 1$. For example, $f(x) = e^x$ and $f(x) = 1 + x$ describe respectively exponential and linear variations of the consistency index with pressure, the latter case corresponding to the Barus formula for the viscosity (Barus, 1893). Function f is increasing while g can be either decreasing or increasing. The pressure dependence of the yield stress and the viscosity is well established in the mechanics of granular materials (Ionescu et al., 2015) and in oil-drilling fluids (Hermoso et al., 2014b). The reader is referred to Panaseti et al. (2018) for a detailed literature review of experimental data on yield-stress materials with pressure-dependent rheological parameters.

Fusi et al. (2015) presented a novel technique for modelling the lubrication flow of a Bingham plastic (with constant rheological parameters) in a two-dimensional channel of non-uniform thickness. This is based on the application of Reynold's transport theorem over the unyielded core. The advantage of the method is that it avoids the lubrication paradox and predicts at zero order the correct shape of the yield surface, whose behavior is opposite to that of the wall function, i.e. the width of the unyielded core increases when the channel width is reduced and vice versa. With other lubrication-approximation methods, the correct shape of the yield surface is obtained only at higher orders (Frigaard and Ryan, 2004; Putz et al., 2009). A limitation of the method of Fusi et al. (2015), however, is that it applies only when the unyielded region (plug) extends continuously from the inlet to the outlet plane, i.e. it is not applicable when the plug is broken.

More recently, Panaseti et al. (2018) extended the method of Fusi et al. (2015) to solve the lubrication flow of a Herschel-Bulkley fluid with pressure-dependent consistency index and yield stress. For the case of a channel of constant width, they demonstrated that the width of the unyielded core is also constant, despite the pressure dependence of the yield stress, and that the pressure distribution is not affected by the yield-stress function. They also derived analytical solutions for certain choices of the functions f and g corresponding to linear or exponential pressure-dependence of the two rheological parameters. Subsequently, Housiadas et al. (2018) considered the axisymmetric flow following the approach proposed by Fusi and Farina (2018) and assuming that both the plastic viscosity and the yield stress vary linearly with the total pressure. They calculated the total pressure and the radius of the unyielded core solving numerically the

resulting nonlinear system of an ordinary differential equation and an algebraic one. Their calculations revealed that the variation of the radius of the central unyielded core depends on the relative values of a^* and β^*. The latter contracts when $\beta^* < \alpha^*$, expands when $\beta^* > \alpha^*$, and remains cylindrical when $\beta^* = \alpha^*$. More recently, Fusi (2018) revisited the symmetric planar flow problem assuming that the flow is driven by a prescribed inlet flux and not by a given pressure drop. In this case, the mathematical problem is much simpler reducing to a full nonlinear algebraic equation for the plug speed.

The objectives of the present work are: (a) to apply the method of Fusi et al. (2015) in order to solve the lubrication flow of a Herschel-Bulkley fluid with pressure-dependent consistency index and yield stress in an asymmetric channel; and (b) to derive analytical solutions for certain limiting cases, such as the flow in an asymmetric channel of linearly-varying width.

A prerequisite for the application of the method is the continuous extension of the unyielded core from the inlet to the outlet plane of the channel. The flow domain is thus divided into a lower and an upper yielded region and a central unyielded region defined by two unknown yield surfaces. The governing equations and the lubrication method are presented in section 5.2, where the zero-order solution is derived semi-analytically, in the sense that closed-form expressions are obtained for the positions of the upper and lower yield surfaces and for the two velocity components in terms of the pressure, which is found by solving a first-order integro-differential equation numerically. In section 5.3, the equations for a symmetric channel are outlined and the analytical solutions for a flat channel are provided for different functions describing the pressure-dependence of the consistency index and the yield stress. In section 5.4, we derive analytical solutions for the case of an asymmetric channel with linearly changing width and for special forms of the functions describing the variation of the consistency index and the yield stress with pressure. The symmetric channel constitutes a special case of the derived solution. In section 5.5, representative results demonstrating the effects of the Bingham number and the consistency-index and yield-stress growth parameters are presented and discussed. Finally, in section 5.6 concluding remarks are provided and some possibilities for further research are discussed.

5.2 Analysis of lubrication flow

Consider the pressure-driven flow of an incompressible Herschel-Bulkley fluid in an asymmetric long channel of length L^* and variable width $h_2^*(x^*) - h_1^*(x^*)$, where $h_1^*(x)$ and $h_2^*(x)$ are the lower and upper wall functions, respectively, as illustrated in Fig. 5.1.

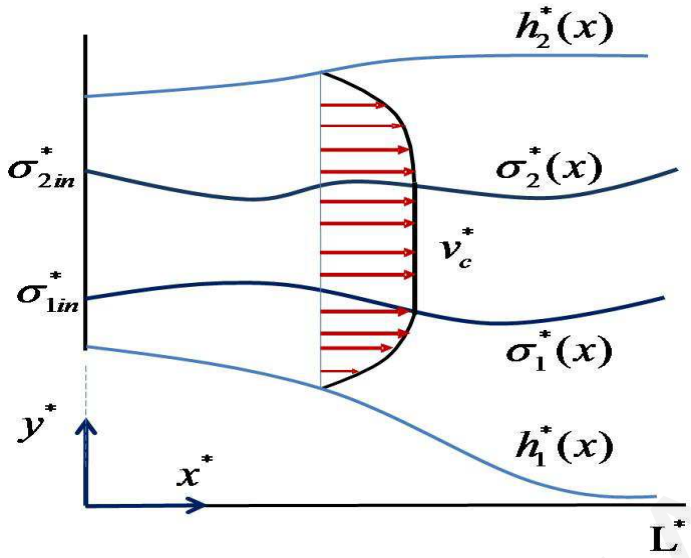

Figure 5.1: Geometry and boundary conditions for the dimensional flow in an asymmetric channel of length L^* and variable width $h_2^*(x^*) - h_1^*(x^*)$. The unyielded core extends from the inlet to the outlet plane and is bounded by the two yield surfaces $\sigma_1^*(x^*)$ and $\sigma_2^*(x^*)$.

A pressure p_{in}^* is applied at the inlet of the channel ($x^* = 0$) while the pressure at the exit ($x^* = L^*$) is $p_{out}^* < p_{in}^*$, i.e., the imposed pressure difference is $\Delta p^* = p_{in}^* - p_{out}^* > 0$, and thus the flow is from the left to the right. Without loss of generality, we assume here that p_{out}^* is the reference pressure that appears in Eqs. (5.3) and (5.4), i.e. $p_{out}^* = p_0^*$. The main flow is in the x^* direction while the z^* – velocity component is zero. Hence, the velocity vector is of the form $\mathbf{v}^* = v_x^*(x^*, y^*)\mathbf{i} + v_y^*(x^*, y^*)\mathbf{j}$. Given the asymmetry of the flow (Fig. 5.1), the yielded and unyielded regions are separated by two asymmetric interfaces, i.e. $y^* = \sigma_1^*(x^*)$ and $y^* = \sigma_2^*(x^*)$ for $0 \le x^* \le L^*$, where $0 \le h_1^*(x^*) < \sigma_1^*(x^*) < \sigma_2^*(x^*) < h_2^*(x^*)$. The unyielded region extends from the inlet to the outlet plane, i.e. the plug is not broken. Let also $\sigma_{1in}^* \equiv \sigma_1^*(0)$, $\sigma_{1out}^* \equiv \sigma_1^*(L^*)$, $\sigma_{2in}^* \equiv \sigma_2^*(0)$ and $\sigma_{2out}^* \equiv \sigma_2^*(L^*)$.

For convenience, we will work with the dimensionless equations. We assume that the length L^* of the channel is much greater than say the channel width or half-width at the inlet H^* ($L^* \gg H^*$), and use the aspect ratio

$$\varepsilon \equiv \frac{H^*}{L^*} \ll 1 \tag{5.5}$$

to apply the classical lubrication approximation or thin-film approach (Frigaard and Ryan, 2004). The flow problem is non-dimensionalised by scaling x^* by L^*, y^*, h_i^*, and σ_i^* by H^*, $(p^* - p_{out}^*)$ by Δp^*, v_x^* by $H^*(\varepsilon \Delta p^* / k_0^*)^{1/n}$, v_y^* by $\varepsilon H^*(\varepsilon \Delta p^* / k_0^*)^{1/n}$, and the stress

components by $\varepsilon \Delta p^*$. The dimensionless forms of the continuity equation and the two components of the momentum equation are as follows:

$$\frac{\partial v_x}{\partial x} + \frac{\partial v_y}{\partial y} = 0 \tag{5.6}$$

$$\varepsilon^{2/n-1} Re\left(v_x \frac{\partial v_x}{\partial x} + v_y \frac{\partial v_x}{\partial y} \right) = -\frac{\partial p}{\partial x} + \varepsilon \frac{\partial \tau_{xx}}{\partial x} + \frac{\partial \tau_{yx}}{\partial y} \tag{5.7}$$

$$\varepsilon^{2/n+1} Re\left(v_x \frac{\partial v_y}{\partial x} + v_y \frac{\partial v_y}{\partial y} \right) = -\frac{\partial p}{\partial y} + \varepsilon^2 \frac{\partial \tau_{yx}}{\partial x} + \varepsilon \frac{\partial \tau_{yy}}{\partial y} \tag{5.8}$$

where all variables are dimensionless (notice that there are no stars) and *Re* is the Reynolds number defined by

$$Re \equiv \frac{\rho^* H^{*3} \Delta p^{*2/n-1}}{k_0^{*2/n} L^*} \tag{5.9}$$

ρ^* being the constant mass density of the material. The non-zero components of the stress tensor in the yielded regime $\{(x, y) : x \in [0,1],\ y \in [h_1, \sigma_1] \cup [\sigma_2, h_2]\}$ read:

$$\left.\begin{aligned} \tau_{xx} &= 2\varepsilon \left[\frac{Bn\, g(\beta p)}{\dot\gamma} + f(\alpha p) \dot\gamma^{n-1} \right] \frac{\partial v_x}{\partial x} \\ \tau_{yx} &= \left[\frac{Bn\, g(\beta p)}{\dot\gamma} + f(\alpha p) \dot\gamma^{n-1} \right] \left(\frac{\partial v_x}{\partial y} + \varepsilon^2 \frac{\partial v_y}{\partial x} \right) \\ \tau_{yy} &= 2\varepsilon \left[\frac{Bn\, g(\beta p)}{\dot\gamma} + f(\alpha p) \dot\gamma^{n-1} \right] \frac{\partial v_y}{\partial y} \end{aligned}\right\}, \quad y \in [h_1, \sigma_1] \cup [\sigma_2, h_2] \tag{5.10}$$

where

$$\dot\gamma = \sqrt{4\varepsilon^2 \left(\frac{\partial v_x}{\partial x} \right)^2 + \left(\frac{\partial v_x}{\partial y} + \varepsilon^2 \frac{\partial v_y}{\partial x} \right)^2} \tag{5.11}$$

In Eq. (5.10), there appear three dimensionless numbers, the Bingham number *Bn* and the consistency-index and yield-stress growth numbers *a* and *β*, which are defined by

$$Bn \equiv \frac{\tau_0^*}{\varepsilon \Delta p^*}, \quad \alpha \equiv a^* \Delta p^*, \quad \beta \equiv \beta^* \Delta p^* \tag{5.12}$$

It is clear that when $\beta \geq 0$ the dimensionless yield stress is reduced from $g(\beta)Bn$ at the inlet plane to Bn at the exit plane. When $\beta < 0$, then the dimensionless yield stress increases from $g(\beta)Bn$ to Bn. We thus have the constraint $g(\beta) > 0$ so that the unyielded core extends from the inlet to the outlet plane (otherwise the present model is not applicable).

The unyielded core, defined by $\Omega = \{(x, y) : x \in [0,1],\ y \in [\sigma_1, \sigma_2]\}$, moves as a solid, i.e. at a constant velocity $\mathbf{v}^c = v_x^c \mathbf{i} + v_y^c \mathbf{j}$. Thus,

$$v_x = v_x^c \quad \text{and} \quad v_y = v_y^c \quad \text{for} \quad \sigma_1(x) \leq y \leq \sigma_2(x) \tag{5.13}$$

Remark 1. The transverse velocity of the unyielded core becomes zero only in the symmetric case.

For steady-state flow in the absence of body forces, the integral balance of linear momentum of the whole plug core yields the following equation (Fusi et al., 2015; Panaseti et al., 2018)

$$\int_0^1 \left\{ \left[-\sigma_{2x}(-p+\varepsilon\tau_{xx})+\tau_{yx} \right]_{y=\sigma_2} - \left[-\sigma_{1x}(-p+\varepsilon\tau_{xx})+\tau_{yx} \right]_{y=\sigma_1} \right\} dx + \left(\sigma_{2in}-\sigma_{1in}\right) p_{in} = 0 \tag{5.14}$$

where $\sigma_{ix} \equiv d\sigma_i / dx,\ i=1,2$. Finally, the dimensionless pressure satisfies the following boundary conditions:

$$p(0,\sigma_{1in}) = p(0,\sigma_{2in}) = 1, \quad p(1,\sigma_{1out}) = p(1,\sigma_{2out}) = 0 \tag{5.15}$$

The zero-order problem

As in our previous works (Panaseti et al., 2018; Housiadas et al., 2018), we solve the zero-order problem. For the sake of simplicity, we will avoid introducing new symbols for the zero-order variables. At zero order, the *y*-component of the momentum equation is simplified to $\partial p / \partial y = 0$ and thus $p = p(x)$. The continuity and *x*-momentum equations at zero order then read as follows:

$$\frac{\partial v_x}{\partial x} + \frac{\partial v_y}{\partial y} = 0 \tag{5.16}$$

$$-\frac{\partial p}{\partial x} + \frac{\partial \tau_{yx}}{\partial y} = 0 \tag{5.17}$$

Moreover, $\tau_{xx} = \tau_{yy} = 0$, while the shear stress component is given by

$$\tau_{yx} = \left[\frac{Bn\, g(\beta p)}{\dot\gamma} + f(\alpha p)\dot\gamma^{n-1} \right] \frac{\partial v_x}{\partial y}, \quad y \in \left[h_1,\sigma_1\right] \cup \left[\sigma_2,h_2\right] \tag{5.18}$$

In the lower yielded region $\dot\gamma = \left|\partial v_x / \partial y\right| = \partial v_x / \partial y$ and thus

$$\tau_{yx} = Bn\, g(\beta p) + f(\alpha p)\left(\frac{\partial v_x}{\partial y} \right)^n, \quad y \in \left[h_1,\sigma_1\right] \tag{5.19}$$

Substituting the above expression into the *x*-momentum equation (5.17), integrating twice, and applying the boundary conditions $\partial v_x / \partial y(x,\sigma_1) = v_x(x,h_1) = 0$, the following expression is obtained for v_x:

$$v_x(x,y) = \left[1 - \frac{(\sigma_1 - y)^{1+1/n}}{(\sigma_1 - h_1)^{1+1/n}} \right] v_x^c, \quad y \in \left[h_1,\sigma_1\right] \tag{5.20}$$

where

$$v_x^c = \frac{\left(-p_x\right)^{1/n} (\sigma_1 - h_1)^{1+1/n}}{(1+1/n)\, f^{1/n}(\alpha p)} \tag{5.21}$$

and $p_x \equiv dp/dx$. Similarly, in the upper yielded region where $\dot\gamma = \left|\partial v_x / \partial y\right| = -\partial v_x / \partial y$ the shear stress is given by

$$\tau_{yx} = -Bn\, g(\beta p) - f(\alpha p)\left(-\frac{\partial v_x}{\partial y}\right)^n, \quad y \in \left[\sigma_2, h_2\right] \tag{5.22}$$

Substituting in the momentum equation, integrating twice, and applying the boundary conditions $\partial v_x / \partial y(x, \sigma_2) = v_x(x, h_2) = 0$, one gets:

$$v_x(x, y) = \left[1 - \frac{(y - \sigma_2)^{1+1/n}}{(h_2 - \sigma_2)^{1+1/n}}\right] v_x^c, \quad y \in \left[\sigma_2, h_2\right] \tag{5.23}$$

where

$$v_x^c = \frac{(-p_x)^{1/n}(h_2 - \sigma_2)^{1+1/n}}{(1+1/n)\, f^{1/n}(\alpha p)} \tag{5.24}$$

Since the core velocity is constant, the pressure satisfies the first-order ODEs defined by

$$\frac{p_x}{f(\alpha p)}(\sigma_1 - h_1)^{n+1} = \frac{p_x}{f(\alpha p)}(h_2 - \sigma_2)^{n+1} = -(1+1/n)^n (v_x^c)^n \tag{5.25}$$

The pressure p and the core velocity v_x^c can be determined upon integration and application of the two conditions for p,

$$p(0) = 1, \quad p(1) = 0 \tag{5.26}$$

The transverse velocity component in the lower and upper yielded regions is found by integrating the continuity equation (5.16) and applying the no-penetration boundary condition at the two walls, $v_y(x, h_1) = v_y(x, h_2) = 0$:

$$\left.\begin{aligned} v_y &= -\int_{h_1}^{y} \frac{\partial v_x}{\partial x} dy, \quad y \in \left[h_1, \sigma_1\right] \\ v_y &= \int_{y}^{h_2} \frac{\partial v_x}{\partial x} dy, \quad y \in \left[\sigma_2, h_2\right] \end{aligned}\right\} \tag{5.27}$$

Substituting v_x from Eq. (5.20) into Eq. (5.27) and carrying out the required differentiation and integration one gets for the lower yielded region:

$$v_y = \frac{v_x^c}{2+1/n}\left[\sigma_{1x} + (1+1/n)h_{1x} - (2+1/n)\left(\frac{\sigma_1 - y}{\sigma_1 - h_1}\right)^{1+1/n} \sigma_{1x} + (1+1/n)(\sigma_{1x} - h_{1x})\left(\frac{\sigma_1 - y}{\sigma_1 - h_1}\right)^{2+1/n}\right], \quad y \in [h_1, \sigma_1] \tag{5.28}$$

where $h_{1x} \equiv dh_1 / dx$. The satisfaction of condition $v_y(x, \sigma_1) = v_y^c$ requires that

$$\sigma_{1x} + (1+1/n)h_{1x} = (2+1/n)\frac{v_y^c}{v_x^c} \tag{5.29}$$

Combining Eqs. (5.28) and (5.29) and simplifying leads to the following expression for the transverse velocity in the lower yielded region:

$$v_y = v_y^c + \frac{(\sigma_1 - y)^{1+1/n}}{(\sigma_1 - h_1)^{2+1/n}}\left\{(1+1/n)\left(y - h_1\right)h_{1x} v_x^c - \left[\sigma_1 - h_1 + (1+1/n)(y - h_1)\right] v_y^c\right\}, \quad y \in [h_1, \sigma_1] \tag{5.30}$$

Working similarly in the upper yielded region, one finds that

$$\sigma_{2x} + (1+1/n)h_{2x} = (2+1/n)\frac{v_y^c}{v_x^c} \tag{5.31}$$

and

$$v_y = v_y^c + \frac{(y-\sigma_2)^{1+1/n}}{(h_2-\sigma_2)^{2+1/n}}\left\{(1+1/n)(h_2-y)h_{2x}v_x^c - \left[h_2-\sigma_2+(1+1/n)(h_2-y)\right]v_y^c\right\}, \quad y\in[\sigma_2,h_2] \tag{5.32}$$

where $h_{2x} \equiv dh_2/dx$.

We still need to find the equations corresponding to the unknown positions of the two yield surfaces. Since the unyielded core moves at constant velocity, $v_x(y=\sigma_1) = v_x(y=\sigma_2) = v_x^c$. Equating Eqs. (5.21) and (5.24) results in

$$\sigma_1 + \sigma_2 = h_1 + h_2 \tag{5.33}$$

Remark 2. Since $\sigma_1 - h_1 = h_2 - \sigma_2$, the widths of the lower and upper yielded regions are equal for any *x*.

Combining now Eqs. (5.29) and (5.31) we get:

$$\sigma_{2x} - \sigma_{1x} = -\left(1+\frac{1}{n}\right)(h_{2x}-h_{1x}) \tag{5.34}$$

Integrating the above equation with respect to *x*, we get the following expression for the thickness of the unyielded core:

$$\sigma_2(x) - \sigma_1(x) = -\left(1+\frac{1}{n}\right)\left[h_2(x)-h_1(x)\right] + C \tag{5.35}$$

where *C* is an unknown constant to be determined. From the system of Eqs. (5.33) and (5.35) we find that

$$\sigma_1(x) = -\frac{1}{2n}h_1(x) + \left(1+\frac{1}{2n}\right)h_2(x) - \frac{C}{2} \tag{5.36}$$

and

$$\sigma_2(x) = \left(1+\frac{1}{2n}\right)h_1(x) - \frac{1}{2n}h_2(x) + \frac{C}{2} \tag{5.37}$$

Remark 3. The above results generalize those of Panaseti et al. (2018) for a symmetric channel, in which case $v_y^c = 0$. The width of the unyielded core increases if the width of the channel decreases and vice versa. The variation of the width of the unyielded core is enhanced by shear thinning and is independent of the other material and flow parameters, which affect only the constant *C*. As noted in Panaseti et al. (2018), reducing the power-law exponent *n* in a converging channel causes the plug to expand faster, which is expected, given that the velocity profile becomes flatter as shear thinning is enhanced.

Remark 4. From Eqs. (5.33) and (5.34) one observes that

$$\sigma_{1x} = \left(1+\frac{1}{2n}\right)h_{2x} - \frac{1}{2n}h_{1x} \tag{5.38}$$

which upon substitution into Eq. (5.29) yields

$$\frac{v_y^c}{v_x^c} = \frac{h_{1x} + h_{2x}}{2} \tag{5.39}$$

Given that the LHS is constant, the solution derived above is valid provided that $h_{1x} + h_{2x}$ is constant, or equivalently when the sum $h_1 + h_2$ is a linear function of x. This condition is satisfied when the channel is symmetric as well as when both the wall functions are linear. In the general case, for a given lower wall function the upper wall function must be of the form

$$h_2(x) = -h_1(x) + c_1 x \tag{5.40}$$

where c_1 is any constant.

Remark 5. If the width of the channel, $h_2(x) - h_1(x)$, is constant then the two walls are flat (and parallel) and the width $\sigma_2(x) - \sigma_1(x)$ of the unyielded core is also constant.

Remark 6. It is easily shown that the constant *C* is related to the volumetric flow rate through the channel, for which we have:

$$Q = \int_{h_1}^{h_2} v_x(x, y)\, dy = \int_{h_1}^{\sigma_1} v_x(x, y)\, dy + (\sigma_2 - \sigma_1) v_x^c + \int_{\sigma_2}^{h_2} v_x(x, y)\, dy \tag{5.41}$$

Substituting the velocity from Eqs. (5.20) and (5.23) for the lower and upper yielded regions and taking into account that in the unyielded region the velocity is v_x^c we obtain

$$Q = \frac{v_x^c}{2 + 1/n}\left[\sigma_2 - \sigma_1 + (1 + 1/n)\left(h_2 - h_1\right)\right] \tag{5.42}$$

The expression within the brackets is the constant *C* of Eq. (5.35). Thus,

$$C = (2 + 1/n)\frac{Q}{v_x^c} \tag{5.43}$$

To determine the constant *C*, we return to the plug momentum balance equation (5.14), which at zero order becomes

$$\int_0^1 \left\{\left[-\sigma_{2x}(-p) + \tau_{yx}\right]_{y=\sigma_2} - \left[-\sigma_{1x}(-p) + \tau_{yx}\right]_{y=\sigma_1}\right\} dx + \left(\sigma_{2in} - \sigma_{1in}\right) p_{in} = 0 \tag{5.44}$$

From Eqs. (5.19) and (5.22) we get

$$\tau_{yx}\Big|_{y=\sigma_1} = Bn\, g(\beta p) \quad \text{and} \quad \tau_{yx}\Big|_{y=\sigma_2} = -Bn\, g(\beta p) \tag{5.45}$$

Substituting into Eq. (5.44), using integration by parts, and applying the boundary conditions (5.26), we find that

$$\int_0^1 \left(\sigma_2 - \sigma_1\right) p_x dx + 2Bn \int_0^1 g\left(\beta p\right) dx = 0 \tag{5.46}$$

Substituting Eq. (5.35) into Eq. (5.46) and integrating, one gets

$$C = 2Bn \int_0^1 g(\beta p)\, dx - (1 + 1/n) \int_0^1 p_x \left(h_2 - h_1\right) dx \tag{5.47}$$

or

$$C = 2Bn\int_0^1 g(\beta p)\,dx + (1+1/n)\left[h_{2in} - h_{1in} + \int_0^1 p\left(h_{2x} - h_{1x}\right)dx\right] \tag{5.48}$$

Substituting C from Eq. (5.48) into Eq. (5.36) yields

$$\sigma_1 = -Bn\int_0^1 g(\beta p)\,dx - \frac{1}{2n}h_1 + \left(1+\frac{1}{2n}\right)h_2 - \frac{1}{2}(1+1/n)\left[h_{2in} - h_{1in} + \int_0^1 p\left(h_{2x} - h_{1x}\right)dx\right] \tag{5.49}$$

Finally, combining the above equation with Eq. (5.25) we get the following integro-differential equation

$$p_x\left\{-Bn\int_0^1 g(\beta p)\,dx + \left(1+\frac{1}{2n}\right)(h_2 - h_1) - \frac{1}{2}(1+1/n)\left[h_{2in} - h_{1in} + \int_0^1 p\left(h_{2x} - h_{1x}\right)dx\right]\right\}^{n+1} = K\,f(\alpha p) \tag{5.50}$$

which is subject to conditions (5.26). Once the pressure is calculated, C, $\sigma_1(x)$, and $\sigma_2(x)$ are readily calculated from Eqs.(5.48), (5.36), and (5.37), respectively. The two velocity components can then be calculated by means of Eqs. (5.20) and (5.30) in the lower yielded region and Eqs. (5.23) and (5.32) in the upper yielded region. The two components of the velocity of the core are calculated by means of Eqs. (5.21) and (5.29). For the latter velocity component, we get:

$$v_y^c = \frac{\sigma_{1x} + (1+1/n)h_{1x}}{(2+1/n)}v_x^c \tag{5.51}$$

The velocity distributions in the asymmetric channel are thus given by:

$$v_x(x,y) = v_x^c\begin{cases} 1 - \left(\dfrac{\sigma_1 - y}{\sigma_1 - h_1}\right)^{1+1/n}, & y \in [h_1, \sigma_1) \\ 1, & y \in [\sigma_1, \sigma_2] \\ 1 - \left(\dfrac{y - \sigma_2}{h_2 - \sigma_2}\right)^{1+1/n}, & y \in (\sigma_2, h_2] \end{cases} \tag{5.52}$$

and

$$v_y(x,y) = v_y^c + \begin{cases} \dfrac{(\sigma_1 - y)^{1+1/n}}{(\sigma_1 - h_1)^{2+1/n}}\left\{(1+1/n)\left(y - h_1\right)h_{1x}v_x^c - \left[\sigma_1 - h_1 + (1+1/n)(y - h_1)\right]v_y^c\right\}, & y \in [h_1, \sigma_1] \\ 0, & y \in [\sigma_1, \sigma_2] \\ \dfrac{(y - \sigma_2)^{1+1/n}}{(h_2 - \sigma_2)^{2+1/n}}\left\{(1+1/n)\left(h_2 - y\right)h_{2x}v_x^c - \left[h_2 - \sigma_2 + (1+1/n)(h_2 - y)\right]v_y^c\right\}, & y \in [\sigma_2, h_2] \end{cases} \tag{5.53}$$

It should be pointed out that in order for the present model to be applied, $Bn_{c1} \le Bn \le Bn_{c2}$, where Bn_{c1} is the critical value of the Bingham number at which the plug is broken ($\sigma_1 = \sigma_2$) and Bn_{c2} is the critical Bingham below which flow occurs, i.e. the Bingham number at which the core touches the walls and the flow ceases. If the plug is broken, which implies that $\sigma_1 = \sigma_2 = \sigma$ at some point x_c, then $2\sigma = h_1 + h_2$ and therefore the plug breaks in the middle of the channel at $x = x_c$. Equation (5.35) then gives:

$$C_c = \left(1+\frac{1}{n}\right)\left[h_2(x_c) - h_1(x_c)\right] \tag{5.54}$$

Substituting the above equation into Eq. (5.48) yields the critical Bingham number below which the plug is broken:

$$Bn_{c1} = \frac{\left(1+\frac{1}{n}\right)\left[h_2(x_c) - h_1(x_c) - h_{2in} + h_{1in} - \int_0^1 p\left(h_{2x} - h_{1x}\right)dx\right]}{2\int_0^1 g\left(\beta p\right)dx} \tag{5.55}$$

Now, if $\sigma_1 = h_1$ at any point x_w, then $\sigma_2(x_w) = h_2(x_w)$, which implies that the two unyielded surfaces touch the two walls at the same distance x_w downstream. In this case, there is obviously no flow and Eq. (5.35) gives:

$$C_w = \left(2+\frac{1}{n}\right)\left[h_2(x_w) - h_1(x_w)\right] \tag{5.56}$$

The second critical value Bn_{c2} above which there is no flow is the critical number at which there is no flow in a flat channel of width equal to the minimum width of the channel:

$$Bn_{c2} = \frac{\left(h_2 - h_1\right)_{\min}}{2\int_0^1 g\left(\beta p_F\right)dx} \tag{5.57}$$

where p_F is the pressure corresponding to flow in the aforementioned flat channel.

5.3 Flow in a symmetric channel

The flow in a symmetric channel constitutes a special case of the flow problem analyzed in section 5.2. Letting

$$h(x) = -h_1(x) = h_2(x) \tag{5.58}$$

and

$$\sigma(x) = -\sigma_1(x) = \sigma_2(x) \tag{5.59}$$

Eq. (5.35) is simplified as follows:

$$\sigma\left(x\right) = -\left(1+\frac{1}{n}\right)h(x) + \frac{C}{2} \tag{5.60}$$

which also implies that

$$\sigma_x + (1+1/n)h_x = 0 \tag{5.61}$$

Hence, from Eq. (5.29) it is deduced that $v_y^c = 0$, as expected by symmetry. From Eq. (5.48) one finds that

$$\frac{C}{2} = Bn\int_0^1 g(\beta p)\,dx + (1+1/n)\left[h_{in} + \int_0^1 p h_x\,dx\right] \tag{5.62}$$

Finally, from Eq. (5.25) we observe that the pressure satisfies the simplified equation

$$\frac{p_x}{f(\alpha p)} = -\frac{(1+1/n)^n (v_x^c)^n}{(h-\sigma)^{n+1}} \tag{5.63}$$

After calculating the pressure, the constant C and the location of the yield surface $\sigma(x)$ are computed via Eqs. (5.62) and (5.60), respectively. The velocity above the symmetry plane is then given by

$$v_x(x,y) = v_x^c \begin{cases} 1, & y \in [0,\sigma] \\ 1-\left(\dfrac{y-\sigma}{h-\sigma}\right)^{1+1/n}, & y \in (\sigma,h] \end{cases} \tag{5.64}$$

where

$$v_x^c = \frac{(-p_x)^{1/n}(h-\sigma)^{1+1/n}}{(1+1/n) f^{1/n}(\alpha p)} \tag{5.65}$$

The expressions (5.55) and (5.57) for the two critical Bingham numbers are simplified as follows:

$$Bn_{c1} = \frac{\left(1+\dfrac{1}{n}\right)\left[h(x_c) - h_{in} - \int_0^1 p h_x \, dx\right]}{\int_0^1 g(\beta p)\, dx} \tag{5.66}$$

and

$$Bn_{c2} = \frac{h_{\min}}{\int_0^1 g(\beta p_F)\, dx} \tag{5.67}$$

Below we focus on the case of a flat channel with $h=1$ and derive the complete analytical solutions for various combinations of the functions f and g, which describe the dependence of k and τ_0 on pressure. As noted in Panaseti et al. (2018), the yield surface is flat despite the pressure dependence of the rheological parameters, given by

$$\sigma = Bn \int_0^1 g(\beta p)\, dx \tag{5.68}$$

The pressure satisfies the following first-order integro-differential equation

$$\frac{p_x}{f(\alpha p)} = -\frac{(1+1/n)^n (v_x^c)^n}{(h-\sigma)^{n+1}} = -K' \tag{5.69}$$

where K' is an unknown constant. Solving the above equation and applying the boundary conditions (5.26) yields the pressure $p(x)$ and the constant K'. Then σ and the velocity $v_x(x,y)$ are computed by means of Eqs. (5.68) and (5.64), respectively, where

$$v_x^c = \frac{K'^{1/n}(1-\sigma)^{1+1/n}}{1+1/n} \tag{5.70}$$

Table 5.1: Expressions for the pressure $p(x)$, the constant K', and the elevation of the yield surface σ for different forms of the consistency-index growth function f and the yield stress growth function f in the case of a symmetric planar channel with constant width ($h=1$). The velocity is calculated by means of Eq. (5.64).

$f(\alpha p)=1$	
$p(x)=1-x, \quad K'=1$	
$g(\beta p)=1$	$\sigma = Bn$
$g(\beta p)=1+\beta p$	$\sigma=\left(1+\frac{\beta}{2}\right)Bn$
$g(\beta p)=e^{\beta p}$	$\sigma=\frac{e^{\beta}-1}{\beta}Bn$
$f(\alpha p)=1+\alpha p$	
$p(x)=\frac{1}{\alpha}\left[(1+\alpha)^{1-x}-1\right], \quad K'=\frac{\ln(1+\alpha)}{\alpha}$	
$g(\beta p)=1$	$\sigma = Bn$
$g(\beta p)=1+\beta p$	$\sigma=\left[1-\beta\left\{\frac{1}{\alpha}-\frac{1}{\ln(1+\alpha)}\right\}\right]Bn$
$g(\beta p)=e^{\beta p}$	No analytical solution
$f(\alpha p)=e^{\alpha p}$	
$p(x)=\frac{1}{\alpha}\ln\frac{1}{(1-e^{-\alpha})x+e^{-\alpha}}, \quad K'=\frac{1-e^{-\alpha}}{\alpha}$	
$g(\beta p)=1$	$\sigma = Bn$
$g(\beta p)=1+\beta p$	$\sigma=\left[1-\frac{\beta(1+\alpha+e^{a})}{\alpha(e^{a}-1)}\right]Bn$
$g(\beta p)=e^{\beta p}$	$\sigma=\begin{cases}\frac{a}{1-e^{-a}}Bn, & \beta=\alpha \\ \frac{1-e^{\beta-\alpha}}{(1-\beta/a)(1-e^{-a})}Bn, & \beta\neq\alpha\end{cases}$

The analytical solutions for $f, g \in \{1, 1+x, e^{x}\}$ are tabulated in Table 5.1. It is readily observed that the pressure is independent of the yield-stress growth function, which affects only the semi-width σ of the unyielded core. It turns out that, there is no analytical solution only when f is linear and g is exponential. From Eq. (5.68), it is deduced that for flow to occur, it must be $\sigma<1$, and thus the critical number below which flow occurs is

$$Bn_{c2}=\frac{1}{\int_0^1 g(\beta p)\,dx} \tag{5.71}$$

It is also evident from Eq. (5.66) that in the case of a flat channel the first critical Bingham number Bn_{c1} is zero.

5.4 Flow in a channel with linearly-varying upper wall

In this section we consider the flow in a channel described by

$$h_1 = 0, \quad h_2 = 1 + \Delta h\, x \tag{5.72}$$

where Δh is a constant. It is clear that the upper wall may be diverging ($\Delta h > 0$), flat ($\Delta h = 0$), or converging ($\Delta h < 0$). The positions of the two yield surfaces (Eqs. (5.36) and (5.37)) are then simplified as follows:

$$\sigma_1(x) = \left(1 + \frac{1}{2n}\right)(1 + \Delta h\, x) - \frac{C}{2} \tag{5.73}$$

and

$$\sigma_2(x) = -\frac{1}{2n}(1 + \Delta h\, x) + \frac{C}{2} \tag{5.74}$$

Therefore, $\sigma_1(x)$ is increasing while $\sigma_2(x)$ is decreasing downstream in a diverging channel and vice versa in a converging channel. As shown in section 5.3 and also in Panaseti et al. (2018), in the symmetric case of a horizontal channel with two parallel walls, the two yield surfaces are also horizontal.

In order to simplify the resulting solution expressions for this particular flow, we introduce a constant *A*, replacing the constant *C* by means of

$$A \equiv \frac{1}{\Delta h}\left(1 - \frac{C}{2 + 1/n}\right) \quad \Leftrightarrow \quad C = (2 + 1/n)(1 - \Delta h A) \tag{5.75}$$

Equation (5.48) for this particular geometry (as described by Eq. (5.72)) gives

$$(2 + 1/n)(1 - \Delta h A) = 2Bn \int_0^1 g(\beta p)\, dx + (1 + 1/n)\left(1 + \Delta h \int_0^1 p\, dx\right) \tag{5.76}$$

which can be written as follows:

$$1 - \left[(2 + 1/n)A + (1 + 1/n)I(A)\right]\Delta h = 2Bn \int_0^1 g(\beta p)\, dx \tag{5.77}$$

where

$$I(A) = \int_0^1 p\, dx \tag{5.78}$$

The expressions (5.73) and (5.74) for the two yield surfaces now become:

$$\sigma_1(x) = \left(1 + \frac{1}{2n}\right)\Delta h(A + x) \tag{5.79}$$

and

$$\sigma_2(x) = 1 - \Delta h A - \frac{1}{2n}\Delta h(A + x) \tag{5.80}$$

In this case, the ODE for the pressure (5.25) can be written as

$$\frac{p_x}{f(\alpha p)} = -\frac{K'}{(A+x)^{n+1}} \tag{5.81}$$

where

$$K' = \frac{(1+1/n)^n \left(v_x^c\right)^n}{(1+1/2n)^{n+1}(\Delta h)^{n+1}} \tag{5.82}$$

It is easily seen that once K' is calculated the velocity of the unyielded core in the x-direction can be found:

$$v_x^c = \frac{\left[(1+1/2n)\Delta h\right]^{1+1/n} K'^{1/n}}{1+1/n} \tag{5.83}$$

In the general case, for given functions f and g, the pressure $p(x)$ and the constant K' can be found by integrating Eq. (5.81) and applying the boundary conditions (5.26). The constant A is computed numerically solving Eq. (5.77) where the integral of the RHS as well as $I(A)$ are also computed numerically. Then σ_1 and σ_2 are computed by means of Eqs. (5.79) and (5.80), respectively. The component v_x^c is given by Eq. (5.83) whereas from Eq. (5.29) we get

$$v_y^c = \frac{\sigma_{1x} + (1+1/n)h_{1x}}{2+1/n} v_x^c = \frac{(1+1/2n)\Delta h}{2+1/n} v_x^c \quad \Rightarrow \quad v_y^c = \frac{\Delta h}{2} v_x^c \tag{5.84}$$

We observe that the ratio v_y^c / v_x^c depends only on Δh, i.e. it is independent of the material parameters. Finally, the two velocity components in the two yielded regimes are calculated by means of Eqs. (5.52) and (5.53).

Explicit expressions for the pressure $p(x)$ and the constant K' can be derived when f is linear or exponential. These expressions are tabulated in Table 5.2. It should be noted that the effects of the yield-stress growth parameter β and the Bingham number Bn are incorporated in the value of the constant A. The integral $I(A)$ can be calculated analytically only for the case $f(\alpha p) = 1$:

$$I(A) = \begin{cases} A\left[(A+1)\ln(1+1/A) - 1\right], & n = 1 \\ \dfrac{(A+1)(1+1/A)^{n-1} - A - n}{(n-1)\left[(1+1/A)^n - 1\right]}, & n \neq 1 \end{cases} \tag{5.85}$$

Table 5.2: Analytical solutions for the pressure $p(x)$, the constant K', and v_x^c for different forms of the consistency-index growth function f in the case of a channel with linearly varying wall ($h_1 = 0, \quad h_2 = 1 + \Delta h\, x$). The constant A is computed numerically solving Eq. (5.77).

$f(\alpha p) = 1$	$K' = \dfrac{n}{1/A^n - 1/(A+1)^n}$ $p(x) = \dfrac{\left(\dfrac{A+1}{A+x}\right)^n - 1}{(1+1/A)^n - 1}$ $v_x^c = \dfrac{n^{1/n}\left[(1+1/2n)\Delta h\right]^{1+1/n}}{(1+1/n)\left[1/A^n - 1/(A+1)^n\right]^{1/n}}$
$f(\alpha p) = 1 + \alpha p$	$K' = \dfrac{n\ln(1+\alpha)/\alpha}{1/A^n - 1/(A+1)^n}$ $p(x) = \dfrac{1}{\alpha}\left\{(1+\alpha)^{\left[(A+1)^n/(A+x)^n - 1\right]/\left[(1+1/A)^n - 1\right]} - 1\right\}$ $v_x^c = \dfrac{\left[(1+1/2n)\Delta h\right]^{1+1/n}}{1+1/n}\left[\dfrac{n\ln(1+\alpha)/\alpha}{1/A^n - 1/(A+1)^n}\right]^{1/n}$
$f(\alpha p) = e^{\alpha p}$	$K' = \dfrac{n\left(1-e^{-\alpha}\right)/\alpha}{1/A^n - 1/(A+1)^n}$ $p(x) = -\dfrac{1}{\alpha}\ln\left\{1 - \left(1-e^{-\alpha}\right)\left[\left(\dfrac{A+1}{A+x}\right)^n - 1\right]/\left[(1+1/A)^n - 1\right]\right\}$ $v_x^c = \dfrac{\left[(1+1/2n)\Delta h\right]^{1+1/n}}{1+1/n}\left[\dfrac{n\left(1-e^{-\alpha}\right)/\alpha}{1/A^n - 1/(A+1)^n}\right]^{1/n}$

An analytical expression for Eq. (5.77) can be derived only in the case of linear *g*, i.e. $g(\beta p) = 1 + \beta p$:

$$1 - \left[(2+1/n)A + (1+1/n)I(A)\right]\Delta h = 2Bn\left[1 + \beta I(A)\right] \tag{5.86}$$

As noted above the unyielded core expands downstream in the case of a converging channel and contracts in the diverging channel. As a result, the present lubrication method is applicable only in a range of Δh values:

$$(\Delta h)_{\min} < \Delta h < (\Delta h)_{\max} \tag{5.87}$$

The lower bound is the critical value at which no flow can occur in a converging channel: the expanding core touches the wall at the outlet and breaks at the inlet plane, i.e. $\sigma_1(0) = 1/2$ and $\sigma_1(1) = 0$. From Eq. (5.79), we get $A = -1$ and

$$(\Delta h)_{\min} = -\frac{1}{1+\frac{1}{2n}} \tag{5.88}$$

The upper bound is the critical value at which the contracting unyielded core in an expanding channel breaks at the outlet plane while it touches the wall at the inlet plane, i.e. $\sigma_1(0) = 0$ and $\sigma_1(1) = (1+\Delta h)/2$. In this case, Eq. (5.79) yields $A = 0$ and

$$(\Delta h)_{\max} = \frac{1}{1+1/n} \tag{5.89}$$

In Bingham-plastic flow ($n = 1$), $-2/3 < \Delta h < 1/2$.

Critical Bingham numbers

In the case of a diverging channel ($\Delta h > 0$), $\sigma_1(x)$ is increasing while $\sigma_2(x)$ is decreasing downstream. Therefore, the plug breaks at $x_c = 1$ and $C_c = (1+1/n)(1+\Delta h)$, which gives

$$A_c = \frac{1-(1+1/n)\Delta h}{(2+1/n)\Delta h} \tag{5.90}$$

The first critical Bingham number is given by

$$Bn_{c1} = \frac{(1+1/n)\Delta h(1-I_c)}{2\int_0^1 g(\beta p)\,dx} \tag{5.91}$$

where

$$I_c \equiv I(A_c) = \int_0^1 p_c(x)\,dx \tag{5.92}$$

The flow stops when the two yield surfaces touch the wall at the inlet plane, $x_w = 0$. In this case, $C_w = 2+1/n$, which gives $A_w = 0$. For the second critical Bingham number we get:

$$Bn_{c2} = \frac{1}{2\int_0^1 g(\beta p_F)\,dx} \tag{5.93}$$

where p_F is the pressure corresponding to a flat channel. It should be noted that the integrals $\int_0^1 g(\beta p_F)\,dx$ have been already calculated in Table 5.1, in order to derive the analytical expressions for the yield point σ. By means of Eq. (5.68), these can simply be deduced from Table 5.1 as the ratios σ / Bn. For example, when $f = g = 1+x$,

$$\int_0^1 g(\beta p_F)\,dx = 1-\beta\left[\frac{1}{\alpha}-\frac{1}{\ln(1+\alpha)}\right] \tag{5.94}$$

and therefore

$$Bn_{c2} = \frac{1}{2\left\{1-\beta\left[\frac{1}{\alpha}-\frac{1}{\ln(1+\alpha)}\right]\right\}} \tag{5.95}$$

Similarly, for a converging channel ($\Delta h < 0$), $\sigma_1(x)$ is decreasing while $\sigma_2(x)$ is increasing and thus the plug breaks at $x_c = 0$, $C_c = 1+1/n$ and

$$A_c = \frac{2}{(2+1/n)\Delta h} \tag{5.96}$$

Hence

$$Bn_{c1} = \frac{(1+1/n)(-\Delta h)I_c}{2\int_0^1 g(\beta p)\,dx} \tag{5.97}$$

The flow stops when the two yield surfaces touch the wall at the exit plane, $x_w = 1$, which yields $C_w = (2+1/n)(1+\Delta h)$ and $A_w = -1$. Finally, the second critical Bingham number is given by:

$$Bn_{c2} = \frac{1+\Delta h}{2\int_0^1 g(\beta p_F)\,dx} \tag{5.98}$$

5.5 Numerical results

All the results of this section have been obtained solving numerically Eq. (5.50) by means of forward finite differences and considering only the Bingham-plastic case (n=1) with the rheological parameters depending linearly on pressure. The interval [0,1] has been partitioned using 1001 nodes. In the case of a linearly varying channel, the numerical results compare well with the semi-analytical solution derived in Section 5.4. It should be noted that the latter solution requires the numerical solution of Eq. (5.77) for the constant A, which is not a straightforward task. In the case of linear g, we experimented with an iterative calculation of this constant by means of

$$A^{(m+1)} = \frac{1+2Bn\left[1+\beta I(A^{(m)})\right]-(1+1/n)I(A^{(m)})\Delta h}{2+1/n}, \quad m = 0,1,\cdots \tag{5.99}$$

which is obtained by re-arranging Eq. (5.86). The numerical experiments showed that the above iterative method works very well except only when the Bingham number approaches Bn_{c2}. However, in these flows the numerical method also encounters difficulties due to the very high pressure gradients in the regions where the unyielded core approaches the wall. These are resolved by considering a finer partition of the flow domain.

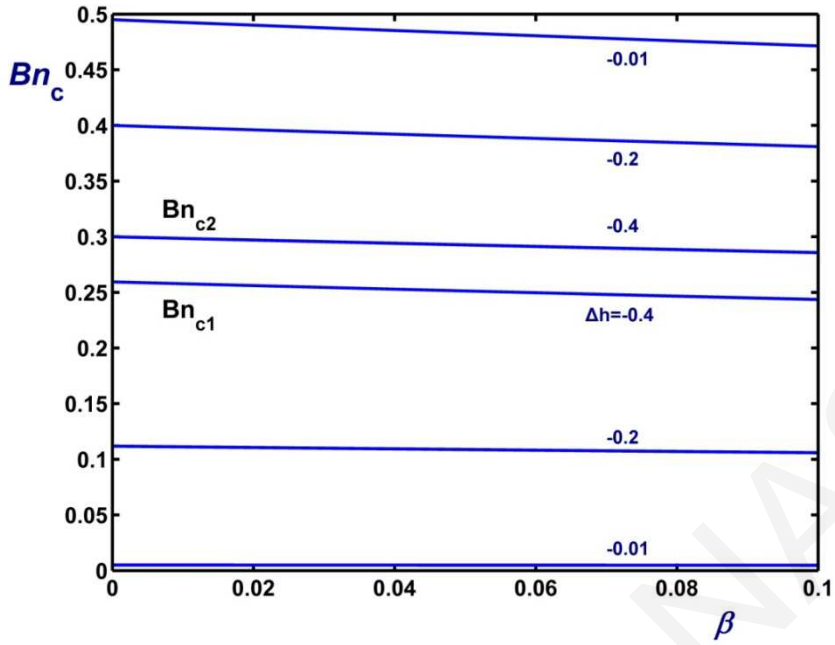

Figure 5.2: Critical Bingham numbers for Bingham flow (n=1) in an asymmetric converging channel ($h_1 = 0, \quad h_2 = 1 + \Delta h, \quad \Delta h < 0$) for $\alpha = 0$ (pressure-independent plastic viscosity).

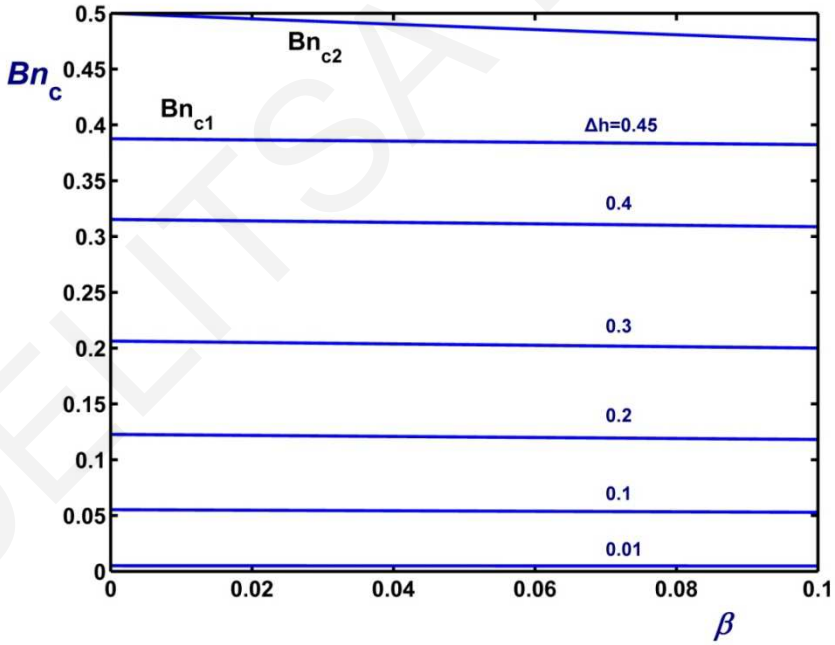

Figure 5.3: Critical Bingham numbers for Bingham flow (*n*=1) in an asymmetric diverging channel ($h_1 = 0, \quad h_2 = 1 + \Delta h, \quad \Delta h > 0$) for $\alpha = 0$ (pressure-independent plastic viscosity).

In Fig. 5.2 we plotted the critical Bingham numbers versus the yield-stress growth parameter β for different values of Δh in the case of flow of a Bingham fluid ($n = 1$) with pressure-independent plastic viscosity ($\alpha = 0$) in a converging channel ($\Delta h < 0$). It can be observed that the window of the method's applicability becomes narrower as Δh tends

towards the critical value of -2/3. This is also true for flow in a diverging channel, as illustrated in Fig. 5.3. However, Bn_{c2} is independent of Δh, as indicated also by Eq. (5.93). We can see in Figs. 5.2 and 5.3 that as Δh goes to zero (flat channel) Bn_{c1} tends to zero.

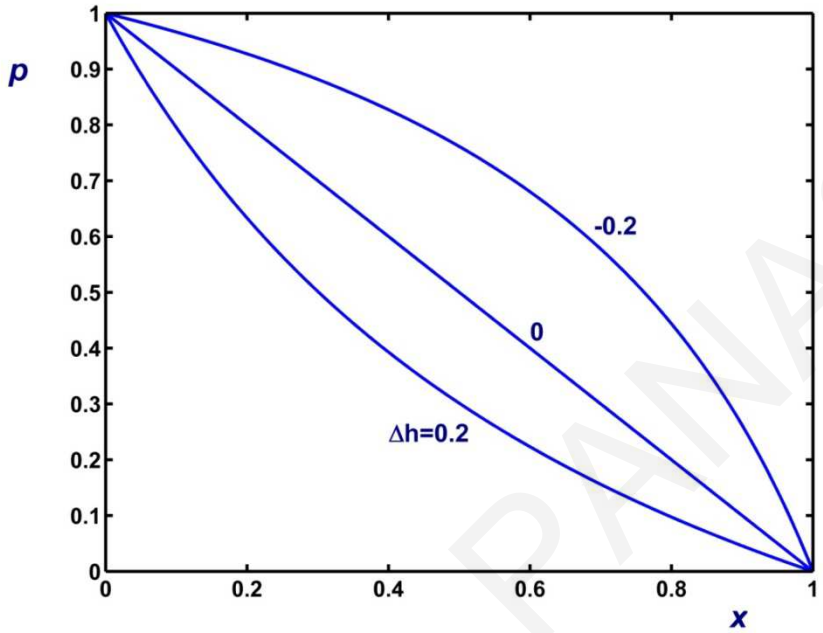

Figure 5.4: Pressure distribution in Bingham flow (n=1) in an asymmetric linearly varying channel with pressure-independent rheological parameters ($\alpha = \beta = 0$) and Bn=0.2 for different values of Δh.

Figure 5.4 shows the pressure distributions for $Bn = 0.2$, $\alpha = \beta = 0$, and different values of Δh. The pressure is linear in the case of a flat channel. In a converging channel, the pressure distribution is concave and the pressure gradient tends to zero at the inlet and to infinity at the outlet as Δh approaches the critical value of -2/3 at which the unyielded core touches the wall at the outlet plane and the flow ceases. In a diverging channel, the pressure distribution is convex and the pressure gradient tends to zero at the outlet and to infinity at the inlet as Δh approaches the critical value of 1/2 at which the unyielded core touches the wall at the inlet plane and the flow ceases. The velocity contours for the three geometries considered in Fig. 5.4 are given in Fig. 5.5, where the shaded regions correspond to the unyielded core. In all the contour plots presented here, 19 equidistant contour lines are drawn.

As dictated by the analysis of the previous sections, the unyielded core in a flat channel is flat and converges in a diverging channel and vice versa. It should be noted that the horizontal velocity of the core is 0.0600, 0.045, and 0.030 for $\Delta h = 0.2, 0$ and -0.2, respectively, whereas the corresponding values of the transverse velocity are 0.0060, 0, and -0.0030, as dictated by Eq. (5.84). The absence of transverse velocity contour lines above the unyielded core indicates that the variation of this component is small in this region.

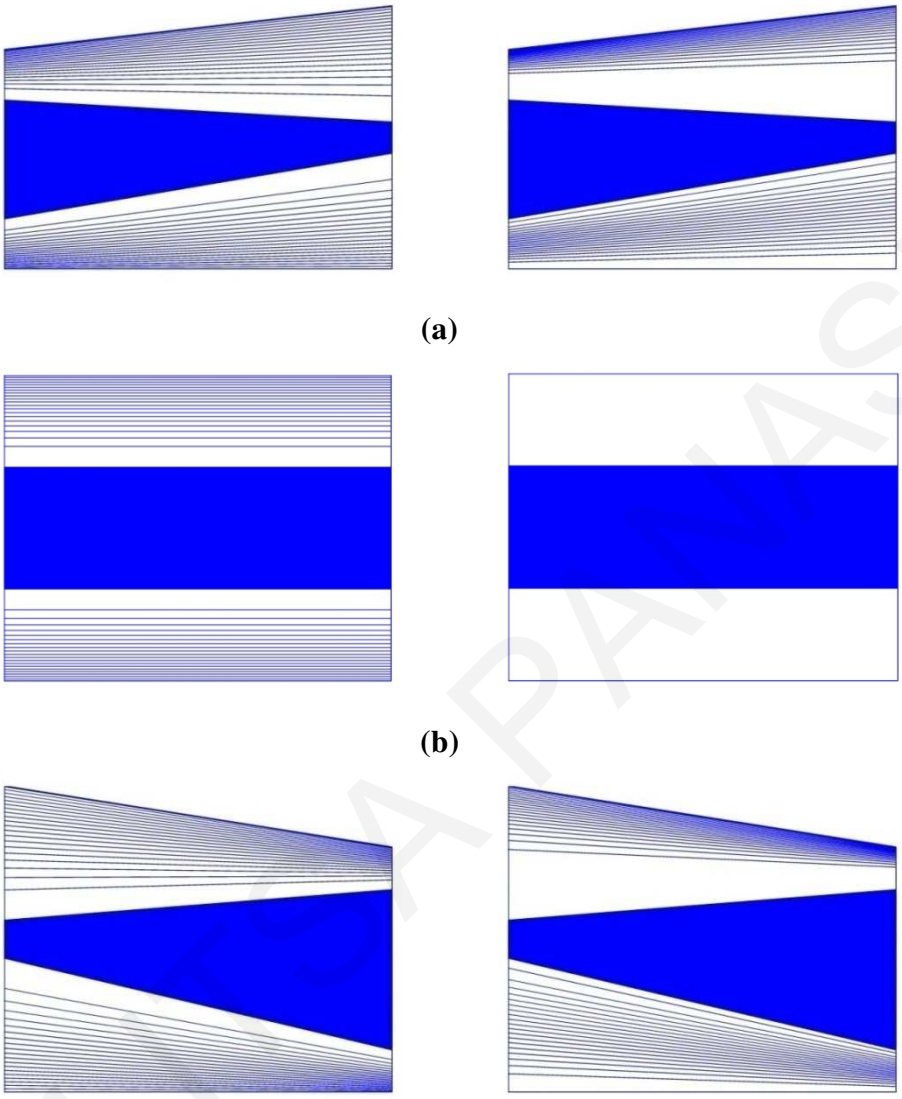

(a)

(b)

(c)

Figure 5.5: Effect of Δh on the contours of the two velocity components (u_x in the left and u_y in the right column) in a linearly varying channel for $Bn = 0.2$, $n = 1$ (Bingham plastic), and $\alpha = \beta = 0$ (constant plastic viscosity and yield stress): (a) $\Delta h = 0.2$ (diverging channel); (b) $\Delta h = 0$ (flat channel); (c) $\Delta h = -0.2$ (converging channel). The unyielded region is shaded.

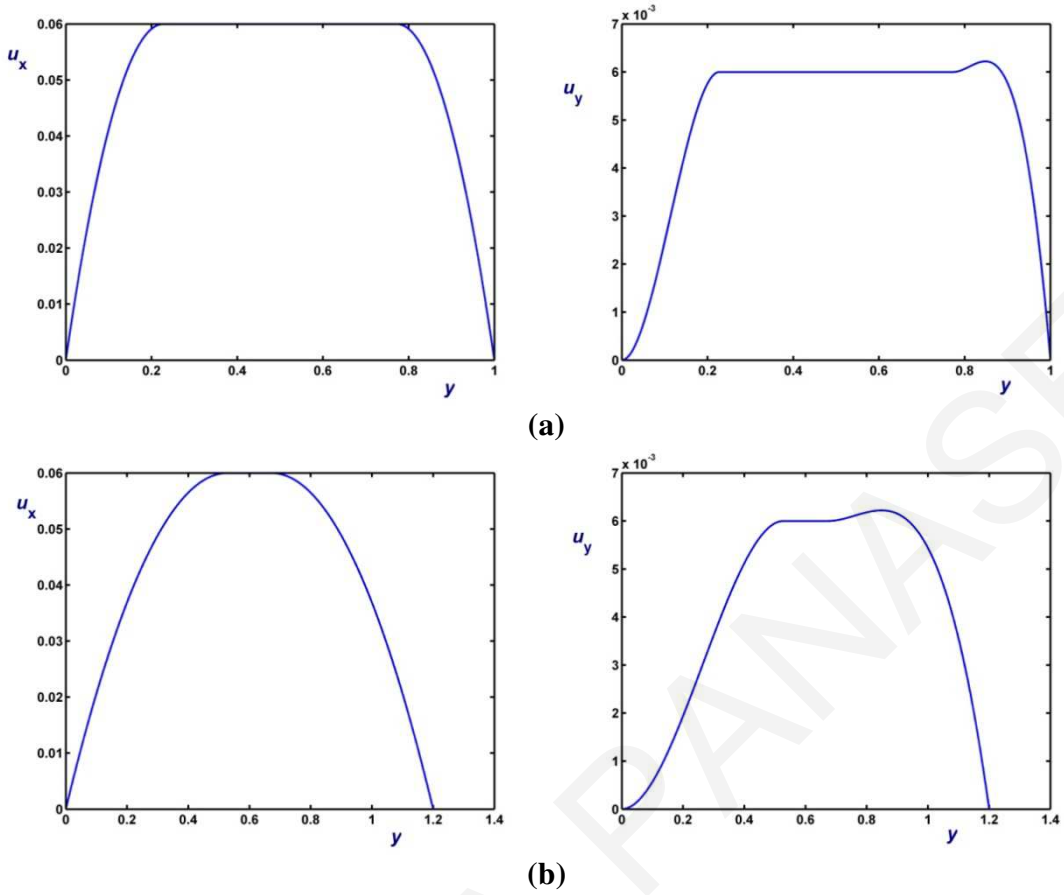

Figure 5.6: Inlet (a) and outlet (b) velocity profiles in the case of flow of a Bingham plastic (n=1) in linearly diverging channel with $\Delta h = 0.2$ when $Bn = 0.2$ and $\alpha = \beta = 0$ (constant plastic viscosity and yield stress).

Indeed, the distributions of u_y are characterized by a global extremum in the aforementioned region which is slightly higher than the positive core velocity in the diverging channel (Fig. 5.6) and slightly lower than the negative core velocity in the converging channel (Fig. 5.7). Note that Figs. 5.6 and 5.7 show the profiles of the two velocity components at the inlet and the outlet planes.

The effect of the Bingham number on the pressure distribution in the case of a converging channel with $\Delta h = -0.2$ is illustrated in Fig. 5.8. Again, the rheological parameters are assumed to be pressure independent ($\alpha = \beta = 0$). As the Bingham number increases from $Bn = Bn_{c1}$=0.1118 towards $Bn_{c2} = 0.4$ the pressure gradient tends to zero near the inlet and to infinity near the exit. The velocity contours for $Bn = Bn_{c1}$, 0.25 and 0.35 are given in Fig. 5.9.

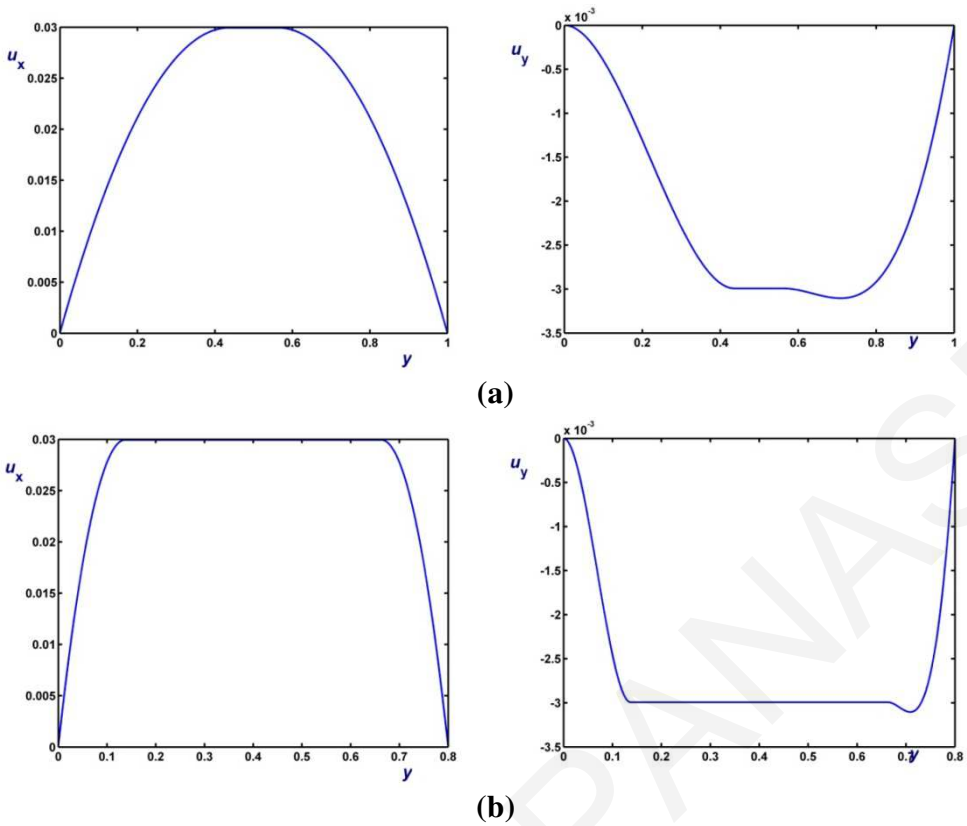

Figure 5.7: Inlet (a) and outlet (b) velocity profiles in the case of flow of a Bingham plastic (n=1) in linearly converging channel with $\Delta h = -0.2$ when $Bn = 0.2$ and $\alpha = \beta = 0$ (constant plastic viscosity and yield stress).

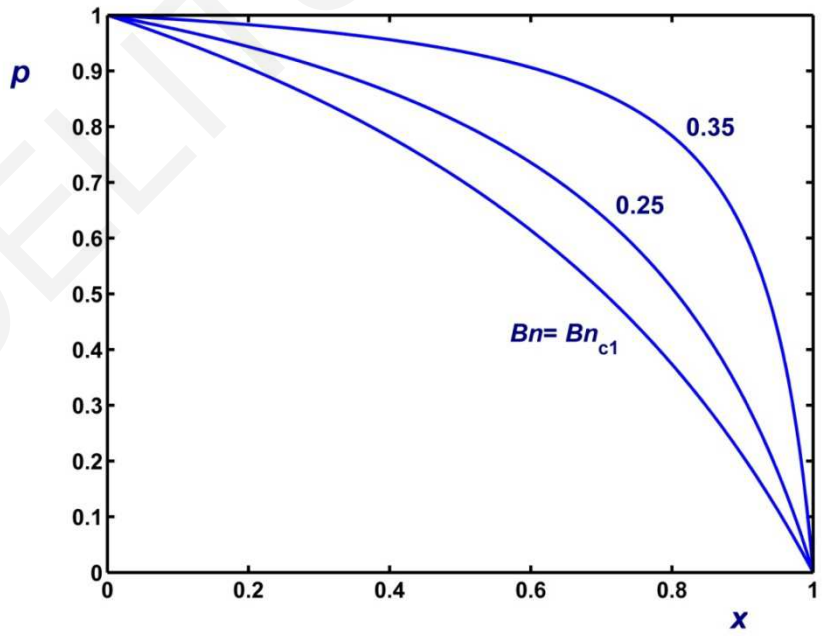

Figure 5.8: Pressure distribution in Bingham flow (n=1) in an asymmetric converging channel with $\Delta h = -0.2$ for various Bingham numbers and $\alpha = \beta = 0$ (pressure-independent rheological parameters).

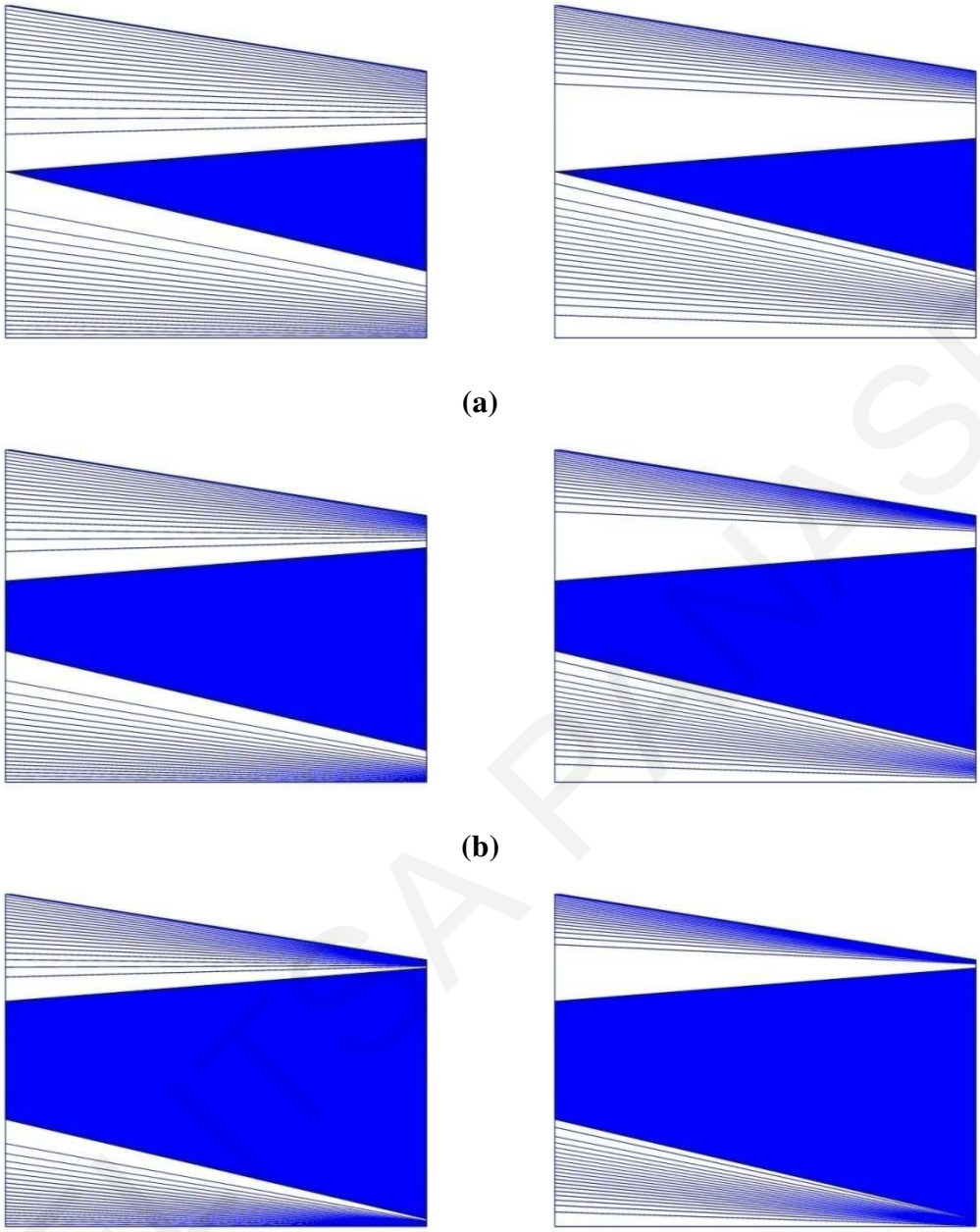

(a)

(b)

(c)

Figure 5.9: Effect of the Bingham number on the contours of the two velocity components (u_x in the left and u_y in the right column) in a linearly channel for $\Delta h = -0.2$, $n = 1$ (Bingham plastic), and $\alpha = \beta = 0$ (constant plastic viscosity and yield stress): (a) $Bn = Bn_{c1} = 0.1118$; (b) $Bn = 0.25$; (c) $Bn = 0.35$. The unyielded region is shaded.

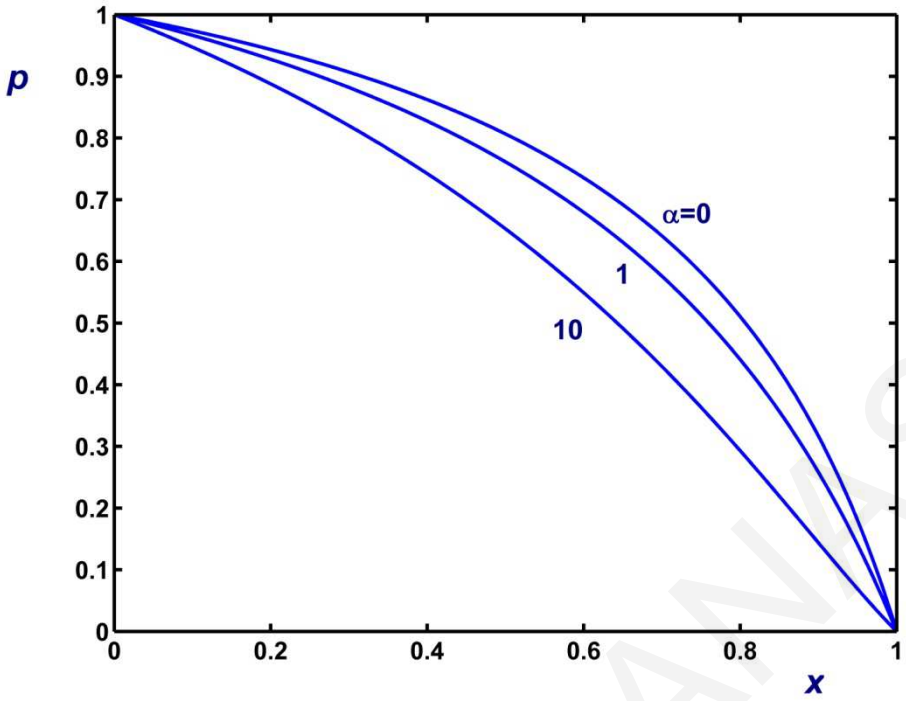

Figure 5.10: Pressure distribution in Bingham flow (n=1) in an asymmetric converging channel with $\Delta h = -0.2$, for $Bn = 0.25$, constant yield stress ($\beta = 0$) and different values of α.

The effect of the plastic-viscosity growth number α for $Bn = 0.25$ and $\beta = 0$ on the pressure distribution is illustrated in Fig. 5.10. The values of α were taken to be rather high in order to magnify the effect of the parameter. As α increases, the pressure distribution tends to become linear while the unyielded core expands slightly, as can be observed in Fig. 5.11, where the velocity contours are also shown.

The effect of the yield-stress growth number β for $Bn = 0.25$ and $\alpha = 0$ is illustrated in Fig. 5.12. Again, rather high values of β are used, in order to enhance the differences. The effect of β is similar to that of the Bingham number, i.e. the pressure gradient increases very rapidly near the exit plane and the unyielded core expands to eventually touch the walls at the exit (Fig. 5.13).

Results have also been obtained for geometries with non-linear wall functions. Figures 5.14 and 5.15 show results obtained in a channel with the following wall functions:

$$h_1(x) = 0.02\sin(2\pi x), \quad h_2(x) = 1 - 0.02\sin(2\pi x) - 0.2x \tag{5.100}$$

These results have been obtained for $Bn = 0.2$, $a = 0$ and three values of the yield-stress growth coefficient, i.e. $\beta = 0, 0.5, \text{and } 1$. The pressure distributions are similar to those obtained for a linearly converging slide. However, the transverse velocity contours exhibit more interesting features. This is also the case with similar geometries, such as that with

$$h_1(x) = 0.1\sin(2\pi x), \quad h_2(x) = 1 - 0.1\sin(2\pi x) - 0.2x \tag{5.101}$$

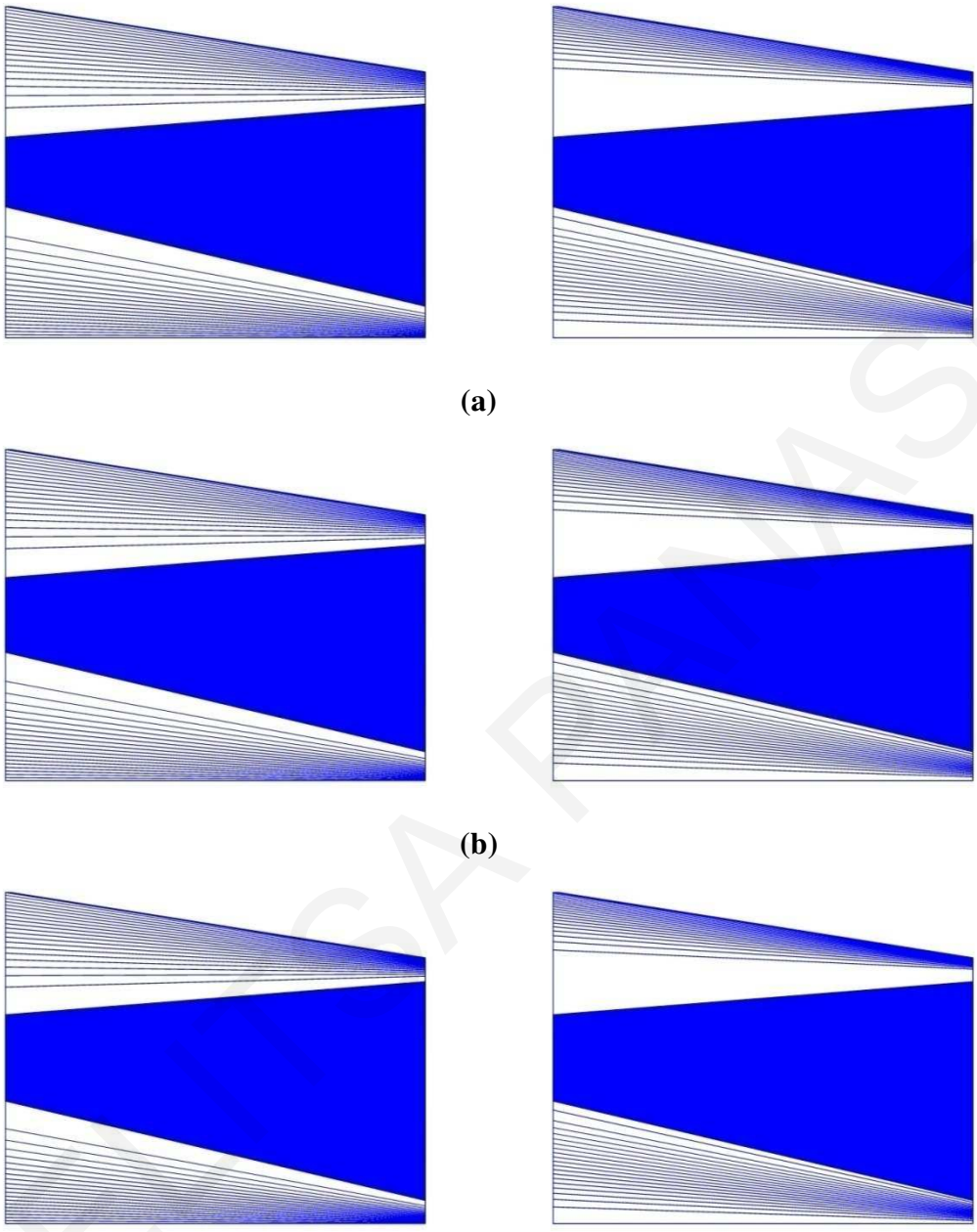

(a)

(b)

(c)

Figure 5.11: Effect of α on the contours of the two velocity components (u_x in the left and u_y in the right column) in a converging channel ($\Delta h = -0.2$) for $Bn = 0.25$, $n = 1$ (Bingham plastic), $\beta = 0$ (constant yield stress): (a) $\alpha = 0$ (constant plastic viscosity); (b) $\alpha = 1$; (c) $\alpha = 10$. The unyielded region is shaded.

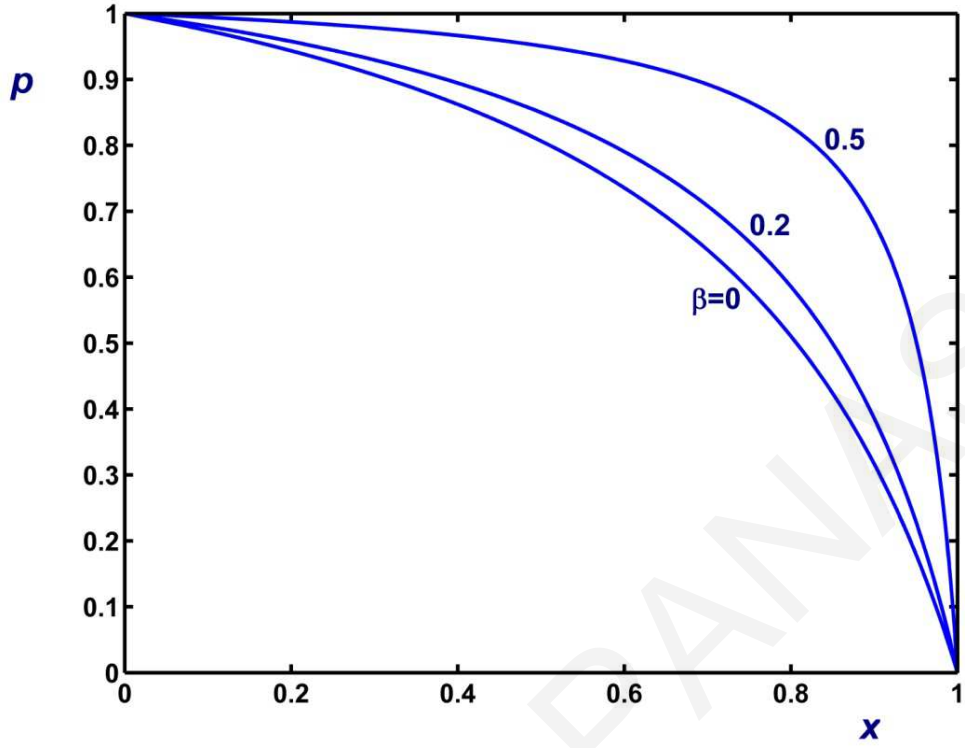

Figure 5.12: Pressure distribution in Bingham flow (n=1) in an asymmetric converging channel with $\Delta h = -0.2$, for $Bn = 0.25$, constant plastic viscosity ($\alpha = 0$) and different values of β.

The results in Figs. 5.16 and 5.17 have been obtained for $\beta = 0, 0.2, \text{and } 0.4$. It can be observed in Fig. 5.17, where the unyielded core is shown together with the velocity contours, that the value of the Bingham number $(Bn = 0.2)$ is close to Bn_{c1} when $\beta = 0$ and gets closer to Bn_{c2} when $\beta = 0.4$, which simply means that the range of Bingham numbers in which the method is applicable is reduced with the yield-stress growth parameter. Recall, however, that the values of β have intentionally been chosen to be high in order to enhance the effects of this parameter.

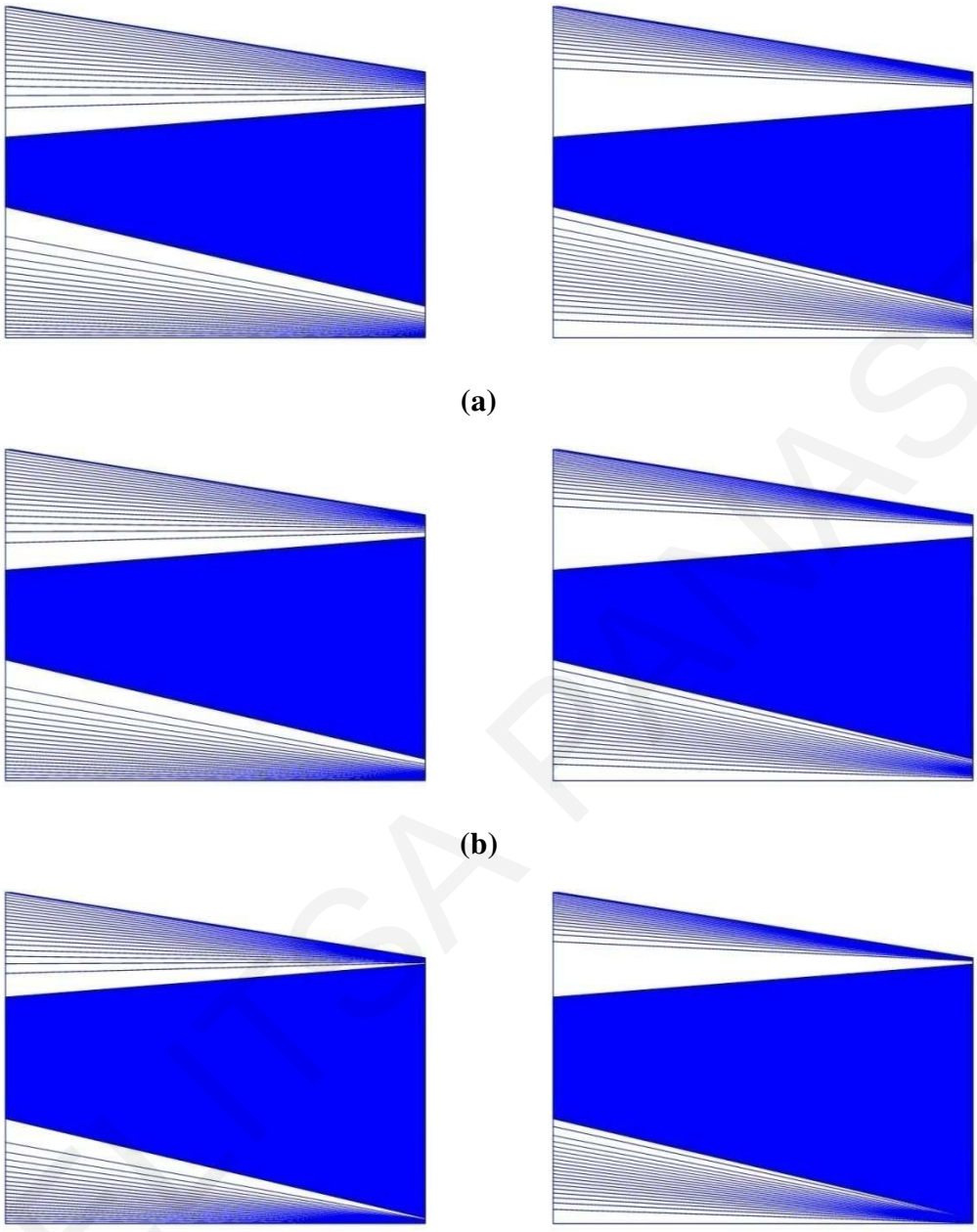

Figure 5.13: Effect of β on the contours of the two velocity components (u_x in the left and u_y in the right column) in a converging channel ($\Delta h = -0.2$) for $Bn = 0.25$, $n = 1$ (Bingham plastic), $\alpha = 0$ (constant plastic viscosity): (a) $\beta = 0$ (constant yield stress); (b) $\beta = 0.2$; (c) $\beta = 0.5$. The unyielded region is shaded.

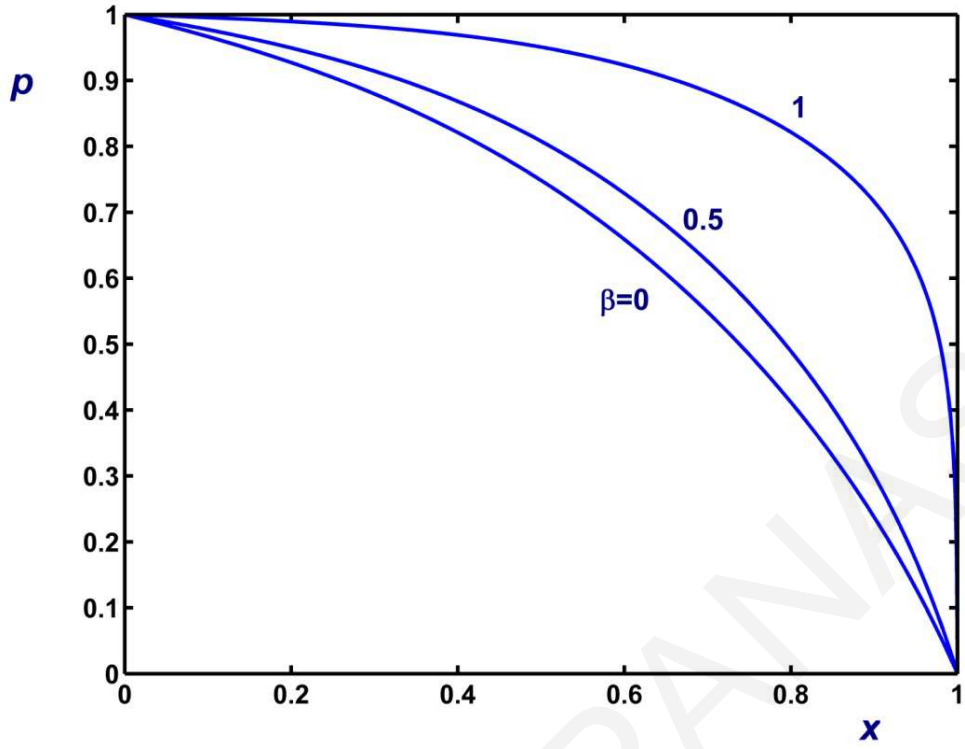

Figure 5.14: Pressure distribution in Bingham flow (n=1) in an asymmetric converging channel described by Eq. (5.100) for $Bn = 0.2$, constant plastic viscosity ($\alpha = 0$) and $\beta = 0, 0.5$ and 1.

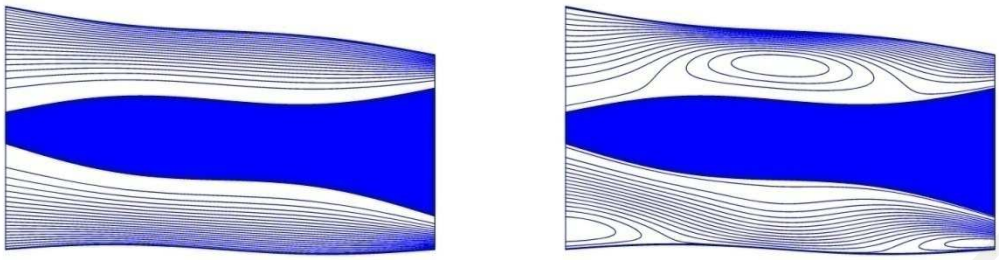

(a)

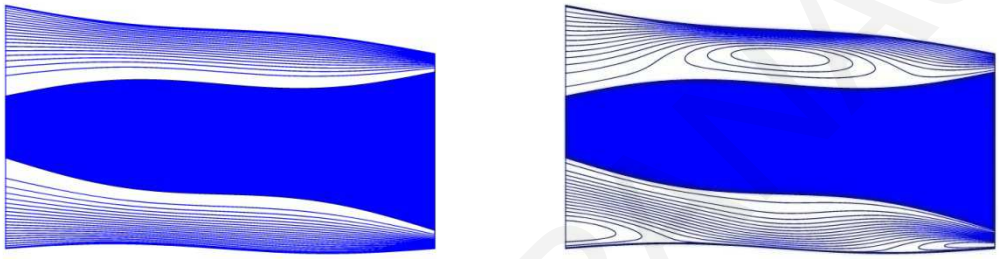

(b)

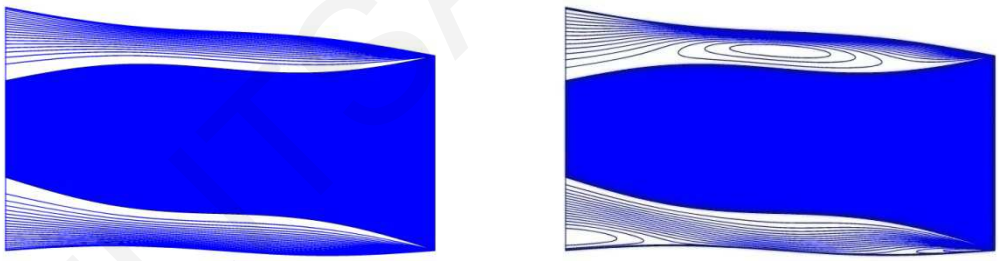

(c)

Figure 5.15: Effect of β on the contours of the two velocity components (u_x in the left and u_y in the right column) in an asymmetric channel described by Eq. (5.100) for $Bn = 0.2$, $n = 1$ (Bingham plastic) and $\alpha = 0$ (constant plastic viscosity): (a) $\beta = 0$ (constant yield stress); (b) $\beta = 0.5$; (c) $\beta = 1$. The unyielded region is shaded.

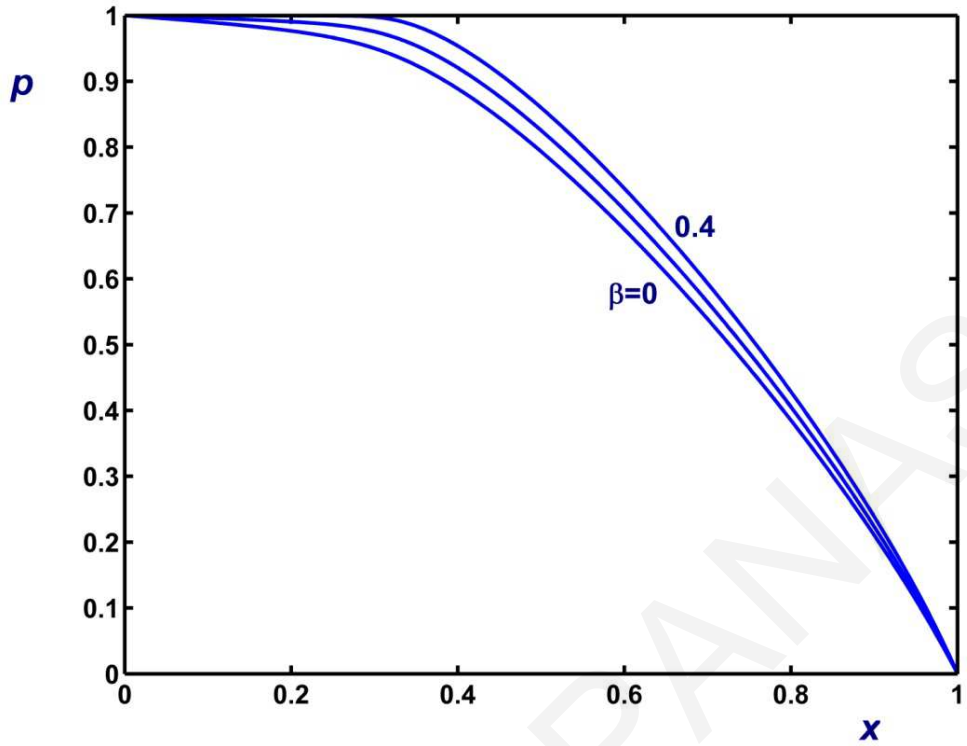

Figure 5.16: Pressure distribution in Bingham flow (n=1) in an asymmetric converging channel described by Eq. (5.101) for $Bn = 0.2$, constant plastic viscosity ($\alpha = 0$) and $\beta = 0, 0.2$ and 0.4.

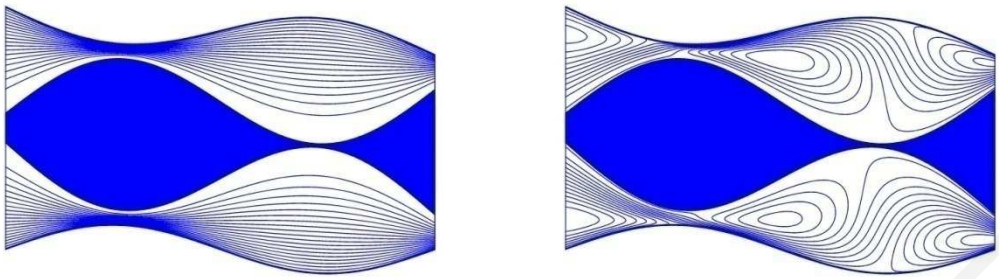

(a)

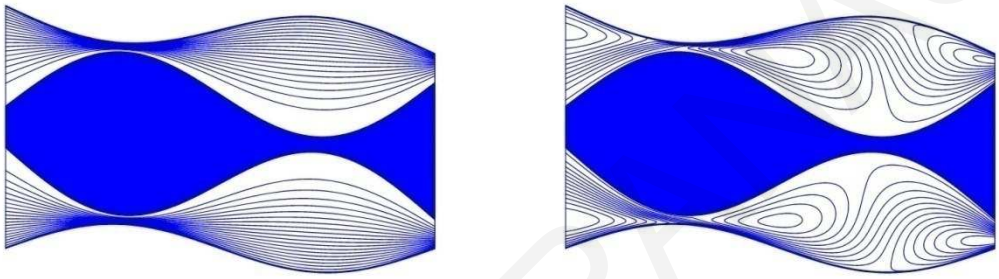

(b)

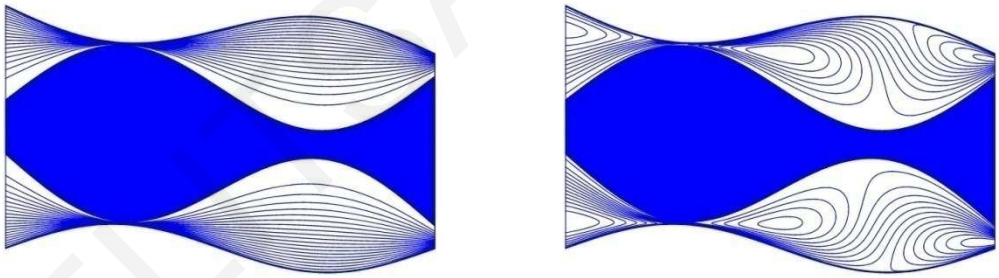

(c)

Figure 5.17: Effect of β on the contours of the two velocity components (u_x in the left and u_y in the right column) in an asymmetric channel described by Eq. (5.101) for $Bn = 0.2$, $n = 1$ (Bingham plastic) and $\alpha = 0$ (constant plastic viscosity): (a) $\beta = 0$ (constant yield stress); (b) $\beta = 0.2$; (c) $\beta = 0.4$. The unyielded region is shaded.

5.6 Conclusions

We have extended the lubrication approximation method of Fusi et al. (2015) to analyze the flow of a Herschel-Bulkley fluid with pressure-dependent rheological parameters in a long, asymmetric channel described by two wall functions, under the assumption that the unyielded core extends from the inlet to the outlet plane of the channel. At zero order, the pressure obeys a first-order integro-differential equation, which is numerically solved in the general case. Then the positions of the yield surfaces as well as the two velocity components are calculated via closed-form analytical expressions. The applicability of the method is restricted to channels where the sum $h_1(x)+h_2(x)$ is a linear function of x and for Bingham numbers between the two critical values corresponding to the breaking of the plug region and to the complete cessation of the flow.

Our analysis revealed that unlike the symmetric case, the transverse velocity of the unyielded core is nonzero. Moreover, the widths of the lower and upper yielded regions are equal for any x and increase with the width of the channel, which implies that the width of the unyielded core increases if the width of the channel decreases and vice versa. The variation of the width of the unyielded core is enhanced by shear thinning and is independent of the other material and flow parameters.

Currently, we are exploring the possibility of applying the present model to non-inertial flows of single-phase yield-stress fluids along an asymmetric fracture (Roustaei et al., 2016) and to the upstream flow in sheet- or wire-coating (Denn, 2008).

Chapter 6

Summary and recommendations for future work

The main objectives of this thesis were the following:

√ To solve the plane Poiseuille flow of a Herschel-Bulkley fluid with asymmetric wall slip, in order to determine the critical conditions for the transition to different flow regimes when the degree of confinement varies, in an attempt to interpret experimental data.

√ To review an extension of Philippou et al. (2016) to the case of viscoplastic flow and investigate the development of the flow in the particular case of a channel with slip only along one wall (asymmetric flow).

√ To extend the lubrication method of Fusi et al. (2015) and derive an approximate semi-analytical solution of both planar and axisymmetric flow of a Herschel-Bulkley fluid with a general wall function and pressure-dependent yield stress and consistency index.

√ To derive analytical lubrication solutions of a Herschel-Bulkley fluid with a general wall function and pressure-dependent yield stress and consistency index, in the case of an asymmetric long channel.

In Chapter 2, the steady, pressure-driven flow of a Herschel-Bulkley fluid in a microchannel was considered assuming that different power-law slip equations apply at the two walls due to slip heterogeneities, allowing the velocity profile to be asymmetric. Three different flow regimes were observed as the pressure gradient was increased. The extension of the different flow regimes depends on the channel gap; in particular the intermediate asymmetric flow regime dominates when the gap becomes smaller than a characteristic length which incorporates the wall slip coefficients and the fluid properties. The theoretical results compared well with available experimental data on soft glassy suspensions. These results open new routes in manipulating the flow of viscoplastic materials in applications where the flow behavior depends not only on the bulk rheology of the material but also on the wall properties.

In Chapter 3, the flow development of a Herschel-Bulkley fluid in a horizontal channel was subsequently considered assuming that slip occurs only on the upper wall due to slip heterogeneities. Hence, the velocity profile was allowed to be asymmetric as was the case in recent experiments on softy glassy suspensions (Vayssade et al., 2014). A power-law slip equation was employed, which generalizes the Navier-slip law. The one-dimensional fully-developed solutions were derived and the different flow regimes were identified. The two-dimensional development flow was solved numerically using finite elements along with the Papanastasiou regularization for the constitutive equation. Numerical results were presented for two values of the power-law exponent, i.e. n=1 (Bingham plastic) and n=1/2 (Herchel-Bulkley fluid). It was demonstrated that the global development length increases with the Bingham number and that flow development was slower near the no-slip wall. The global development length increases with slip exhibiting two plateaus and an intermediate rapid increase zone and doubles in the limit of infinite slip.

Furthermore, in Chapter 4, the lubrication flow of a Herschel-Bulkley fluid in a symmetric long channel of varying width was modeled extending the approach proposed by Fusi et al. (2015) for a Bingham plastic. Moreover, both the consistency index and the yield stress were assumed to be pressure-dependent. With the present model, the pressure was calculated numerically solving an integro-differential equation and then the position of the yield surface and the two velocity components were computed using analytical expressions. Some analytical solutions were also derived for channels of constant and linearly-varying widths. The lubrication solutions for other geometries were calculated numerically. The implications of the pressure-dependence of the material parameters and the limitations of the method were discussed.

In Chapter 5, our investigation was extended to an asymmetric channel. The lubrication flow of a Herschel-Bulkley fluid in a long asymmetric channel was solved extending the method of Fusi et al. (2015), which avoids the lubrication paradox approximating satisfactorily the correct shape of the yield surface at zero order. Both the consistency index and the yield stress were assumed to be pressure-dependent. An interesting feature of the asymmetric flow was that the unyielded zone moves not only in the main flow direction but also in the transverse direction. The two velocity components in both the yielded and unyielded regions were calculated by means of closed-form expressions in terms of the calculated pressure and the two yield surfaces.

As a continuation of the particular thesis, new routes in manipulating the flow of viscoplastic materials in applications can be opened. In that case, the flow behavior depends not only on the bulk rheology of the material but also on the wall properties. Changing the particle-wall interactions and topography, the flow can be manipulated and different velocity profiles can be derived, something that is important in real situations (e.g. oil migration in porous media, inkjet printing). Additionally, an interesting issue that can be also studied is the accurate determination of yielded and unyielded regions in viscoplastic flow development. Furthermore, the method studied in Chapter 4 can be extended to the axisymmetric flow, which is more important in applications.

Even though Housiadas et al. (2018) considered the axisymmetric flow following the approach of Fusi and Farina (2018), they have not studied the case of converging or diverging tubes. Currently, we are exploring the possibility of applying the present model to non-inertial flows of single-phase yield-stress fluids along an asymmetric fracture (Roustaei et al., 2016) and to the upstream flow in sheet- or wire-coating (Denn, 2008).

Bibliography

Adams M.J., Aydin I., Briscoe B.J., Sinha S.K. (1997) A finite element analysis of the squeeze flow of an elasto-viscoplastic paste material, *J. Non-Newtonian Fluid Mech.* **71**, 41-57.

Ahonguio F., Jossic L., Magnin A. (2016) Influence of slip on the flow of a yield stress fluid around a flat plate, *AIChE J.* **62**, 1356-1363.

Aktas S., Kalyon D.M., Marín-Santibáñez B.M., Pérez-González J. (2014) Shear viscosity and wall slip behavior of a viscoplastic hydrogel, *J. Rheology* **58**, 513-535.

Astarita G. (1990) Letter to the Editor: The engineering reality of the yield stress, *J. Rheology* **34**, 275-277.

Ballesta P., Petekidis G., Isa L., Poon W.C.K., Besseling R. (2008) Slip and flow of hard-sphere colloidal glasses, *Phys. Rev. Lett.* **101**, 258301.

Ballesta P., Petekidis G., Isa L., Poon W.C.K., Besseling R. (2012) Wall slip and flow of concentrated hard-sphere colloidal suspensions, *J. Rheology* **56**, 1005-1037.

Ballesta P., Koumakis N., Besseling R., Poon W.C.K., Petekidis G. (2013) Slip of gels in colloid-polymer mixtures under shear, *Soft Matter* **9**, 3237-3245.

Balmforth N.J., Craster R.V. (1999) A consistent thin-layer theory for Bingham plastics, *J. Non-Newtonian Fluid Mech.* **84**, 65-81.

Balmforth N.J., Frigaard I.A., Ovarlez G. (2014) Yielding to stress: Recent developments in viscoplastic fluid mechanics, *Annu. Rev. Fluid Mech.* **46**, 121-146.

Barnes H.A. (1995) A review of the slip (wall depletion) of polymer solutions, emulsions and particle suspensions in viscometers: Its cause, character, and cure, *J. Non-Newtonian Fluid Mech.* **56**, 221-251.

Barnes H.A. (1999) The yield stress - a review or 'πάντα ρει' - everything flows?, *J. Non-Newtonian Fluid Mech.* **81**, 133-178.

Barnes H.A., Walters K. (1985) The yield stress myth?, *Rheol. Acta* **24**, 323-326.

Barus C. (1893) Isothermals, isopiestics and isometrics relative to viscosity, *Amer. J. Sci.* **45**, 87-96.

Bécu L., Manneville S., Colin A. (2006) Yielding and flow in adhesive and nonadhesive concentrated emulsions, *Phys. Rev. Lett.* **96**, 138302.

Bingham E.C. (1922) *Fluidity and Plasticity*, McGraw Hill, New-York.

Bonn D., Denn M.M., Berthier L., Divoux T., Manneville S. (2017) Yield stress materials in soft condensed matter, *Rev. Mod. Phys.* **89**, 035005.

Cloitre M., Borrega R., Monti F., Leibler L. (2003) Glassy dynamics and flow properties of soft colloidal pastes, *Phys. Rev. Lett.* **90**, 068303.

Cloitre M., Bonnecaze R.T. (2017) A review on wall slip in high solid dispersions, *Rheol. Acta* **56**, 283-305.

Cohen Y., Metzner A.B. (1985) Apparent slip of polymer solutions, *J. Rheology* **29**, 67-102.

Coussot P., Ya A., Ovarlez G. (2017) Introduction: yield stress – or 100 years of rheology, *Rheol. Acta* **56**, 161-162.

Damianou Y., Georgiou G.C. (2017) On Poiseuille flows of a Bingham plastic with pressure-dependent rheological parameters, *J. Non-Newtonian Fluid Mech.* **250**, 1-7.

Darley H.C.H., Gray G.R. (1988) *Composition and Properties of Drilling and Completion Fluids*, Gulf Professional Publishing, Houston, Texas.

Daviet G., Bertails-Descourbes F. (2016) Nonsmooth simulation of dense granular flows with pressure-dependent yield stress, *J. Non-Newtonian Fluid Mech.* **234**, 15-35.

Denn M.M. (1980) *Process fluid mechanics*, Prentice Hall, New Jersey.

Denn M.M. (2001) Extrusion instabilities and wall slip, *Ann. Rev. Fluid Mech.* **33**, 265-287.

Denn M.M. (2008) *Polymer Melt Processing*, Cambridge University Press, Cambridge.

Dimakopoulos Y., Makrygiorgos G., Georgiou G.C., Tsamopoulos J. (2018) Your new PAL (Penalized Augmented Lagrangian) Method for Computing Viscoplastic Flows: a Fast Converging Scheme, *J. Non-Newtonian Fluid Mech.* **236**, 23-51.

Dinkgreve M., Denn M.M., Bonn D. (2017) "Everything flows?": elastic effects on startup flows of yield-stress fluids, *Rheol. Acta* **56**, 189-194.

Ellwood K.R.J., Georgiou G.C., Papanastasiou T.C., Wilkes J.O. (1990) Laminar jets of Bingham plastic liquids, *J. Rheology* **34**, 787-812.

Estellé P., Lanos C. (2007) Squeeze flow of Bingham fluids under slip with friction boundary condtion, *Rheol. Acta* **46**, 397-404.

Frigaard I.A., Ryan D.P. (2004) Flow of a visco-plastic fluid in a channel of slowly varying width, *J. Non-Newtonian Fluid Mech.* **123**, 67-83.

Fusi L. (2017) Non-isothermal flow of a Bingham fluid with pressure and temperature dependent viscosity, *Meccanica* **52**, 3577-3592.

Fusi L. (2018) Channel flow of viscoplastic fluids with pressure-dependent rheological parameters, *Physics of Fluids* **30**, 073102.

Fusi L., Farina A. (2018) Peristaltic axisymmetric flow of a Bingham plastic, *Appl. Math. Comp.* **320**, 1-15.

Fusi L., Farina A., Rosso F. (2014) Bingham flows with pressure-dependent rheological parameters, *Int. J. Nonlinear Mech.* **64**, 33-38.

Fusi L., Farina A., Rosso F., Roscani S. (2015) Pressure-driven lubrication flow of a Bingham fluid in a channel: A novel approach, *J. Non-Newtonian Fluid Mech.* **221**, 66-75.

Fusi L., Rosso F. (2018) Creeping flow of a Herschel-Bulkley fluid with pressure-dependent material moduli, *Euro. J. Applied Math.* **29**, 352-368.

Goubert A., Vermant J., Moldenaers P., Göttfert A., Ernst B. (2001) Comparison of measurement techniques for evaluating the pressure dependence of viscosity, *Applied Rheology* **11**, 26-37.

Hartnett J.P., Hu Y.Z. (1989) Technical note: The yield stress – An engineering reality, *J. Rheology* **33**, 671-679.

Hatzikiriakos S.G. (2012) Wall slip of molten polymers, *Progr. Polym. Sci.* **37**, 624-643.

Hatzikiriakos S.G., Dealy J.M. (1991) Wall slip of molten high density polyethylenes. I. Sliding plate rheometer studies, *J. Rheology* **35**, 497-523.

Hatzikiriakos S.G., Dealy J.M. (1992) Wall slip of molten high density polyethylenes. II. Capillary rheometer studies, *J. Rheology* **36**, 703-741.

Hay G., Mackay M.E., McGlashan S.A., Park Y. (2000) Comparison of shear stress and wall slip measurement techniques on a linear low density polyethylene, *J. Non-Newtonian Fluid Mech.* **92**, 187-201.

Hermoso J., Martinez-Boza F., Gallegos C. (2014a) Influence of viscosity modifier nature and concentration on the viscous behaviour of oil-based drilling fluids at high pressure, *Applied Clay Sci.* **87**, 14-21.

Hermoso J., Martinez-Boza F., Gallegos C. (2014b) Combined effect of pressure and temperature on the viscous behaviour of all-oil drilling fluids, *Oil & Gas Sci. and Tech. – Rev. IFP Energies nouvelles* **69**, 1283-1296.

Herschel W., Bulkley R. (1926) Measurement of consistency as applied to rubber-benzene solutions, *Proc. Am. Soc. Test. Mater.* **26**, 621-633.

Hesthaven J.S., Gottlieb S., Gottlieb D. (2007) *Spectral methods for time-dependent problems*, Cambridge University Press, Cambridge.

Housiadas K.D., Ioannou I., Georgiou G.C. (2018) Lubrication solution of the axisymmetric Poiseuille flow of a Bingham fluid with pressure-dependent rheological parameters, *J. Non-Newtonian Fluid Mech.* **260**, 76-86.

Houwen O.H., Geehan T. (1986) Rheology of oil-base muds. *SPE Annual Technical Conference and Exhibition*, Society of Petroleum Engineers, SPE 15416, New Orleans.

Ibeh C.S. (2007) *Investigation on the effects of ultra-high pressure and temperature on the rheological properties of oil-based drilling fluids*, MSc Thesis: Texas A&M University.

Ionescu I.R., Mangeney A., Bouchut F., Roche O. (2015)Viscoplastic modeling of granular column collapse with pressure-dependent rheology, *J. Non-Newtonian Fluid Mech.* **219**, 1-18.

Jiang T.Q., Young A.C., Metzner A.B. (1986) The rheological characterization of HPG gels: Measurement of slip velocities in capillary tubes, *Rheol. Acta* **25**, 397-404.

Kalogirou A., Poyiadji S., Georgiou G.C. (2011) Incompressible Poiseuille flows of Newtonian liquids with a pressure/dependent viscosity, *J. Non-Newtonian Fluid Mech.* **166**, 413-419.

Kalyon D.M. (2005) Apparent slip and viscoplasticity of concentrated suspensions, *J. Rheology* **49**, 621-640.

Khouja N.L., Roquet B., Cazacliu B. (2015) Analysis of a regularized Bingham model with pressure-dependent yield stress, *J. Math. Fluid Mech.* **17**, 723-739.

Kountouriotis Z., Philippou M., Georgiou G.C. (2016) Development lengths in Newtonian Poiseuille flows with wall slip, *Appl. Maths. Comp.* **291**, 98-114.

Langlois W.E., Deville M.O. (2014) *Slow Viscous Flow*, Springer International Publishing, Switzerland.

Lau H.C., Schowalter W.R. (1986) A model of adhesive failure of viscoelastic fluids during flow, *J. Rheology* **30**, 193-206.

Lauga E., Stone H. (2003) Effective slip in pressure-driven Stokes flow, *J. Fluid Mech.* **489**, 55-77.

Laun H.M. (2003) Pressure dependent viscosity and dissipative heating in capillary rheometry of polymer melts, *Rheol. Acta* **42**, 295-308.

Lawal A., Kalyon D.M. (1994) Single screw extrusion of viscoplastic fluids subject to different slip coefficients at screw and barrel surfaces, *Polymer Eng. Sci.* **34**, 1471-1479.

Leal L.G. (1992) *Laminar Flow and Convective Transport Processes*, Elsevier.

Málek J., Rajagopal K.R. (2007) *Mathematical properties of the solutions to the equations governing the flow of fluids with pressure and shear rate dependent viscosities, in Handbook of Mathematical Fluid Dynamics*, Elsevier.

Malkin A., Kulichikhin S., Ilyin S. (2017) A modern look on yield stress fluids, *Rheol. Acta* **56**, 177-188.

Martín-Alfonso M.J., Martinez-Bozam F.J. Navarro F.J., Fernández M., Gallegos C. (2007) Pressure-temperature-viscosity relationship for heavy petroleum fractions, *Fuel* **86**, 227-233.

Meeker S.P., Bonnecaze R.T., Cloitre M. (2004a) Slip and flow of soft particle pastes, *Phys. Rev. Lett.* **92**, 198302.

Meeker S.P., Bonnecaze R.T., Cloitre M. (2004b) Slip and flow in pastes of soft particles: direct observation and rheology, *J. Rheology* **48**, 1295-1320.

Mitsoulis E. (2007) Flows of viscoplastic materials; Models and computation, *Rheology Reviews* **2007**, 135-178.

Mitsoulis E., Tsamopoulos J. (2017) Numerical simulations of complex yield-stress fluid flows, *Rheol. Acta* **56**, 231-258.

Müller-Mohnssen H., Löbl P., Schauerte W. (2007) Direct determination of apparent slip for a ducted flow of polyacrylamide solutions, *J. Rheology* **31**, 323-336.

Muravleva L. (2016) Squeeze flow of Viscoplastic Bingham Material. *VII European Congress on Computational Methods in Applied Sciences and Engineering*, Crete, Greece.

Navier C.L.M.H. (1827) Sur les lois du mouvement des fluides, *Mem. Acad. R. Sci. Inst. Fr.* **6**, 389-440.

Neto C., Evans D.R., Bonaccurso E., Butt H.J., Craig V.S.J. (2005) Boundary slip in Newtonian liquids: a review of experimental studies, *Rep. Prog. Phys.* **68**, 2859-2897.

Ookawara S., Ogawa K., Dombrowski N., Amooie-Foumeny E., Riza A. (2000) Unified entry length correlation for Newtonian, power law and Bingham fluid in laminar pipe flow at low Reynolds numbers, *J. Chem. Eng. Japan* **33**, 675-678.

Oron A., Davis S.H., Bankoff S.G. (1997) Long-scale evolution of thin liquid films, *Rev. Mod. Phys.* **69**, 931-980.

Ortega-Avila J.B., Pérez-González J., Marín-Santibáñez B.M., Rodríguez-González F., Aktas S., Malik M., Kalyon D.M. (2016) Axial annular flow of a viscoplastic microgel with wall slip, *J. Rheology* **60**, 503-515.

Osisanya S.O., Harris O.O. (2005) Evaluation of equivalent circulating density of drilling fluids under high pressure/high temperature conditions, *SPE Annual Technical Conference and Exhibition*, Society of Petroleum Engineers, SPE 97018.

Ovarlez G, Rodts S., Ragouilliaux A., Coussot P., Goyon J., Colin A. (2008) Wide-gap Couette flows of dense emulsions: Local concentration measurements, and comparison between macroscopic and local constitutive law measurements through magnetic resonance imaging, *Phys. Rev. E.* **78**, 036307.

Panaseti P., Vayssade A.L., Georgiou G.C., Cloitre M. (2017) Confined viscoplastic flows with heterogeneous wall slip, *Rheol. Acta* **56**, 539-553.

Panaseti P., Damianou Y., Georgiou G.C., Housiadas K.D. (2018) Pressure-driven flow of a Herschel-Bulkley fluid with pressure-dependent rheological parameters, *Phys. Fluids* **30**, 030701.

Panaseti P., Georgiou G.C. (2017) Viscoplastic flow development in a channel with slip along one wall, *J. Non-Newtonian Fluid Mech.* **248**, 8-22.

Papanastasiou T.C. (1987) Flows of materials with yield, *J. Rheology* **31**, 385-404.

Papanastasiou T.C. (1989) Lubrication Flows, *Chem. Eng. Educ.* **24**, 50-56.

Papanastasiou T.C., Georgiou G.C., Alexandrou A. (2000) *Viscous Fluid Flow*, CRC Press, Boca Raton.

Pérez-González J., López-Durán J.J., Marín-Santibáñez B.M., Rodríguez-González F. (2012) Rheo-PIV of a yield-stress fluid in a capillary with slip at the wall, *Rheol. Acta* **51**, 937-946.

Philippou M., Kountouriotis Z., Georgiou G.C. (2016) Viscoplastic flow developemt in tubes and channels with wall slip, *J. Non-Newtonian Fluid Mech.* **234**, 69-81.

Piau J.M., El Kissi N. (1994) Measurement and modeling of friction in polymer melts during macroscopic slip at the wall, *J. Non-Newtonian Fluid Mech.* **54**, 121-142.

Politte M.D. (1985) Invert oil mud rheology as a function of temperature and pressure, *SPE/ IADC Drilling Conference*, SPE 13458, New Orleans.

Poumaere A., Moyers-González M., Castelain C., Burghelea T. (2014) Unsteady laminar flows of a Carbopol gel in the presence of wall slip, *J. Non-Newtonian Fluid Mech.* **205**, 28-40.

Princen H.M. (1985) Rheology of foams and highly concentrated emulsions. II. Experimental study of the yield stress and wall effects for concentrated oil-in-water emulsions, *J. Colloid Interface Sci.* **105**, 150-171.

Putz A., Frigaard I.A., Martinez D.M. (2009) On the lubrication paradox and the use of regularization methods for lubrication flows, *J. Non-Newtonian Fluid Mech.* **163**, 62-77.

Rajagopal K.R. (2006) On implicit constitutive theories for fluids, *J. Fluid Mech.* **550**, 243-249.

Renardy M. (2003) Parallel shear flows of fluids with a pressure-dependent viscosity, *J. Non-Newtonian Fluid Mech.* **114**, 229-236.

Roustaei A., Chevalier L., Talon L., Frigaard I.A. (2016) Non-Darcy effects in fracture flows of a yield stress fluid, *J. Fluid Mech.* **805**, 222-261.

Salmon J.B., Bécu L., Manneville S., Colin A. (2003) Towards local rheology of emulsions under Couette flow using Dynamic Light Scattering, *Eur. Phys. J. E.* **10**, 209-223.

Saramito P., Wachs A. (2017) Progress in numerical simulation of yield stress fluid flows, *Rheol. Acta* **56**, 211-230.

Seth J., Cloitre M., Bonnecaze R.T. (2008) Influence of short-range forces on wall-slip inmicrogel pastes, *J. Rheology* **52**, 1241-1268.

Seth J.R., Mohan L., Locatelli-Champagne C., Cloitre M., Bonnecaze R.T. (2011) A micromechanical model to predict the flow of soft particle glasses, *Nat. Mater.* **10**, 838-843.

Seth J., Locatelli-Champagne C., Monti F., Bonnecaze R.T., Cloitre M. (2012) How do soft particle glasses yield and flow near solid surfaces?, *Soft Matter* **8**, 140-148.

Shah R., London A. (1978) *Laminar flow forced convection in ducts: a source book for compact heat exchanger analytical data*, Academic Press, New York.

Shewan H.M., Stokes J.R., Cloitre M. (2017) Particle-wall tribology of slippery hydrogel particle suspensions, *Soft Matter* **13**, 2099-2106.

Sochi T. (2011) Slip at fluid-solid interface, *Polymer Reviews* **51**, 309-340.

Spikes H., Granick S. (2003) Equation for slip of simple liquids at smooth solid surfaces, *Langmuir* **19**, 5065-5071.

Staron L., Lagrée P.Y., Popinet S. (2012) The granular silo as a continuum plastic flows: the hour-glass vs the clepsydra, *Phys. Fluids* **24**, 103301.

Stokes G.G. (1845) On the theories of the internal friction of fluids in motion, and of the equilibrium and motion of elastic solids, *Trans. Camb. Phil. Soc.* **8**, 287-305.

Suslov S.A., Tran T.D. (2008) Revisiting plane Couette-Poiseuille flows of piezo-viscous fluid, *J. Non-Newtonian Fluid Mech.* **154**, 170-178.

Vayssade A.L., Lee C., Terriac E., Monti F., Cloitre M., Tabeling P. (2014) Dynamical role of slip heterogeneities in confined flows, *Phys. Rev. E.* **89**, 052309.

Venner C., Lubrecht A.A. (2000) *Multilevel methods in lubrication*, Elsevier.

Wang Y. (1998) Axial flow of generalized viscoplastic fluids in non-circular ducts, *Chem. Eng. Commun.* **168**, 13-43.

Yilmazer U., Kalyon D.M. (1989) Slip effects in capillary and parallel disk torsional flows of highly filled suspensions, *J. Rheology* **33**, 1197-1212.